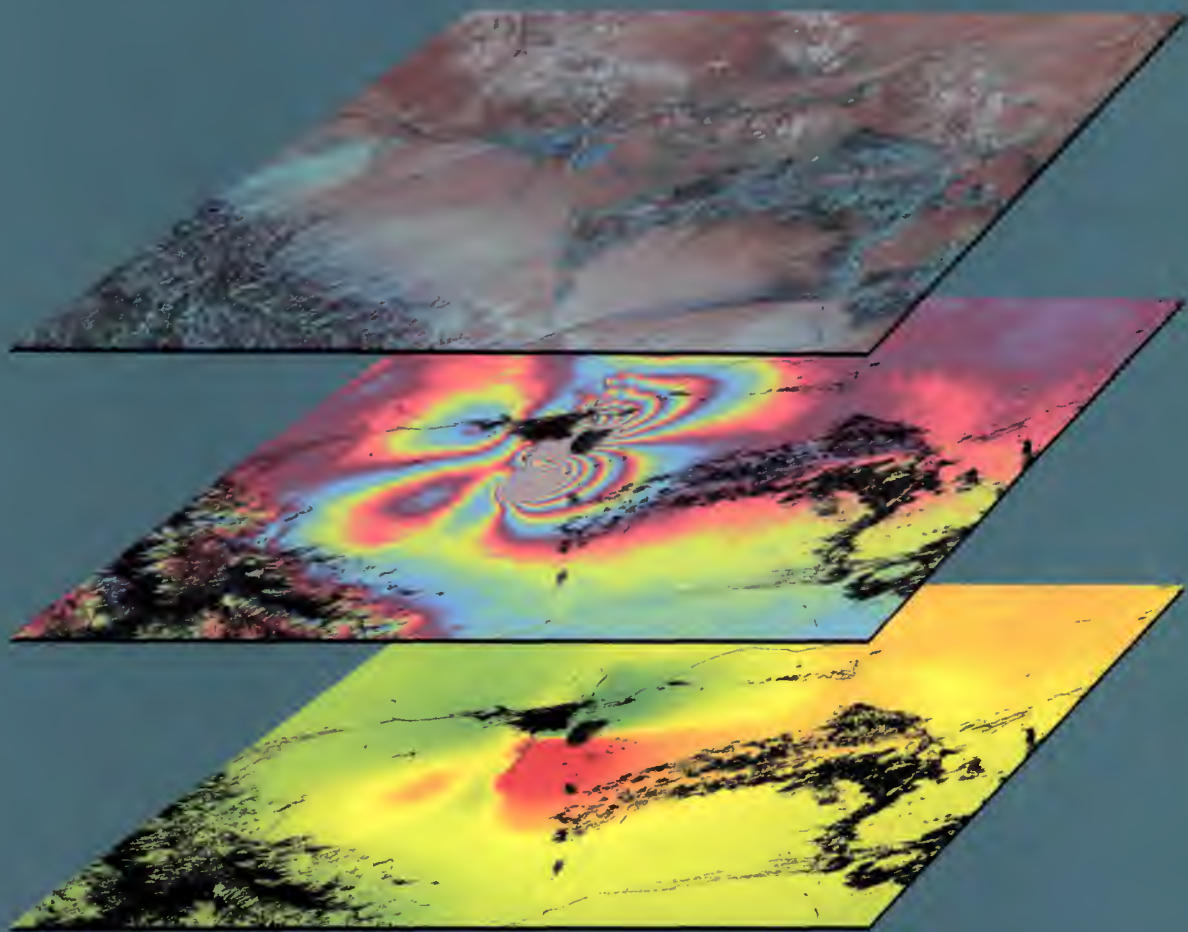
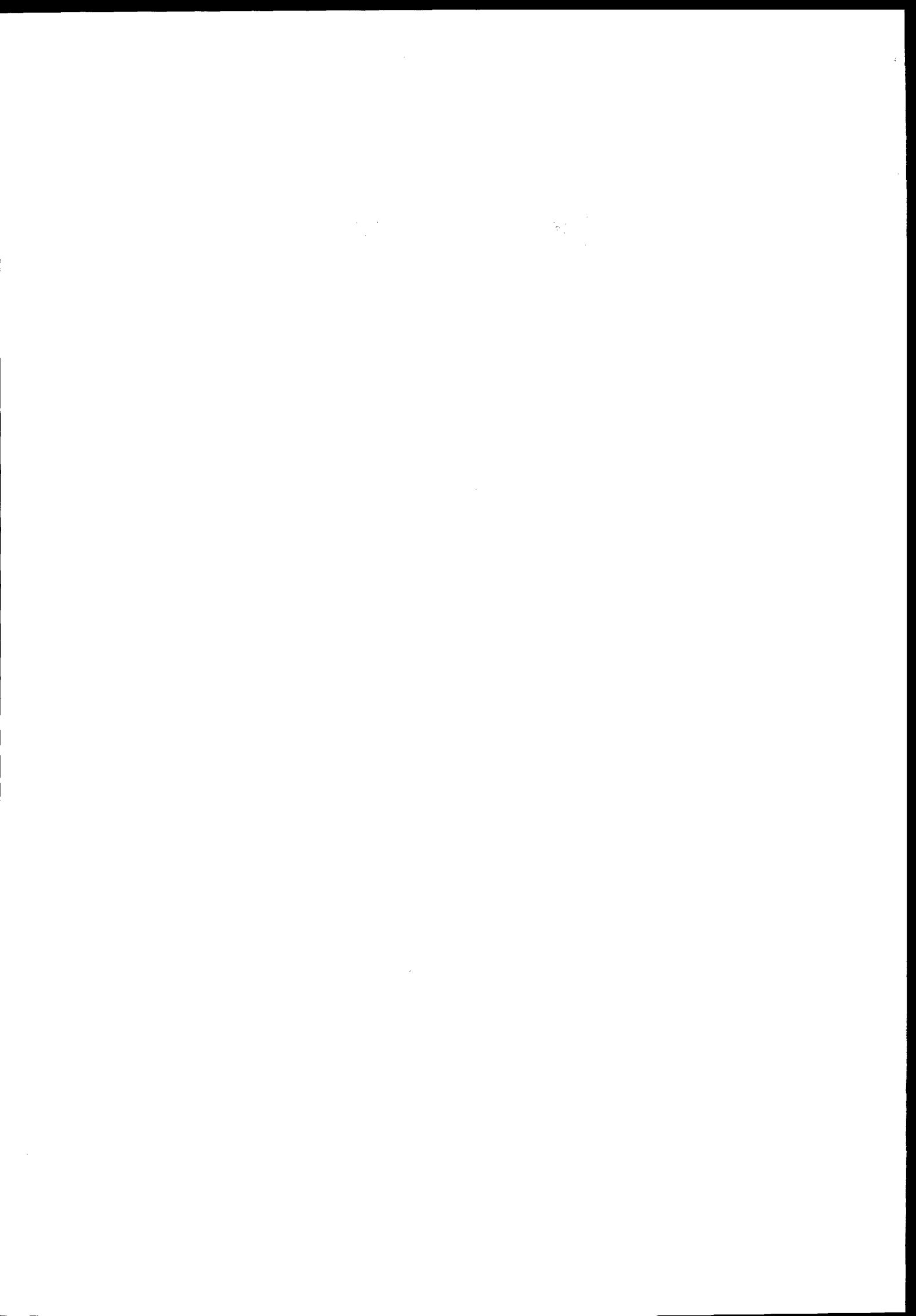


Spaceborne radar applications in Geology



An introduction to imaging radar, and application examples
of ERS SAR in Geology and Geomorphology

GEN137



Spaceborne radar applications in Geology

**An introduction to imaging radar,
and application examples of ERS SAR
in Geology and Geomorphology**

Cover: the Bam earthquake

Images for analysis of the earthquake of 26 December 2003 in Bam (Iran), based on a data pair from the ENVISAT ASAR acquired in IM mode, on 3 December 2003 (before) and 11 February 2004 (after).

Top: combination of coherence (red), difference (green) and mean amplitude (blue) of the two images.

- Reddish indicates high coherence and magenta also high backscatter, but overall no change in backscatter between the two dates. Features appearing in these colours are: plains, hills and gentle slope mountains with little or no vegetation
- Greenish indicates change in backscatter but low coherence. Probably indicates local changes in the soil moisture
- Cyan/greenish indicates low coherence and change in backscatter. Shows irrigated agriculture, vegetated mountains, but also trees and shrubs along dry river courses
- Blue indicates high backscatter on both acquisitions plus low coherence. The destroyed town of Bam and other newly-eroded areas are blue. The steep mountainous regions (bottom left corner) are blue due to high mean backscatter and very low coherence, typical of layover zones.

Middle: differential interferogram: a reference InSAR DEM was used to subtract topography-induced fringes. One colour cycle indicates a change in distance towards the satellite of 2.8 cm or a multiple thereof. Here, the maximum rupture in the strike-slip fault at the surface was about 30 cm horizontally. The narrower the fringes, the greater the Earth movement, and hence the greater the stress on the surface. This can indicate the destructive power on buildings in those locations.

Bottom: Coloured deformation map, black indicating the areas of low coherence (irrigated or vegetated zones, and some river beds, but also urban areas if much changed or, as in this case, there has been major destruction). The colours show that the sense of the displacement was different in the two areas of high co-seismic deformation (also shown by the fringe colour trend in the differential interferogram). Bam lies amid the areas showing opposite displacement direction; this suggests that an active fault actually crosses the town.

(Images generated by the SARscape® commercial software package, copyright sarmap s.a.)

Authors

Case Studies, Chapters 6 to 19:

Damien Dhont, Assistant Professor at University of Pau et des pays de l'Adour (France)
Jean Chorowicz, Professor at University of Paris 6 (France)
Bernard Collet, PhD Doctor at University of Paris 6 (France)

Introduction to SAR for Geology, Chapters 1 to 5 and 20 to 22:

Massimo Barbieri, SARMap (Switzerland)
Juerg Lichtenegger, ESA/ESRIN, Frascati (Italy)

Scientific and technical coordination:

Juerg Lichtenegger
Damien Dhont

Publication: Spaceborne radar applications in Geology
(ESA TM-17, December 2005)

Editor: Karen Fletcher

Design and layout: Isabel Kenny

Published by: ESA Publications Division, ESTEC
Postbus 299, 2200 AG Noordwijk, The Netherlands
Tel: +31 71 565 3400
Fax: +31 71 565 5433

Printed in: The Netherlands

Price: €40

ISBN: 92-9092-225-7

ISSN: 1013-7076

Copyright: © 2005 European Space Agency

Abstract

This document is intended for geologists who are interested in broadening their knowledge of interpretation of imaging radar data, but also addresses the general public for reference and information. It introduces imaging radar as it may be used by technicians and image interpreters, stressing the use of synthetic aperture radar (SAR) for Earth observation in general and for geology in particular. Interferometric SAR is briefly treated, with some basic and practical hints. An illustrated application study on land subsidence is included. SAR/optical data fusion is explained, with examples of the different methods suggested.

The main part of the document, part II, consists of 14 case studies that demonstrate the potential of SAR imagery for geology. These studies cover themes such as the detection and mapping of neotectonic activity, tectonic mapping, and recognition of karst structures, as well as analysis of active lahars and other volcanic events. They look into drainage systems in desert areas, consider lithofacies changes and morphostructure texture analysis, and they demonstrate the geological mapping of active tectonic compression. Finally, the document mentions the key points of the ESA SAR missions. Contacts for further information are also provided.

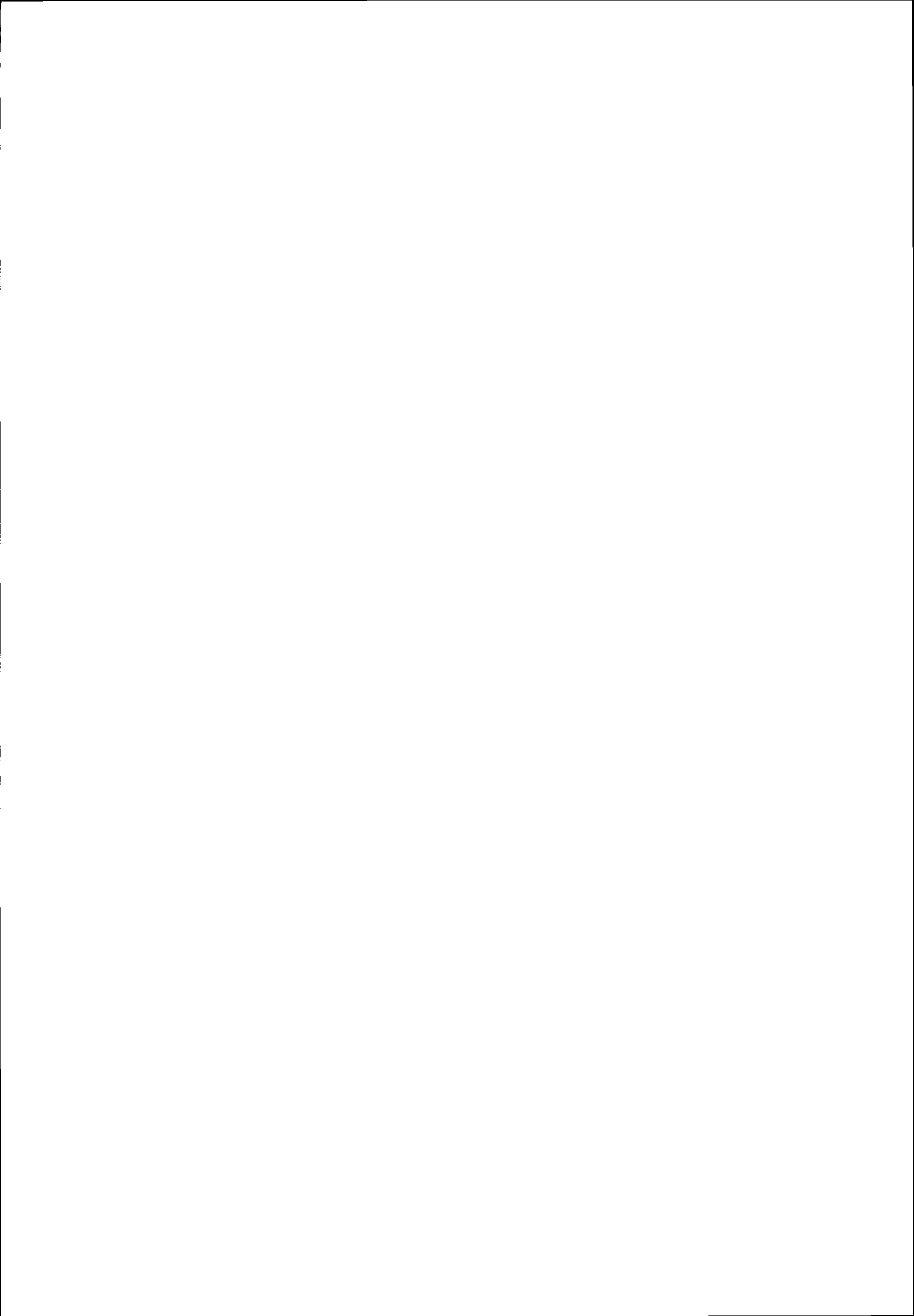


Table of contents

Abstract	iii
List of Figuresix
Preamblexiii

Part I - Introduction to SAR

1. Radar basic characteristics	
1.1 Introduction	1-1
1.2 The electromagnetic spectrum	1-4
1.3 Basic characteristics of SAR data	1-6
1.4 Geometric and radiometric distortions in SAR imagery	1-9
1.5 References	1-12
2. SAR data post-processing	
2.1 Introduction	2-1
2.2 Brief description of ERS SAR product specifications	2-1
2.3 Image filtering	2-4
2.4 Integrated use of radar and radar/optical imagery	2-7
2.5 References	2-12
3. Data processing in SAR interferometry	
3.1 Introduction	3-1
3.2 Interferometry concepts and applications	3-2
3.3 Practical hints for interferometry	3-6
4. Principles of radar image analysis	
4.1 Radar characteristics of natural objects	4-1
4.2 Extraction of geological features from ERS SAR imagery	4-4
4.3 Radar characterisation of geological objects	4-8
4.4 Radar imagery of meteorite impact craters on Earth	4-10
5. Detection and mapping of neotectonic activity	
5.1 Earthquake	5-1
5.2 Volcanism	5-3
5.3 Mining Subsidence	5-4
5.4 Conclusions	5-13
5.5 References	5-14

Part II - Case studies

Overview of the case studiesII-iii
6. Detection of structures related to strike-slip deformation	
Case study: the Erzincan area along the North Anatolian Fault (Turkey)	
6.1 Geological framework	6-1
6.2 Analysis of SAR ERS images	6-3
6.3 References	6-6

7. Karst features	
Case study: Collision area of Eastern Anatolia	
7.1 Geologic framework	7-1
7.2 Approach	7-2
7.3 Analysis of the Afsin-Elbistan region	7-3
7.4 References	7-6
8. Analysis of active lahar events	
Case study: SAR ERS imagery of the Pinatubo (Philippines)	
8.1 Overview of the studied event	8-1
8.2 SAR image dated 9 July 1993	8-2
8.3 SAR image dated 13 August 1993	8-5
8.4 Colour composition	8-7
8.5 References	8-9
9. Drainage systems in desert areas covered by sand veil	
Case study: Southern Tanezrouft system (Sahara)	
9.1 Overview of the studied area	9-1
9.2 Analysis of southern Tamanrasset-El Djouf system	9-2
9.3 Tectonic deformations	9-4
9.4 Conclusions	9-5
9.5 References	9-5
10. Rain and flood effects	
Case study: Vaison-la-Romaine area (France)	
10.1 Maps of the studied area	10-1
10.2 Approach	10-2
10.3 Image analysis	10-4
10.4 Conclusion	10-5
11. Morphology analysis and foreshortening effects	
Case study: Rift tectonics in the West Afar Margin	
11.1 Geologic framework	11-1
11.2 ERS SAR data analysis	11-3
11.3 References	11-10
12. Morphology and major faults	
Case study: Large shear zones between the Dinarides-Albanides-Hellenides and the Balkans	
12.1 Geological framework	12-1
12.2 Data and image processing	12-2
12.3 Analysis	12-4
12.4 Reference	12-5
13. Evidence of mountain uplift from slope analysis using SAR ERS image	
Case study: The Alps	
13.1 Geological context	13-1
13.2 SAR ERS image	13-3
13.3 Interpretation from ECORS-CROP profile	13-4
13.4 References	13-4

14. Lithofacies change revealed by SAR ERS imagery	
Case study: the sigmoid of Przemysl, Carpathians	
14.1 Regional geological framework	14-1
14.2 The sigmoid of Przemysl	14-2
14.3 Analysis of the SAR ERS imagery	14-3
14.4 Model of evolution	14-6
14.5 References	14-7
15. SAR ERS images used to relate tectonics to shape and distribution of volcanic vents	
Case study: Iceland	
15.1 Geodynamic setting	15-1
15.2 Satellite imagery analysis	15-2
15.3 Tectonics	15-8
15.4 Volcanic vents	15-9
15.5 Geometric relationships between tectonic features and vents	15-9
15.6 References	15-10
16. Expression of morpho-structures on SAR ERS imagery – escape tectonics at a front belt	
Case study: SW Irian Jaya (West Papua)	
16.1 Geologic framework	16-1
16.2 Morphotectonics and satellite imagery analysis	16-2
16.3 Early compression	16-4
16.4 Aiduna fault zone: wrenching followed by normal faulting	16-6
16.5 Late escape tectonics	16-7
16.6 References	16-9
17. Texture analysis for geological mapping in tropical Africa	
Case study: Côte d'Ivoire	
17.1 Regional geological context	17-1
17.2 Local geomorphological context	17-2
17.3 Method of analysis	17-4
17.4 Lithologic mapping	17-7
17.5 New mapping of the granites	17-7
17.6 Distinction within the volcano-sedimentary series	17-10
17.7 Mapping of known ductile faults	17-10
17.8 New mapping of faults	17-10
17.9 Conclusions	17-11
17.10 References	17-11
18. Detection of active compressional structures on SAR ERS imagery	
Case study: the Central Japan seismic area	
18.1 Structural framework	18-1
18.2 SAR ERS imagery	18-2
18.3 Observations and interpretations	18-5
18.4 Conclusions	18-8
18.5 References	18-8

19. Radar imagery observation	
Case study: the “Levant” transform structure in Lebanon	
19.1 Geologic framework	19-1
19.2 Satellite imagery analysis	19-2
19.3 References	19-7

Part III - Potential applications of ERS SAR data

20. Monitoring sea ice	
20.1 Drilling activities in polar regions	20-1
20.2 Offshore operations	20-2
21. Coastal zones	
21.1 Ocean floor and coastal zone surveys	21-1
21.2 References	21-4
22. Open ocean	
22.1 Sea surface height	22-1
22.2 Seafloor mapping	22-1
22.3 Marine gravity anomaly measurements	22-1
22.4 References	22-6

Annexes

Annex A: Key points of ESA SAR missions and data application	
On the oceans	A-1
On land	A-1
Envisat	A-2
Annex B: Finding out more	B-1
Annex C: Geological timescale	C-1
Annex D: Glossary	D-1

List of Figures and Tables

Table i:	Polar-orbiting satellite SAR missions	.xiv
Table ii:	Space shuttle SAR missions	.xiv
Figure 1-1:	Concept of an imaging radar	.1-1
Figure 1-2:	Imaging radar geometry and spatial resolution	.1-2
Figure 1-3:	ERS SAR (synthetic aperture radar) imaging parameters	.1-3
Figure 1-4:	Envisat ASAR modes	.1-3
Figure 1-5:	Electro-magnetic spectrum	.1-4
Figure 1-6:	Microwave band nomenclature	.1-5
Table 1-1:	Frequency bands used in telecommunication and radar	.1-5
Figure 1-7:	Synthetic antenna (aperture) concept for radar	.1-6
Figure 1-8:	Multitemporal SAR scene of Pavia (Italy)	.1-7
Figure 1-9:	Foreshortening and shadowing	.1-9
Figure 1-10:	Layover and elongation	.1-10
Figure 1-11:	Comparison between Landsat 5 TM and ERS SAR images	.1-12
Figure 2-1:	ERS.SAR.PRI product	.2-2
Figure 2-2:	ERS.SAR.GEC product	.2-2
Figure 2-3:	ERS.SAR.GTC product	.2-3
Figure 2-4:	ERS SAR image of Rome and surroundings before and after temporal filtering	.2-4
Figure 2-5:	SAR data filtering using the mean	.2-5
Figure 2-6:	Comparison of original SAR data with a Gamma Map filtered image	.2-6
Figure 2-7:	Principal Component Analysis	.2-8
Figure 2-8:	The colour double-cone	.2-9
Figure 2-9:	SAR/optical data fusion (Wadi El' Allaqi, Egypt & Sudan Boundary)	.2-10
Figure 2-10:	Combination of SAR and Landsat data by PCA (Hoggar, Algeria)	.2-12
Figure 3-1:	Interferometric imaging geometry: two passes pointing to one resolution element	.3-2
Figure 3-2:	Example of a coherence image	.3-4
Figure 3-3:	Interferogram of the Tiber Valley area (Italy)	.3-5
Figure 3-4:	Interferogram of the area of the Kronsneen in northwestern Svalbard	3-7
Figure 4.1:	ERS SAR scene of the Strait of Tunis (Tunisia), in the Mediterranean Sea	.4-2
Figure 4-2:	Microwave interactions with vegetation	.4-3
Figure 4-3:	Bosumtwi meteorite impact crater, Nigeria (parallel orbits)	.4-5
Figure 4-4:	Bosumtwi meteorite impact crater, Nigeria (crossing orbits)	.4-5
Figure 4-5:	Barringer meteorite impact crater in Arizona (USA)	.4-11
Figure 5-1:	Interferogram of an earthquake	.5-2
Figure 5-2:	Mount Etna, fringes from a differential interferogram	.5-4
Figure 5-3:	Location map of studied areas of mining subsidence (Poland)	.5-5
Figure 5-4:	SAR images of mining subsidence	.5-6

Figure 5-5:	Diagram of subsidence trough with photographed landscape superimposed	5-7
Figure 5-6:	Interpretation of a SAR interferogram in a subsidence trough	5-8
Table 5-1:	Characteristics of ERS SAR SLCI data for interferometric processing	5-9
Figure 5-7:	Subsidence within the Muchowiec airport area (Poland)	5-9
Figure 5-8:	Series of three interferogram pairs of subsidence in Katowice Poland	5-11
Figure 5-9:	GIS display of subsidence in the Szczyglowice Coal Mine	5-12
Table 5-2:	Summary of coal seams mined in Szczyglowice	5-13
Figure II-i:	Locations of the case studies	II-iii
Table II-i:	Case studies and data application types	II-iv
Figure 6-1:	Geological framework of Anatolia and location of the studied area (rectangle)	6-1
Figure 6-2:	Fault pattern in the eastern NAF area from maps, DEM and satellite image interpretations	6-2
Figure 6-3:	ERS scenes of the Erzincan basin area acquired in descending orbits	6-3
Figure 6-4:	ERS scenes of the Erzincan basin area acquired in ascending orbits	6-4
Figure 6-5:	ERS image of the Ovacik fault showing left-lateral displacement of the Euphrates	6-5
Figure 6-6:	Interpretation of the tectonic evolution of the Erzincan basin	6-6
Figure 7-1:	Location of the Anatolian area studied	7-2
Figure 7-2:	Fault pattern from interpretation of the DEM	7-3
Figure 7-3:	SAR ERS image of the Afsin-Elbistan region	7-4
Figure 7-4:	Structural analysis	7-5
Figure 7-5:	Karst morphology expressed in the positive radar image	7-6
Figure 7-6:	Detail of the typical high backscatter and karst macro-texture	7-6
Figure 8-1:	Location map of the two Pinatubo SAR ERS-1 scenes	8-1
Figure 8-2:	Pinatubo area at the end of the dry season	8-2
Figure 8-3:	Pinatubo area during a typhoon event	8-2
Figure 8-4:	Mount Pinatubo area (Philippines)	8-3
Figure 8-5:	SAR ERS images of the Bucao river region	8-4
Figure 8-6:	SAR ERS images of the Sto. Tomas-Marella river region	8-5
Figure 8-7:	Fan-like structure formed during typhoon Pining	8-7
Figure 8-8:	Colour composite SAR ERS images for identification of lahars	8-8
Figure 9-1:	Location of the Tanezrouft desert	9-1
Figure 9-2:	SAR ERS-1 image of southern Tamanrasset-El Djouf system	9-3
Figure 9-3:	SPOT image of southern Tamanrasset-El Djouf system	9-3
Figure 10-1:	Location in France	10-1
Figure 10-2:	Study area	10-2
Figure 10-3:	The river location before the flood	10-3
Figure 10-4:	The river location after the flood	10-3
Figure 10-5:	The forested location before the flood	10-3
Figure 10-6:	The forested location after the flood	10-3
Figure 10-7:	Colour composite image of positive SAR ERS-1	10-4
Figure 11-1:	Location of the Afar case study	11-1
Figure 11-2:	Location of the Afar study area	11-2
Figure 11-3:	SAR mosaic of the Afar & Borkena graben	11-4

Figure 11-4: Key observations of Figure 11-3	11-5
Figure 11-5: Layover effect giving false dips	11-6
Figure 11-6: Explanation of relief distortion	11-6
Figure 11-7: Landsat image of the West Afar margin shown in Figure 11-5	11-7
Figure 11-8: ERS-1 SAR image of the Borkena basin	11-8
Figure 11-9: Structural interpretation of Figure 11-8	11-8
Figure 11-10: Tectonic models	11-9
Figure 11-11: Model of the Borkena graben evolution in two tectonic stages	11-9
Figure 12-1: The studied area of the Balkans	12-1
Figure 12-2: Mosaic of three SAR ERS images	12-2
Figure 12-3: Landsat-TM scene as RGB colour composition	12-3
Figure 12-4: Digital elevation model of the area	12-4
Figure 13-1: DEM showing a general view of the Alps	13-1
Figure 13-2: Structural scheme of the Western Alps	13-2
Figure 13-3: Geological cross-section of the Western Alps	13-2
Figure 13-4: SAR ERS image of the studied area	13-3
Figure 13-5: ECORS-CROP profile interpretation	13-4
Figure 14-1: Structural framework of the Western and Central Carpathians	14-1
Figure 14-2: Structural sketch-map of the Przemysl area (location shown in Figure 14-1)	14-2
Figure 14-3: ERS-1 SAR image of Przemysl	14-3
Figure 14-4: Explanation of lines in Figure 14-3	14-4
Figure 14-5: Detailed analysis of the SAR ERS image of Figure 14-3 (southern part)	14-5
Figure 14-6: Model of structural evolution	14-6
Figure 15-1: Location of the two SAR ERS scenes of Iceland	15-1
Figure 15-2: The studied area in Iceland	15-2
Figure 15-3: SAR ERS-1 scene of 31 August 1992	15-3
Figure 15-4: SAR ERS-1 scene of 30 July 1992	15-3
Figure 15-5: Stereo set of SAR ERS images	15-3
Figure 15-6: Anaglyph image of the stereo set of Figure 15-5 (3-D glasses required)	15-4
Figure 15-7: Window from SPOT over Iceland, and its interpretation	15-5
Figure 15-8: Statistics concerning structural and volcanic features in Iceland	15-6
Figure 15-8 (continued)	15-7
Figure 15-9: Interpretation of the right-hand image of Figure 15-5	15-8
Figure 16-1: Simplified geodynamic setting of New Guinea	16-1
Figure 16-2: SAR ERS-1 image of Irian Jaya	16-2
Figure 16-3: Interpretation of the SAR ERS-1 image of Figure 16-2	16-3
Figure 16-4: Landsat and ERS-1 views of the SW Yera Umar Block	16-5
Figure 16-5: Landsat and ERS-1 views of the Aiduna River	16-6
Figure 16-6: Extract of a SAR-ERS-1 image of the fossilised, uplifted and eroded alluvial fan	16-7
Figure 16-7: Map sketch and cross section of the post-collisional setting	16-8
Figure 17-1: Geological framework of Côte d'Ivoire study	17-1
Figure 17-2: Synthetic geological map of the Côte d'Ivoire region studied	17-3
Figure 17-3: Synthetic tele-analytic geological map	17-4

Figure 17-4: SAR ERS scene of Ferkessedougou-Ouangolodougou region	17-5
Table 17-1: Characteristics of major image-facies in the Ferkessedougou area . . .	17-6
Figure 17-5: Tele-analytic geological map from SAR ERS image of Figure 17-4 .	17-7
Figure 17-6: SAR ERS scene of Tafiré region	17-8
Figure 17-7: Tele-analytic geological map obtained from SAR ERS image of Figure 17-6	17-9
Figure 18-1: DEM of Japan and location of the studied area	18-1
Figure 18-2: Plate diagram of the Japan area	18-2
Figure 18-3: Image of SAR ERS-1 scene 1	18-2
Figure 18-4: Image of SAR ERS-1 scene 2	18-3
Figure 18-5: Image of SAR ERS-1 scene 3	18-3
Figure 18-6: Synthetic map of tectonic and volcanic features from SAR ERS images	18-4
Figure 18-7: Estimate of the displacement X of the Main Tectonic Line	18-6
Figure 18-8: Windows extracted from the SAR images (location in Figure 18-6) .	18-7
Figure 19-1: Tectonic setting of the Levant Transform Zone	19-1
Figure 19-2: Northern Lebanon and Western Syria	19-2
Figure 19-3: Detail of the pull-apart structure A from Figure 19-2	19-3
Figure 19-4: SAR ERS image covering Northern Lebanon and Western Syria . . .	19-3
Figure 19-5: Detail of the pull-apart basin, C	19-4
Figure 19-6: Structural observations in the Faraya Valley, east of Beirut City . .	19-5
Figure 19-7: SAR image of the Beirut region	19-6
Figure 19-8: ERS SAR image of Beirut region, ascending orbit	19-7
Figure 20-1: ERS SAR image of the Fram Strait (between Greenland and Norway)	20-1
Figure 20-2: ERS SAR images of the pipeline project site	20-2
Figure 21-1: Geo-referenced ERS SAR image along the Belgian coast	21-1
Figure 21-2: Detail of the geo-referenced ERS SAR image	21-2
Figure 21-3: Imaging mechanism of a SAR of a sea surface	21-2
Figure 21-4: Bottom topography map	21-3
Figure 22-1: Measuring the effect of a seamount on water surface	22-2
Figure 22-2: Gravity anomaly map derived from satellite geoid height measurements	22-3
Figure 22-3: The Indian Ocean Triple Junction	22-4
Figure 22-4: Gravity map of the Gulf of Mexico	22-5

Preamble

This document is not only intended for people with a background in geology; it can be leafed through by anyone involved in environment-related studies, or by young students eager to learn about new technologies which can be applied for a better understanding of geological and geophysical phenomena on our planet.

The document content deals essentially with the use of ERS (European Radar Satellite) synthetic aperture radar (SAR) data as a primary and/or secondary source of information. In this context, it provides details on other data types (e.g. optical images, high-resolution data, geophysical data, field surveys, etc.) that can be integrated with ERS SAR products in order to investigate geological issues more thoroughly.

When introducing a complex subject such as the use of SAR for geological applications, one can start by speaking about the instrument, or equally about the geological features to be detected. It was decided firstly to introduce the principles of microwaves, continuing with SAR instrument peculiarities and with the SAR image geometry. Secondly, the SAR data products are explained and some basics of SAR image post-processing introduced. Thirdly, the document explores the different image-processing techniques aimed at the extraction of geological information from ERS SAR data. New and very promising InSAR (SAR interferometry) methodologies have recently been developed as tools both for monitoring the stability of large engineering works and for detecting and measuring ground deformations on the Earth's surface (e.g. subsidence, earthquakes, landslides, volcanic activity, etc.). Finally, the greater part of the document provides practical examples (case studies) that highlight the potential of SAR imagery for geology-related applications.

Some characteristics of radar remote sensing have demonstrated their usefulness since the early seventies:

- Radar is independent of solar illumination and atmospheric conditions, thus it is an important source of information for mapping areas where it is almost impossible to acquire data by optical sensors due to persistent cloud coverage (e.g. the tropics), or for arctic regions where solar illumination is limited to the summer months
- Where soil density and humidity are extremely low, radar also permits one to obtain information on subsurface features
- Radar imaging parameters are very different from those of optical images

The first civilian imaging radar sensors were side-looking airborne radar (SLAR), which acquired data over North America and over some tropical regions. One of the main constraints for using radar instruments on space-borne missions was the low spatial resolution, and it needed the development of the synthetic aperture radar (SAR) in order to achieve spatial resolution of the order of 5 to 30 m. The first SAR systems were launched starting at the end of the seventies by the USA and the Soviet Union. The USA launched Seasat-1, the first satellite mission, which failed after only 100 days, followed by a series of shuttle missions: SIR-A, SIR-B; SIR-C and SRTM of 1 to 2 weeks duration each. The Soviet Union launched Almaz-1. Tables 1 and 2 provide some key statistics on the space-borne SAR missions from 1978 onwards.

Satellite	Agency & country	Launch year	Altitude (km)	Frequency band (GHz)	Polarisation	Incidence angle	Antenna size (m x m)	Noise equiv. σ^0 (dB)	Swath width (km)	Azimuth resolution (m)
Seasat	NASA, USA	1978	800	L (1.3)	HH	23°	10.7 x 2.2	-18	100	23
Almaz	RSA, USSR	1991	280	S (3)	HH	30° - 60°	15 x 1.5 (two)		25 - 50	15
ERS	ESA, Europe	1991	785	C (5.3)	VV	23°	10 x 1	-18	100	25
J-ERS	NASDA, Japan	1992	565	L (1.2)	HH	35°	12 x 2.2	-20	75	30
Radarsat	CCRS, Canada	1995	792	C (5.3)	HH	20° - 50°	15 x 1.6	-21	50 - 500	5-28
Envisat	ESA, Europe	2002	800	C (5.3)	VV HH	20° - 50°	10 x 1.5	-18	100-400	25-100

Table i: Polar-orbiting satellite SAR missions

The launch of ERS-1 (European Radar Satellite no.1) in 1991 by the European Space Agency marked the beginning of the first long-term Earth observation radar mission. The use of ERS data has initially been applied to environmental studies mainly related to oceanography, geology, and agriculture.

Satellite	Agency & country	Launch year	Altitude (km)	Frequency band (GHz)	Polarisation	Incidence angle	Antenna size (m x m)	Noise equiv. σ^0 (dB)	Swath width (km)
SIR-A	NASA, USA	1981	259	L (1.28)	HH	50°	9.4 x 2.2	-25	50
SIR-B	NASA, USA	1984	225	L (1.28)	HH	15° - 60°	10.7 x 2.2	-35	15 - 50
SIR-C	NASA, USA	1993, 1994	215	L (1.28); C (5.3)	HH, HV, VH, VV	15° - 60°	12.1 x 2.8 (L); 12.1 x 0.8 (C)	-50 (L); -40 (C)	30 - 100
X-SAR	NASA, USA	1993, 1994	215	X (9.6)	VV	15° - 60°	12.1 x 0.4	-26	10 - 45
X-SAR/SRTM	NASA, USA; DLR, Germany	2000	300	X (9.6); C (5.3)					C (225); X (50)

Table ii: Space shuttle SAR missions

Later, especially with the availability of two identical SAR sensors on board the ERS-1 and ERS-2 satellites, the assessment and monitoring of disasters and environmental hazards (such as earthquake, volcanic eruption, flood, fire, and oil pollution at sea) has become a close-to-operational reality. With Envisat and its Advanced Synthetic Aperture Radar (ASAR), the continuation of data availability is assured both for scientific and operational use.

Research into new technologies aimed at widening the application field of radar remote sensing from space is currently being performed on multi-frequency and multi-

polarisation systems, in order to study the characteristics of microwave backscatter over different types of land and sea environments.

It is important to stress the difference between radar and optical remote sensing for its use in geology, and, in particular, which disciplines can potentially profit from using radar remote sensing techniques.

Optical sensors are passive: they mostly rely on sun illumination. The information acquired mainly concerns the 'colour' of the target surface (visible and infrared reflectance or emittance). Images from optical sensors (aerial photographs, CIR-films, multi-spectral scanner data) have been widely used for geological applications in the last 30 years. The main use of satellite optical images, besides the analysis of brittle and ductile deformation structures, is to assess the spectral signature of objects on the ground. Spectral analysis permits the identification of typical rocks, which in general leads to description of the surface lithology. Colour composite images are mainly used in geological surveys for identifying the boundaries between different rock formations.

Radar sensors, on the other hand, are active instruments, as they use their own energy source to 'illuminate' the Earth's surface. A portion of this radar beam is scattered back to the transmitting and receiving antenna, where it is processed. Radar imagery provides information about the surface roughness and the dielectric constant of the target. Radar sensors are most sensitive to the roughness of the ground in all its forms, and to its moisture levels. Radar images provide useful information for geological applications, mainly with respect to geomorphologic studies, identification of tectonic features and measurements of soil moisture.

It is important to note that the information obtained by SAR instruments is often complementary to that collected by optical sensors.



Part I

Introduction to SAR

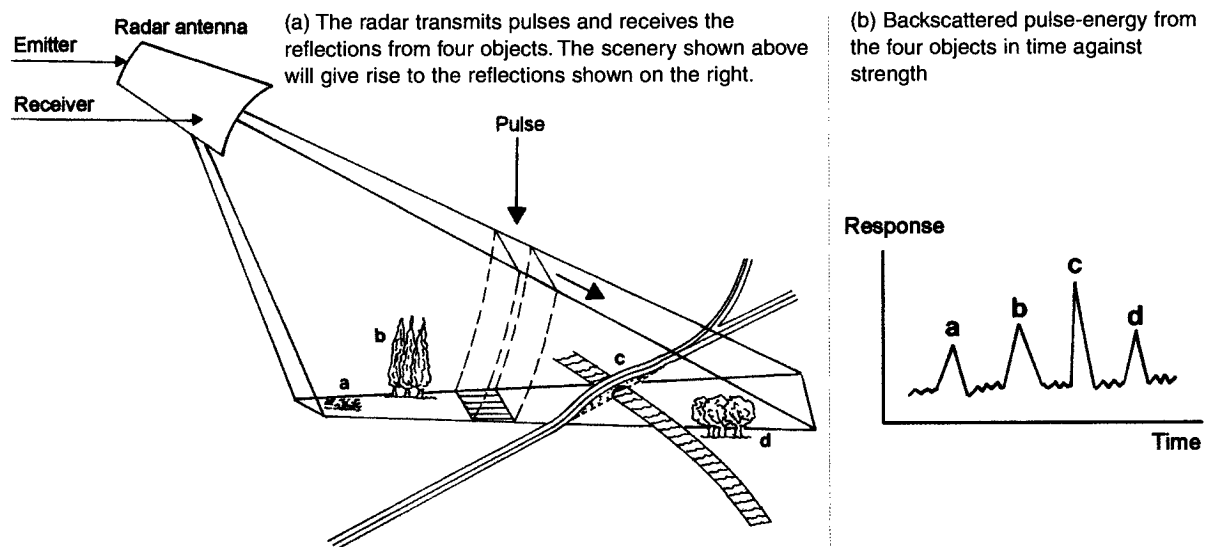


1. Radar basic characteristics

1.1 Introduction

'Radar' is an acronym for RADio Detection And Ranging. It operates in the part of the electromagnetic spectrum known as 'microwave', which covers the frequency interval between 0.3 and 300 Gigahertz (GHz), with wavelengths between 1 mm and 1 m. Unlike most instruments, which passively acquire radiation from objects illuminated by the sun or by other sources, radar generates its own illumination. By doing so, radar can operate day and night, and, in general, in all weather conditions, since cloud droplets and most raindrops are much smaller than the wavelength used by the radar. Note that optical instruments use wavelengths of the order of 1000 times smaller, hence of similar size to cloud droplets, which thus disperse their electromagnetic energy.

As in a camera flash, the radar instrument directs a beam of energy pulses towards a scene (Figure 1-1). Typically, there are about 1500 pulses per second.



Fractions of these pulses are reflected back, or 'backscattered', from objects that are hit, and the system measures both the return signal and the distance from the sensor to the objects as a function of the round-trip travel time, as shown in (b) above. The radar beam travels at the speed of light.

The detail discernible in an image is dependent on the spatial resolution of the sensor, which refers to the size of the smallest possible feature that can be detected. The area on the Earth's surface that is 'seen' at one particular moment in time is called the resolution cell and determines a sensor's maximum spatial resolution. (See 1.3.1 for more on spatial resolution.) The information retrieved from each spatial resolution cell on the ground is related to the backscatter strength, the time delay (giving the distance, or 'range' – in the sideways direction relative to satellite travel – to the object) and the phase of the pulses

Figure 1-1:
Concept of an
imaging radar

backscattered from each object within such a spatial resolution cell. The ability of radar to illustrate the ground surface (and especially its topography) is the prime benefit of this instrument for geological investigations.

Figure 1-2 illustrates the concept of an imaging radar, showing the terms and basic formulas for the imaging geometry and spatial resolution.

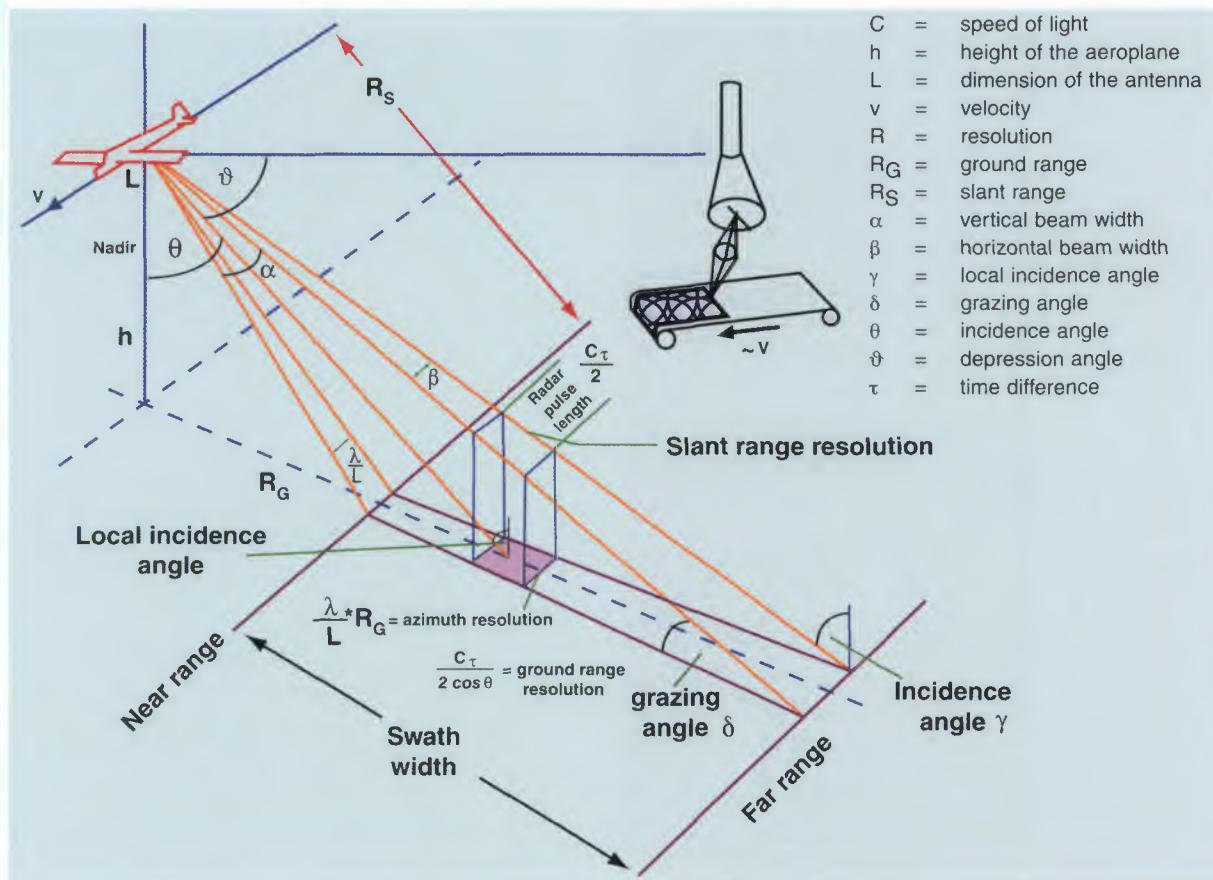


Figure 1-2:
Imaging radar
geometry and
spatial resolution

The operational space-borne radars in use nowadays are single band instruments, but experimental instruments, e.g. on board the Space Shuttle, can use up to three frequencies simultaneously. Radars can also transmit and collect data of different wave polarisations. Conventional imaging radars frequently operate either in horizontal (HH) or vertical (VV) polarisation. In addition, the polarisation, which is determined by the SAR antenna, may be adjusted to be different for transmit and receive (HV or VH).

The ERS radar instrument works in C band (wavelength 5.66 cm, frequency 5.3 GHz) with VV polarisation. The mid-range incidence angle of that radar is 23° from the vertical and the image swath is 100 km (Figure 1-3). Note that the incidence angle to any particular point depends on the slope angle of the surface, and on where in the swath the point is.

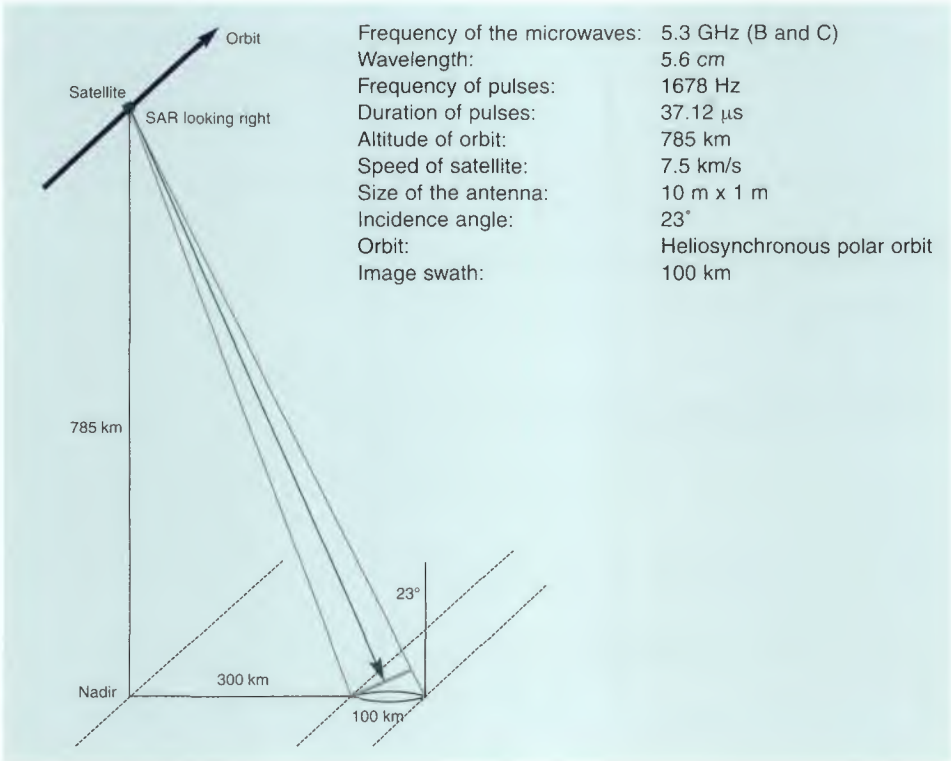


Figure 1-3: ERS SAR (synthetic aperture radar) imaging parameters

The Envisat ASAR advanced synthetic aperture radar) likewise works in C-band but includes HH and VV polarisation, two different swath widths, and seven incidence angle settings (Figure 1-4).

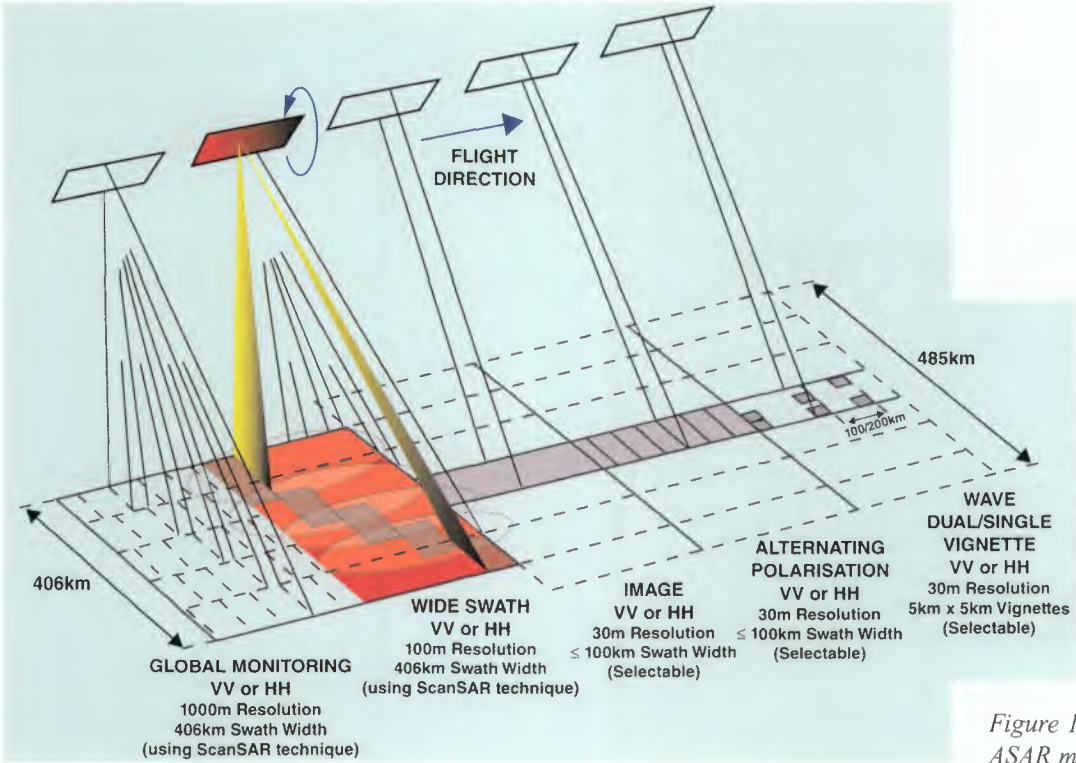


Figure 1-4: Envisat ASAR modes

The introduction of space-borne radar systems fostered the use of this technology for the observation of Earth environments for unprecedented applications such as:

- Near-real-time monitoring of floods
- Assessment of small earth movements caused by earthquakes, landslides and volcanic eruptions (interferometry)
- Near-real-time monitoring of sea pollution
- Operational observation and mapping of sea ice

1.2 The electromagnetic spectrum

Figure 1-5 shows the whole electromagnetic spectrum. It is a continuum of electromagnetic waves arranged according to frequencies and wavelengths. Optical sensors use the wavelength in the visible and infrared region of the spectrum, while radars operate with waves in the microwave region.

This microwave region is made up of P, L, S, C, X, K, Q, V and W bands, as shown in Figure 1-6.

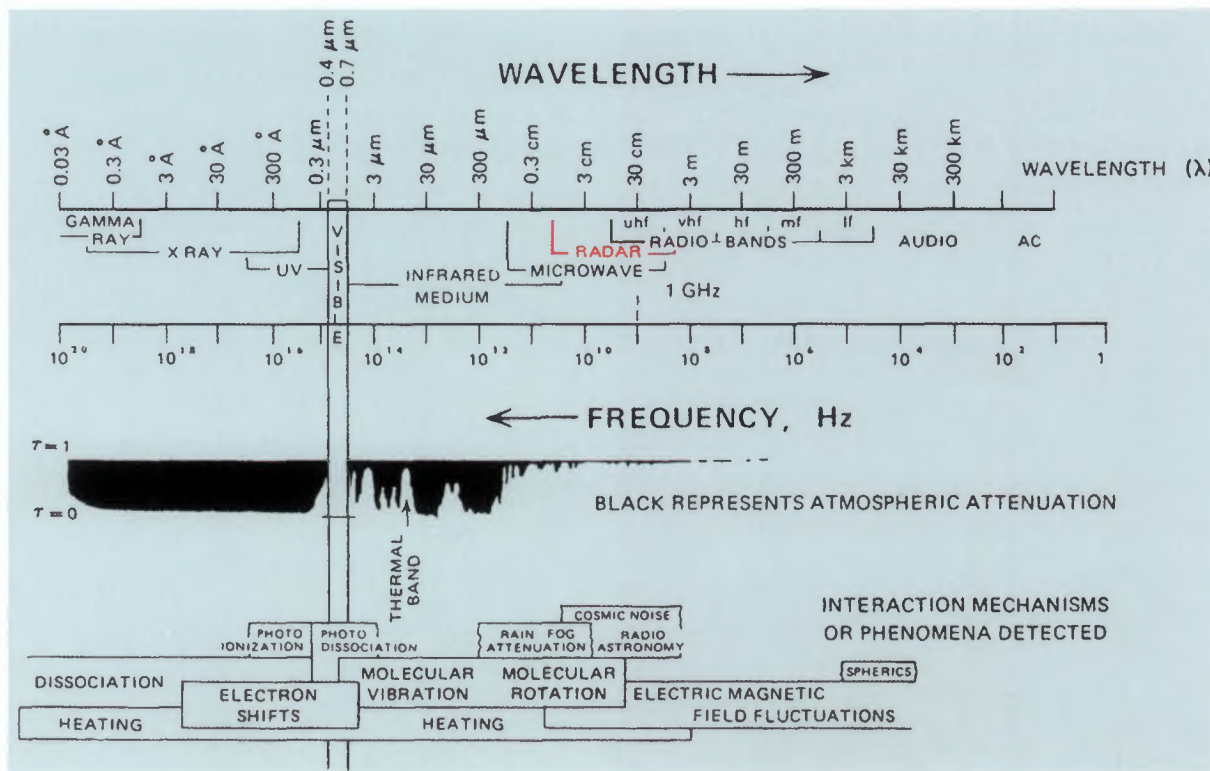


Figure 1-5: Electro-magnetic spectrum

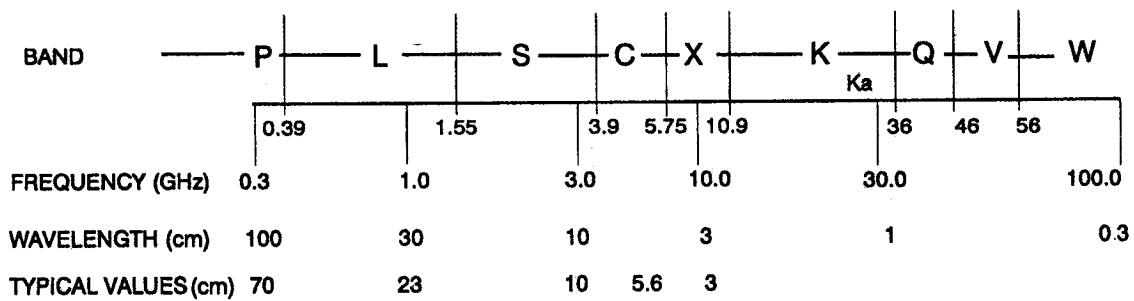


Figure 1-6: Microwave band nomenclature

The microwave region between 1 GHz and 10 GHz and between 14 GHz and 16 GHz represents that part of the spectrum used by space-borne radar instruments for remote sensing (Tables 1 and 2 in the preamble).

The frequencies and wavelengths corresponding to each microwave band are shown in Table 1-1.

Band	Frequency (GHz)	Wavelength (cm)
P	0.255 – 0.390	133 – 76.9
L	0.390 – 1.550	76.9 – 19.3
S	1.550 – 4.20	19.3 – 7.1
C	4.20 – 5.75	7.1 – 5.2
X	5.75 – 10.90	5.2 – 2.7
K	10.90 – 36.0	2.7 – 0.83
Ku	10.90 – 22.0	2.7 – 1.36
Ka	22.0 – 36.0	1.36 – 0.83
Q	36.0 – 46.0	0.83 – 0.65
V	46.0 – 56.0	0.65 – 0.53
W	56.0 – 100.0	0.53 – 0.30

Table 1-1: Frequency bands used in telecommunication and radar

The ability of the radar signal to penetrate clouds and raindrops depends on the wavelength. Radar operating with wavelengths greater than 2 cm can penetrate clouds, and if the wavelength is greater than 4 cm the radar beam also penetrates rain.

In particularly dry conditions of a medium, the microwaves also see through soils: the longer the microwave wavelength, the deeper the signal penetrates. This behaviour is due both to the low dielectric constant of very dry soils or very dry snow, and to the small dimensions of the sediment grains with respect to the radar wavelength, which attenuate microwaves much less than larger grains. Such penetration may unveil buried surfaces or underground drainage channels and tectonic structures.

However, this concept is based on theory. In reality, only reports from the SIR-B and C missions prove that, for L-band, subsurface features can be detected (in the Sahara). For C-band (ERS, Envisat, Radarsat), similar evidence has been suspected but never proven. Nevertheless, it is certain that this phenomenon can be exploited only in arid areas covered by unconsolidated deposits (e.g. pebbles, sands, etc.).

1.3 Basic characteristics of SAR data

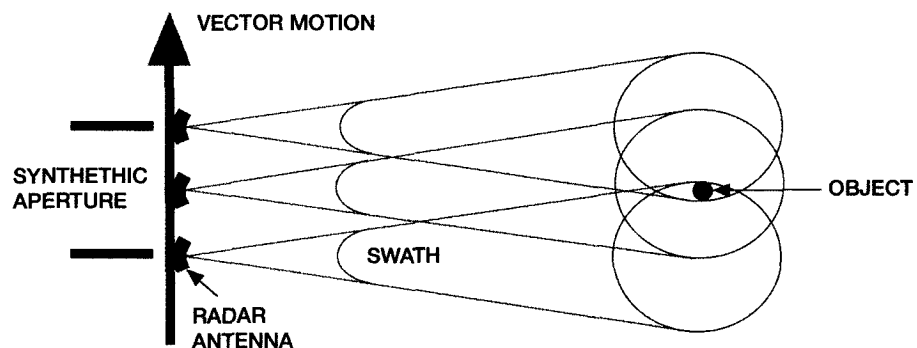
1.3.1 Spatial resolution

In order to achieve a spatial resolution of better than 100 m with a so-called space-borne Real Aperture Radar (RAR), the antenna needs to be of a dimension of several kilometres (for the formula, please see Figure 1-2). To overcome these limitations in order to use imaging radar also in space and not only from aeroplanes, a technique is applied that allows simulation of such antenna sizes. This technique consists of using the phase of the return signal and the well-known Doppler effect. Radars using this technique are called synthetic aperture radars (SARs).

The Doppler effect is usually described as a change in the observed return frequency of an acoustic or electromagnetic wave due to the relative motion of the source and the observer. In this case, it results from the relative movement (with respect to the satellite) of the return signal ahead, abeam, and behind, within the beam of a side-looking radar. In fact, some 1500 pulses per second are emitted by the ERS imaging radar, which generates a beam covering a ground area of about 5 km in azimuth (the travel direction of the satellite) and 100 km in range (sideways direction). The synthetic aperture is thus 5 km.

Considering a satellite velocity of about 6.5 km/s with respect to the ground, each object is illuminated over a thousand times as the satellite passes by (Figure 1-7).

Figure 1-7:
Synthetic antenna
(aperture) concept
for radar



Each of these thousand return signals from a specific object will have a slightly different frequency, as it is seen firstly ahead, an instant later abeam, and a little later again behind, within the side-looking beam of the moving satellite. All return signals are recorded with respect to time, strength, and phase. Applying complex matching filters to the data stream with respect to travelling-time and phase, the location of each single resolution cell is detected, together with the strength of the signal (giving a grey value in SAR imagery). In this way, the data is focused in azimuth.

SARs can achieve azimuth resolution of the order of half the dimension of the antenna length, independent of the distance to the object.

The range resolution, which corresponds to the minimum distance between two reflecting points in the range direction (i.e. on a line between the imaged objects and the sensor), depends on the pulse duration, which for practical reasons cannot be as short as desired (for the formula see Figure 1-2). However, by applying a chirp-technique

(variation of the frequency within the pulse), a very high resolution can also be achieved in the range direction.

1.3.2 Some image interpretation principles

The strength of the radar signal scattered from the Earth's surface to the satellite is related to the surface roughness, among other parameters. A stony desert is considered to be a very rough surface for C-band radar, and a freshly ploughed field is also very rough; both appear very bright in the image. In contrast, a large sandy beach is characterised as a smooth surface and hence is dark in the SAR image. Short grasslands are also smooth, thus dark in the image. Paved roads or runways are very smooth surfaces and appear almost completely black in SAR imagery, similarly to calm water bodies. Man-made constructions are very often made of vertical structures with smooth rectangular surfaces. Nevertheless, they appear bright because of the double bounce of the radar signal (corner effect): reflections at the wall and subsequently at the ground result in a very strong backscatter. A smooth surface such as a roof, casually exposed at right angles to the radar beam, causes an extremely high backscatter, appearing as a star-like cluster with side-lobes visible in both range and azimuth.

Backscatter also depends on the dielectric properties of the target: for metal and water the dielectric constant is high, while for most other materials it is relatively low. Metal structures such as high-power masts or railways are frequently brightly visible (Figure 1-8). For the most common materials in dry conditions the dielectric constant ranges from 3 to 8, while for water it is much higher (80). This means that wetness of soils or vegetated surfaces can produce a notable increase in radar signal reflectivity.

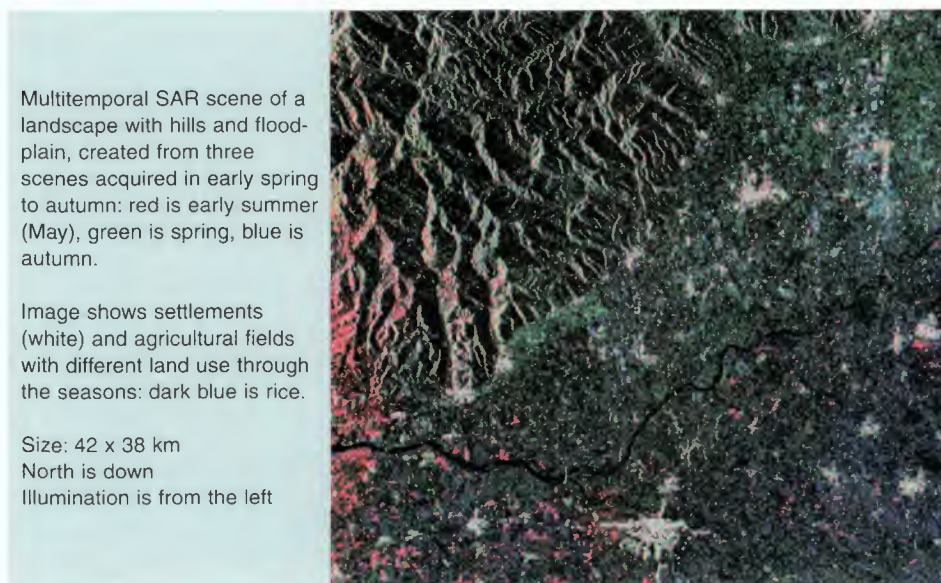


Figure 1-8:
Multitemporal SAR
scene of Pavia
(Italy)

The intensity of the radar backscatter is also influenced by the inclination of the ground surface with respect to the incident signal. There will be a high backscatter from a slope facing the sensor, and a low backscatter or no signal (a shadow zone) from a slope facing away from the sensor.

1.3.3 SAR image noise

Detailed analysis of a radar image shows that, even for a homogeneous surface, significant grey level variations between adjacent resolution cells occur, creating a grainy texture. Each variation is caused by coherent radiation and is called 'speckle'. It is explained by the presence of the scattering from many different objects within each resolution cell interfering positively or negatively with each other. The resulting brightness is random, but it is grouped around a typical mean value for a homogeneous object observed. Visually it creates a 'salt and pepper' effect.

Speckle is a multiplicative noise (i.e. the higher the signal, the stronger the noise) typical in microwave sensing. It originates from the coherent nature of the radar waves and it produces a wide range of pixel values even in homogeneous areas.

To compute the calibrated value (a sigma zero value – explained in 1.3.4 below) of an object, a so-called distributed target (field, homogeneous surface) is required. It is therefore important to consider a statistically significant number of pixels. Unlike optical data, for which complex atmospheric corrections are needed in order to get absolute reflectance values, SAR delivers backscatter values almost perfectly calibrated.

1.3.4 The radar equation

The radar equation describes how the physical parameters influence the power received from each radar pulse. The radar equation reads as following:

$$\langle P_r \rangle = \frac{C_t G^2(\vartheta_i) \Delta x \Delta R \sigma^0}{R^3 \sin(\vartheta_i)}$$

where:

$\langle P_r \rangle$ = Mean received power per pixel

(ϑ_i) = Incidence angle

$G(\vartheta_i)$ = One-way antenna power gain

R = Distance between antenna and reflecting terrain patch (range)

C_t = Constant of the system including transmitted power, wavelength, various gains and losses, etc.

Δx = Pixel spacing in azimuth direction

ΔR = Pixel spacing in slant (range) direction

σ^0 = Average reflectivity per unit area of the scene (radar backscattering coefficient)

Among these parameters, one of the most important is sigma nought (σ^0 , also called sigma zero). It is usually called the radar backscattering coefficient. It is independent of the radar cross-section (the scattering surfaces of an object). The radar backscattering coefficient corresponds to the energy backscattered from a sufficiently large area (a distributed target, consisting of many resolution cells) or from a point target (small, strong-scattering, single object). The sigma nought is directly related to the properties (geometry, conductivity/ dielectricity) of the distributed scatterer such as an agricultural field, for instance. It depends on the incidence angle, wavelength, and polarisation of the instrument. It can be computed even from the single digital value of an image, provided it is a significant measure (very strong point scatterer). It is usually expressed in dB (decibels):

$$\text{Sigma nought (decibel)} = 10 \log (\text{digital number} + \text{calibration constant})$$

It is to be noted that the calibration constant is related to the mid-range incidence angle. Hence a relative correction for any other range position is still to be performed [1].

1.4 Geometric and radiometric distortions in SAR imagery

In optical instruments, positioning of objects in the image is achieved by angular pointing with respect to the sub-satellite track. In contrast, radars use the signal travel time of an impulse from the antenna to an object on the ground to position it in the image: the assumed distance between two points is dependent on the time delay between the radar signal response coming from each of these points on the ground. Every object is imaged and represented in the data in time sequence.

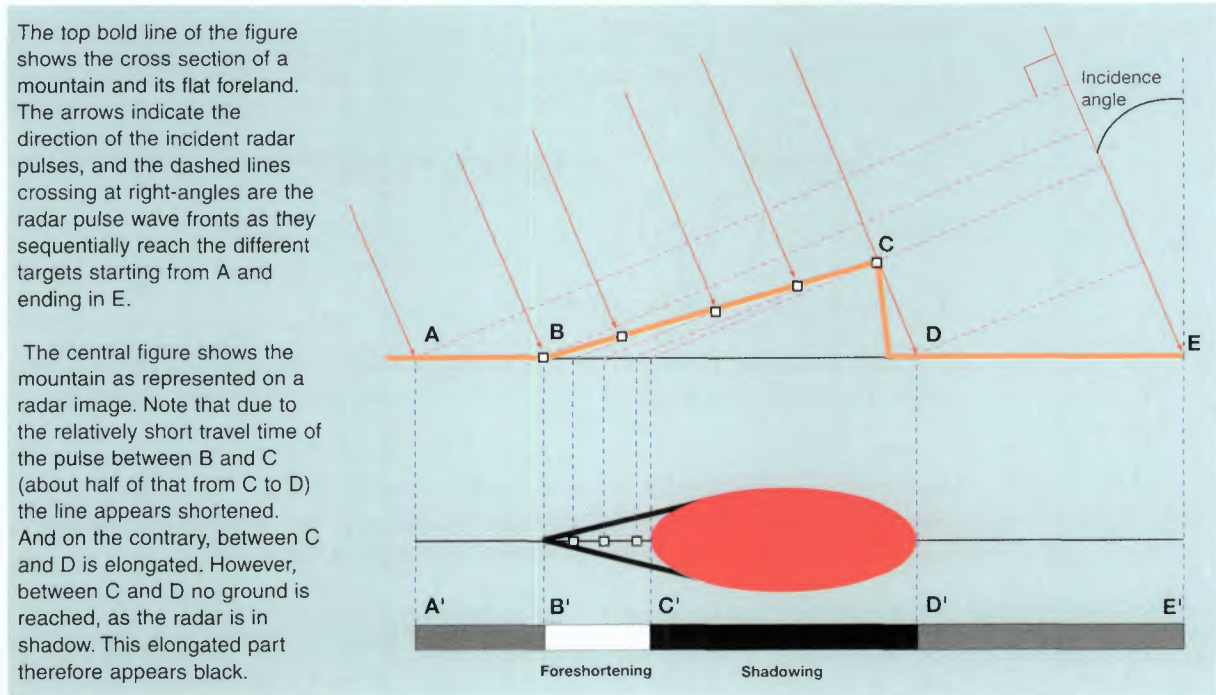
Unfortunately, as a result of this way of acquiring data, slopes on the ground are distorted in ERS SAR images. There are two different types of distortion: geometric distortions are distortions of the geometry (or shape) of a surface; radiometric distortions are distortions in the brightness of the image, resulting from the terrain (hence 'terrain-induced radiometric effects').

There are different kinds of geometric distortions, e.g. the distances between imaged objects along a slope that is exposed towards the sensor are relatively foreshortened. In fact, in SAR images one observes short, bright slopes exposed towards the sensor, and at the same time, enlarged, dark back-slopes. This is explained in the figures below.

1.4.1 Foreshortening and shadowing

Figure 1-9 illustrates and explains the distortions that result in foreshortening and shadowing of an image.

Figure 1-9: Foreshortening and shadowing



In Figure 1-9, point or object A is the first to be seen by the radar (it is closest to the antenna). The next object is B, and a very little later, C. Although the extension of the foreslope of the mountain is rather large, the travelling distance of the radar signal is short, because of the viewing angle. Thus, all elements on this slope (represented by squares) are squeezed into the shortened area. This deformation of the real distance along slopes facing the radar is called 'foreshortening'. The shortened area also appears very bright, since it accumulates all the backscattered energy between B and C.

Between C and D the radar does not reach any surface, due to the extreme steepness of the back slope. This area as well as a part of the flat foreland is in the shadow of the radar beam. It appears black in the image, and contains no information. This is called 'shadowing'.

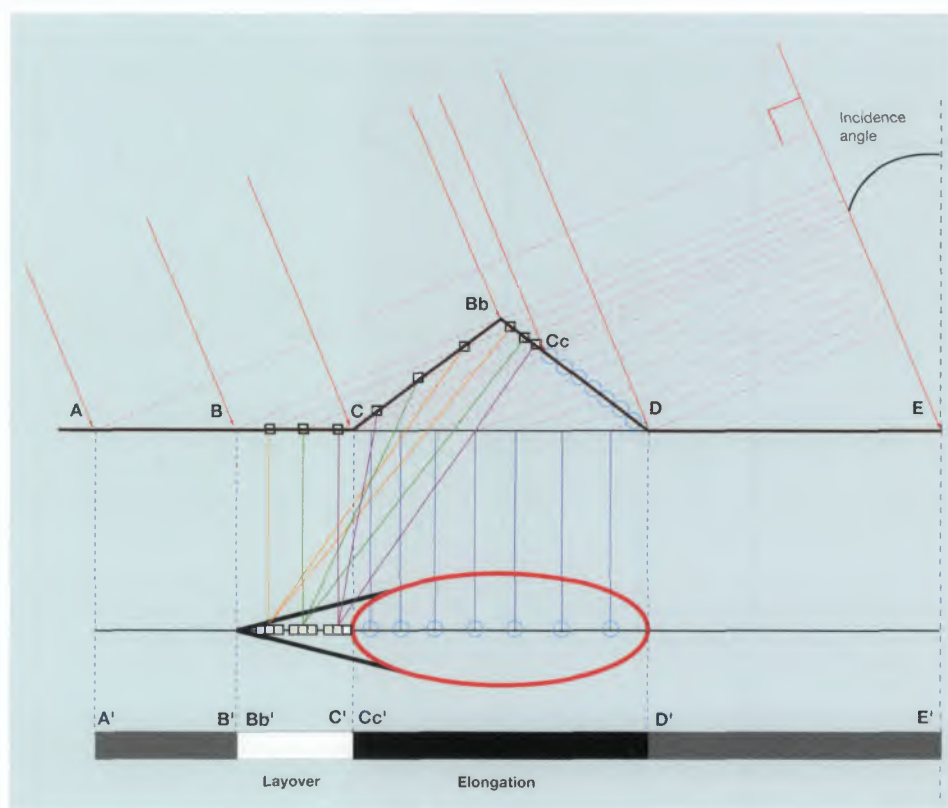


Figure 1-10:
Layover and
elongation

1.4.2 Layover and elongation

In Figure 1-10, point or object A is seen first by the radar, and between A and B pulses hit the ground in only one place. The backscatter produced is of medium strength.

At B the irradiating energy from the SAR antenna simultaneously hits the flat area and the top of the mountain, Bb (they are on the same line of equal travelling time), and hence they are also mapped in the same location. This mountain peak is thus represented, in the SAR image, at the extreme of the layover position (B'Bb').

C is the foot of the mountain, and Cc is an arbitrary point on the far side of the mountain. Between B and C a radar pulse always hits the terrain simultaneously at three different sites: on the flat area before the fore-slope (BC), on the fore-slope (CBb) and on the top

of the back-slope (BbCc). Thus the backscattered signal in the area from B to C is of multiple origins; the energy from multiple image elements is superimposed and hence there is a bright area in the image. However, it is ambiguous and therefore almost always useless. All the signals returned from between B and Cc (represented by squares) are echoed back to the radar within a relatively short time span, and are therefore squeezed into a short distance on the image, despite the ground distance being relatively great.

Since the radar signal reaches the top of the mountain before the foot, this effect is called 'layover' – an extreme form of foreshortening. A layover area contains ambiguous information and therefore is not meaningful and cannot be corrected for its geometry or its radiometry.

On the far side of the mountain, between Cc and D the real distance is rather small but the distance in signal travelling time is relatively big. Therefore the area is 'elongated' in the radar image (represented by small circles). The backscattered energy is spread over a large area and therefore this part of the mountain appears dark.

Between D and E, another flat area is illuminated and a medium high backscatter can be expected.

In a ground (and slant) range image an interpreter can recognise the base of a mountain (dark part) and the layover part (BC), and he can estimate the relative altitude of a crest and the position of its peaks. Moreover, radar-clinometry techniques allow, by analysis of the back-slope grey levels, evaluation of the inclination of the slope itself. However, the position of the peak within the base of the mountain cannot be recovered directly from the image but only using map information (DEM) or a SAR stereo-pair. The foot is clearly marked by an abrupt change from bright (high backscatter) to dark (low backscatter). On the upper back-slope an unknown piece of information from the crest or peak downwards is lost (from B' to C') due to the above-mentioned ambiguity.

1.4.3 Geometric distortion conclusions

The steeper the incidence angle of the radar, the more an image of a hilly or mountainous terrain is affected by foreshortening and layover, but the less by shadowing. For imaging such terrain a shallow incidence angle is recommended.

In ERS image data, slope angles of 19 to 27 degrees already cause layover, depending on the location within the image, i.e. whether it is near range or far range (Figure 1-2). However, shadowing only occurs in highly mountainous areas with slopes steeper than 63 to 72 degrees.

Envisat provides images up to an incidence angle of 45 degrees, which decreases foreshortening and avoids layover in hilly terrain. However shadowing may occur in backslopes steeper than 45 degrees.

The displacement of an object in radar imagery, with respect to its real position on the ground, depends on its height (positive or negative) with respect to the reference height assumed for the image generation processing. Only objects that are perfectly aligned along this reference height are relatively (for the SAR.PRI product) and absolutely (for the SAR.GEC product) map corrected. As a rule of thumb, the displacement is 2.35 times the height difference. The displacement is calculated by the cotangent of the incidence angle, e.g. objects 100 m above the reference height are displaced by 235 m in

slant range towards the sub-satellite track. Even a height difference of merely 10 m would shift an object by almost two pixels (12.5 m pixel sampling).

Figures 2-1 to 2-3 in the next chapter illustrate an example of SAR data geocoding, with explanations.

1.4.4 Example of distorted ERS image

Figure 1-11 shows a comparison between Landsat 5 TM (left) and ERS SAR (right) images. Radar illumination is from the left; north is down. The area is situated in the

The area is situated in the Eastern Alps near the town of Udine (Italy).
Size is 14 x 14 km; radar illumination is from the left; north is down.

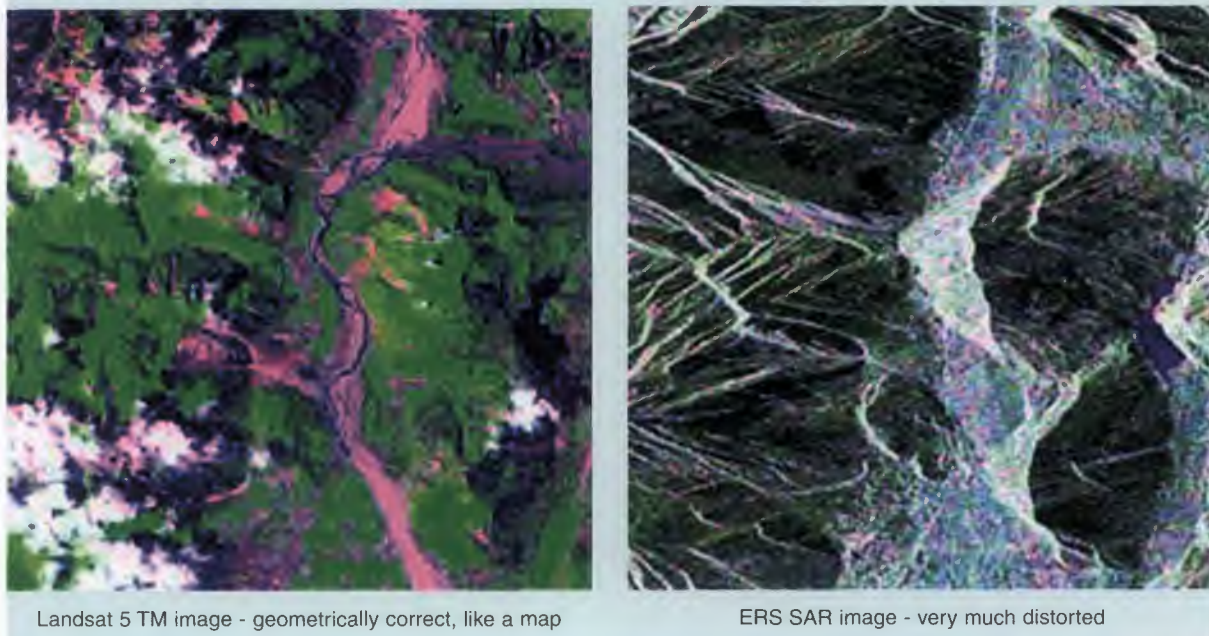


Figure 1-11:
Comparison
between Landsat 5
TM and ERS SAR
images

Eastern Alps near the town of Udine (Italy). While the Landsat image is geometrically correct, like a map, the SAR image is very much distorted. The highest mountain (San Simeone) to the left of the lake is about a thousand metres higher than the valley bottom. It shows a large white part towards the sensor, hence towards the left, consisting of information not only from the exposed slope but also from the flat valley bottom. The position in azimuth of the highest point of the crest can be determined, but its position in range has to be compensated for.

1.5 References

- [1] Laur H., Bally P., Meadows P., Sanchez J., Schaettler B., and Lopinto E.
ERS SAR Calibration: Derivation of the backscattering coefficient in ESA ERS SAR products, ESA Document No: ES-TN-RS-PM-HL09, Issue 2.2, 26 June 1996.

2. SAR data post-processing

2.1 Introduction

With the launch of ERS-1 in July 1991, continuous access to SAR data worldwide became possible. However, image-processing software packages were mainly developed to support the analysis of *optical* data from airborne and space-borne sensors. SAR data post-processing is rather different from optical image processing, mainly due to the image geometry (section 1.4) and due to the nature of the image noise. This chapter describes not only SAR image processing, but also techniques for combining information from several sources (optical data, SAR data, and topographic maps).

The different processing steps are described, starting from data import of ESA ERS SAR products. A typical image post-processing chain is explored, starting from filters and other enhancement tools to be used on optical and radar data, before performing mosaics and/or merges of the different data sets.

An assessment of software algorithms used for geocoding images is also included. For ERS SAR data interferometry processing and applications, please see chapter 3.

2.2 Brief description of ERS SAR product specifications

This section is focused on the ERS SAR data import for ESA-generated ERS SAR products. All the products described below are generated from raw data to a standard 'three-look' product to reduce speckle (see section 1.3.3).

SAR high-resolution images are usually provided on CD-ROM or EXABYTE tape unit. A basic software tool for reading headers and scenes of standard products is provided on-line by ESA.

It is called the SAR Tool Box and can be found on the internet at:

http://earth.esa.int/services/tools_table.html.

The images used in the subsections below were provided by RSL, University of Zurich.

2.2.1 SAR precision image (PRI)

Figure 2-1 represents the original ERS.SAR.PRI product. This is the standard off-line ERS SAR product corrected to ground range and projected to WGS 84.

The PRI product shows strong geometric distortions. The accuracy of the pixel location depends on the precise determination of the sensor position, the surface height relative to the geoid, and the range.

100 x 102.5 km
Illumination from right

PRI product acquired on
24 November 1991
over the north-western
part of Switzerland
It shows strong
geometric distortions



Figure 2-1:
ERS.SAR.PRI
product

The location accuracy is 100 m in range and 200 m in azimuth. The pixel spacing is 12.5 m, both azimuth and range, and the area covered by a scene is about 100 x 102.5 km. The image is composed of at least 8200 lines, with 8200 pixels per line; each record contains 16012 bytes. The pixel depth is 16-bit unsigned.

Figure 2-2:
ERS.SAR.GEC
product

There are two header files at the beginning of the product files, containing geographic information and other auxiliary data related to the sensor itself and to orbital parameters. These two files have to be consulted for purposes such as geocoding or image analysis for which information concerning geographic positioning and calibration is required. The size of the full frame is about 130 Mbytes.

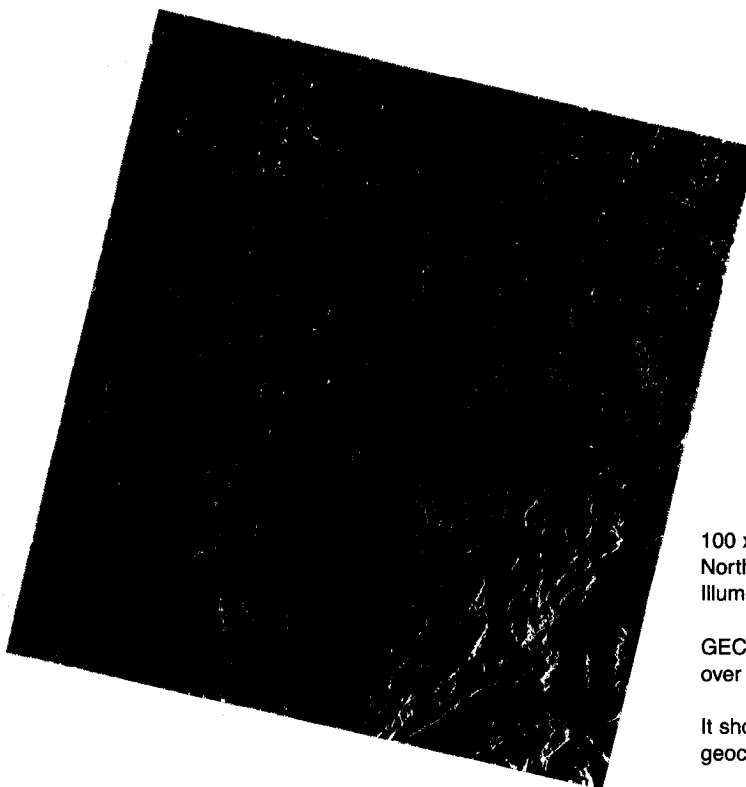
2.2.2 SAR ellipsoid geocoded image (GEC)

The GEC product consists of a PRI product referred to a geographical coordinate system (UTM for

100 x 102.5
North is up
Illumination from right

GEC product acquired on 24 November 1991
over the north-western part of Switzerland.

It shows strong geometric distortions but is
geocoded with respect to a reference height



latitudes within 70° North and 70° South, and UPS for the higher latitudes). It is not corrected for foreshortening and layover distortions.

The image pixel size and depth remain the same as the PRI product. The geographical coverage of a scene is 100 x 100 km; the number of lines and columns of the image is variable between 9000 and 12000 pixels (for lines and columns); the actual pixel number can be found in the header. The location accuracy for a specific pixel is better than 100 m over flat land. In areas of relief, a correction with respect to the scene-dependent reference height needs to be done.

The reference height is also in the header. For any pixel not positioned at reference height, a correction has to be done in range direction (towards the sensor if the referred point is lower than the reference height, or away from the sensor if the referred point is located above the reference surface - see section 1.4). The size of the full frame ranges from 160 to 290 Mbytes.

2.2.3 SAR geocoded and terrain corrected image (GTC)

Figure 2-3 corresponds to the geometrically corrected image. This is a PRI product precisely referred to a geographic coordinate system. It is corrected for foreshortening and layover distortions using a Digital Elevation Model. There is no correction for terrain-induced radiometric effects (i.e. brightness changes).

This correction is possible only when a DEM is available. The reference scene was acquired on 24 November 1991 over the north-western part of Switzerland. It includes the city of Basel and the Rhine (top-left corner), the chain of Jura Mountains (north-western part of the image), the Aare River crossing through the centre of the image with the capital Berne near the lower left corner. The southern part consists of lowland hills belonging to the molassic foreland basin, the Napf area and the sub-alpine mountain chains. The shores of the Lake of Lucerne (Vierwaldstätter See), in the southeast are not well defined due to wind-roughening effects.

This product includes a shadow and layover mask file and a file with the

100 x 102.5 km
North is up
Illumination from right

GTC product acquired on 24 November
1991 over the north-western part of
Switzerland.

The image is geocoded and corrected
for the relief displacement effect. The
distortion of the radiometry due to the
relief is still present.

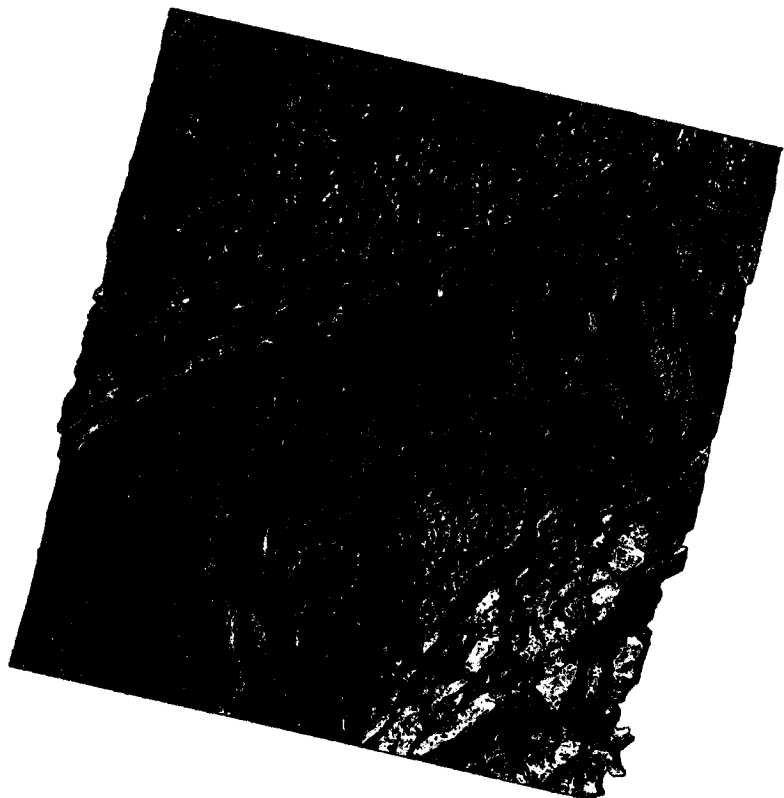


Figure 2-3:
ERS.SAR.GTC
product

local incidence angle for each pixel. The local incidence angle is calculated between the radar beam and a vector perpendicular to the ground surface at the pixel location. The other parameters of the image (lines, columns, size, etc.) remain the same as for the ERS. SAR.GEC product. The location accuracy is better than 50 m, but depends on the precision and sampling of the DEM used.

2.3 Image filtering

Radar images have certain characteristics that are fundamentally different from those of images acquired by optical sensors such as Landsat, SPOT or photo cameras. These specific characteristics are the consequence of the imaging radar technique, and they are essentially related to the radiometry (speckle, texture) and to the image geometry. Speckle is an inherent noise that is characteristic in SAR images. For more about speckle, see section 1.3.3.

The commonly used methods of reducing the speckle are:

- SAR image multi-look processing

This is performed on ERS SAR raw data, and consists of making independent measurements of the same target, which are then averaged in order to smooth out the speckle. Actually, it is obtained by splitting the synthetic aperture into smaller sub-apertures, the so-called 'looks'. Each sector is separately processed and the resulting images superimposed and then averaged. This is how the three-look images of ERS are generated.

- Temporal filtering

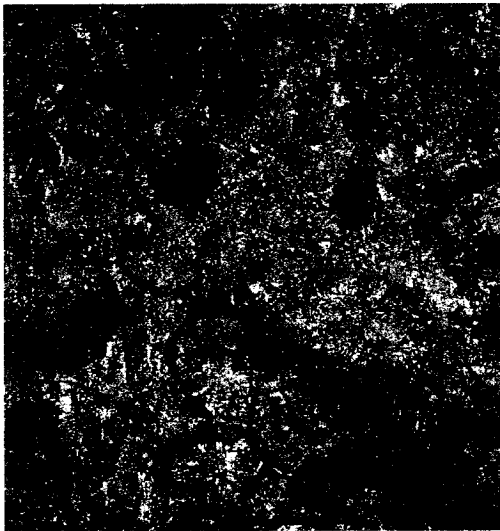
This consists of averaging a series of precisely superimposed data sets acquired at several different times over the same satellite track and frame. This technique is very promising, as it is not too expensive and can be performed easily. By using at least six data sets, a full-resolution, practically speckle-free, SAR image (comparable with a 1:50,000 scale map) can be produced. Such an image is an excellent basis for mapping geological features such as fracture zones, regional foliation, or structural line, drainage networks and many other elements of interest for geological and geomorphologic studies. Such an image appears black and white with all temporal changes averaged out, i.e. not visible.

Figure 2-4 shows the same image based on a single frame and a mean of 16 frames.

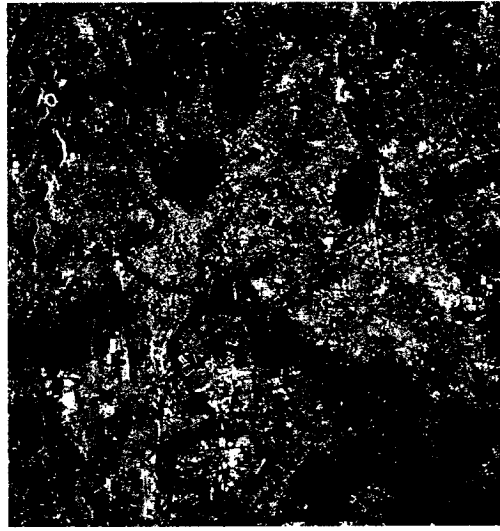
- Spatial filtering

A moving filter window (a selection of pixels called a kernel) is used. Within the window, the intensity of the central pixel changes depending on the intensity of all pixels within the window. Different algorithms have been proposed to properly shape the impulse response of the filter within the window.

The behaviour of filters for speckle suppression is strongly related to the characteristics of the radar image. Thus, as a general concept, it is recommended to try different de-speckle filters before choosing the best one. It might be interesting to display different filters of the same scene as RGB colour composite images. It has also to be noted that visual image interpretation is best performed by analysing unfiltered and filtered images simultaneously.



A single frame with the image noise (speckle) evident
10 x 8 km, North is up
Illumination from right



An image of mean values from a combined image consisting of 16 single frames. There is no noise in the image. In practice, six images are sufficient to suppress speckle.

*Figure 2-4:
ERS SAR
image of
Rome and
surroundings
before and
after
temporal
filtering*

The examples below (Figure 2-5) describe the Mean, Frost and Gamma Map filters of an agricultural area in the Tiber River alluvial plain (near Rome, Italy). It can be seen that the presence of speckle is reduced by filtering, but that the possibility of distinguishing various ground surfaces by texture might be suppressed, and some field boundaries may disappear.



Comparison of original SAR data with a mean filtered image, of an agricultural area in the Tiber River (just north of Rome, Italy)
Size: 4.5 x 6.4 km, North is up,
Illumination is from left



*Figure 2-5:
SAR data
filtering
using the
mean*

Taking the example of homogeneous areas such as agricultural zones with a defined field pattern, the filters to be used must preserve the average backscattering value, and maintain sharp edges between adjacent fields. Figure 2-5 shows an original ERS.SAR.PRI subscene (left image) and a filtered version of the same image. The filter applied in this case is the mean filter. It substitutes the central pixel of each filter kernel with the mean value computed from that kernel, and then moves on to the next kernel. It results in a less noisy, but blurred image.

A slightly better filter than the mean is the median, since it does not introduce new data values and hence smoothes better. Both filters are very fast for computing but not especially effective.

More complex filters are based on an assessment of the noise statistic. The Frost filter [1] assumes a Gaussian distribution of the data and smoothes a window only if all elements are part of such a distribution. In other words, if a filter kernel contains a large range of data values because it contains one or more point scatterers (strong scattering features such as houses, single trees, ships etc.), it will not comply with the above criterion and the filter will leave the central value of that kernel untouched.

An even more refined technique of speckle filtering is performed with the Gamma Map filter [2]. This filter assumes a Gamma distribution of the data, which is closer to the statistical distribution of radar data than the Gaussian distribution. It applies different thresholds for detecting separate kernels containing point scatterers, lines, and edges. After this distinction is made, the respective filter is applied to that kernel. The result of the filtering process is shown on the right hand side of Figure 2-6, together with the unfiltered SAR image (left side). Filtering with this technique results in a smoothed image with sharp borders and linear features, while preserving texture and any strong scattering objects contained in the scene.

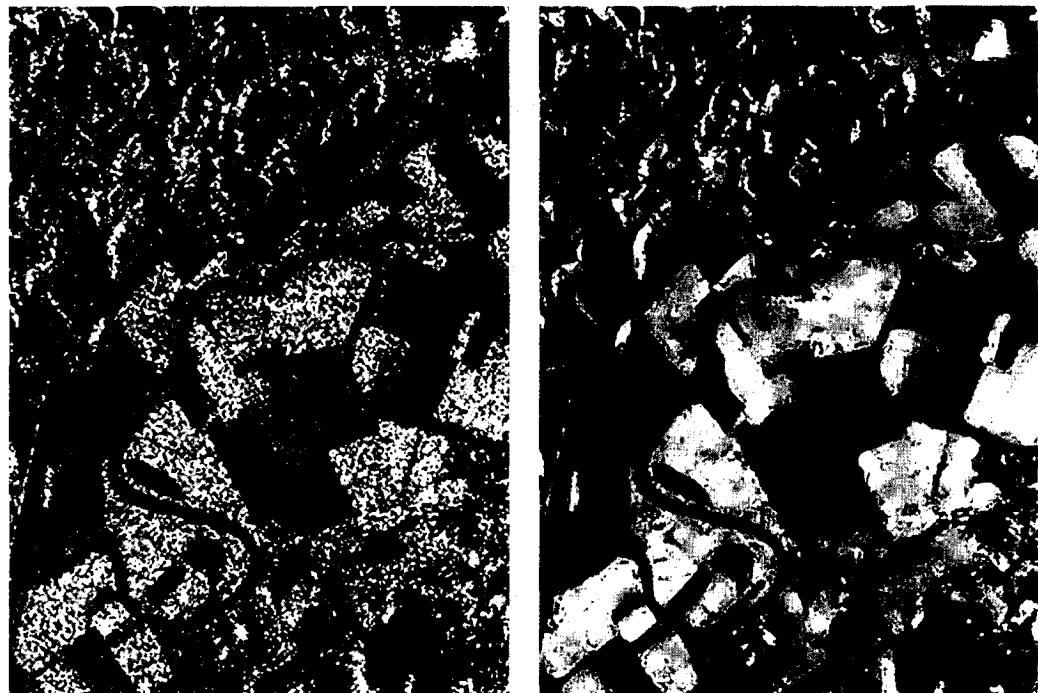


Figure 2-6:
Comparison of
original SAR
data with a
Gamma Map
filtered image

This filter is successfully used prior to conventional supervised or unsupervised data classification. A Gamma Map filter adapted to ERS and Envisat SAR original products is also included in the SAR Tool Box (see 2.2).

2.4 Integrated use of radar and radar/optical imagery

2.4.1 Multitemporal SAR images

Colour-composite multitemporal images are useful for revealing any changes with time between the data acquisitions. All such changes will appear in colours. It is important to combine appropriate data acquisitions for the required purpose. For example:

- For the identification of crops: several acquisitions during the growing seasons
- For flood mapping: acquisition before (normal situation), during, and, if possible, just after the peak of the flooding
- To detect longer term changes: combine acquisitions of the same season but from different years

With respect to image interpretation, the following can be stated:

- Unchanged features appear in black and white
- Any change in the scene (expressed in a change of backscatter) from one acquisition to the other appears in colour
- The reason for a change could be:
 - A rougher surface on a particular date (vegetation growth, etc.)
 - More humidity on the ground
 - A new object or a new form of an already existing object
 - A different viewing angle (if images from ascending and descending orbits are combined).

The colours that appear are combinations of red, green and blue, such that

red + green = yellow
 red + blue = magenta
 green + blue = cyan
 red = green + blue missing
 green = red + blue missing
 blue = red + green missing

If only two images are combined, only three basic colours instead of six will be present (one primary and two combinations).

If only two dates are available, a third colour band can be generated by a linear combination of the two data sets (mean of the two, subtraction, and ratio, first principal component (1st PC – see below), etc.).

Figure 1.8 presents a multitemporal SAR image composed of three scenes acquired in early spring, in summer and in autumn.

2.4.2 SAR/optical data fusion

Images provided by optical sensors contain information about the reflected or re-emitted light energy (colour, infrared) and hence 'chemical' properties of the surface layer, while microwave images provide information about the geometric properties (surface roughness, physical structure and dielectricity) of a surface, or the volume (penetration) of a scene. Therefore these two data sources are highly complementary. The data fusion technique consists of geometrically merging data from different sensors, if necessary processing them further (band-combination or transformation) and displaying them for visual inspection. Once the data set is referred to the same map coordinates, there are different ways to display such a data set.

An integration of optical and SAR data can be performed with the help of a Principal Components Analysis (PCA). It is based on a linear transformation converting correlated bands into an equal number of non-correlated dimensions. The PCA is used to reduce the number of bands in a data set with a minimum loss of information.

Consider, for simplicity, a scatterogram of a data set of only two bands, i.e. a display of the values of band 1 in x and the values of band 2 in the y direction (Figure 2-7).

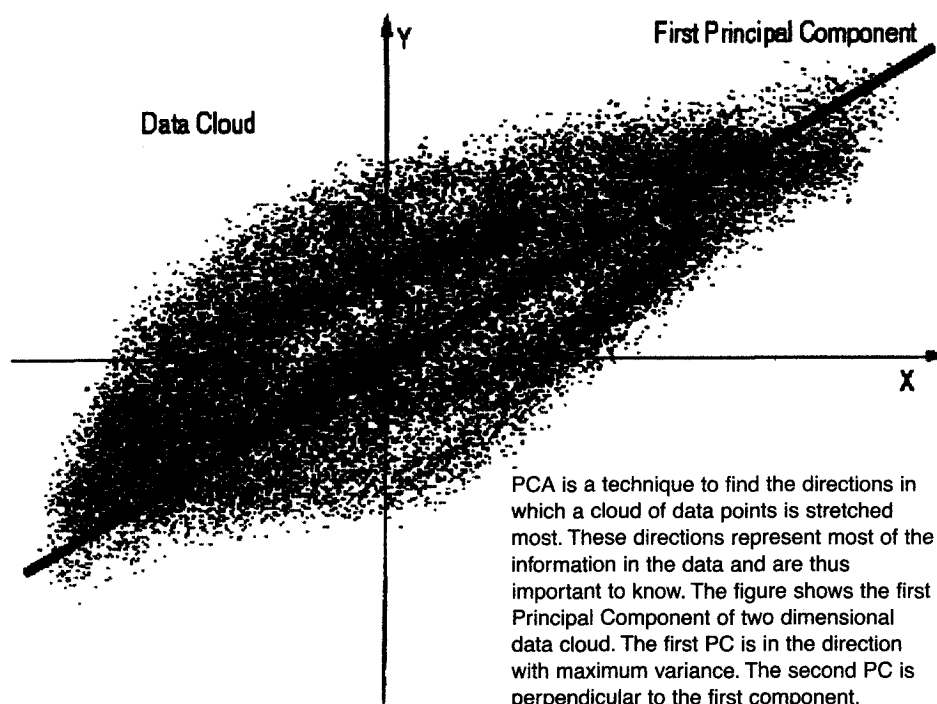


Figure 2-7:
Principal
Component
Analysis

The two principal components are linear combinations of the original two bands, resulting from a rotation of the coordinate system. The first principal component (PC) is found by rotating the x-axis in the direction of the maximum of variance. All values of the scatterogram are then projected on this axis. The second principal component is represented by an axis rectangular to the first one. The disadvantage of this technique is that PCA transformed images show the same features (e.g. vegetation coverage or arid surfaces) acquired at different times or in different places in different colours. This means, for instance, that vegetation, which is always shown by reddish tones in the Landsat 4-5-3 (RGB) band combination, will appear in variable and also various colours on PCA transformed images (Figure 2-9).

- 1) Replacement of one channel of a multispectral image by SAR data. The results will be physically meaningful, with interpretation being made through the colour triangle.

e.g. if red = IR, green = panchromatic, blue = SAR, the results could mean:

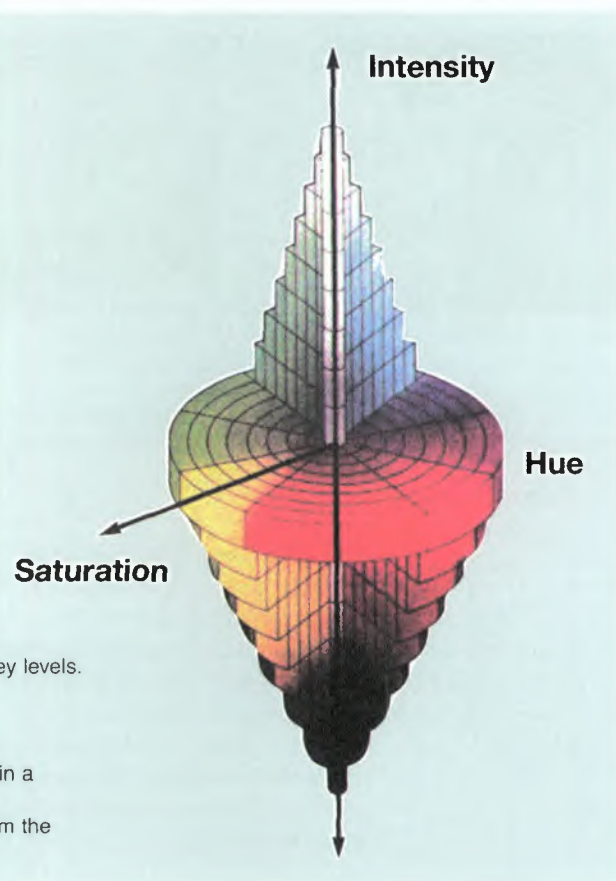
 - The red area is fully covered with vital but low (smooth) vegetation
 - Magenta means rough vegetation, hence deciduous trees
 - Yellow could mean a 50% soil coverage of low (smooth) vegetation
- 2) Principal Component Analysis (PCA) of a combined SAR/optical data set (a full set of bands) and display of the first three components. If there is only one SAR scene, it is combined with the two first principal components resulting from PCA of a multi-band optical scene, using IHS colouration. This provides a maximum of information – but there is no immediate physical meaning of the resulting colours. Therefore, ground knowledge is essential for producing a legend for the colours.
- 3) Intensity-Hue-Saturation (IHS) transformation of three ‘best’ optical bands; then replacement of intensity by SAR and application of backwards transformation. The resulting colours are physically meaningful and can be explained, since the colour and saturation are preserved from the optical bands used, and only the intensity is altered by the SAR data. This is particularly interesting when, in addition to colours, roughness also has to be detected (high/low vegetation or flooded/unflooded area).

The IHS concept needs to be explained more closely. To describe a colour within the colour space, usually three axes are used: red, green, blue. However, there are also ways of defining colours in a double-cone coordinate system using intensity, hue, and saturation (Figure 2-8).

Figure 2-8: The colour double-cone

The three parameters have the following meanings:

- **Intensity:**
This represents the sum of all values of the three input RGB-channels. It is related to the colour brightness and is represented by the central axis of the double-cone.
- **Hue:**
This is the angular position of the pixel in a polar coordinate system in which, depending on the definition, pure red would be located at 0° and pure green at 85° . A pixel situated at 90° would be green with a little component of blue.



The colour double-cone contains all possible colours and grey levels. It is organised in the Intensity-Hue-Saturation concept:

- Intensity is read from the vertical axis (black to white)
- Hue (a specific colour) is found by the angular position in a horizontal plain (cross-section) within the double-cone
- Saturation (of that colour) is defined as the distance from the vertical centre line.

Hue relates to the colour; it changes with moving around the central circle in Figure 2-8.

- Saturation: This value is related to the strength of the colour. Reducing the saturation makes the image become paler. The more coloured a picture is, the higher the saturation is. It increases from the central axis (grey) to the maximum of the colour circle (full colour) in Figure 2-8.

In an RGB-to-IHS transformed optical image, the intensity (the first channel) can be replaced by the SAR data (previously merged geometrically with the optical image), and the new resulting IHS combination can be converted back into RGB for display. In this procedure, a balanced stretching of the channels is necessary in order to improve the quality of the final RGB representation.

The optical-radar integrated analysis allows, in particular conditions, exploration of features of different geological meaning: some of them are only faintly visible on both types of data, and can therefore be enhanced in a combined data set. However, sometimes they can be completely hidden for optical sensors and clearly shown by radar imagery, or vice versa.

Figure 2-9 shows an example of a data fusion of ERS-SAR with Landsat Thematic Mapper (TM) based on an IHS transformation. The area is located between the political and administrative boundary lines of Egypt and Sudan.

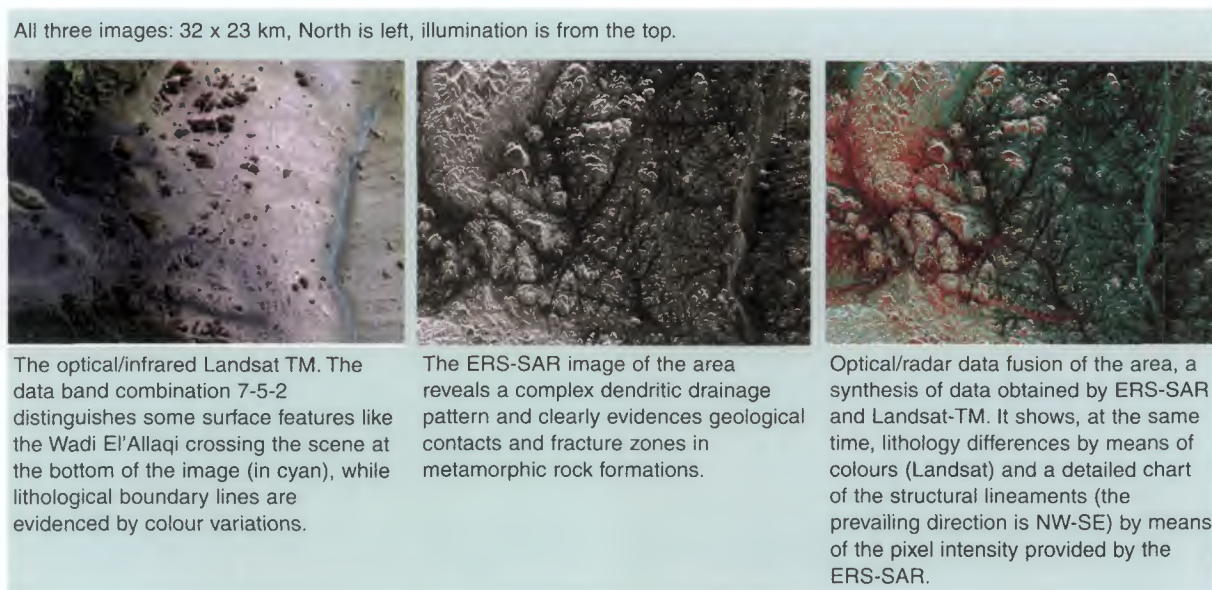


Figure 2-9: SAR/optical data fusion (Wadi El'Allaqi, Egypt & Sudan Boundary)

The outcrop consists of metamorphic and sedimentary rocks (appearing as large and small hills) that have been essentially eroded by water and wind weathering processes. The ERS-SAR image (centre) reveals a complex dendritic drainage pattern and clearly evidences geological contacts and fracture zones in metamorphic rock formations. These features, which sometimes are covered by a thin layer of sand, are mostly obscured on conventional imagery such as Landsat TM. The SAR image appearance results both from different surface roughness conditions and from the ability to penetrate very dry and loose sediments.

Nevertheless the colour differentiation of the Landsat image (RGB band combination 7-5-2) makes it possible to distinguish between several rock types characterised by definite chemical compositions, and consequently by typical spectral signatures with respect to certain minerals.

The optical/radar data merge is performed in an IHS layer combination. It permits highlighting of both surface and potential underground information, because the brighter a colour, the rougher its surface or subsurface. The right-hand image is such a synthesis of data gathered by ERS-SAR and Landsat-TM. It shows, simultaneously, lithology differences by means of colours (Landsat) and a detailed chart of the structural features (the prevailing direction is NW-SE) by means of the pixel intensity provided by the ERS-SAR. The drainage pattern visible in the imaged area is typical for superficial or shallow water systems having tributaries joining the main Wadi at all angles, and today carrying water only episodically.

An example of a PCA computation is given in Figure 2-10, overleaf.

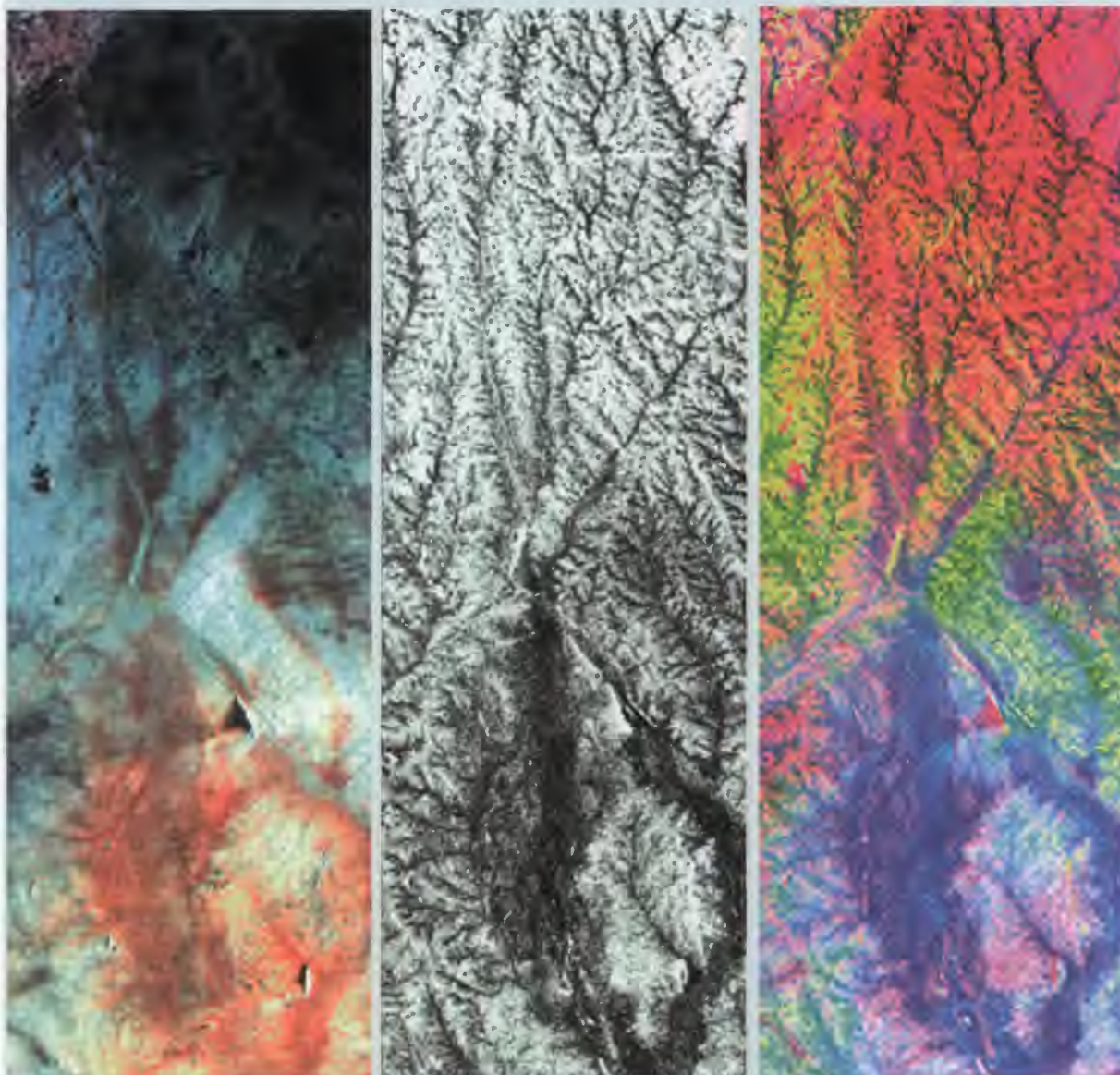
The area presented is situated south of the Hoggar in southern Algeria, with a mountainous northern part and a sand-covered flat part to the south. The Landsat 357 band image (left) shows a net colour separation due to prevailing minerals, indicating a larger response of band 7 in the southern part (mica-richer area). The middle image is the SAR representation of the area, showing an astonishingly dense drainage system. The SAR image was then superimposed on the Landsat data set consisting of six bands. A PCA was performed with all 7 channels and the right-hand image shows the result, a colour image composed of principal component one (PC1) in red, PC2 in green and PC3 in blue.

This colourful image needs to be interpreted with the help of a geological map and ground truth in order to find the significance of the colours. However, by decomposing the image, one can observe that the red contribution stems from the SAR, hence is linked to the roughness of the ground. In order to have more complete colour-coded information from the optical-infrared, a possibility would be to perform a PCA with all the Landsat bands, and combine the first three PC with the SAR image applying an Intensity-Hue-Saturation combination using the method described above.

Another de-correlation stretch technique, less conventional than IHS and PCA, is the Direct De-correlation Stretch (DDS). It resembles the IHS transformation but is easier to control and simpler for achieving a well-balanced saturation enhancement.

Most of the commercially-available image-processing software products include all of the above described modules.

All three images: 24 x 72 km North is up, Illumination is from the right



A Landsat 357 band image of an area situated south of the Hoggar in southern Algeria, with a mountainous northern part and a sand-covered flat part to the south

The ERS-SAR image, showing a dense drainage system not visible on an optical image

Combination of a SAR image and Landsat data after PCA performed with 7 channels (6 Landsat and 1 SAR). The result is composed of principal component one (PC1) in red, PC2 in green and PC3 in blue.

Figure 2-10:
Combination of SAR
and Landsat data by
PCA (Hoggar,
Algeria)

2.5 References

- [1] V.S. Frost, J.A. Stiles, K.S. Shanmugan, J.C. Holtzman, A model for radar images and its application to adaptive digital filtering of multiplicative noise. *IEEE transactions on pattern analysis and machine intelligence*, vol.4 no.2 March 1982
- [2] E. Nezry, A. Lopes, R. Touzi, Detection of structural and textural features for SAR images filtering. CH2971-0/91/0000-2169\$01.00 copyright 1991 IEEE

3. Data processing in SAR interferometry

3.1 Introduction

Effects resulting from interference are well known both in optics (e.g. ‘Newton’s rings’ formed when a convex lens is placed on a plane surface) and acoustics (e.g. ‘beating’ generated by two sound waves of similar frequency). Radar interferometry is the analogous phenomenon in the microwave region of the electromagnetic spectrum.

SAR interferometry applications for mapping the surfaces of Venus and the Moon have been very successful, and initial radar interferometric processing was carried out to assess the topography of Earth by using data from side-looking airborne radar (SLAR). An enormous stimulus to develop InSAR (Interferometric SAR) techniques resulted from the wide availability of SAR data after the launch of ERS in 1991.

Radars operate with coherent and monochrome waves of allocated frequencies (e.g. 5.3 GHz for ERS and Envisat). Originally, each pixel in the image data contains information on both the intensity and phase of the received radar signal. The intensity depends on the radar scattering properties of the object, while the phase is related to the satellite path length (the distance between object and sensor). However, most of the SAR data that is distributed contains only the intensity (e.g. ERS.SAR.PRI products, see 2.2.1), as in this form the data is ready to use and similar in format to the more conventional optical data.

$$\text{Amplitude} = \sqrt{I^2 + Q^2}$$

$$\text{Phase} = \tan\left(\frac{I}{Q}\right)$$

The more informative product of ERS is the SLCI, the single-look complex image. In this, each pixel contains two components, I and Q (real and complex values). By means of simple operations the amplitude (or power) and the phase can be recovered:

Although the phase as such is an arbitrary value, it is the cross-correlation of the phases originating at two different times from the same or two slightly different viewpoints in space that makes it an interesting measure.

It is the phase information only (and not the image intensity) that is exploited in interferometry. Three different products can be derived: a coherence map, an interferogram, and a phase difference image.

- A coherence map is an overall assessment of the change of phase between two images. The change may originate from phase de-correlation due to vegetation growth between the two acquisition dates, or multiple scattering in high vegetation, or surface roughness changes (e.g. a water surface, arable field preparation or new objects).

- An interferogram consists of fringes representing a 2π cycle. It provides information about height variations present on the imaged surface.
- A phase difference image ('Differential InSAR') relates to changes of the distance to objects within the wavelength (for ERS it is 5.6 cm). One cycle would mean a shift of a large number of objects in the scene of 2.8 cm relative to a neighbouring area. In an interferogram, both types of fringes may appear.

Using these techniques, digital elevation models (DEMs) and crust deformation maps can be generated and used to investigate a wide variety of morphological and geophysical processes. The results achieved are astonishingly accurate, except in areas of layover and shadow (section 1.4), and in zones of low coherence (see 3.2.1). The former problems can be reduced by means of multi-pass data acquired during ascending and descending satellite passes; the latter perhaps by the choice of another data-pair.

3.2 Interferometry concepts and applications

Using SAR interferometry, detailed three-dimensional relief maps of the Earth's surface (digital elevation models) can be produced from multiple-pass SAR data sets. The result is similar to that obtained from a stereo image pair with a large baseline, either from optical or from SAR data. The baseline for an InSAR pair must be well within 1 km, otherwise de-correlation will be large.

In a SAR interferogram from two scenes, fringes from phase differences may appear (this is called simple interferometry). By compensating for the topography, these fringes become clearly visible and indicate very small relative movements of the ground surface (of the order of millimetres or centimetres). This is called differential interferometry. Both interferometry techniques open up many new potential application areas for spaceborne SAR data in disciplines such as cartography, volcanology, structural geology, glaciology, and geotechnics, and for work relevant to land subsidence and landslide monitoring.

Figure 3-1:
Interferometric
imaging geometry:
two passes pointing
to one resolution
element

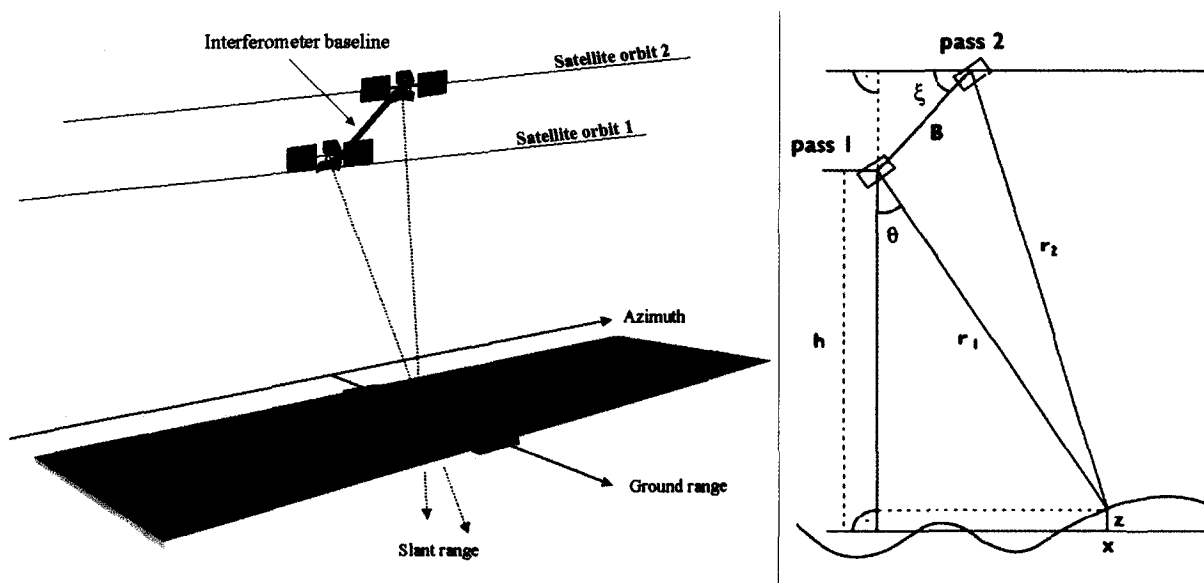


Figure 3-1 shows the interferometric imaging geometry related to two orbits on the same track with range vectors r_1 and r_2 to a specific resolution cell (pixel). The perpendicular baseline B is tilted by the angle ζ , relative to a horizontal plane.

The first step in simple interferometric processing is to register two SAR complex data sets to sub-pixel accuracy. The next step is to subtract the phase of the first image from the second image. This operation results in an interferogram. The interferogram contains fringes, which reflect the phase change due to topography expressed in $(n \times 2\pi)$.

Fringes may also appear over flat land. They need to be compensated for by tilting the image plain until they disappear. Further, non-topography related fringes may become visible due to atmospheric phenomenon, or, very rarely, due to Earth terrain movements. To recognise and eliminate them, several pairs of data sets need to be processed and compared.

The next step is to convert the fringes into absolute height values. The process is called 'unwrapping of the phase'. One cycle corresponds to the so-called 'ambiguity height'. This can be approximated by:

$$A = \frac{\text{const}}{B}$$

where:

- A = Altitude of ambiguity (height difference corresponding to each fringe (2-pi) cycle)
- B = Perpendicular baseline (vertical distance between the satellite positions during the two acquisitions)
- const = A constant that is related to the altitude of the spacecraft etc, specific to the orbit. For ERS-1 and Envisat, const. = 9080.

With a perpendicular baseline of 90 m, the ambiguity height will be 100 m; and hence 20 fringes will represent a relief of 2000 m. However, a pair of data sets with a perpendicular baseline of 200 m might also be available. In this case, about 40 fringes will outline a 2000 m relief. This would mean a higher accuracy in representing the topography. However, the higher the baseline, the lower the coherence between two images, and the coherence is a measure for the visibility and hence reliability of fringes! In low coherence areas fringes tend to disappear. Hence, the DEM accuracy is proportional to the baseline. Short baselines (less than 100 m) cause major errors due to phase instability and atmospheric artefacts; long baselines (more than 600 m) cause low coherence, and consequently difficulties during the interferogram unwrapping step. The best baseline range for DEM generation is 100 m to 300 m.

The perpendicular baseline between individual sets (orbit and frame) can be looked-up in the ESA ERS/Envisat on- and off-line catalogues (DESCW and EOLI respectively; see <http://earth.esa.int/services/catalogues.html>).

3.2.1 Coherence

This consists of the phase coherence between two scenes. The coherence information is independent of the radiometry, and therefore any influence due to the topography is not visible. Areas of low coherence are: dense high-growing vegetation (forest), layover areas, and areas with very low backscatter (smooth surfaces or steep back-slopes). Water

surfaces also show no coherence. Coherence maps are useful for land-cover classification and for detection of changes.

As an example of an interferometric product, Figure 3-2 shows a coherence image. White means high coherence and dark means low coherence.

Dark: water bodies
(lakes, rivers)

Dark grey: woods

White: low vegetated
fields or bare soil

Location: Swiss
plateau, North is the
Jura

Size: 46 x 42 km

North is up

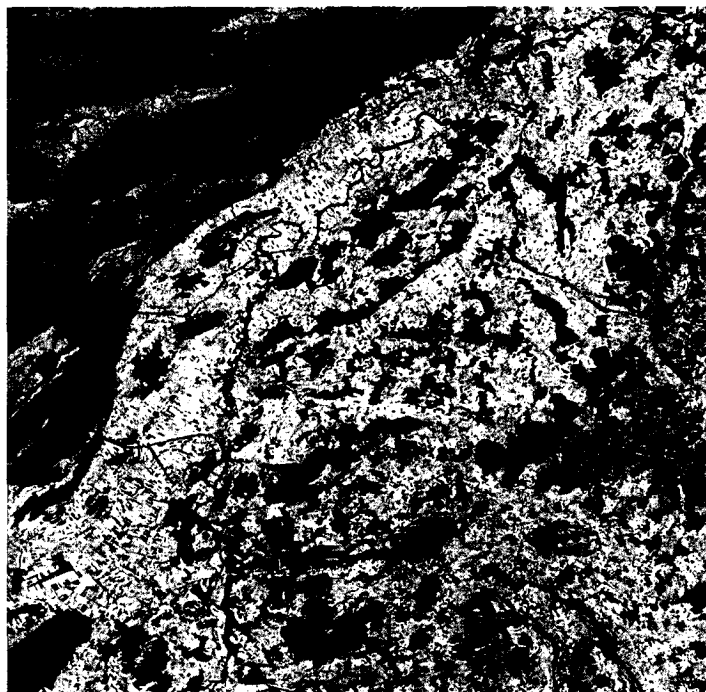


*Figure 3-2:
Example of a
coherence image*

Compared with Figure 2-1 it is noteworthy that because of the sole use of the phase, the topography does not show up at all. This means that the radiometric distortion (the white stripes) due to the topography is largely compensated for. Coherence images are therefore suitable for automatic classification, even in hilly terrain. The same can be applied for (optical-infrared) normalised differential vegetation index (NDVI) images.

3.2.2 DEM generation

Ideally the ERS SAR data set for DEM generation consists of a tandem pair, of ERS-1 and ERS-2 data acquired on two consecutive days. A one-day time lapse between the two acquisitions minimises phase variations due to environmental and atmospheric changes, which reduce coherence and introduce artefacts (fake fringes).

The sequence in data processing for DEM generation starts with acquisition of two ERS SAR SLCI products and is followed by:

- Careful selection of the image pair of the area of interest (see also section 3.3)
- Co-registration of images
- Coherence and interferogram image generation
- Interferogram unwrapping
- DEM generation from unwrapped image

Potential applications for DEMs related to geology are:

- Perspective views helping with image analysis and interpretation in disciplines such as geomorphology, hydrogeology, structural geology
- Possibility of superimposing the DEM onto either microwave or optical images and illuminating such a data set from any direction, using appropriate image processing software, to enhance tectonic features

Figure 3-3 shows an interferogram (left) and the corresponding DEM (right) of the Tiber Valley area (near Rome, Italy). ERS-1 and ERS-2 data were acquired, one day apart, during the tandem phase on a satellite ascending pass. In this case, the baseline is 200 m and the height of ambiguity 45 m, which is equal to one colour cycle of a fringe.

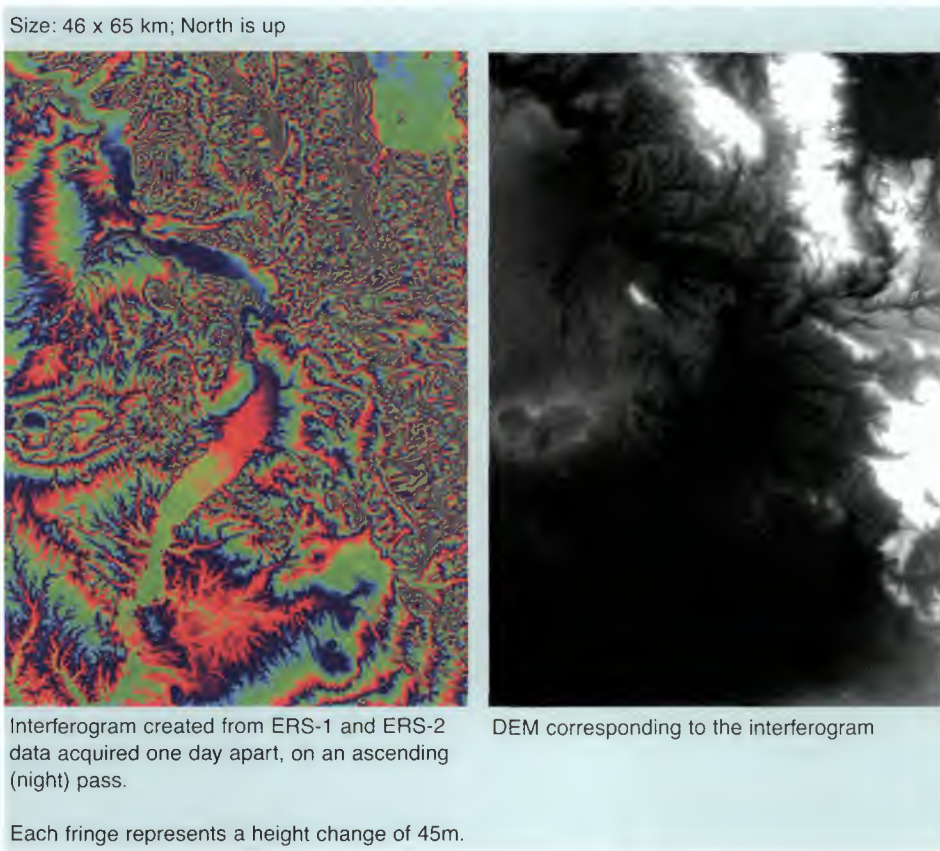


Figure 3-3:
Interferogram of the
Tiber Valley area
(Italy)

3.2.3 Differential interferometry

Ground deformations can be detected in particular conditions by means of this interferometric analysis. This technique is based on the phase comparison between two SAR images acquired before and after a deformation event and referred to a DEM. The choice for the most suitable baseline depends essentially on two factors:

- Morphology of the area of interest
- Availability of an accurate DEM (generated from maps etc.)

If SAR data is available with a small baseline, i.e. with A (height of ambiguity) much larger than the height differences in the area of interest, the fringes will not be related to

the topography but only to the displacement effect. If A is smaller than the height difference, an external DEM is needed in the processing chain in order to remove fringes caused by the topography. In the second case, the DEM accuracy is fundamental to get a good result: the DEM resolution must be better than A to remove topographic fringes completely. In order to do that the DEM is subtracted from the interferogram; any resulting fringes are the representation of ground deformation. Since each fringe corresponds with a phase difference of 2π (360 degrees), one fringe indicates a displacement in the line of sight, the range (or away from it) of exactly 2.6 cm, or a multiple of this. With respect to stable and permanent strong scatterers (corner reflectors), movements in the range direction of the order of a few millimetres can be assessed.

Possible applications related to geology of differential interferometry are:

- Glacier motion determinations
- Topography changes due to phenomena such as subsidence and landslides
- Monitoring of volcanic activity by measuring small surface changes due to movements of magma
- Assessment of deformations along active faults
- Movements produced as foreshock, mainshock, and aftershock during seismic sequences

3.3 Practical hints for interferometry

The basic requirements for an image pair that are suitable for interferometry data processing (such as two ERS-1 images or an ERS-1/ERS-2 tandem pair) can be summarised as follows:

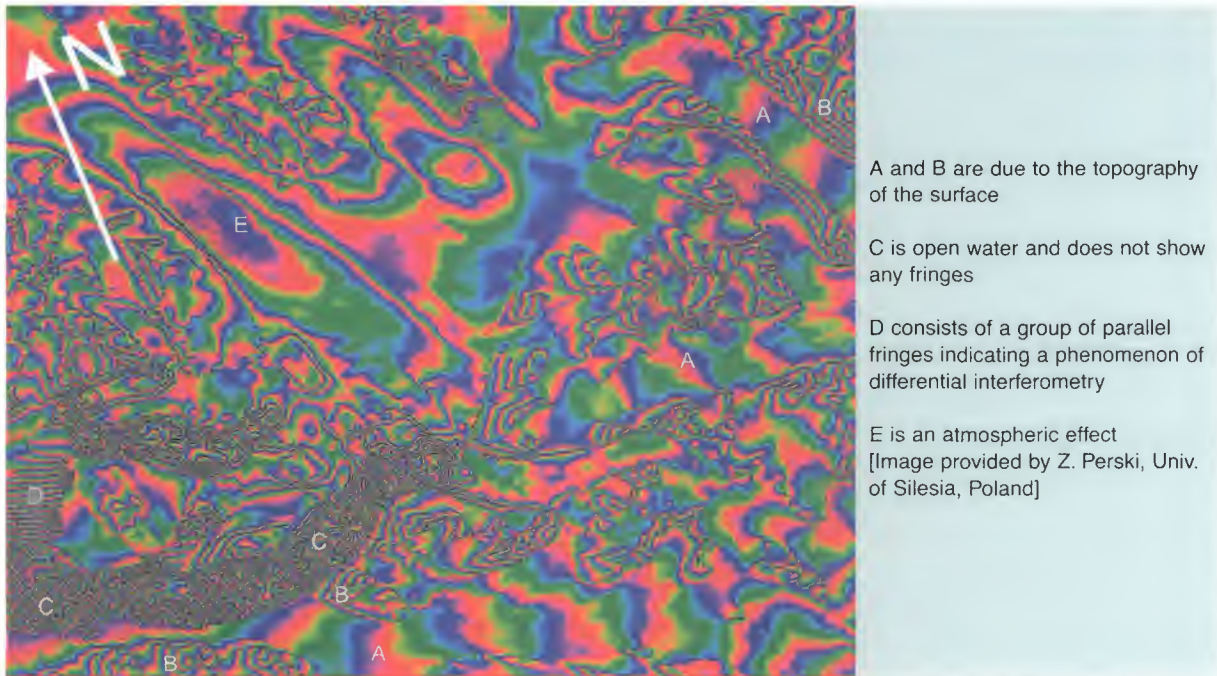
- Availability of stable backscatter conditions on ground (area of no or very little change, in terms of surface roughness, minimum foliage, no change in humidity between the two acquisitions)
- Similar atmospheric conditions during the two acquisitions: calm and good weather, same temperature conditions, no freezing/thawing, no rain or snow
- Stable SAR sensor viewing geometry (provided by ERS/Envisat)
- Preservation of inherent phase information during SAR data processing (provided by ERS/Envisat)

The problems that may arise during data processing are:

- Image co-registration can be affected by low coherence or by high image noise
- Erroneous phase changes can be produced by variable atmospheric conditions. These effects, usually known as 'atmospheric artefacts', are caused by strong winds (e.g. jetstreams), temperature inversions, or other meteorological phenomena, on one of the acquisition dates.
- Occurrence of strong winds on the ground or precipitation (rain, snow) can cause variable backscatter intensity and loss of coherence.

- Further, note that steep slopes producing layover result in discontinuities in the fringe image.

Figure 3-4 provides a general frame of the problems that the interpreter of a fringe image may face. It shows fringes of different origin.



The image shows phase shifts from three different origins:

- Features like A and B are due to the topography of the surface, where A's are gently descending huge glaciers and the B's are the steep mountain slopes surrounding them.
- C is open water; it does not show any coherence and hence also no fringes.
- D consists of a group of parallel fringes indicating a phenomenon of differential interferometry. It is an effect of the tidal height difference of the sea between two data acquisitions of ERS-1 and ERS-2, spanning 24 hours (11 and 12 April 1996). There are some 15 fringes in this area, indicating 42 mm movement in range or in the direction of the line of sight.
- The large feature E is an atmospheric effect and is provoked by layers of different air masses, which influence the travel speed of the microwaves and hence alter the phase difference.

Figure 3-4:
Interferogram of the
area of the
Kronsneen in
northwestern
Svalbard

In order to optimise the choice of SAR image pairs to be used for interferometry, two parameters must be taken into account:

- Temporal de-correlation

Long time periods between two SAR acquisitions usually lead to considerable variations in backscatter and hence a loss of coherence. This inevitably prevents the generation of reliable interferograms. The environmental characteristics of the area of interest must be considered as key factors in choosing the acquisition dates of InSAR image pairs. For instance, a one-day interval could be too much when data is acquired over glaciers during the melting season, whereas data acquired several years apart over arid landscapes often allows the generation of high quality interferograms.

- Baseline length

Above a critical value for the baseline length, which for the ERS and Envisat satellites is approximately 1000 m (practically, an upper limit of 600 m should be considered), there is a complete loss of coherence. This is detrimental to the height measurement accuracy. Perpendicular baselines ranging from 100 m to 300 m are optimal for land mapping (DEM generation). Shorter baselines are useful for detecting shifts on land surfaces and glacier movements (differential interferometry).

In conclusion, interferometry applications for geological purposes are feasible over large parts of the globe; the only real limitation is due to dense and high vegetation coverage. Coherence is generally low and fringes are weak or even absent over forested areas. As outlined before, the presence of steep slopes requires the use of a multi-pass data set (ascending and descending satellite tracks).

The ERS-1/ERS-2 tandem mission (with a one-day time interval between ERS-1 and ERS-2 passes) started in September 1995 and ended in May 1996. It provided a huge dataset practically worldwide, mostly with several sets of data of each location, and good for a variety of applications ranging from DEM generation to the extrapolation of the evolution of slow moving geophysical processes.

4. Principles of radar image analysis

4.1 Radar characteristics of natural objects

The strength of the radar signal backscattered from different objects (water, ice, soil, forest, etc.) in general depends on the following factors:

- Look direction
- Viewing angle (incidence angle)
- Parameters of the sensing system (e.g. wavelength)
- Geometry
- Surface roughness
- Electric properties of the target (see section 1.3)

4.1.1 Water surfaces

Microwaves do not penetrate water. The radar signal backscattered from water surfaces is influenced essentially by surface roughness (waves).

Wind speed, wave direction, and currents are also important factors for the intensity of the returning radar signal.

Atmospheric phenomena (unstable air masses, local winds and gravity waves in the air), sea currents, and natural or man-made oil slicks can all induce sea surface variations, visible on SAR imagery (Figure 4-1, overleaf). Currents can enhance or diminish low wind phenomena, and are visible as current fronts, linear dark or bright features. In the presence of continental shelves, sills, and seamounts, internal waves are generated, visible as a series of parallel lines.

On the other hand, sea surface features in shallow water can also be related to the bottom floor topography (see Chapter 21).

4.1.2 Inland ice

Radar images acquired over ice sheets and glaciers may provide useful information regarding:

- the surface (humid or dry)
- the upper layer of the firn, snow or ice
- the glacier bottom topography
- ice movement

The latter two are expressed as height changes and related backscatter variations due to the oblique viewing and ice surface roughness changes (Chapter 20). Interferometric techniques are used to assess quantitative height variations and movements.

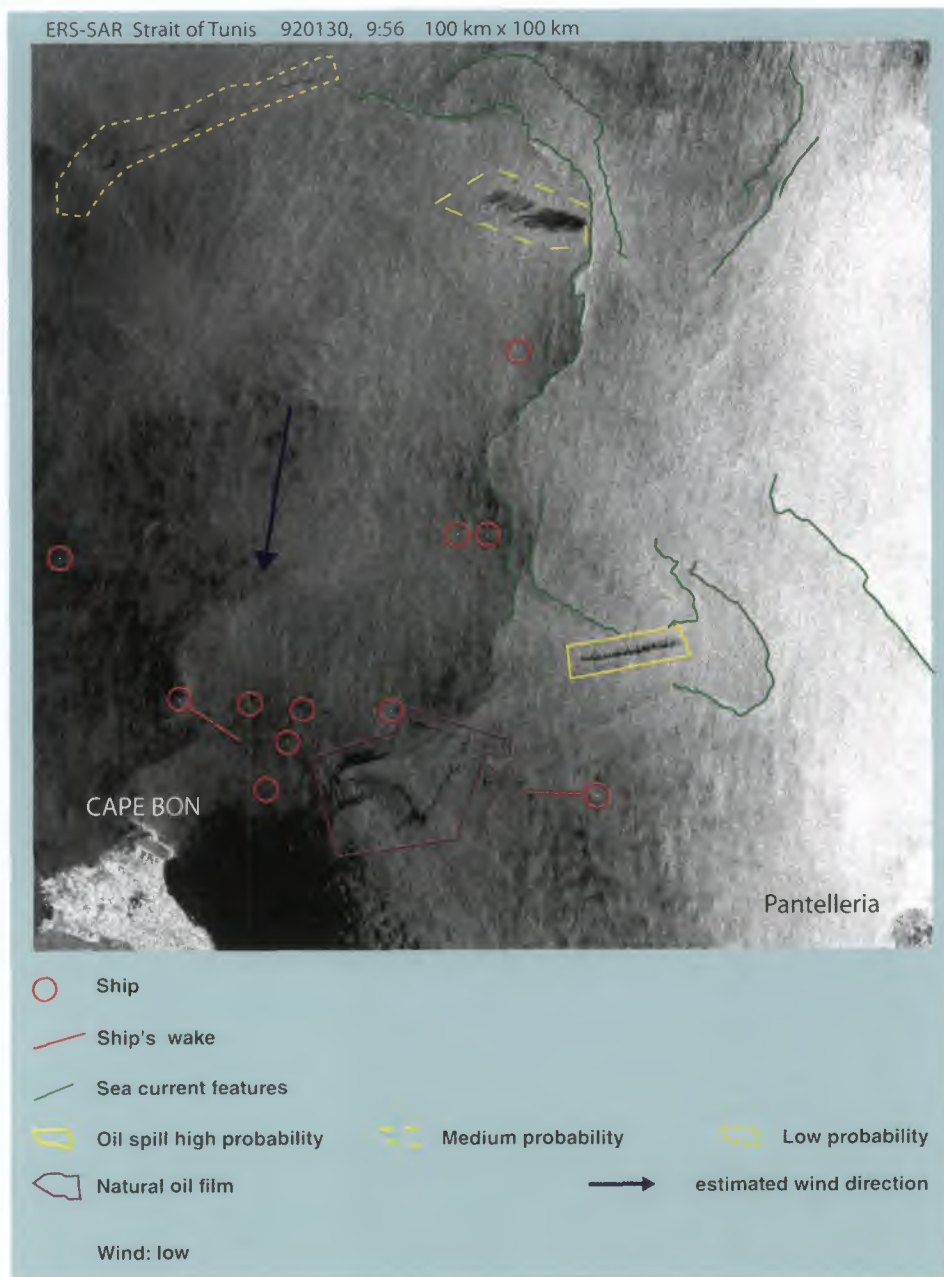


Figure 4.1: ERS SAR scene of the Strait of Tunis (Tunisia), in the Mediterranean Sea

4.1.3 Land

The responses from different soil types depend mainly on roughness and soil moisture. The latter conditions both the backscatter intensity and the microwave soil penetration: soil moisture drastically reduces the penetrating capabilities of the radar into the ground. For ERS C-band the detection of soil moisture as deep as 5 cm has been reported, while for SIR-C L-band, several metres of penetration into dry sands was determined.

The vegetation coverage is another important factor influencing the radar signal response. Microwaves interact with the vegetation canopy in multiple ways, by penetrating and in some cases reaching the underlying terrain (Figure 4-2).

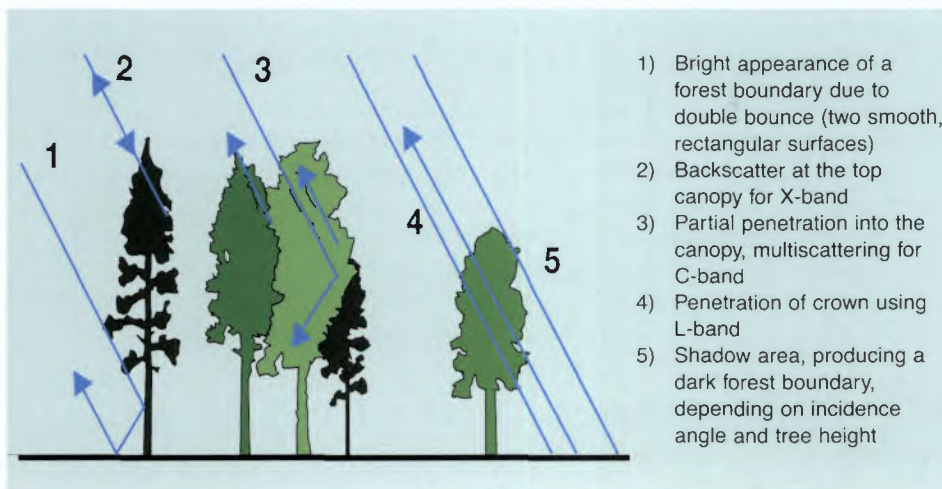


Figure 4-2:
Microwave interactions with vegetation

It is fundamental to consider the radar wavelength with respect to the mean size of different plant components. If the radar wavelength is much greater, penetration is consistent, as in the case of long wavelengths (L-band); and it is negligible in the case of small wavelengths (X-band).

Other factors to be considered are:

- The water content of the vegetation (the higher it is the stronger is the backscatter)
- The radar beam polarisation (like-polarisation HH or VV penetrates the vegetation more than cross-polarisation HV or VH)
- The geometric distribution of the vegetation (alignments in azimuth direction scatter back more energy than alignments in range direction), in particular when using like-polarisation
- The incidence angle of the microwave beam (the bigger or steeper the incidence angle, the deeper the signal penetration into the vegetation canopy)
- The multiple scattering of the radar signal inside the vegetation produces a depolarising effect on microwaves. This means that there is a considerable contribution of depolarised returns. For interferometry applications, vegetation decreases coherence. This means that when the observed coherence is low then there is a higher biomass present. Coherence and biomass are thus in inverse proportion.

For the application of ERS SAR data in geology the following activities have been reported:

- Mapping of boundaries between different soils and rock formations
- Mapping of tectonic structures (e.g. folds, faults, joints, fractures)
- Assessment of displacements caused by seismic activity and localisation of epicentres
- Mapping of drainage patterns and flood monitoring
- Mapping of features in shallow seas and coastal zones
- Mapping and monitoring of great ice masses (ice sheets and glaciers)
- Monitoring of volcanic activity

- Assessment of slow movements in landslide-prone areas, and subsidence effects due to underground excavations and/or mining exploitation

For some specific geological analyses, a combined approach using optical, infrared and microwave remote sensing is recommended. In radar imagery there is no difference between bare soils and rocks; in both cases backscatter depends on surface roughness and possibly on humidity. No direct mineral identification is possible by using radar imagery. However, backscatter variations can be evidenced, since different lithologies may behave in different ways when they have undergone geological processes such as weathering and tectonic stress. In some cases these processes cause large roughness variations. These variations can be highlighted by means of radar imagery.

4.2 Extraction of geological features from ERS SAR imagery

Any particularities of the radar instrument must be well understood in order to correctly analyse this type of remote sensing data, get the best results, and avoid mistakes.

In general, any grey tone variations and changes of texture in SAR images point towards an alteration of the morphology or lithology. Structural lines might be further enhanced by the presence of smooth surfaces, either rectangular or perpendicular to the microwave beam, acting as corner reflectors. A SAR image will be very bright in the area, as the reflected radar signal saturates the pixel of that cell and those around it.

Image interpretation and the related analysis result in the production of structural contour maps (representations of subsurface stratigraphic and tectonic units) and structural sections (observed or inferred distribution of rock deformations on a vertical plane). This kind of study has proven to be useful, both from the technical and from the economical point of view, for identifying possible water resources and oil or gas structural traps. The topographic emphasis of radar imagery becomes essential for this purpose.

With the help of textural characteristics, discrimination can be achieved within rock formations, such as between lava flows of different ages, or among adjacent fluvial deposits having different grain size and shape. The effect of weathering, or in general of erosion, and the subsequent clastation into evaporite ponds or basins containing chemical deposits, produces great variations in the sediment roughness and therefore in the radar image brightness. Often an important contribution to backscatter could come from a dry-cracked crust. Such changes can in general not be identified in optical images, in which the chemical composition of the target is the most important factor influencing the relative reflectance factor.

4.2.1 SAR image coverage

Radar systems offer more imaging opportunities than other remote sensing sensors. On the one hand, they can acquire data in ascending orbits (night) as well as in descending orbits (day), because they produce their own electromagnetic waves. This possibility of using crossing orbits allows the observation of hidden slopes.

On the other hand, microwaves are transmitted even across clouds, allowing all-weather observations. An example is given with the Pinatubo lahar occurrence observed across thick clouds during a typhoon event (see Pinatubo example, Chapter 8).

4.2.2 Radar stereoscopy

Radar stereoscopy provides a very detailed view of the landforms. In general, stereoscopy can be obtained from two overlapping scenes acquired on parallel and adjacent orbits, hence showing the same or a partially overlapping scene. The pair can be matched for a three-dimensional viewing by naked eye or with the help of a pocket-stereoscope.

An example is given in Figure 4-3 of a stereo pair taken on parallel orbits from the Bosumtwi, Nigeria – a meteorite impact crater.

Scale: 52 x 56 km; North is up; Illumination is from the right

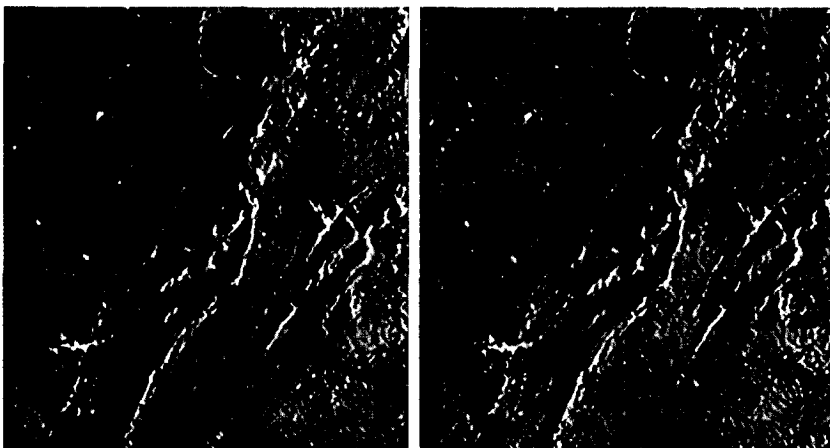
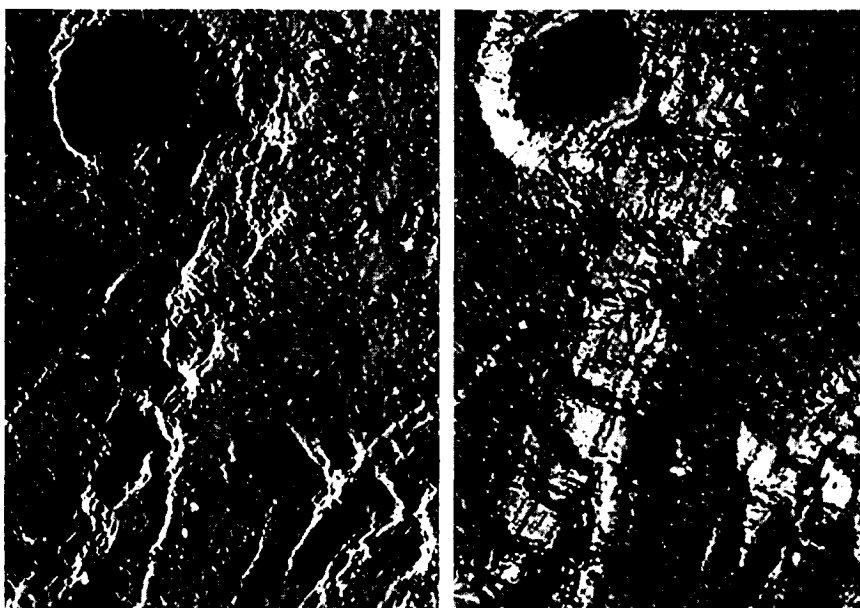


Figure 4-3:
Bosumtwi meteorite
impact crater,
Nigeria
(parallel orbits)

Figure 4-4 shows a pair taken from crossing orbits (ascending, descending). One of the images is displayed as a negative in order to simulate the same 'illumination'.

Scale: 28 x 26 km; North is up



Illumination right

Illumination left

Figure 4-4:
Bosumtwi meteorite
impact crater,
Nigeria
(crossing orbits)

The stereo effect is very much exaggerated for higher relief such as the crater, but for lower relief such as the hilly landscape elsewhere in the scene, a three-dimensional effect can be achieved.

In fact, ascending and descending cross-orbits of the same satellite may be used for stereoscopic observation of areas having slope angle values less than 15° . When only one single radar scene is available, it can be matched with a Digital Elevation Model to produce a simulated stereoscopic view (e.g. one vertical and one oblique, regarding the DEM). This may provide a good stereoscopic couple (see the case study of Iceland, Chapter 15).

4.2.3 SAR image orientation

Orientation of the slope against radar beam incidence is the major factor controlling the intensity recorded (Figure 1-9). For steep slopes facing radar illumination, the returned intensity is high. An application is given, showing mountain uplift (see the case study of the Alps, Chapter 13). For surfaces that are sub-perpendicular to the radar beam, most of the incident energy is returned to the instrument, resulting in over-bright surfaces and general saturation of the signal. For gentle slopes facing radar illumination, the returned energy is quite important, rendering the small relief features well. When the topographic slope is away from the radar illumination, the intensity of the backscatter signal is lower than that of a horizontal surface, supposing that roughness and moisture are similar in the two slopes. In this case, the backscatter intensity decreases when the slope becomes steeper. If the slope dip is greater than the depression angle, there is no returned energy, and the feature is in radar shadow. More generally, the radar signal is sensitive to slope variations. However, when the radar beams are parallel to topographic features such as crest lines or talwegs, the landforms are badly or not at all expressed, because the angles between the rays and the slopes are the same everywhere for the two valley slopes. The radar may in this case be responsible for directional filtering.

Most geological and morphological features are characterised by their morphology, which is particularly expressed by radar images. Many examples are given in the following chapters (see case studies of the Afar, the Alps, the Carpathians, the Balkans, Irian Jaya, Iceland, Japan, Lebanon, North Anatolian Fault).

4.2.4 Geometric distortions

Geometric distortions occur in contrasted relief, due to oblique illumination. The slopes facing radar illumination are not only brighter but also shortened, whilst the slopes away from radar illumination are elongated, inducing relief foreshortening towards the radar (this is illustrated and explained in section 1.4). The resulting shapes are equivalent to what an observatory would see in diametrically the opposite location. These deformations may create artefacts that resemble chevrons, and, in some cases, give the impression of dips and strikes that are the inverse of the real dips and strikes in the field. This is shown in the case study of the Afar (Chapter 11).

If the illuminated slope is greater than the incidence angle, the radar beams hit the summit before it arrives at the foot of the mountain. This particularity results in a layover effect, in which the peak of the mountain seems to be even before its foot (Figure 1-10).

4.2.5 SAR backscatter intensity

The intensity of the backscattered energy also varies with ground roughness. The concept of roughness comprises micro-roughness, with centimetric variations that are at the scale of the radar wavelength, and macro-roughness, due to metric or decametric size facets of the topographic surface (section 1.3.2). For a smooth ground surface, the return is weak, and specular reflection occurs. For a rough or macro-rough ground surface, the return is greater and the intensity consequently higher. For instance, see the case study of variations in roughness of different granites in Côte d'Ivoire (Chapter 17).

4.2.6 Speckle

Speckle is due to surface macro-roughness characterised by facets that are smaller than the pixel dimension. Each facet scatters back radar energy, especially those facing the radar illumination. These elementary returns have a phase and an amplitude, and random conjunction of them within the frame of a given pixel may result in a randomly weak or strong return signal. However, for a homogeneous area (a distributed target), the values will fluctuate about a typical mean value.

4.2.7 Soil moisture

An increase in soil moisture affects the dielectric constant and induces a greater reflected intensity. When moisture is greater than about 30%, the backscattering remains constant. This increase in backscattering of humid soil is illustrated by the case study of Vaison-la-Romaine (Chapter 10).

4.2.8 Soil penetration

Ground penetration of the radar beam is greater in dry sands, and increases with wavelength. The penetration in dry soil is about 2 m for 22 cm waves of SIR-A. An illustration is described in the case study of the Tanezrouft using ERS-1 images (Chapter 9).

4.2.9 Radar image texture

Radar image texture results from the spatial arrangement (contrast, regularity, periodicity, complexity) of the pixels with different grey levels in the image. There are three types of texture:

- (1) Micro-texture, at pixel groupings in the 3x3, 5x5,... neighbourhood, highly polluted by the speckle
- (2) Meso-texture, at the size of large groups of pixels (tens to hundreds)
- (3) Macro-texture, or image structure, on a more regional scale, is at the scale of the objects and expresses peculiar arrangement of groups of pixels having a certain degree of homogeneity

The terms used to describe the textures are numerous, e.g. thin, medium, coarse, granular, linear, smooth, etc. These terms depend on the scale of the observation. For instance, according to the scale of analysis, a surface may have a smooth or a granular texture. Macro-texture on the radar images primarily expresses changes in slopes and is mainly correlated with the drainage network.

4.2.10 Drainage pattern

There are close relationships between the geology and patterns of the drainage network, and therefore the texture. Description of the drainage network can be qualitative or quantitative, the latter consisting of measuring parameters such as lengths of drain channels, angles of convergence of tributaries, linearity of curves, and the hierarchical structure of networks. The morphology of drainage networks mainly depends on the structure (presence of faults, magmatic intrusions, dip of the layers) and on the lithology. The density of the drainage network (cumulative length of valleys per unit area) depends on many factors such as the climate, the topography, and the physical properties of the rock (structure, resistance to erosion, porosity). Thus, a very dense network presents narrow valleys, whereas a sparse network is organised rather around a few broad rivers.

4.3 Radar characterisation of geological objects

Identification of the geological objects takes into account features that result from actions of climate, erosion, and vegetation on the geological basement. Information is thus given by the analysis of grey levels, textures and shapes. An 'image-facies' denotes a homogeneous zone in the image, characterised by a unique type of grey level interval, texture, and specific shape. Image-facies can be correlated, for example, with lithologic units, patterns of agricultural parcels, burned areas, classified forests or flooded zones.

In optical images, the access to geological information is mainly through analysis of vegetation, soil, and land use characteristics. The image content is essentially expressed by colours, textural patterns, and shapes. The morphology cannot specifically be assessed except by stereoscopy. In contrast, radar backscatter is very sensitive to variations of topographic slopes, enhancing the three-dimensionality of the morphology. However, in flat landscapes, the geological objects are better expressed by the texture.

4.3.1 Lithology

The microwave spectral signature of the different lithologic units is rather poor for single-wave radar imagery. In most cases, exaggeration of the topography and distortions hamper subtle expression of the morphology. However, texture is rather rich in information, especially in plateau areas as is the case in tropical Africa (see case study of Côte d'Ivoire, Chapter 17).

The synoptic view offered by satellite imagery is optimal for the observation of facies changes at regional scale that are not clearly visible in the field. Changes in facies are related to variations in morphology, notably in the hilly relief of low mountains, as is the case in the Carpathians (Chapter 14).

4.3.2 Faults

Faults are mainly expressed by scarps that are related to the offset or interruption of lithologic features. Objects such as pull-apart structures are often associated with strike-slip faults and indicate not only the presence of a fault but also its transcurrent mechanism. These features are mainly expressed by the morphology. When a fault zone, basically with strike-slip mechanism, is continuous for hundreds of kilometres, it constitutes a shear zone (see the example of the Mitrovica shear zone in the Balkans, Chapter 12, and the North Anatolian Fault in Turkey, Chapter 6).

When a fault is active, the cumulated offset is mainly expressed in the morphology by fresh (poorly eroded) relief. Recent age may also be attested by Quaternary rocks affected, for instance pull-apart basins filled with Quaternary sediments. The Dead Sea Fault Zone in Lebanon (Chapter 19), and the NAF in Turkey (Chapter 6) are strongly expressed in the morphology and affect recent rocks.

4.3.3 Basins

Basin formation at local scale is generally the end result of fault activity. Sometimes, complex multi-phase tectonic activity has occurred. This is shown in the case study of the basin of Erzincan along the North Anatolian Fault (Chapter 6).

4.3.4 Folds

Deformed lithologic units generally evidence folds, and their identification on radar imagery depends on the possibility of analysing the geomorphic expression of these lithologic units. Active folds principally affect the topographic surface, and can be detected because radar imagery is able to show these surfaces. In the case of the Kobe region in Japan (Chapter 18), active folds shown by radar imagery are also associated with active faults.

4.3.5 Uplift

Active uplift is associated with steep topographic slopes of relief that is not yet deeply eroded. Steeply dipping slopes are expressed on radar imagery by dark tones of surfaces lying back to radar illumination. In the case study of the French Alps (Chapter 13), uplift is evidenced from the radar image.

4.3.6 Escape tectonics

'Escape tectonics' is a complex structural process associated with active folding and faulting, belt growth and basin formation. All these structures are fairly well expressed by the morphology, as is the case in Irian Jaya (Chapter 16).

4.3.7 Rift tectonics

Rifts are characterised by normal and strike-slip faults associated with tilted blocks, all types of features that are mainly expressed by the morphology. This is the case in the Afar case study (Chapter 11).

Volcanism frequently occurs in rifts, especially in oceanic rifts. In the example of the Iceland rift (Chapter 15), relationships between volcanism and tectonics are clearly established from radar imagery because volcanic edifices as well as faults and tension fractures have well-defined morphology.

4.3.8 Drainage

Drainage in a desert environment is frequently hidden by a veil of sand. Drainage patterns are characterised by continuous channels that can be observed by transparency across dry sands, as is the case for the problem of the end of Wadi Tamanrasset in the Tanezrouft region of the Sahara (Chapter 9).

4.3.9 Karst morphology

Karst morphology is characterised by complex patterns of lime sinks that form a peculiar macro-texture (image structure) on the radar images. Karst morphology is generally associated with limestone, as is the case for the karst case study in Turkey (Chapter 7).

4.3.10 Changing landscape

Rapidly changing landscape can be detected by interferometry, or more simply by changes in backscattering or morphology. The changes can be well expressed by a colour composite of two images acquired at different dates. Changes may be related to erosion, sedimentation, earthquakes, volcanic activity or flooding.

In the case of the Pinatubo volcano (Chapter 8), changes in backscattering and morphology are well expressed by a colour composite image, showing active lahar events.

Changes in backscatter due to variations in ground moisture and surface roughness are enhanced in the case of the Vaison-la-Romaine flood in Southern France (Chapter 10).

4.4 Radar imagery of meteorite impact craters on Earth

As a planetary object, the Earth is subject to planetary processes such as the impact of asteroids and comets. Although it is not obvious, the Earth is subject to about twice as many impacts as the moon, because of its larger gravitational cross section.

The Earth, however, does not look like the moon, as its surface is constantly renewing itself due to erosion, sedimentation, and tectonic and volcanic processes. Currently about 150 terrestrial impact structures have been identified, with the discovery rate of 3-5 new structures per year. The spatial distribution of the known structures is not random, with major concentrations occurring in desert areas concentrated in North America, Europe, West Russia, and Australia.

Terrestrial impacts are responsible for such diverse phenomena as the mass extinction event of 65 Ma, which saw the demise of the dinosaurs (the Chicxulub impact). Such impacts may also have some economic significance: for example, the vast copper-nickel deposits at Sudbury, Canada, are likely the result of a large-scale impact 1,850 million years ago. Several impact structures in sedimentary rocks have also provided suitable reservoirs of economic oil and gas deposits.

Until recently, impacts by extraterrestrial bodies were regarded as perhaps an interesting but certainly not an important phenomenon in the spectrum of geological processes affecting the Earth. Our concept of the importance of impact processes, however, has been changed radically through planetary exploration, which has shown that virtually all planetary surfaces are covered by craters due to the impact of interplanetary bodies. It is now clear from planetary bodies that have retained portions of their earliest surfaces that impact was a dominant geological process throughout the early solar system. For example, the oldest lunar surfaces are literally saturated with impact craters, produced by an intense bombardment of at least a hundred times higher than the present impact flux, which lasted from 4.6 to approximately 3.9 billion years ago. The Earth, as part of the solar system, experienced the same bombardment as the other planetary bodies.

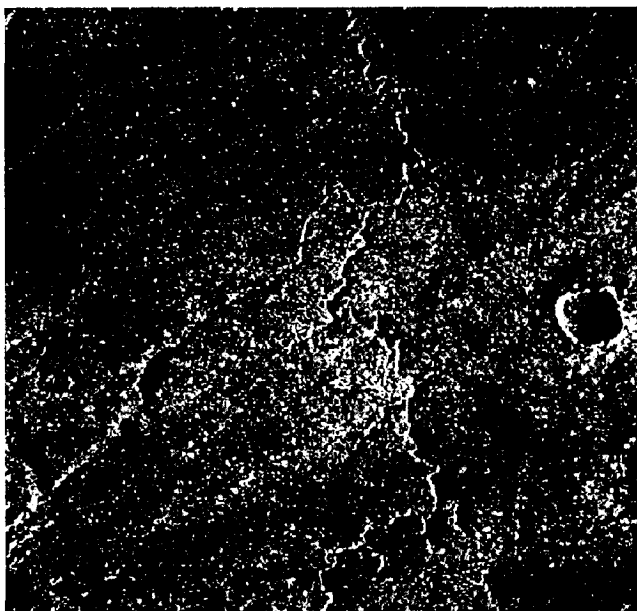
On the Earth, a variety of possible effects have been ascribed to impacts. Heat generated by early impacts may have led to the expulsion of gases from the Earth's initial crust, thus contributing to the primordial atmosphere and hydrosphere. Additionally, the impacting bodies themselves may have contributed to the Earth's budget of volatile chemical components. This early bombardment would also have frustrated the development and evolution of early life, with the largest impacts having the capacity to effectively sterilise the surface of the globe.

The morphology of impact craters changes with crater diameter. This size/morphology relationship is well illustrated by fresh-appearing craters on the moon. Only the smallest impact craters have a bowl-shaped form. As the crater diameter increases, slumping of the inner walls and rebounding of the depressed crater floor create progressively greater rim terracing and central peaks. This same progression in crater morphology is observed throughout the solar system, including on the Earth; although terrestrial craters are less well preserved than on the moon and hence more challenging to classify. One notable difference between lunar and terrestrial impact craters is the lower diameter range for each morphological type on Earth. This difference is due to the higher gravity on Earth.

On Earth, the basic types of impact structures are as follows:

1. Simple structures, generally up to 4 km in diameter, with uplifted and overturned rim rocks, surrounding a bowl-shaped depression. They are partially filled by contact breccia.

The crater diameter is 1186 m, it is located at N35° 2', W111° 1' and it is about 50,000 years old. North is up



As seen by ERS-1



An aerial photo

2. Complex impact structures and basins, generally 4 km or more in diameter, with a distinct central uplift in the form of a peak and/or ring, an annular trough, and a slumped rim. The interiors of these structures are partially filled with breccia and rock melted by the impact.

Figure 4-5:
*Barringer meteorite
impact crater in
Arizona (USA)*

Although the number of known impact craters on Earth is relatively small, the preserved examples form an extremely important resource for understanding impact phenomena. They provide the only ground-truth data currently available, and are amenable to extensive geological, geophysical and geochemical studies. Earth's impact craters also provide important data on the structure of such landforms in all three dimensions. In some cases, the large sizes of terrestrial impact craters, up to approximately 300 km in diameter, require orbital imagery and observation to provide an overall view of their structure and large-scale context.

[Ref. National Geophysics Section of Natural Resources, Canada]

5. Detection and mapping of neotectonic activity

In addition to traditional geophysical methods for mapping neotectonic activity, a new technique based on microwave remote sensing has been developed recently for detecting small movements in volcanic and seismic zones. This chapter reviews the potential of the SAR instrument provided by analysis of the phase of the radar signal (see also Chapter 3). Known as 'differential interferometry', this can detect movements of only a few millimetres of crustal deformations between two SAR data acquisitions.

The phase difference computation between appropriate pairs of images also makes it possible to generate Digital Elevation Models (DEMs) with accuracy of the order of 5 to 10 m, depending on the morphology, the ground coverage of the area, the parameters of the data and certain environmental conditions (see section 3.2.2).

The assessment of ground displacements due to earthquakes, volcanic phenomena, subsidence, or a slowly moving slope is possible by performing the same kind of processing on a series of carefully selected SAR images that are suitable for differential interferometry.

5.1 Earthquake

As a well-studied event, an interferometric application for the Landers earthquake is presented. On 28 June 1992, this earthquake with a magnitude of 7.3 ruptured over 85 km along a complex fault system in the Mojave Desert of California. Near the fault, field investigations show right-lateral slip reaching maxima of 4 m and 6 m, at 10 km and 40 km north of the epicentre respectively. Some three hours after the main shock came the magnitude 6.4 Big Bear earthquake, which did not produce any surface rupture. Co-seismic horizontal displacements as large as 3 m offset were surveyed at some 92 geodetic benchmarks compared before and after the earthquake. Near the fault, displacements detected by pixel correlation using optical images acquired by the SPOT satellite were of the order of one metre.

The Landers earthquake sequence provided an ideal test case for radar interferometry, because its shallow depth produced spectacular surface rupture in an arid area, less than three months after the ERS-1 satellite began acquiring radar images in its 35-day orbital cycle. With 20 fringes in the shape of a crushed butterfly, the first earthquake interferogram (Figure 5-1) illustrated the co-seismic deformation field with over a million pixels [1]. Published on the cover of Nature magazine, the original study launched many others.

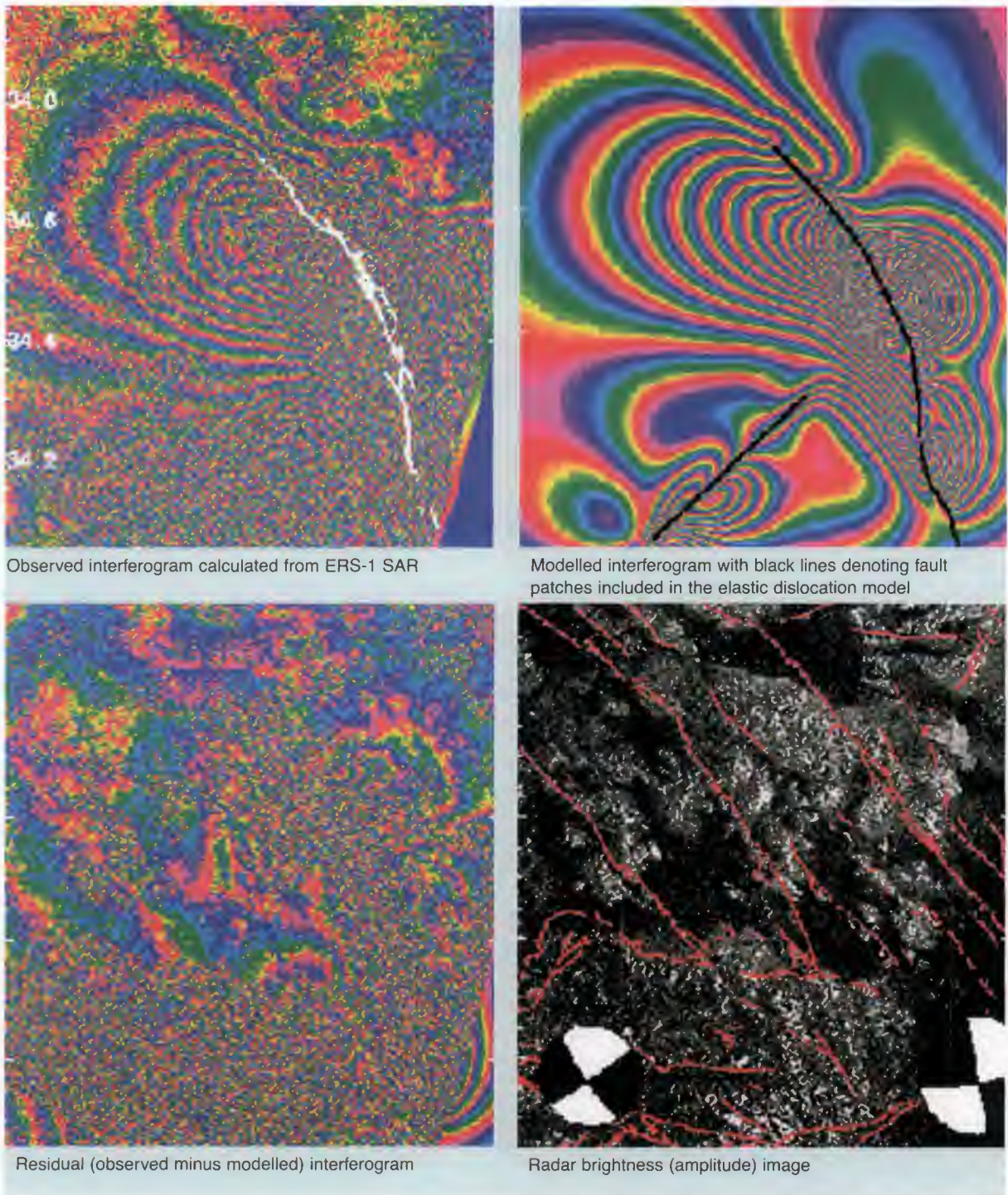


Figure 5-1:
Interferogram of an earthquake

The top left image is produced from images taken before (April 24, 1992) and after (June 18, 1993) the earthquake [1]. Each fringe in the first three images denotes 28 mm of change in range. The number of fringes increases from zero at the northern edge of the image, where no co-seismic displacement is assumed, to at least 20, representing 560 mm in range difference, in the cores of the lobes adjacent to the fault. The asymmetry between the two sides of the fault is due to the curvature of the fault and the

geometry of the radar. Black lines denote the surface rupture mapped in the field. The altitude of ambiguity is 220 m.

Prior to the main shock on June 28, 1992, ERS-1 imaged the Landers area only once, on April 24. Combining this image and the one acquired on August 7, Massonnet et al. [7] [1] used the two-pass technique and a digital elevation model with a third image acquired on July 3 for error budgeting. Zebker et al. [16] avoided the elevation model by including this third image in the interferometric process. These two interferograms, which are called two-pass and three-pass respectively, are qualitatively similar, but also differ in several respects.

In the two-pass interferogram, only one pair of data sets is used, and the relative distance between the satellite tracks of the two passes during the acquisition needs to be less than 100 m. As well as this condition, the technique can only be applied in areas of not too rugged terrain. In the resulting fringe image, two types of fringe are visible: those due to the height changes of the terrain, and those due to very small earth movements.

In three-pass differential interferometry, two pairs of data sets are used (with one set in common) to produce two near-independent fringe images (an intermediate product for generating digital terrain models). Then the two fringe images are processed to get differential fringes, which no longer show the terrain fringes, but only those due to very small earth movements (if any).

5.2 Volcanism

Mount Etna in Sicily has been monitored using SAR interferometry. One of the most recent eruptions started on 14 December 1991 in the Valle del Bove, a large amphitheatre formed by collapse of the eastern flank. Lava erupted along a fracture system that had opened in 1989, and covered most of the southern part of the Valle del Bove. The eruption stopped on 31 March 1993 after 473 days. The rate of lava production remained stable during most of the eruption, and the total erupted volume was in the order of 0.3 km³. The current activity of Etna is monitored by the Istituto Internazionale di Vulcanologia (IIV) in Catania. Ground-based measurements of volcano deformation can be used to assess eruptive hazard, but require the costly (and often hazardous) installation and maintenance of instrument networks. It has been demonstrated that space-borne radar interferometry can be used to monitor long-term volcanic deformation. Such deformation associated with the last large eruption of Mount Etna (1991-93) was measured and interpreted using the InSAR technique for the first time on a volcano. The resulting image (Figure 5-2 overleaf) can then be interpreted as a contour map of the ground.

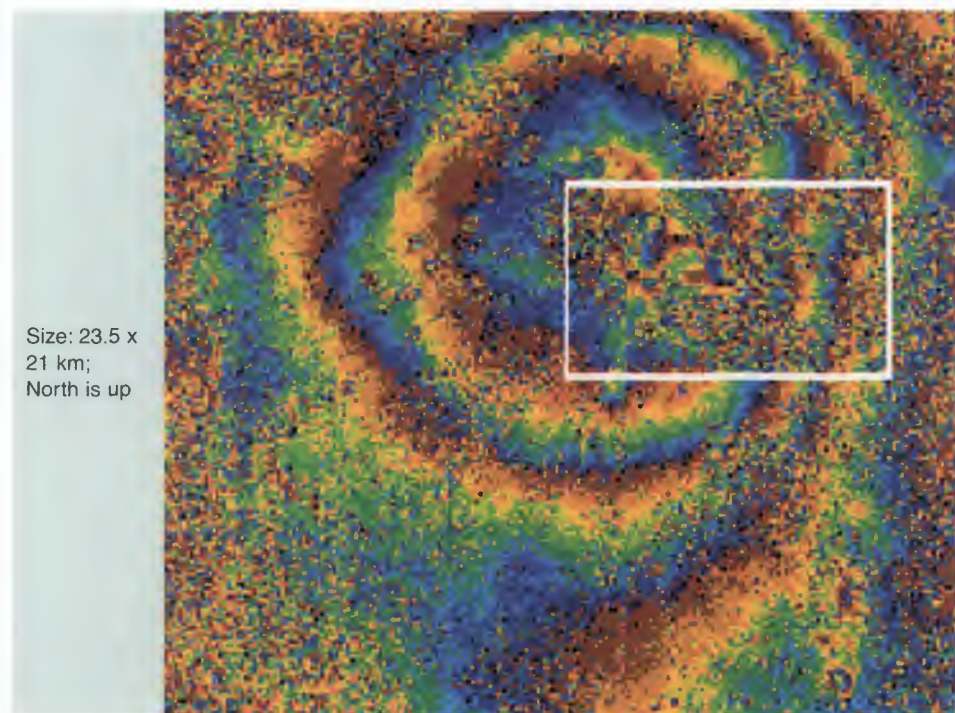


Figure 5-2: Mount Etna, fringes from a differential interferogram

One fringe corresponds to a ground displacement of 28 mm in the direction of the satellite. Tropospheric and ionospheric heterogeneity may also contribute to the results as artefacts. About four concentric fringes are visible in the picture, indicating a subsidence of the volcano of 112 mm in range (line-of-sight towards the satellite). The rectangle shows local subsidence in the E-W striking Valle del Bove. In Figure 5-2 the area does show a discontinuity of the fringes. A close-up study revealed fringes due to shrinking from the cooling of older lava (reported by Groupe de Recherche en Géodésie Spatiale, CNES, Toulouse).

5.3 Mining Subsidence

SAR repeat-pass interferometry can be used to measure man-induced surface subsidence to centimetre resolution [10], [11]. In the case of the Upper Silesian Coal Basin in Poland (Figure 5-3), a densely urbanised, heavily industrialised area is affected. Here mining subsidence causes damage to buildings and other structures: it changes surface drainage patterns and is associated with sink holing and deep fracturing of building grounds.

Although traditional surveying and prediction methods are well developed [6], the effects of mining damages at the surface and the impact on the environment are not yet sufficiently mapped. Newest developments in remote sensing techniques may allow mapping and predictions of mine damage that are more cost-efficient, more accurate, and more frequent. Knowledge of the spatial distribution of damage zones may help in land-use planning and compensation strategies.

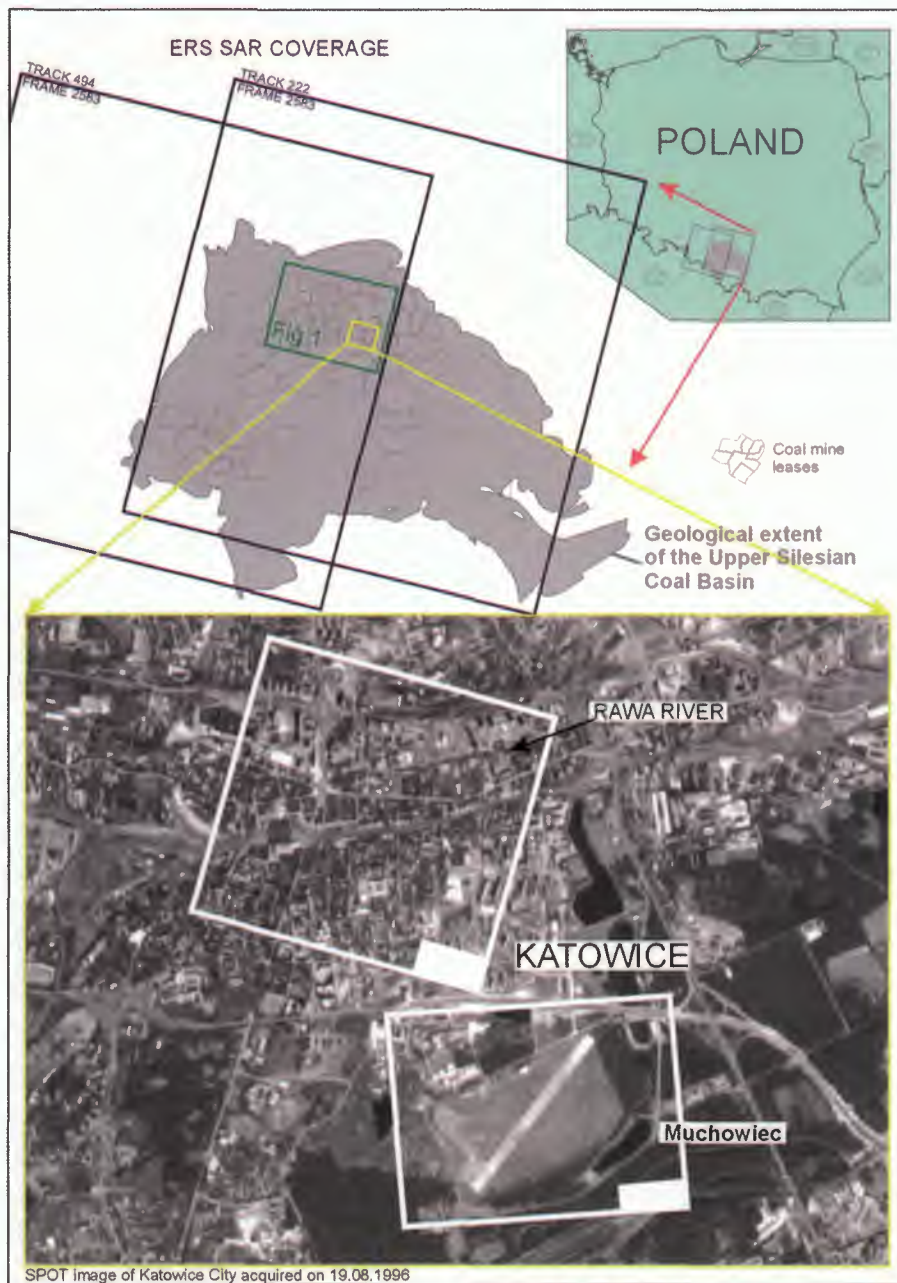
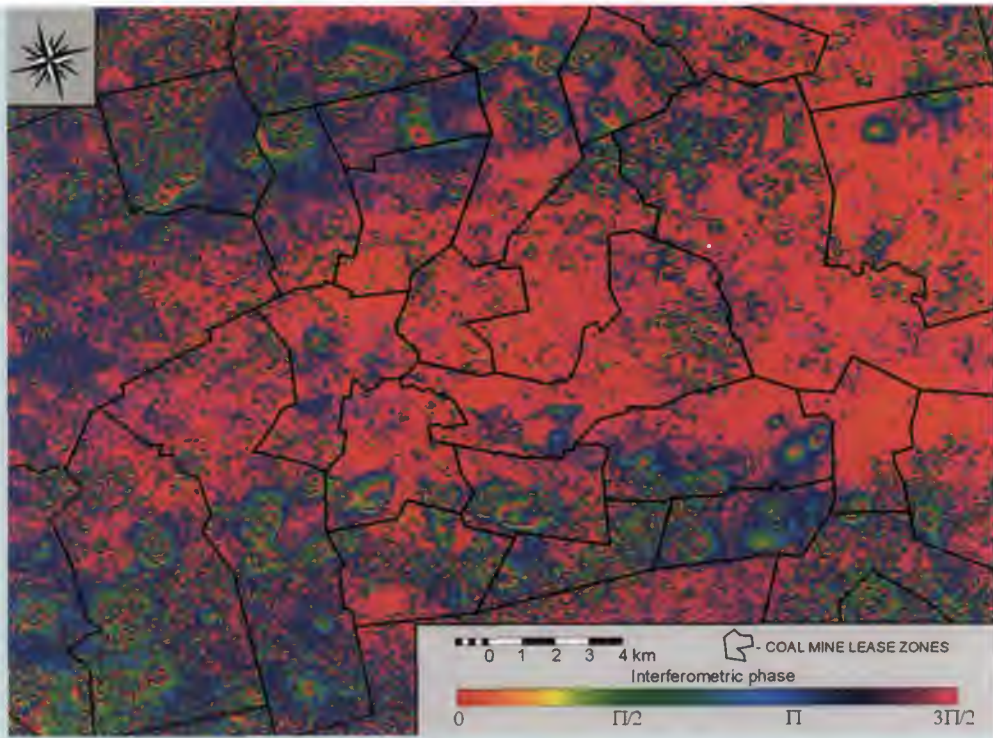


Figure 5-3:
Location map of
studied areas of
mining subsidence
(Poland)

The area under investigation covers approximately 300 km² exploitation of almost horizontal coal seams, and subsequently subsidence troughs develop that are visible at the surface. Initial down-warping was slow, not exceeding a few millimetres daily. After 6-8 months it accelerated to 1 cm per day. After the next 6-12 months the surface movement was fastest, and migrated, following the working front of coal exploitation. After 18 months the subsidence rate decreased and became negligible.

During continuous coal mining, the SAR interferograms show the surface changes at locations of active mining in form of concentric rings (Figure 5-4 top), while a SAR intensity image just shows the land cover of the area (Figure 5-4 bottom).

Interferometric fringes generated from a pair of ERS SAR single-look complex data showing locations of subsidence as concentric rings. One colour-cycle corresponds to a movement of 2.8 mm in the range direction (line-of-sight)



A SAR Intensity image of the same area viewing the land cover such as cities (bright areas), woods (dark grey) and agricultural land (light grey)

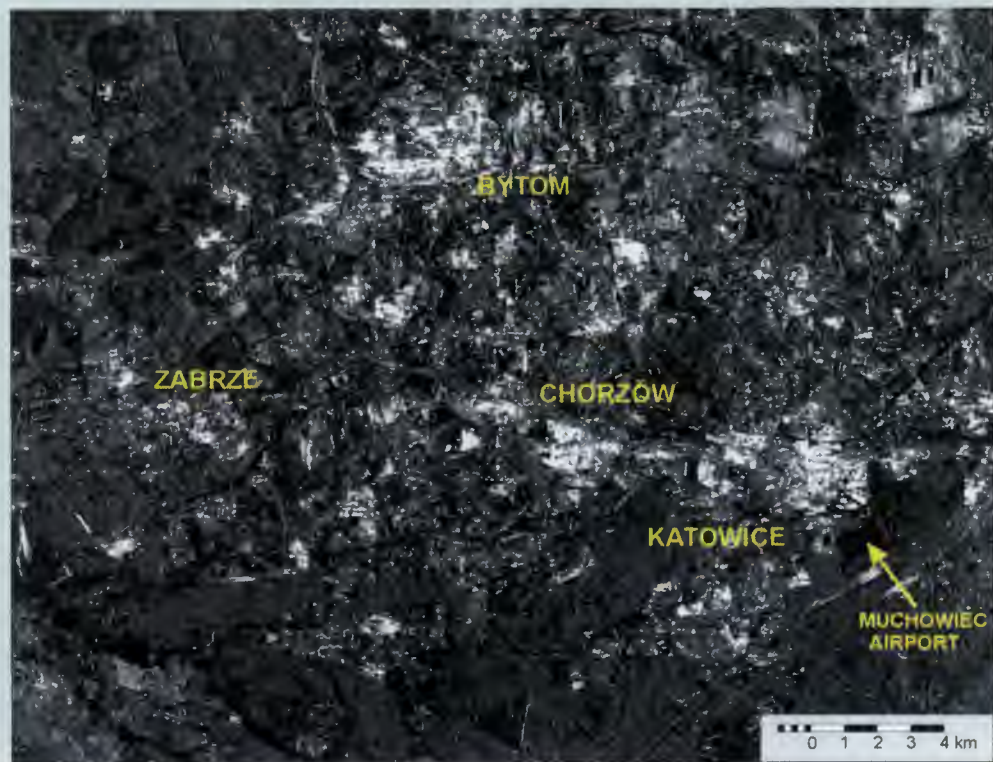


Figure 5-4: SAR images of mining subsidence

The schematic diagram Figure 5-5 shows the effect of the mining activity as observed on the surface.

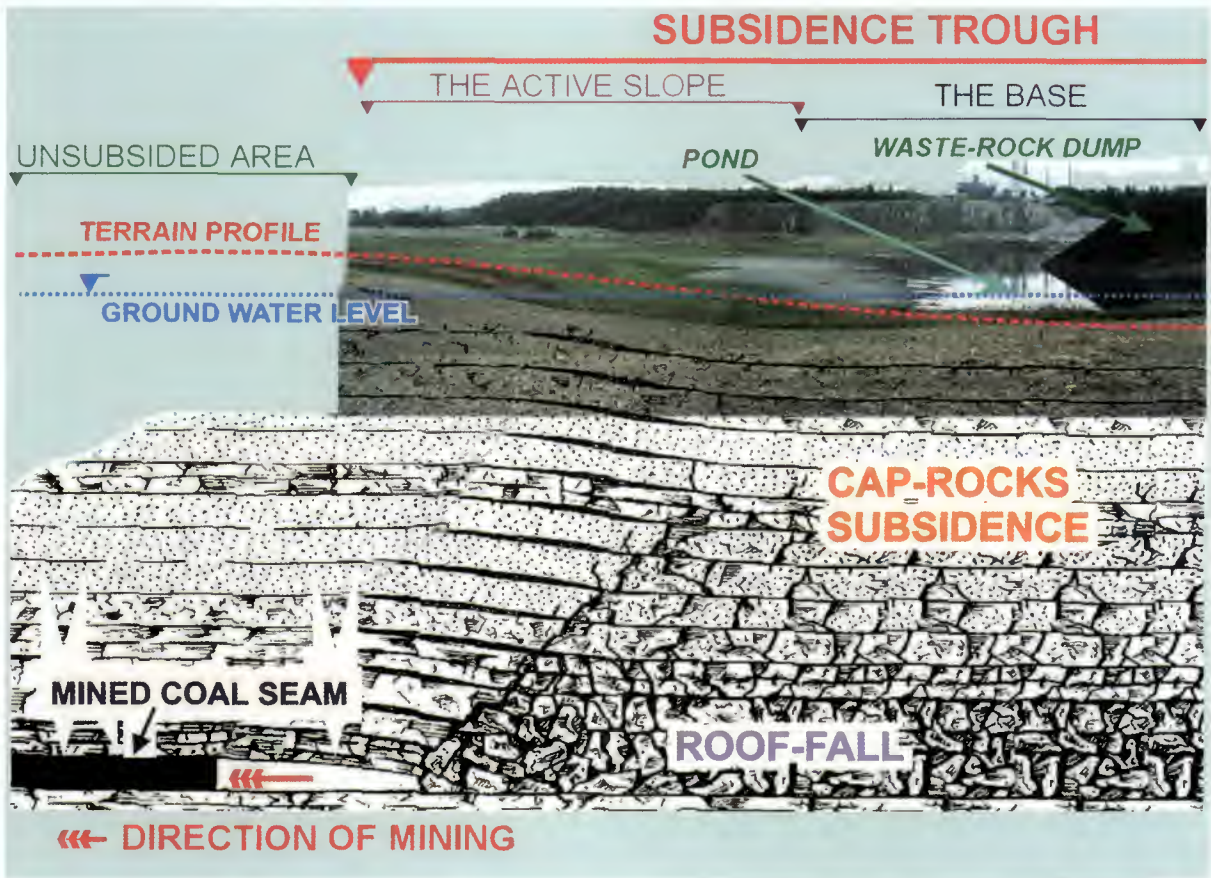


Figure 5-5:
Diagram of
subsidence trough
with photographed
landscape
superimposed

The relationships between the interferometric representation, the mining activity and the advancing subsidence are explained in Figure 5-6.

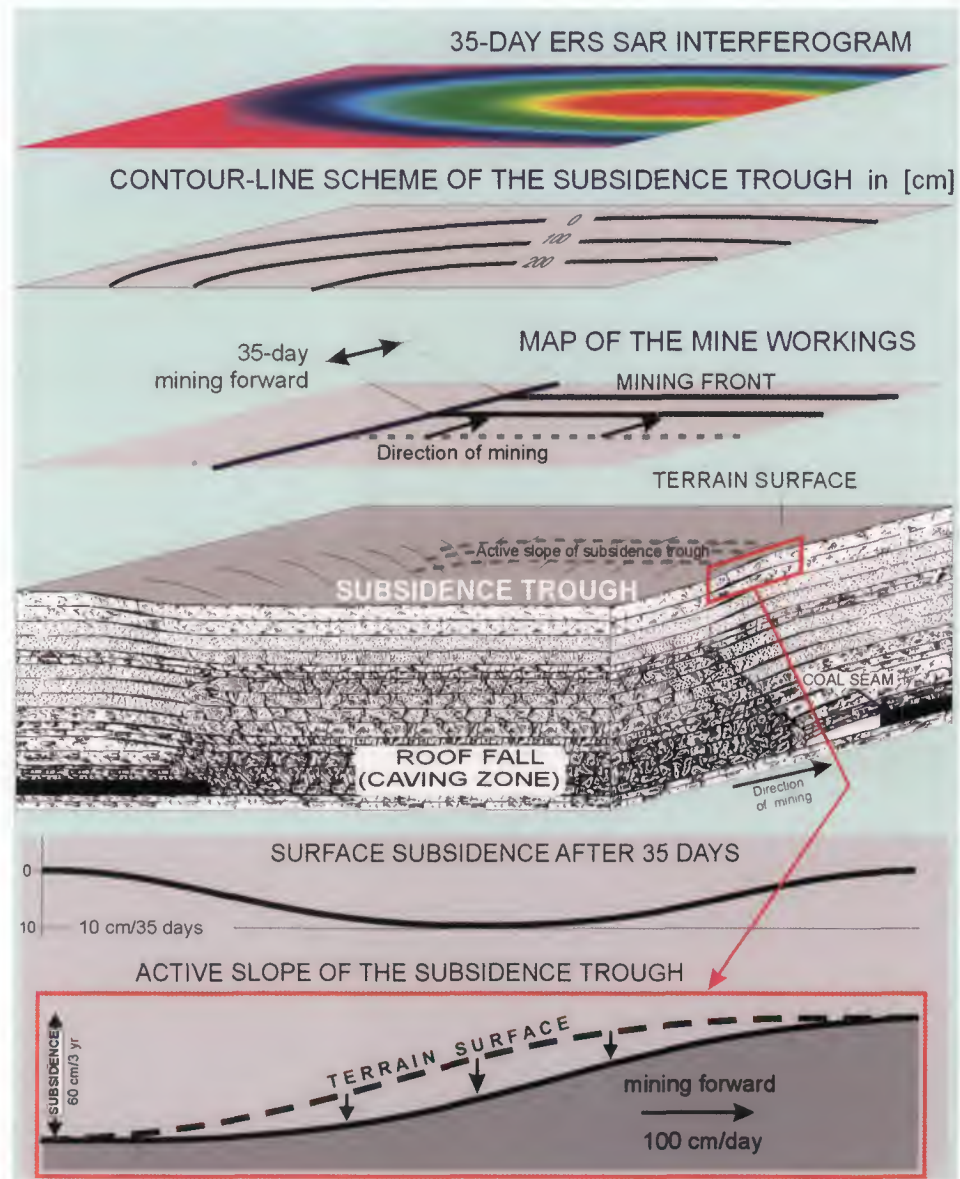


Figure 5-6: Interpretation of a SAR interferogram in a subsidence trough

Fringes (top) appear above an active mining section (below). The centre of the fringe is the area of maximum surface displacement. It is located on the slope of the trough. The contour lines show the subsidence prediction based on ground survey. The actual mining direction is indicated on the 'map of mine workings'. On the surface it produces an advancing (active) slope that enlarges the subsidence trough. Below, the amount of subsidence is shown together with a cross section of the trough. In the centre of the figure, the diagram explains the development of a subsidence trough above a coal mine (based on [2]).

The data used for this study has been carefully selected (Table 5-1). The influence of possible errors (variable seasons and weather conditions) was minimised by the selection

of best-suited pairs of SAR images, so that the observed fringe pattern most probably represents only the surface deformation – i.e. the effect of mining subsidence.

Track	'Master' image			'Slave' image			Temporal separation	Perpendicular baseline
	Satellite	Orbit	Date	Satellite	Orbit	Date		
222	ERS-1	06880	08.11.92	ERS-1	06389	04.10.92	35 days	54 m*
494	ERS-1	11661	08.10.93	ERS-1	11160	03.09.93	35 days	20 m
222	ERS-1	20751	04.07.95	ERS-2	02080	13.09.95	70 days	9 m

ERS-1 and ERS-2 SAR data: track 222, 494, frame 2583

* The topographic effects have been removed from this interferogram by using DEMs computed from ERS SAR tandem mission data

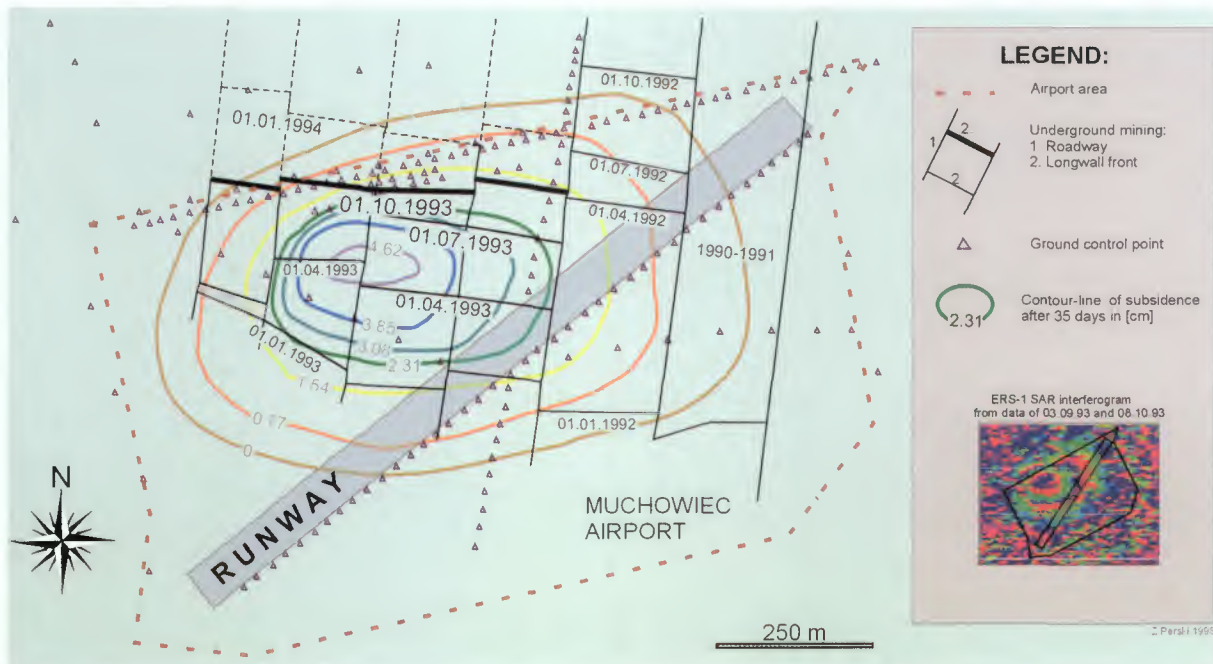
Both the 35-day interval interferograms are characterised by good coherence, especially in urbanised areas. The coherence in farming areas is variable and depends on the season. Overall, the coherence in agricultural regions is acceptable for interferogram processing. However, the 70-day interferogram has much lower coherence: in the pair from late summer 1995 (July and September), a clear seasonal effect is evident.

Table 5-1: Characteristics of ERS SAR SLCI data for interferometric processing

5.3.1 Test in a rural area

The vicinity of Muchowiec airport, near Katowice (Poland), is flat and not urbanised (Figure 5-7). Isolines of the surface changes were traced, based on differential interferograms from data of 3 September and 8 October 1993. The ground control points (black triangles) are surveyed in six-month cycles.

Figure 5-7: Subsidence within the Muchowiec airport area (Poland)



In 1993, coal extraction was carried out at a depth of 700 to 800 m below the surface, in four longwalls, each 100 m long, and subsequently hydraulic filling was applied. At the surface level and above the working front of the longwalls, advancing at a rate of 25 m per month, a migration of the active slope of the subsidence trough could be observed. The predicted maximum subsidence (15 to 20% of the coal seam thickness) was 60 cm over a distance 350 to 400 m from the edge of the mining depression. The map of mining in seam no. 510 has been compared with the 35-day interferogram (Figure 5-9 bottom right corner), through September 1993, by means of a GIS (Geographic Information System).

The fringe pattern on the ERS SAR interferogram shows the subsidence distribution in great detail. The active slope of the subsidence trough is visible on the interferogram as an 800 m by 1250 m elliptical set of fringes. The highest rate of down-warping is observed in the middle of the interferogram between the two central working faces (Figure 5-7), located 100 m behind the current working face. This corresponds to a 3-4 month period of exploitation. The area of lower density of the fringes in a north-easterly direction can be interpreted as an effect of residual subsidence caused by works abandoned in 1991 and 1992. The presence of two full fringes shows that subsidence occurs at a maximum rate of 5.6 cm/month or 2 millimetres per day.

5.3.2 Comparison with ground measurements

The Muchowiec airport is monitored by the Katowice coal mine surveying office by means of 140 control points distributed along four traverses, and including points at the corners of buildings. The ground surveying is done in two cycles per year, ending in April and October respectively. During a 6-month period in 1993 (April to October), some points showed a maximum subsidence of 16 to 25 cm, some 160 m behind the mining front. Analysis of neighbouring points showed that subsidence diminished sidewise to 0 cm at a distance of about 300 m, corresponding to a radius of mining influence at surface level.

The monthly subsidence according to InSAR data is of the order of 2.5 to 5 cm greater than is measured at the survey points. The difference can be explained by the variance in the applied methods: the monthly subsidence data determined by the survey are averaged over six months, while the interferogram shows real subsidence in the specific month (i.e. 35 days). Therefore, interferometric data appear to be more realistic, especially when monitoring the fastest surface displacement that persists for two to three months only.

5.3.3 Test in an urbanised area

The second area studied was located inside the densely urbanised centre of the Katowice City. Here, mining was carried out between 1993 and 1995 within the so-called 'protection pillar' of the city (a protected volume below the city, where mining is officially not permitted). The subsidence resulted from coal extraction at a depth of 300 to 450 m below ground level. Of a system of five longwalls, only three are currently active. A coal layer of 2.5 m thickness was exploited and subsequently hydraulic filling was applied. The total length of the working front of the three longwalls was 700 m and the front advanced at a rate of 200 m per year.

According to predicted deformations and subsidence, mining under the city should have been safe. However, some surface changes turned out to affect buildings, e.g. those of the University of Silesia, and also damaged the banks of the Rawa River. On

interferograms from 1992, 1993 and 1995, a NW-migrating active slope from a subsidence trough is clearly visible and represented by an elliptical set of fringes (Figure 5-8).

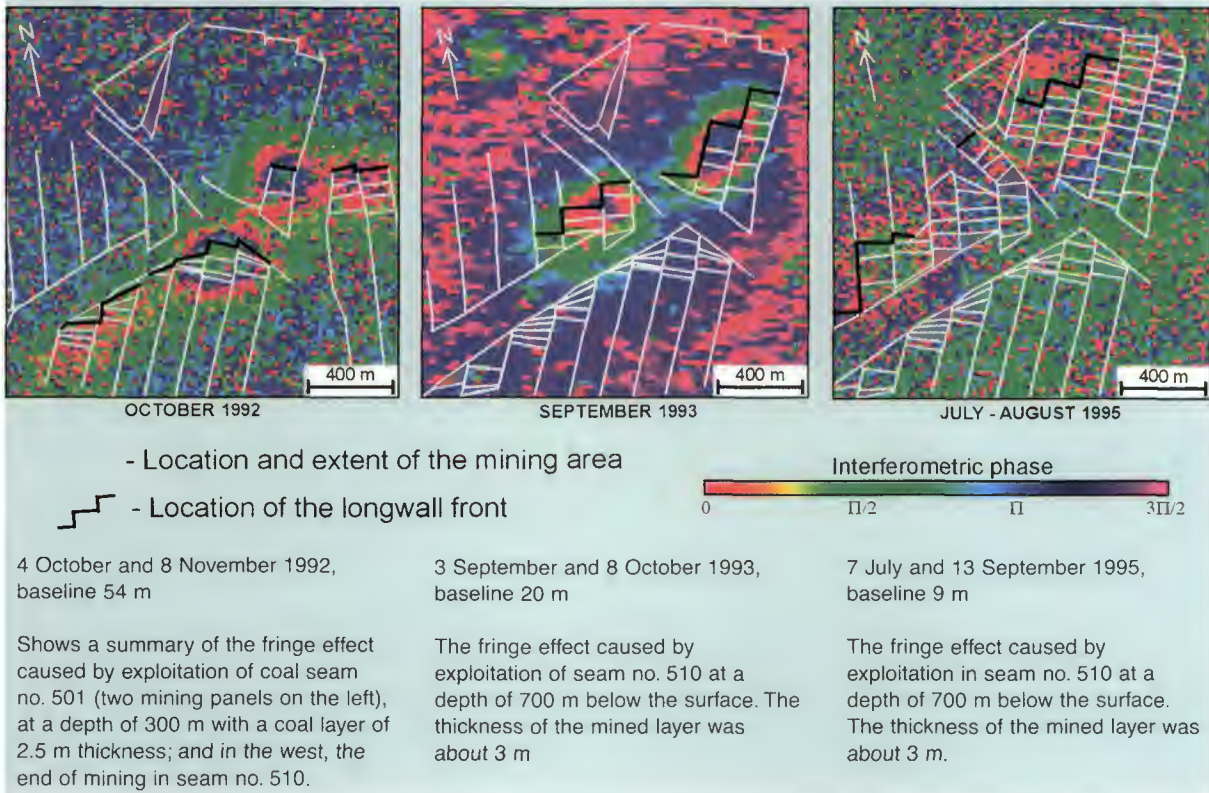


Figure 5.8: Series of three interferogram pairs of subsidence in Katowice Poland

White and black lines show the level of the mine workings with locations and extents of the mining areas and longwall fronts. The maximum of subsidence always occurs some hundred metres behind the mining front.

The centre of the fringes is 80 m behind the working face, and indicates a vertical movement of about 2.8 cm per month or 1 mm per day. The area affected by greatest changes is located in the centre between three active longwalls. The active slope of the subsidence trough perpendicular to the working face is about 1000 m long.

In fact, in Katowice the influence of mining was already observed on the surface after 3 to 4 months. Such a short time of impact can be explained by the relatively shallow exploitation, the presence of 50 m-thick Quaternary deposits in the Rava river valley, and already existing damage to overlying rocks caused by old abandoned workings, some of them from the 19th century. This is in comparison with the exploitation in the southwestern part of seam no. 501 (see above) where surface changes were caused only after 6 months (Figure 5-7) mainly because of a thick series of hard carboniferous rocks covering the exploited seams [17].

Interferometric results are shown on an interferogram from 19.01 to 23.02.1998 with concentric fringes – typical from areas of land subsidence (Figure 5-3). This image corresponds with the pattern of mining works in the following seams: 352/3, 360, 364, 401/1, 403/1, 404/5, 405/3 (Figure 5-9, Table 5-2).

The length of the average working face of the long walls was above 240 m and the faces advanced at a rate of 2.2 to 4.2 m per day. Predictions of deformations and subsidence suggested that it would be safe to mine under urbanised areas. However, the actual surface changes turned out to affect buildings and the banks of the River Bierawka. The length of maximum subsidence is located just behind the mining front of the long-walls with caving (Figure 5-9).

Subsidence situation between 19.1.98 and 23.2.98 in the Szczygłowice Coal Mine [13]

Practically all advancing mining fronts show differential interferometric fringes at the surface, indicating a vertical displacement of at least half the wavelength of the C-band radar (28 mm).

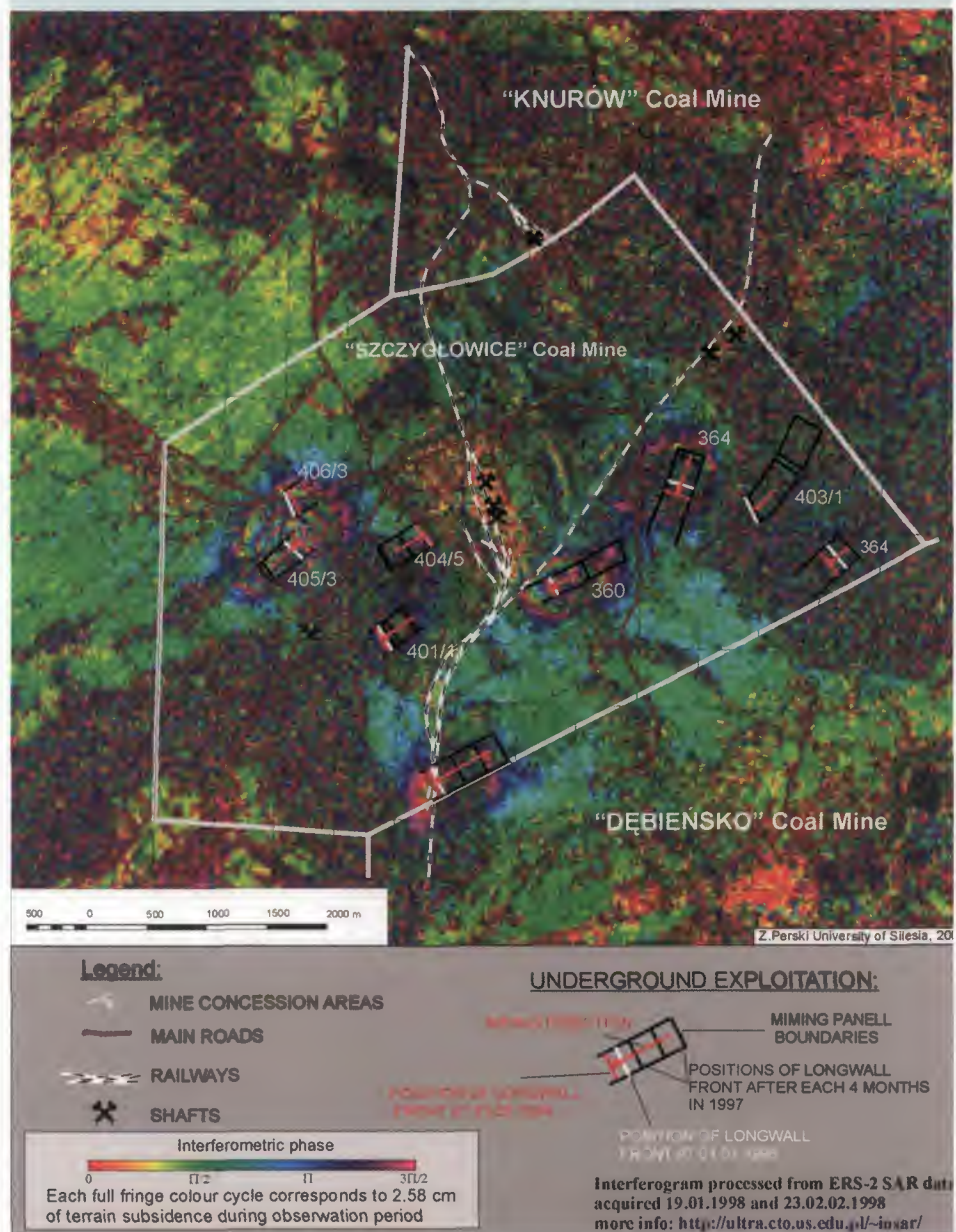


Figure 5-9: GIS display of subsidence in the Szczygłowice Coal Mine

The active slope of the subsidence through measured perpendicular direction to the working face is above 250 m, i.e. 3 - 5 months after mining. The centre of fringe – an

area of maximum surface down-warping – indicates the zone of highest rated mining subsidence between 2.5 and 12 cm per 35 days (Table 5-2).

Coal seam no.	Thickness of coal seam (m)	Exploitation depth (a.s.l) and level below the surface (m)	Length of mining wall and length of face (m)	Rate of mining subsidence (cm/day)	Rate of subsidence (cm/35 days)
352/3	1.72	-360; 650	260; 190	3.1	2.5
360	1.25	-331; 650	330; 180	4.0	5.0
364	1.76	-390; 650	250; 135	2.2	?
364	1.80	-370; 650	230; 220	3.6	7.5
401/1	1.40	-415; 650	60; 240	3.0	2.5
403/1	1.85	-480; 750	240; 25	2.6	?
404/5	3.70	-499; 750	220; 200	3.3	12
405/3	2.26	-234; 450	220; 250	4.2	2.5

Coal seams mined in the period of October 1997 to December 1997 and January 1998 in Szczyglowice Coal Mine (according to the maps of mine workings in scale 1:5000) [12]

Table 5-2: Summary of coal seams mined in Szczyglowice

On the interferogram from 1998 the migrating active slope of the subsidence troughs are represented by the elliptical sets of fringes (Figure 5-9). As explained above, movement occurs on the active slope of the mining depression, so the fringe ellipse, which shows surface changes over a short time period, is as an excellent indicator of changes of the velocity and deformation pattern and can be termed the velocity ellipse. The areas affected by greatest changes during 35 days of InSAR observation are located in the middle of the active long walls. The ERS SAR interferogram clearly displays the dynamics of the active slope of the subsidence trough.

The interferogram of the Szczyglowice mine area shows for the first time the scale of real terrain deformations occurring in narrowly-defined time periods. Application of SAR interferometry to the study and prediction of mining subsidence opens new directions of research, in particular for subsidence dynamics and their spatial distribution. Two new parameters, the field of subsidence velocity ellipse and the acceleration of mining subsidence, can improve subsidence predictions and minimise mining hazards in densely urbanised areas, and help to improve mining safety.

5.4 Conclusions

- Application of SAR interferometry to the study and prediction of mining subsidence opens new research applications, in particular for subsidence dynamics and their spatial distribution. Interferograms of the Upper Silesia area show for the first time (and for rather small time intervals) the scale of real terrain deformations.
- SAR interferograms represent an important source of information for the understanding of subsidence dynamics over 35-day time intervals. The fringe pattern indicates the rate of change, which is related to the shape of the slope of the

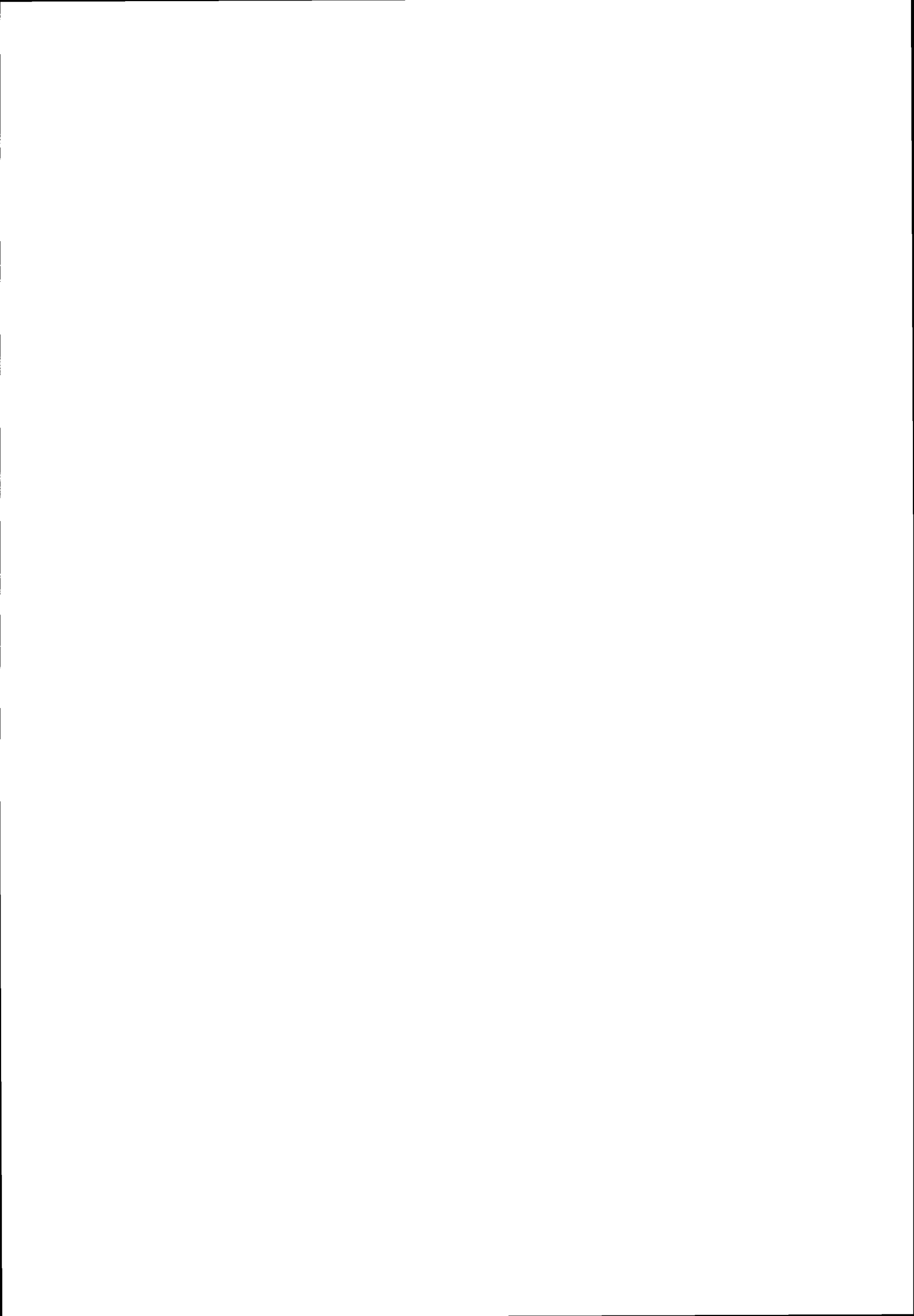
subsidence trough. The number of elliptical fringes represents a real magnitude of the terrain subsidence above the exploited coal seam that is multiple of 2.8 cm. The width of the fringes divided by 2.8 cm represents a ratio of curvature: e.g. 100 m width of one fringe is equal to about 500 m, and 300 m width is equal to a width of 1000 m.

- InSAR images also reveal areas with remnant subsidence of less than 1 cm/month. This marginal displacement of subsidence slopes appears to be as valuable as information derived from conventional surveys, but provides a more complete image of the situation.
- Interferometric analysis allows one to largely differentiate subsidence rates resulting from interruptions during mining, and acceleration or retardation of down-warping caused by differences in the character of the rock mass. This makes it possible to actively steer the operations at the working front. Using such a method of mining control, one can estimate the subsidence in near real-time, which is highly desirable for mining areas under densely urbanised areas.

5.5 References

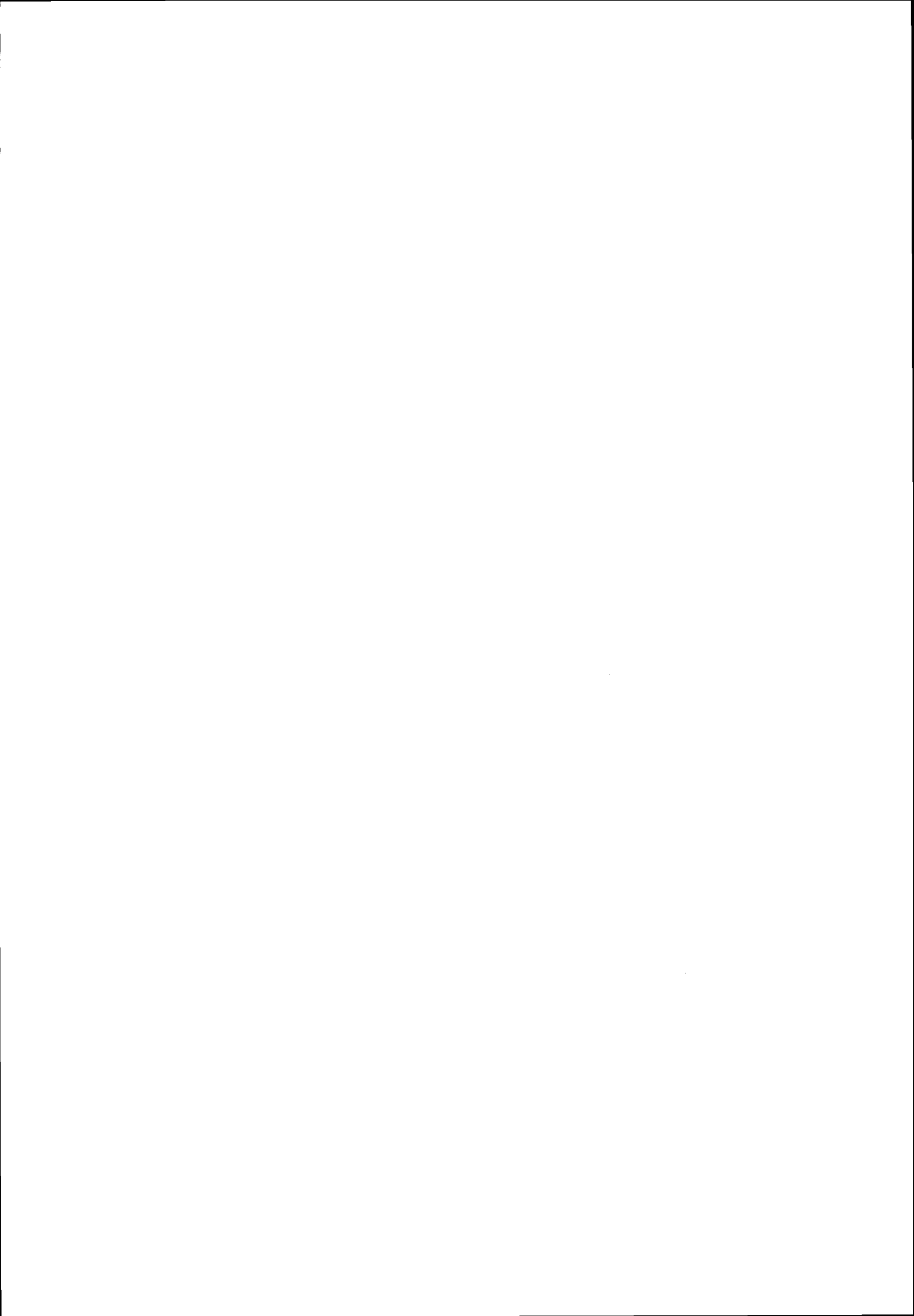
- [1] Massonnet D., Rossi M., Carmona C, Adragna F, Peltzer G, Feigl K, & Rabaute T, 1993, The Displacement Field of the Landers Earthquake Mapped by Radar Interferometry. *Nature*, Vol. **364**, no. 6433, pages 138-142; July 8, 1993
- [2] Boreck M (ed), 1980, Ochrona powierzchni przed szkodami gornicznymi. Wyd. "Slask", Katowice, 1-967 (in Polish).
- [3] Gabriel, AK; Goldstein, RM; and Zebker, HA, 1989: Mapping small elevation changes over large areas: Differential radar interferometry. *Journal of Geophysical Research*, **94**, 9183-9191.
- [4] Haynes, M, Capes, R, Lawrence, G., Smith, A., Shilston, D. and Nicholls, G., 1997: Major Urban Subsidence Mapped by Differential SAR Interferometry. *Proceedings of the Third ERS Symposium*, Florence, Italy; <http://florence97.ers-symposium.org/data/hanssen/index.html>.
- [5] Jura D., 1995: The young-alpine morphotectonics of the Silesian Carpathian foredeep and the recent geodynamics of the Upper Silesian Coal Basin, *Tech. Posz.*, **3**, 13-23
- [6] Kwiatek J. (ed) 1997, Ochrona obiektow budowlanych na terenach gornicznych. Wyd GIG, Katowice, 1-726 (in Polish)
- [7] Kooij, M. van der, 1997, Land Subsidence Measurements at the Belridge Oil Fields from ERS InSAR Data. *Proceedings of the Third ERS Symposium*, Florence, Italy, <http://florence97.ers-symposium.org/data/vanderkooij/index.html>.
- [8] Massonnet D. 1997: Satellite Radar Interferometry, *Scientific American* no. **2**
- [9] Peltzer G., Rosen P., Rogez F., Hudnut K., 1996: Post-seismic rebound in fault step-overs caused by pore fluid flow. *Science* **273**, Number 5279, 30 August 1996
- [10] Perski Z 1998: Applicability of ERS-1 and ERS-2 InSAR for Land Subsidence Monitoring in the Silesian Coal mining region, Poland, *International Archives of Photogrammetry and Remote Sensing* vol **32**, 7, 555-558
- [11] Perski, Z, Jura D, 1999. ERS SAR Interferometry for Land Subsidence Detection in Coal Mining Areas, European Space Agency, *Earth Observation Quarterly* **63**, pp 25-29, Corrigendum in *EOQ* **64**.

- [12] Perski Z, Jura D, 2000: Mining subsidence in the 'Szczygłowice' coal mine and its interpretation by ERS SAR interferometry. *4th European Coal Conference. Guide to Field Trips.* 33-38
- [13] Perski Z, 2002: InSAR and PolInSAR for Land Subsidence Monitoring – User Perspective. *PolInSAR Conference* ESA/ESRIN.
- [14] Pratti C, Rocca F, Monti Guarnieri A, Pasquali P, 1994: port on ERS-1 SAR interferometric techniques and applications. *ESA report 10179/93/YT/1/SC 1-122.* Frascati.
- [15] Tarayre H, Massonnet D, 1994: Effects of a refractive atmospheric processing. *Proceedings of IGARSS'94*, 717-719.
- [16] Zebker HA, Rosen P, Goldstein RM, Gabriel A et Werner CL (1994). On the derivation of co-seismic displacement fields using differential radar interferometry: the Landers earthquake. *J. Geophys. Res.*, **99**, p. 19617-19634
- [17] Perski Z., 2000: Spatial characterisation of the land subsidence above the advancing mining front based on satellite radar interferometry, *11th International Congress of the International Society for Mine Surveying*, vol.1, 76-72, Krakow.



Part II

Case studies



Overview of the case studies

The following 14 chapters of this book consist of a series of case studies, each illustrating one aspect or use of SAR in geology. The locations of the case studies are shown on a map of the world in Figure II-i below, together with the chapter number.

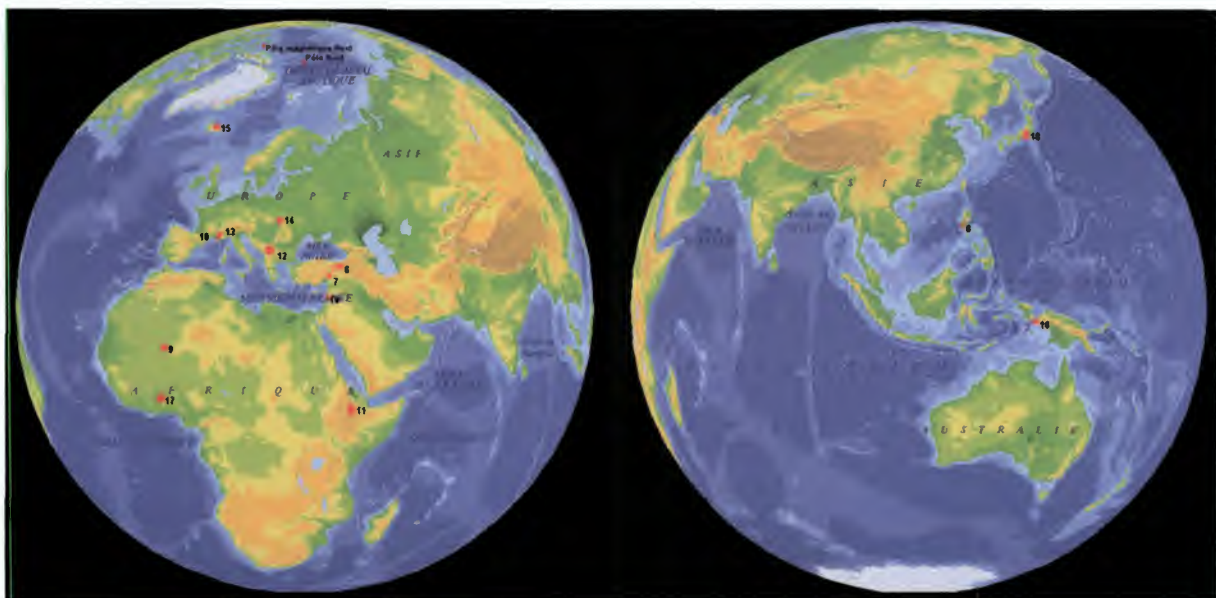


Table II-i summarises all the case studies (with chapter numbers) according to the data applications for which they are useful.

*Figure II-i:
Locations of the
case studies*

Chapter & location	Object characteristics	Radar characteristics							
		Texture	Morphology	All weather	Slope analysis	Relief fore-shortening	Ground moisture	Surface roughness	Ground penetration
6	North Anatolian Fault		X						
7	Eastern Anatolia	X	X						
8	Pinatubo	X		X				X	
9	Tanezrouft								X
10	Vaison			X			X	X	
11	Afar		X			X			
12	Balkans		X						
13	French Alps		X		X	X			
14	Carpathians		X						
15	Iceland		X	X					
16	Irian Jaya		X						
17	Ivory Coast	X							
18	Japan		X						
19	Lebanon		X						

Table II-i: Case studies and data application type

6. Detection of structures related to strike-slip deformation

Case study: the Erzincan area along the North Anatolian Fault (Turkey)

6.1 Geological framework

Anatolia has been defined as a lithospheric continental plate, extruded to the west in response to the north-south relative convergence of Eurasia and Africa-Arabia ([16], [20], [10]). This lateral tectonic escape [6] occurs in between two strike-slip faults, the dextral (right-lateral) North Anatolian Fault (NAF) and the sinistral (left-lateral) East Anatolian Fault (EAF), which meet at the Karliova triangle in Eastern Anatolia (Figure 6-1).

Figure 6-1 shows the shadowed image of a Digital Elevation Model (DEM), illustrating the tectonic context of Anatolia (compiled from [19], [11], [10], [7], [9]). This DEM is generated by linear interpolation of digitised elevation contour lines at 1/1,000,000 scale derived from the Digital Chart of the World [25]. Ground resolution is 2000 m.

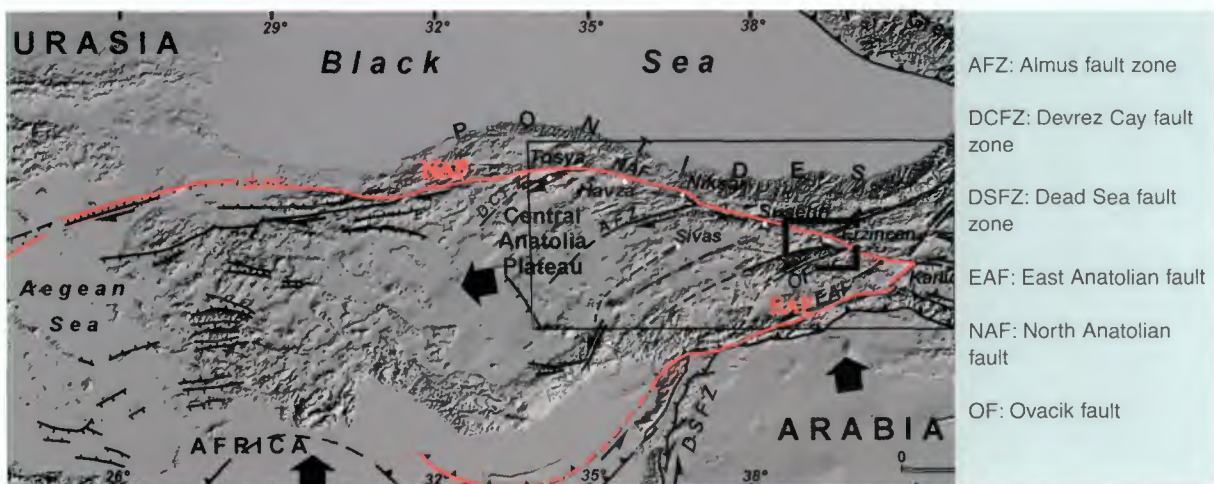


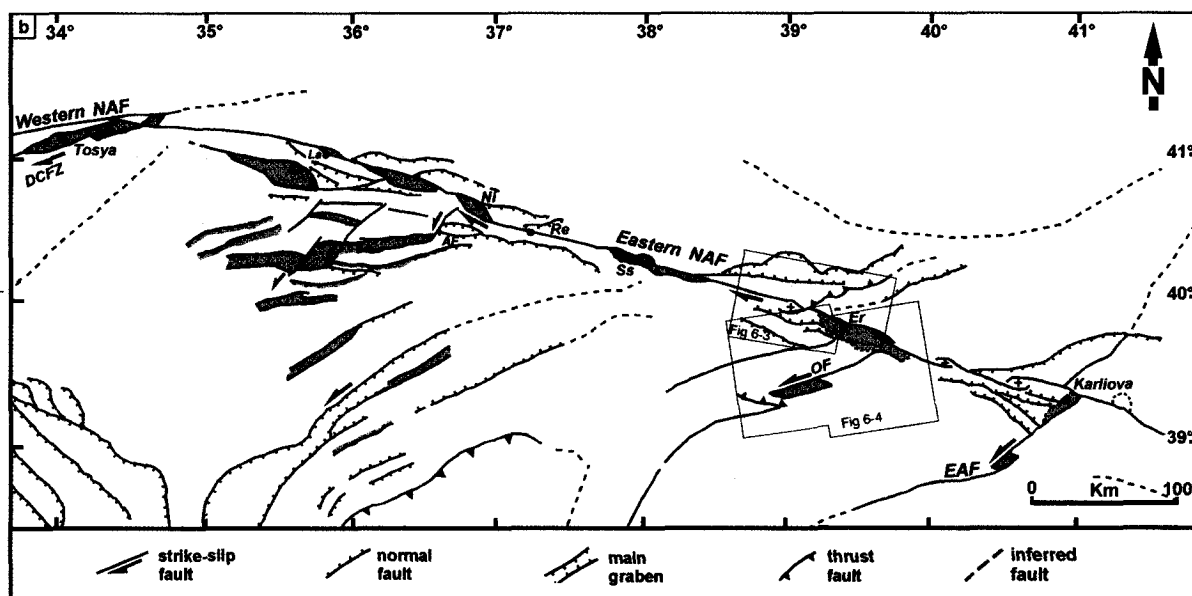
Figure 6-1:
Geological
framework of
Anatolia and
location of the
studied area
(rectangle)

Illumination is from the north. The thick frame is the location of the Erzincan area. The large arrows represent relative plate motions within the Eurasian reference [18].

The NAF has been previously studied using various approaches: geology and geomorphology ([24], [4]), seismology ([16], [14]), aerial photography [3], and Landsat satellite imagery [23]. SAR ERS images can also provide new neotectonic information because they are sensitive to variations in topographic slope [8]. SAR data can describe new geomorphic features such as pull-apart or releasing-bend basins and push-up

structures along the NAF, especially in the Erzincan area where the geometry of deformation is not well constrained.

The NAF is composed of Neogene to Quaternary faults ([1], [21]) and basins, i.e. from west to east, the Tosya, Ladik, Niksar, Susehri, Erzincan and Karliova basins (Figure 6-2). On the large-scale DEM, the Erzincan basin is one of the best-expressed structural features, and deserves a new structural analysis using SAR ERS images.



AF: Almus fault; DCfZ: Devrez Cay fault zone; EAF: East Anatolian fault; Er: Erzincan; La: Kadik; NAF: North Anatolian fault; Ni: Niksar; OF: Ovacik fault; Re: Resadiye; Ss: Susehri; Su: Suluova.

Grey shading represents main Neogene-Quaternary basins.

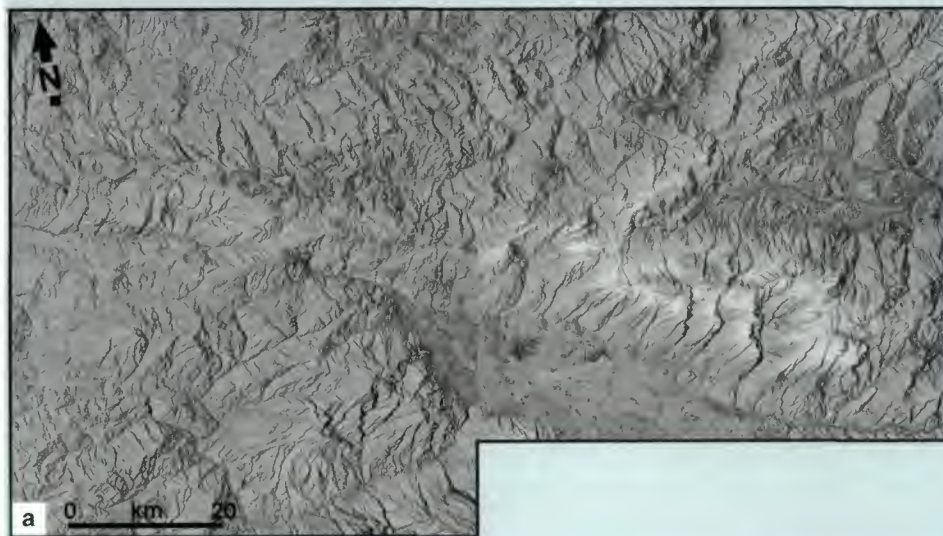
Figure 6-2: Fault pattern in the eastern NAF area from maps, DEM and satellite image interpretations

Two mosaics of SAR ERS-1 images have been used in the Erzincan area (location in Figure 6-2). Two scenes (Figure 6-3a) were acquired in descending node, while two others (Figure 6-4a) were acquired in ascending orbit, illumination being respectively from WSW and ESE. They were respectively matched to form mosaics and displayed in negative prints in order to better show the morphology.

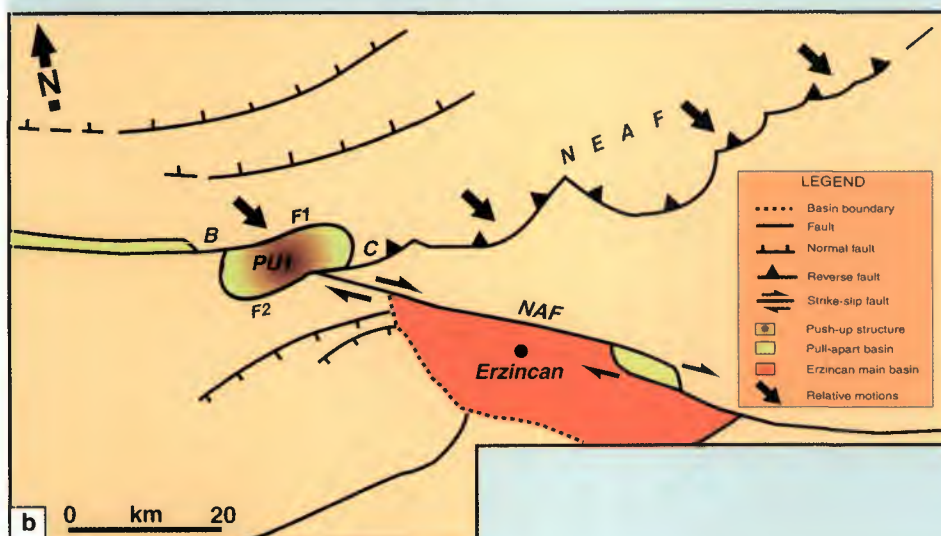
6.2 Analysis of SAR ERS images

West of the Erzincan basin (point B in Figure 6-3), the NAF is a unique fault (F1) bounding a block with distinct relief (PU1) emphasised by a recently uplifted erosion surface.

B: Eastern end of a narrow Pliocene basin; C: NAF-NEAF branching; NAF: North Anatolian fault; NEAF: Northwest Anatolian fault; PU1: push-up structure bounded by faults F1 and F2



Mosaic of SAR ERS images (negative view, descending orbit, looking WSW) of the area west of Erzincan (location in Figure 6-2).



Interpretation of Figure 6.3 (a)

There is a relay with fault F2 that turns eastward to strike N120°E and continues to form the northern boundary of the Erzincan basin. The relay pattern formed by the F1 and F2 – two segments of the dextral NAF – is right stepping and should theoretically have formed a pull-apart basin instead of the PU1 relief. However, at point C, the NAF connects with the North East Anatolian Fault (NEAF), a fault with south-verging thrust component ([17], [23], [15]). To explain the uplifted PU1 structure it is necessary to consider that the NEAF is active and that local compression results in a range.

Figure 6-3: ERS scenes of the Erzincan basin area acquired in descending orbits

The Erzincan basin is filled with Plio-Quaternary sediments ([13], [3]) and is bounded to the northeast by a continuous succession of faults (Figure 6-4).

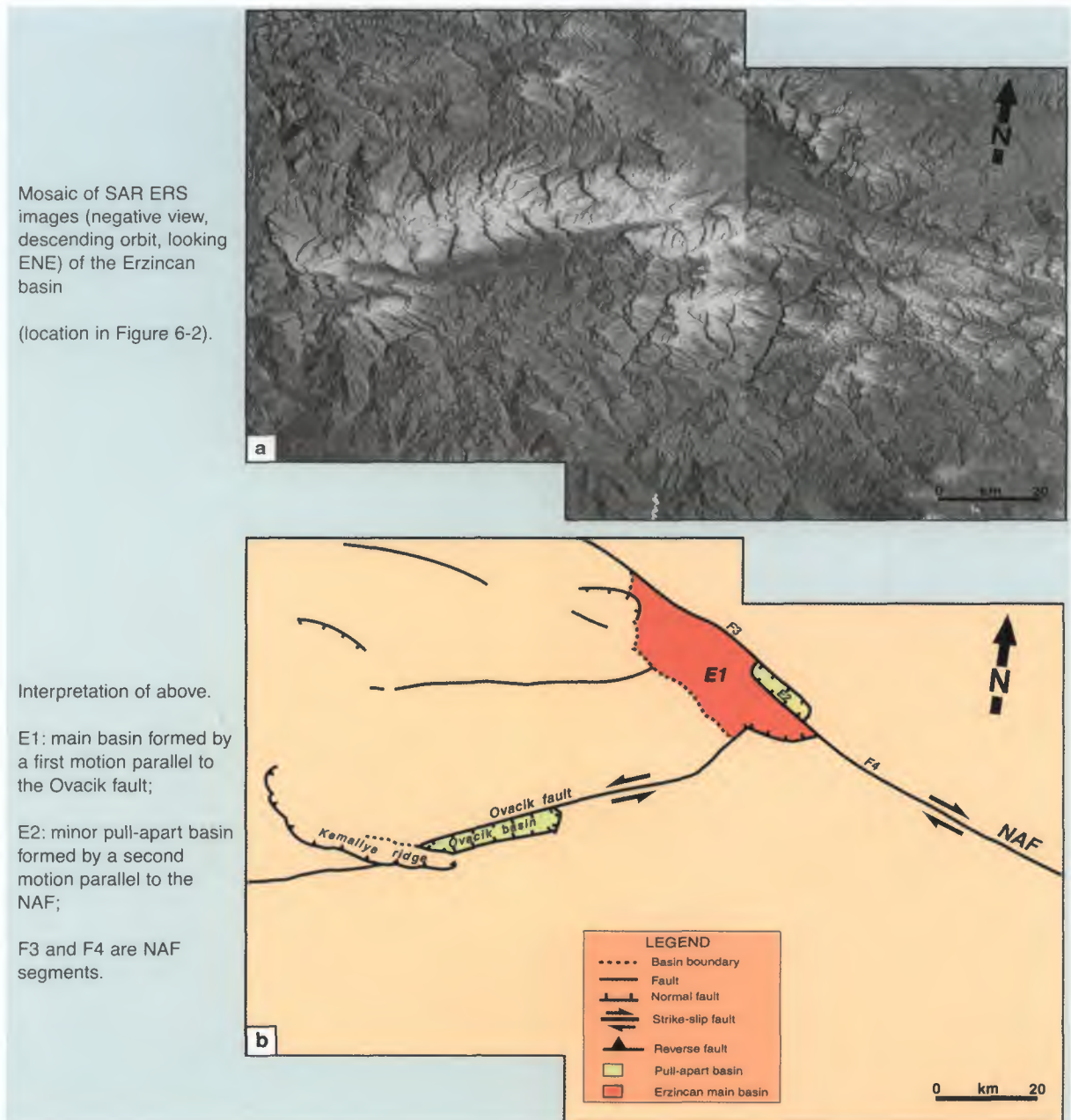


Figure 6-4: ERS scenes of the Erzincan basin area acquired in ascending orbits

The major one (F3) is the south-eastern continuation of the NAF, but to the east it becomes curved in plan view. To the east, another fault line (F4) continues in the N110°E direction as the main NAF trace. The relay zone (E2) is a narrow rhomb-shaped low plain exposing several volcanic cones of Quaternary age [12]. E2 is distinct from the largest main Erzincan basin (E1). The south-western border of E1 does not expose large faults but rather corresponds to a topographic flexure. Several faults can be mapped from the SAR images in the area northwest of the basin.

The southern corner of the Erzincan basin is connected with the Ovacik fault. It is clear in the image of Figure 6-5 that the river Euphrates is displaced by the Ovacik fault. From the offset of the river and an estimate of the shortening in the Kemaliye ridge [9], the finite sinistral strike-slip displacement along the Ovacik fault is ~12.5 km. Part of the movement occurred in the late Quaternary, as attested to by the Ovacik fault cutting alluvial fans and glacial deposits [2].

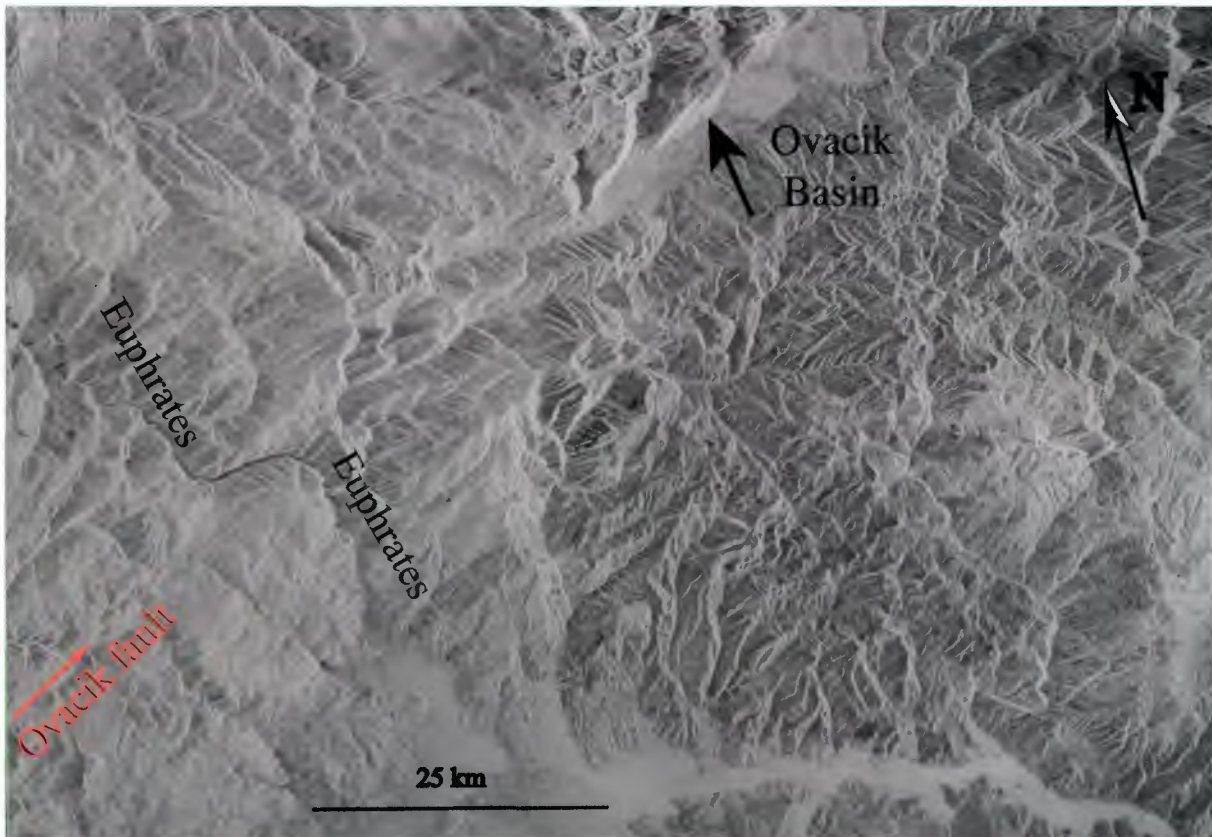


Figure 6-5: ERS image of the Ovacik fault showing left-lateral displacement of the Euphrates

Several interpretations of the formation of the Erzincan basin have been proposed. According to Hempton and Dunne [12], the basin is a simple pull-apart feature. For Barka and Gülen [5], west-directed movements of the Anatolian plate occurred in two stages, both in the east-west direction:

1. Opening of a 'releasing double bend' basin along the NAF
2. Formation of the Ovacik fault and widening of the basin

The use of radar images permits a new interpretation (Figure 6-6).

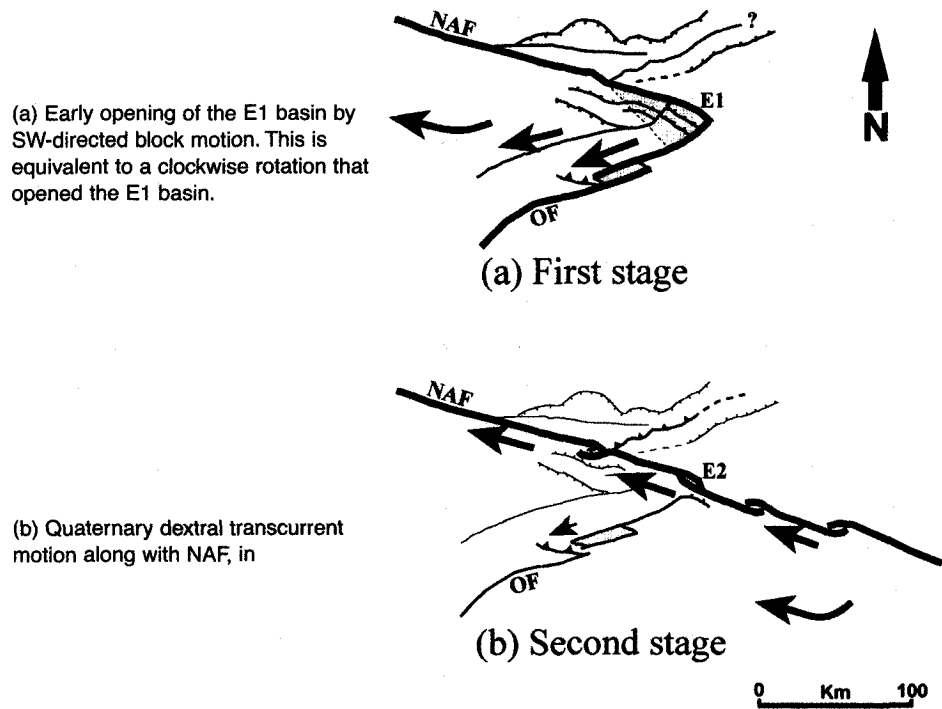


Figure 6-6:
Interpretation of the
tectonic evolution of
the Erzincan basin

During the Pliocene, the first displacement was related to motions turning in space from SW (parallel to the Ovacik fault), to WNW (parallel to the NAF) (Figure 6-6a). This rotation resulted in the opening of the E1 Erzincan basin. This clockwise block rotation is necessary to explain the progressive closing of the E1 basin in the west. Extensional faulting inside the moving blocks, west of the basin, compensated for the opening. During the Quaternary, the movement orientation changed to N110°E, allowing the right-lateral opening of the E2 pull-apart basin and providing a way up for the magma that formed small volcanoes (Figure 6-6b).

The main results of this analysis are:

- 1) Extension and transtension have prevailed since the late Neogene along the NAF in the Erzincan area
- 2) SW-directed movements pre-date strike-slip tectonics along the NAF
- 3) Offset of Quaternary valleys, such as that of the Euphrates, are well exposed in radar images

6.3 References

- [1] Ambraseys, N. N. (1970). Some characteristic features of the North Anatolian Fault Zone. *Tectonophysics*, **9**, 143-165.
- [2] Arpat, E. and Saroglu, F. (1975). Türkiye'deki bazı önemli genç tektonik olaylar (On some important young tectonic events in Turkey). *Türkiye Jeoloji Kurumu, Bülteni* **18**, 91-110.
- [3] Barka, A. A. (1992). The North Anatolian Fault Zone. *Annales Tectonicae* **6**, 164-195.

- [4] Barka, A. A. and Kadinsky-Cade, K. (1988). Strike-slip fault geometry in Turkey and its influence on earthquake activity. *Tectonics* **7**, 663-684.
- [5] Barka, A. A. and Gülen, L. (1989). Complex evolution of the Erzincan basin (eastern Turkey). *Journal of Structural Geology* **11**, 275-283.
- [6] Burke, K., and Sengör, A. M. C. (1986). Tectonic escape in the evolution of the continental crust. In *Reflection Seismology, Continental Crust, Geodynamic Series*, eds M. Barazangi, pp. 41-51. *American Geophysical Union Special Publication* **14**.
- [7] Chorowicz, J., Luxey, P., Lyberis, N., Carvalho, J., Parrot, J-F., Yürür, T. and Gündođdu, N. (1994). The Maras Triple Junction (Southern Turkey) based on digital Elevation Model and satellite imagery interpretation. *Journal of Geophysical Research*, **99**, 20225-20242.
- [8] Chorowicz, J., Koffi, B., Chalah, C., Chotin, P., Collet, B., Poli, J-T., Rudant, J-P., Sykioti, O. and Vargas, G. (1995a). Possibilités et limites de l'interprétation géologique des images (SAR) ERS-1. *Bulletin de la Société Française de Photogrammétrie et Télédétection* **138(2)**, 82-95.
- [9] Chorowicz, J., Luxey, P., Yürür, T., Rudant, J-P., Gündođdu, N. and Lyberis, N. (1995b). Slip-motion estimation along the Ovacik fault near Erzinan (Turkey) using ERS-1 radar image: Evidence of important deformation inside the Turkish plate. *Remote Sensing of Environment* **52**, 66-70.
- [10] Dewey, J. F., Hempton, M. R., Kidd, W. S. F., Saroglu, F. and Sengör, A. M. C. (1986). Shortening of continental lithosphere; the neotectonics of Eastern Anatolia, a young collision zone. In *Collision Tectonics*, eds M. P. Coward and A. C. Ries. *Geological Society Special Publication* **19**, pp. 3-36.
- [11] Hancock, P. L. and Barka, A. A. (1981). Opposed shear senses inferred from neotectonic mesofracture systems in the North Anatolian Fault Zone. *Journal of Structural Geology* **5**, 217-220.
- [12] Hempton, M. R. and Dunne, L. A. (1984). Sedimentation in pull-apart basins: active examples in eastern Turkey. *Journal of Geology* **92**, 513-530.
- [13] Irritz, W. (1971). Neogene and older Pleistocene of the intermontane basins in the Pontic region of Anatolia. *Newsletters on stratigraphy* **1**, 33-36.
- [14] Jackson, J. A. and D. P. McKenzie (1988). The relationship between plate motions and seismic moment tensors, and the rates of active deformation in the Mediterranean and Middle East. *Geophysical Journal* **93**, 45-73.
- [15] Lyberis, N., Yürür, T., Chorowicz, J. and Kasapoglu, E. (1992). The East Anatolian Fault: an oblique collisional belt. *Tectonophysics* **204**, 1-15.
- [16] McKenzie, D. (1972). Active tectonics of the Mediterranean region. *Geophysical Journal of the Royal Astronomical Society* **30**, 109-185.
- [17] Philip H., Cisternas, A., Gvishiani, A. and Gorshkov, A. (1989). The Caucasus: an actual example of the initial stages of continental collision. *Tectonophysics* **161**, 1-21.
- [18] Reilinger, R. E., McClusky, S. C., Oral, M. B., King, R. W., Toksoz, M. N., Barka, A. A., Kinik, I., Lenk, O. and Sanli, I. (1997). Global Positioning System measurements of present-day crustal movements in the Arabia-Africa-Eurasia plate collision zone. *Journal of Geophysical Research* **102**, 9983-9999.
- [19] Sengör, A. M. C. (1979). The North Anatolian transform fault: its age, offset and tectonic significance. *Journal of the Geological Society of America* **136**, 269-282.
- [20] Sengör, A. M. C., Görür, N. and Saroglu, F. (1985). Strike-slip faulting and related basin formation in zones of tectonic escape: Turkey as a case study. In *Strike-Slip Deformation, Basin Formation and Sedimentation*, eds K. T. Biddle and N. Christie-Blick. *Society of Economy, Palaeontology and Mineralogy Special Publication* **37**, pp. 227-264.

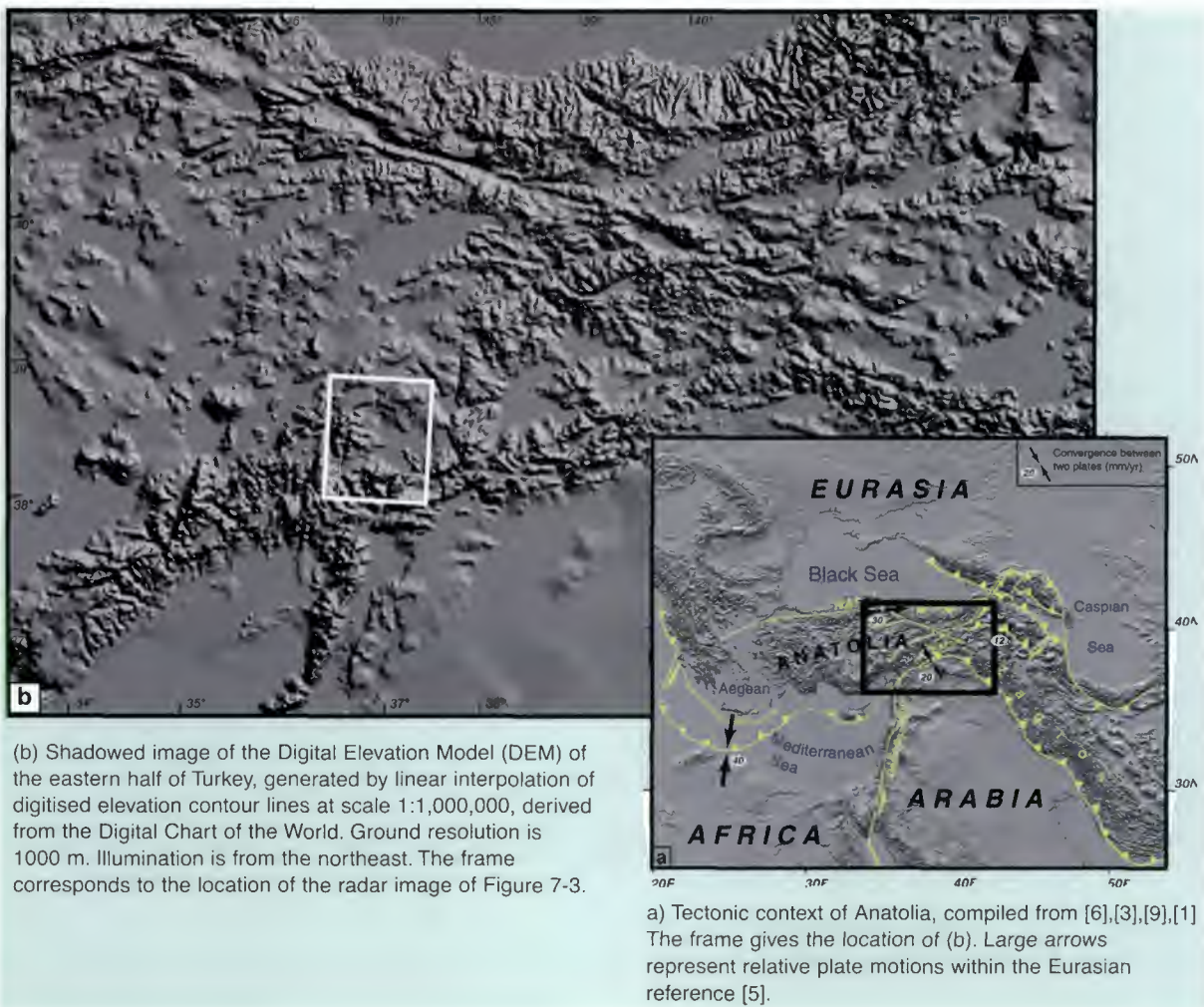
- [21] Stein, R. S., Barka, A. A. and Dietrich, J. H. (1997). Progressive failure on the North Anatolian fault since 1939 by earthquake stress triggering. *Geophysical Journal International* **128**, 594-604.
- [22] Suzanne, P. and Lyberis, N. (1992). Mécanisme de déformation le long de la partie orientale de la Faille Nord Anatolienne. *Annales Tectonicae* **6**, 26-40.
- [23] Suzanne, P., Lyberis, N., Chorowicz, J., Nurlu, M., Yürür, T. and Kasapoglu, E. (1990). La géométrie de la Faille Nord Anatolienne à partir d'images Landsat-MSS. *Bulletin de la Société Géologique de France* **8**, 589-599.
- [24] Tatar, Y. (1978). Tectonic investigations on the North Anatolian fault zone between Erzincan and Refahiye. *Publication of the Institute of Earth Sciences of Hacettepe University* **4**, 136-201.
- [25] Digital Chart of the World: <http://www.maproom.psu.edu/dcw/>
- [26] Chorowicz, J., Dhont, D., and Gündogdu, N. (1999). Neotectonics in the eastern North Anatolian fault region (Turkey) advocates crustal extension: mapping from SAR ERS imagery and Digital Elevation Model. *Journal of Structural Geology*, **21**, 511-532.

7. Karst features

Case study: Collision area of Eastern Anatolia

7.1 Geologic framework

Limestone outcrops can be found in large areas of Anatolia. Mesozoic limestone massifs that have been submitted to several stages of deformation are particularly jointed and faulted. They have developed a karst morphology characterised by alignments of lime sinks and small poljes.



This is the case in the studied area of Afsin-Elbistan, located in Eastern Anatolia (Figure 7-1), where curved belts result from the collision of the Anatolian block with continental parts of Africa and Arabia [1].

Figure 7-1:
Location of the Anatolian area studied

The structure of Eastern Anatolia is the final result of the palaeogeographic and structural evolution of the Tethyan domain characterised by the opening and closure of oceans during the late Palaeozoic-early Mesozoic (e.g. [7]). During the Mesozoic, platform facies limestone was deposited in passive margin environments upon the continental block of Anatolia that at this time separated the Northern Neotethys from the Southern one. At the end of the Mesozoic, convergence was predominant and southward obduction of Northern Neotethyan ophiolite nappes occurred over the carbonate platform of Anatolia.

During the Eocene, a main collision occurred between the Pontides and the Anatolian blocks, inducing important deformation. Anatolia uplifted, and karst evolution began. This was followed (Oligocene), by the deposition of continental molasses filling post-tectonic intra-mountainous basins. The Southern Neotethys Ocean still existed and was subjected to flysch deposits.

In the late Cenozoic (middle Miocene to Present), closure of the Southern Neotethys was accompanied by collision of Anatolia with the African and Arabian continents. The area was again subjected to major deformations. This collision led to the formation of the Bitlis belt along a suture zone, which continues further east in the Zagros (Figure 7-1).

In the studied area, the collision occurred mainly between the Anatolian and African continental blocks, forming local curved belts (the Gürün and Afsin arcs – GA & AA in Figure 7-2) that are related to continental subduction of the Amanos range (belonging to the African plate) underneath Anatolia.

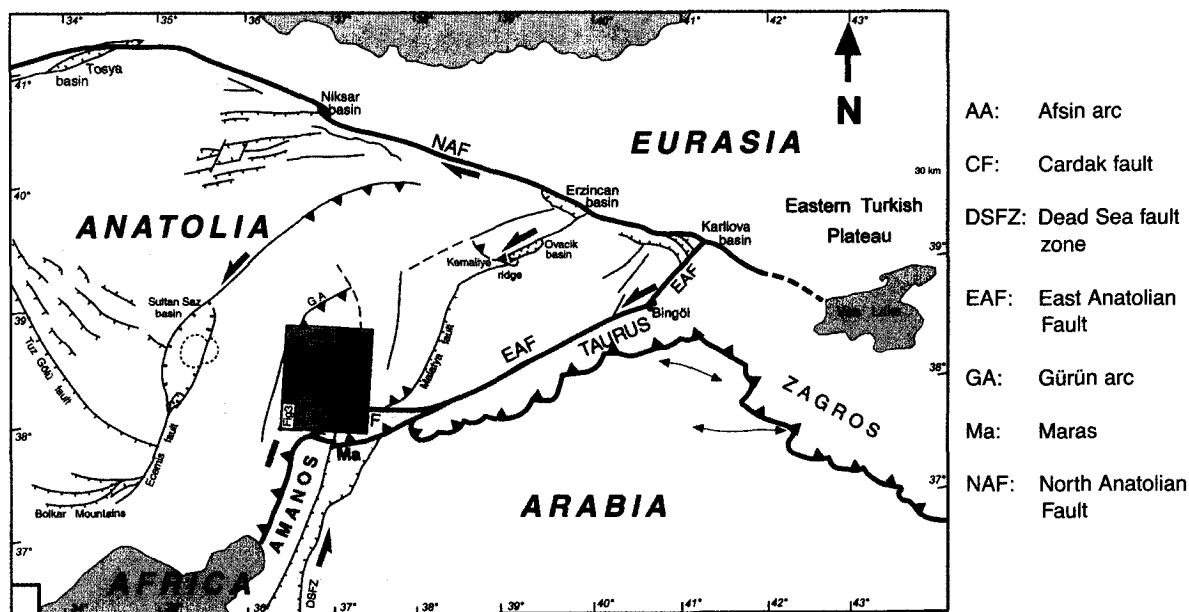


Figure 7-2: Fault pattern from interpretation of the DEM

7.2 Approach

The eastern part of Turkey is still poorly known. SAR ERS imagery is able to provide new tectonic information because radar images are sensitive to variations in topographic slopes [2]. This type of morphological observation is especially powerful in areas dominated by recent deformation.

Figure 7-3 shows a SAR image of the area indicated by the frame in Figure 7-2. Illumination is from WSW (descending orbit). The image has been produced in positive print.



Positive view of the Afsin-Elbistan region, descending orbit, looking WSW. The frame gives the location of Figure 7-5.

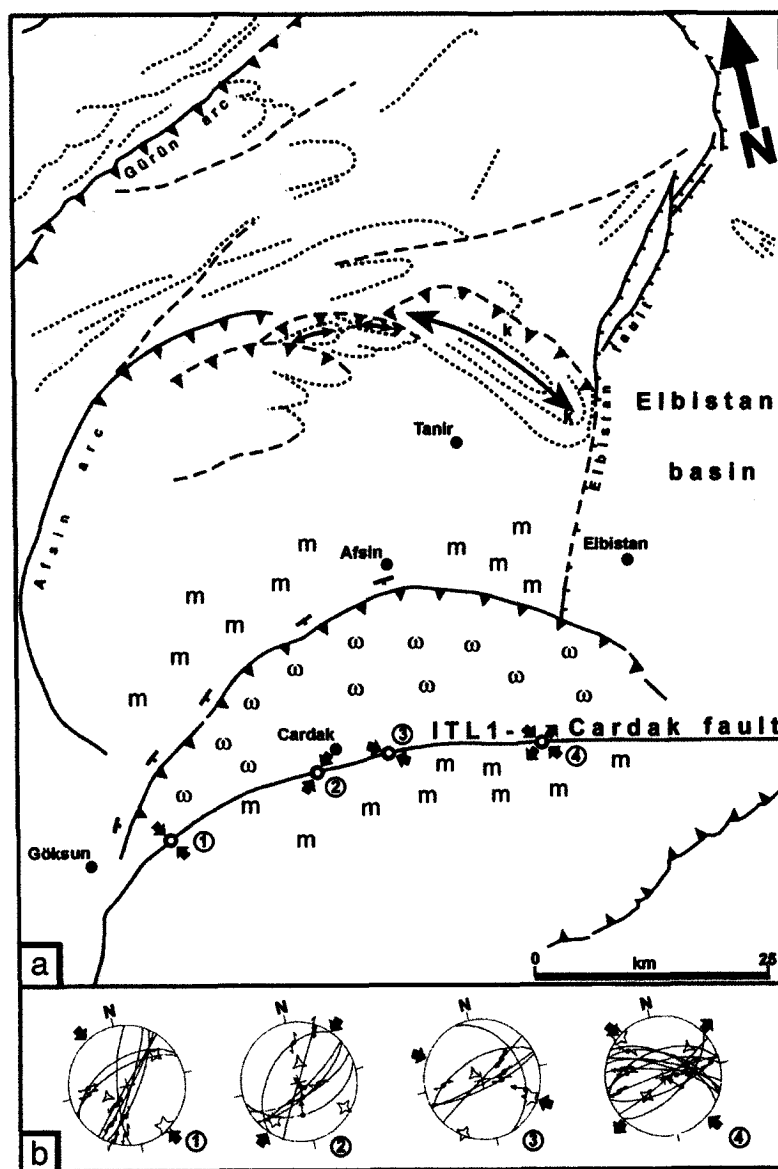
7.3 Analysis of the Afsin-Elbistan region

Folds and thrusts in the Bitlis belt (Figure 7-4a) are expressed on the image of Figure 7-5. Compression structures are associated with folds that are well shown in the topography. They form several arcs, bounded by reverse faults verging west to north

*Figure 7-3: SAR
ERS image of the
Afsin-Elbistan
region*

(Afsin and Gürün arcs). Fold and thrust systems are interrupted to the east by the NNE-striking Elbistan normal fault zone, which on the west bounds the Elbistan basin filled by upper Pliocene continental sediments [8]. The globally E-striking Pliocene extension related to the Elbistan fault zone [4] is older than the Afsin arc thrust, showing that compression is recent in this area.

In the southern part of the image, the main structure is a line (ITL, the Intra-Taurus Line), corresponding to the Cardak fault, located within the belt itself, which continues far further east.



(a) Interpretation of Figure 7-3.

Large dashed lines are inferred faults.

Short dashed lines are structural lineations corresponding to lithologic traces.

Double arrows are anticline axes. Numbers in circles (1 to 4) are sites of structural analysis in the field (part (b) below)

ITL: Intra-Taurus Line

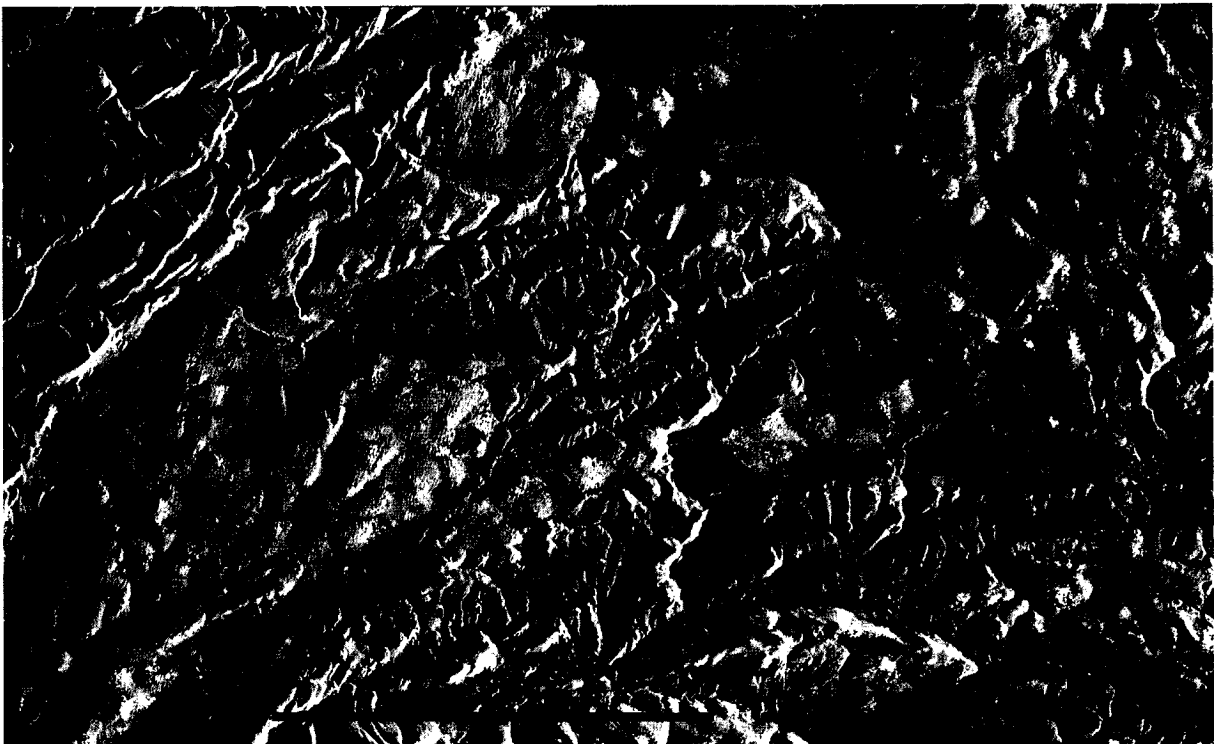
m: metamorphic rocks

ω: ophiolites

(b) Stereo plots of field measurements [1] and computed data inversion. Schmidt nets, lower hemisphere (locations given in (a) above).

Figure 7-4:
Structural analysis

The continental evolution of this area began in the Eocene. Several tectonic phases have occurred since that time, inducing fracturing in the competent limestone and favouring dissolution of carbonates. The Mesozoic limestone outcrops have developed karst morphology that is expressed by a peculiar texture on the SAR ERS image (Figure 7-5).



Karst morphology expressed in the positive radar image by high backscattering and peculiar striped macro-texture. Frame is location of Figure 7-6.

This texture is characterised by light grey tones in the positive image of Figure 7-5, corresponding to high values of backscattering. These values express very rough surfaces related to karst morphology, which develops centimetre- to metre-sized irregularities, forming a complex microtopography. In addition, there is a typical macro-texture consisting of parallel and aligned small crests and depressions. They form elongated lime sinks that are typical aspects of a karst morphology (Figure 7-6). These alignments are representative of the intense fracturing affecting the limestone.

Figure 7-5: Karst morphology expressed in the positive radar image

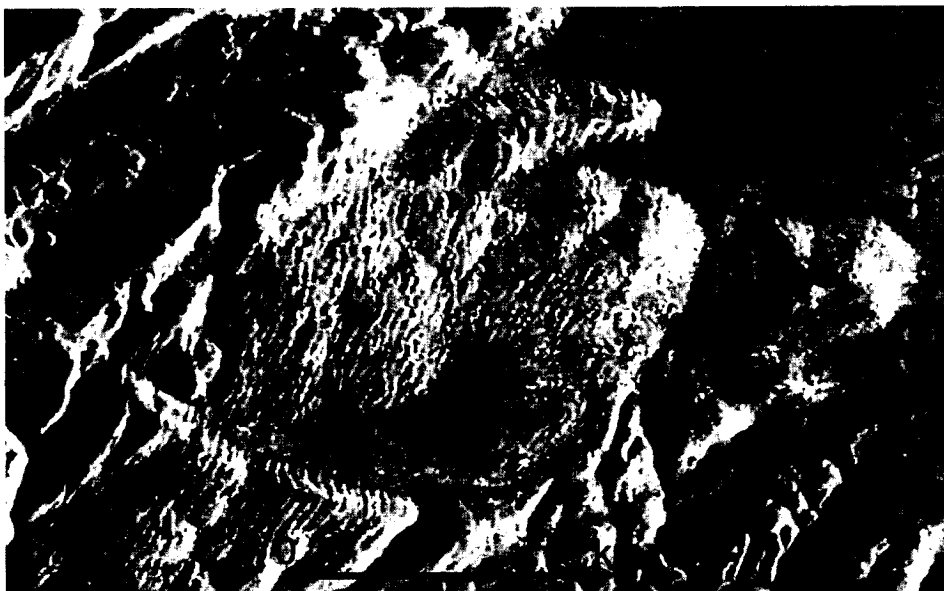


Figure 7-6: Detail of the typical high backscatter and karst macro-texture

7.4 References

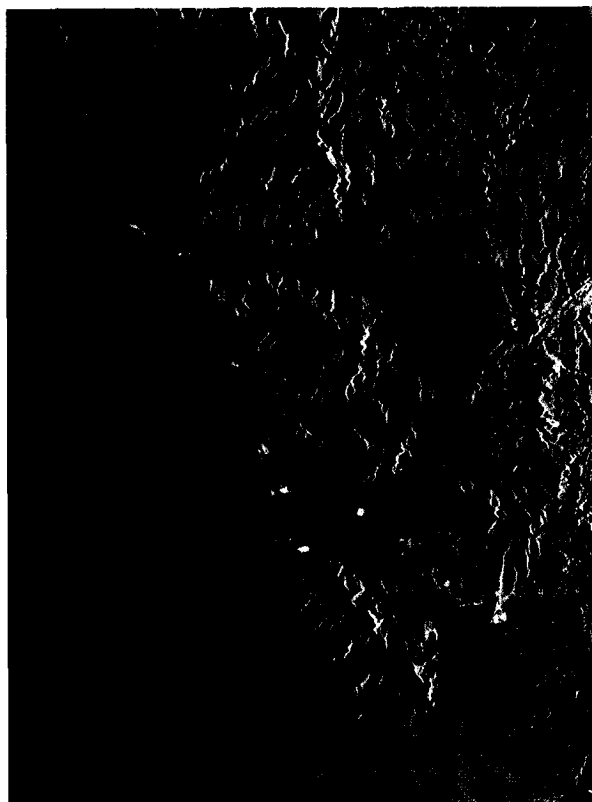
- [1] Chorowicz, J., Luxey, P., Lyberis, N., Carvalho, J., Parrot, J.-F., Yürür T., Gündogdu, 1994. The Maras Triple Junction (Southern Turkey) based on digital Elevation Model and satellite imagery interpretation. *Journal of Geophysical Research* **99**, 20225-20242.
- [2] Chorowicz, J., Koffi, B., Chalah, C., Chotin, P., Collet, B., Poli, J.-T., Rudant, J.-P., Sykioti, O., Vargas G., 1995. Possibilités et limites de l'interprétation géologique des images (SAR) ERS-1. *Bulletin de la Société Française de Photogrammétrie et Télédétection* **138**, 82-95.
- [3] Hancock, P. L. and Barka, A. A., 1981. Opposed shear senses inferred from neotectonic mesofracture systems in the North Anatolian Fault Zone. *Journal of Structural Geology* **5**, 217-220.
- [4] Luxey, P., 1995. Etude de la déformation interne du bloc anatolien (Turquie) dans le cadre de la collision Arabie-Eurasie. Thesis, University Paris 6.
- [5] Reilinger, R. E., McClusky, S. C., Oral, M. B., King, R. W., Toksoz, M. N., Barka, A. A., Kinik, I., Lenk, O. and Sanli, I., 1997. Global Positioning System measurements of present-day crustal movements in the Arabia-Africa-Eurasia plate collision zone. *Journal of Geophysical Research* **102**, 9983-9999.
- [6] Sengör, A. M. C., 1979. The North Anatolian transform fault: its age, offset and tectonic significance. *Journal of the Geological Society of America* **136**, 269-282.
- [7] Sengör, A.M.C., Yilmaz, Y., 1981. Tethyan evolution of Turkey; a plate tectonic approach. *Tectonophysics* **75**, 181-241.
- [8] Staesche, U., 1972. Die geologie des Neogen-Beckens von Elbistan/Türkei und seiner Umrandung. *Geol. Jb.* **4**, 3-52.
- [9] Dewey, J. F., Hempton, M. R., Kidd, W. S. F., Saroglu, F. and Sengör, A. M. C. (1986). Shortening of continental lithosphere; the neotectonics of Eastern Anatolia, a young collision zone. In *Collision Tectonics*, eds M. P. Coward and A. C. Ries. *Geological Society Special Publication* **19**, pp. 3-36.

Two successive scenes will be examined, acquired at a 35-day interval (descending orbits, looking west) over the Pinatubo area (Figure 8-1).

One was acquired on 9 July 1993, at the end of the dry season (Figure 8-2) and the next during the first important typhoon event on 13 August 1993 (Figure 8-3).



Scene acquired on 9 July 1993, at the end of the dry season. Descending orbit, positive point



Scene acquired on 13 August 1993, during typhoon event. Descending orbit, positive point

Figure 8-2: Pinatubo area at the end of the dry season *Figure 8-3: Pinatubo area during a typhoon event*

The following series of images are all in pairs; all images labelled 'a' were taken on 9 July 1993 and all images 'b' were taken on 13 August 1993. They are all selections of Figure 8-2 and Figure 8-3 respectively.

8.2 SAR image dated 9 July 1993

Neither heavy rains nor large typhoons were reported in the area for several months before 9 July 1993, at the end of the dry season, except for minor lahar flows on 3 June 1993 and small muddy stream flows on 26 June [2]. The main sites for lahars covered by this SAR image were the Bucaco and Sto. Tomas-Marella rivers (Figure 8-4).

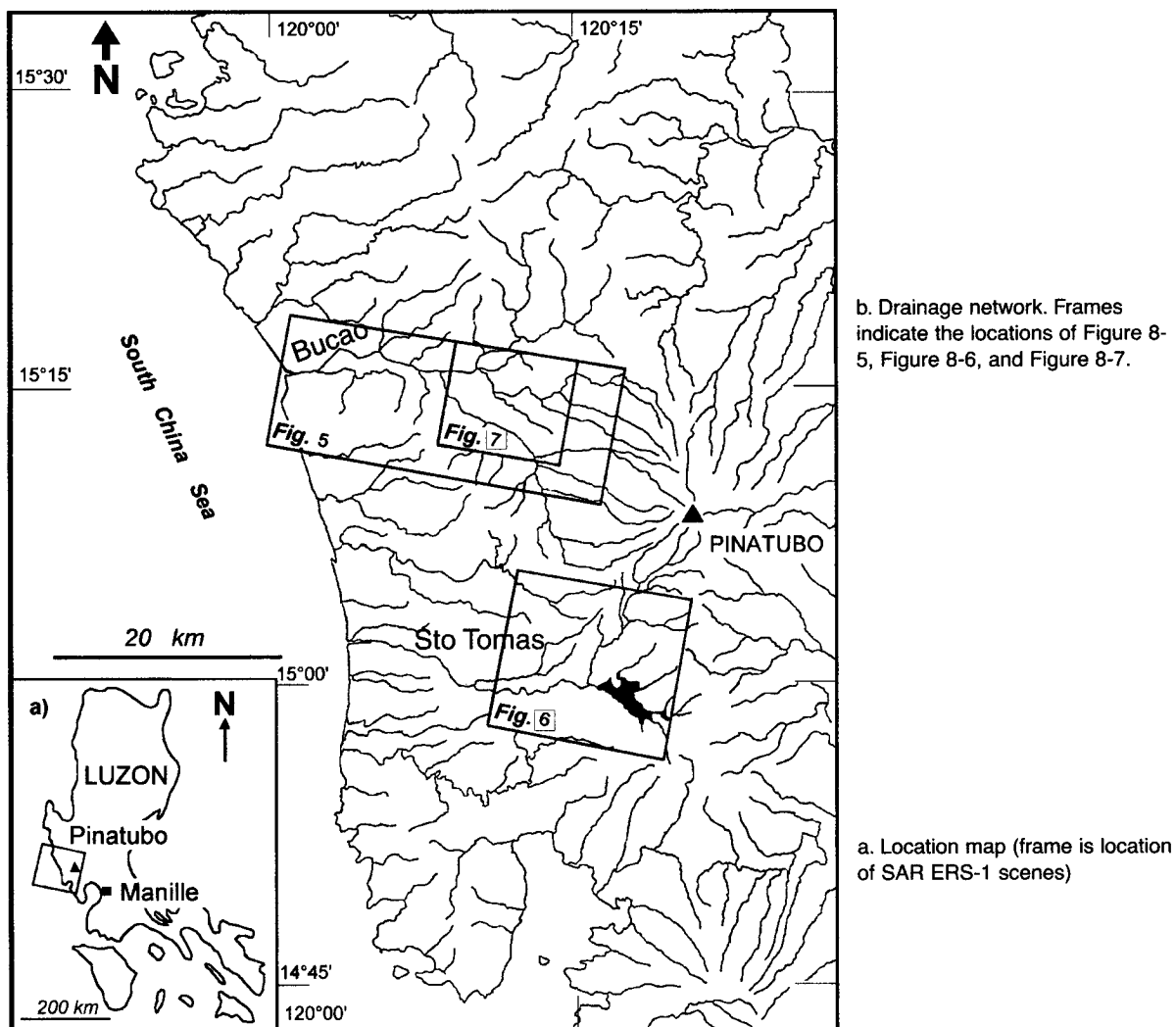


Figure 8-4: Mount Pinatubo area (Philippines)

Lahars were deposited in the channels of these rivers following the eruptions of Pinatubo in 1991 and 1992, and during small events that occurred on 3 and 26 June 1993.

The downstream portions near the mouths of the Bucao river display dark surfaces in the positive black-and-white image (A in Figure 8-5a). Distinct lighter curved lines run along the elongated direction of the dark surface of the river (B).

a) Image acquired on 9 July, 1993



b) Image acquired on 13 August, 1993

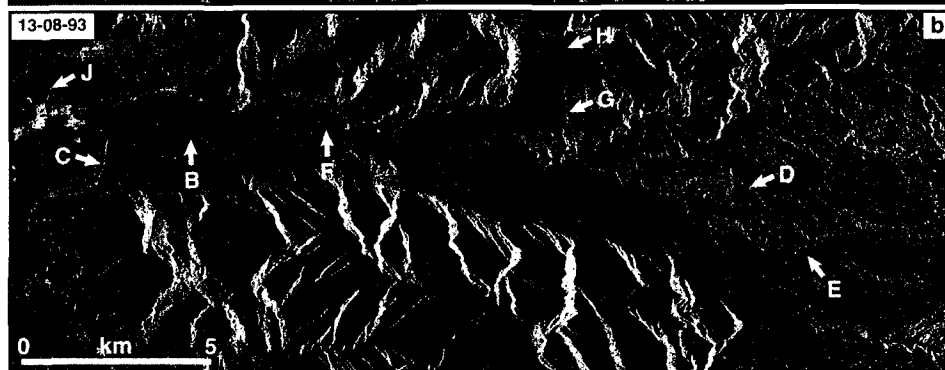


Figure 8-5: SAR ERS images of the Bucao river region

Field observations carried out on May 1995 in the downstream portion of the Bucao river valley showed that the flat lahar deposit surfaces may be dry and composed mainly of fine material, or covered by shallow, gently running, quiet water. In both cases, the backscatter values are low. Rough-surfaced lahar sediments also occur, especially along streams that have washed out fine-grained material and let in coarse materials in its place on the surface, that are composed mainly of pumice pebbles of more than 2 cm in diameter and frequently up to 20 cm. These streams constituted an anastomotic network, still expressed by the distribution of rough surfaces. We assume that this type of surface is frequent at the end of the dry season (May), potentially existing until July. This assumption is based on the lack of large typhoons or heavy rains during 1993, up to the first strong typhoon on 26 July 1993. Flat, fine-grained (smooth) dry surfaces or shallow, quiet, gently running water are consequently both responsible for the low backscatter values. The lighter linear features (B) correspond to rough surfaces along streams, or to walls (several metres depth) of the channel or to levees. Several well-defined, rough-surfaced streams are observed in the dark area of Bucao river (e.g. C, probably the active channel).

Going upstream, there is a progressive transition in tone from dark to light, with the brighter tones in the upstream segment of the Bucao river. This change mainly corresponds to dry lahar deposits exposing coarse material at the surface, or the presence of rill systems. The rough surface explains the high backscatter values. In the 9 July image, these relatively ancient lahar sediments can be identified because they are often separated from more recent lahars formed in 1992 or 1993 and deposited in the channel, or from running water, by a distinct erosion scarp which is white or black, depending on its orientation with respect to the direction of radar illumination. The more ancient lahar deposits seem to be also carved by small gullies (D), suggesting they are terraces pre-dating the 1991 eruption. In these areas, the more ancient lahar deposits have relatively higher backscatter values, similar to the rough-surfaced recent lahars. In many places morphological features such as scarps and gullies are not well exposed and it is

consequently difficult to precisely distinguish the lahar deposits of different generations. The upstream portions do not show clearly defined stream patterns, perhaps because rough running water has backscatter values equal to those of rough lahar surfaces. Some main streams are shown by the morphology of a narrow valley filled with smoother lahar deposits or quietly running water (E in Figure 8-5a and Figure 8-6a).

8.3 SAR image dated 13 August 1993

Since 9 July 1993, several meteorological events have affected the Bucao and Sto. Tomas-Marella rivers. From 25 to 30 July 1993, typhoons Luming and Narsing (local names) induced lahars. On 11 and 12 August, heavy rains affected the area, due to typhoon Pining (local name). On 13 August, high-speed lahars were flowing along the two rivers, with varying speeds from a minimum of 2.7 m/s to a maximum of 4.3 m/s, between 8:40 and 9:40 a.m. local time ([2], [3]). The ERS-1 SAR scene (descending orbit, looking west, positive print) was acquired on the same day at 10:28 a.m. local time and consequently pictured still active lahars.

M = Lake Mapanuepe
E = smooth lahar deposits or quietly running water

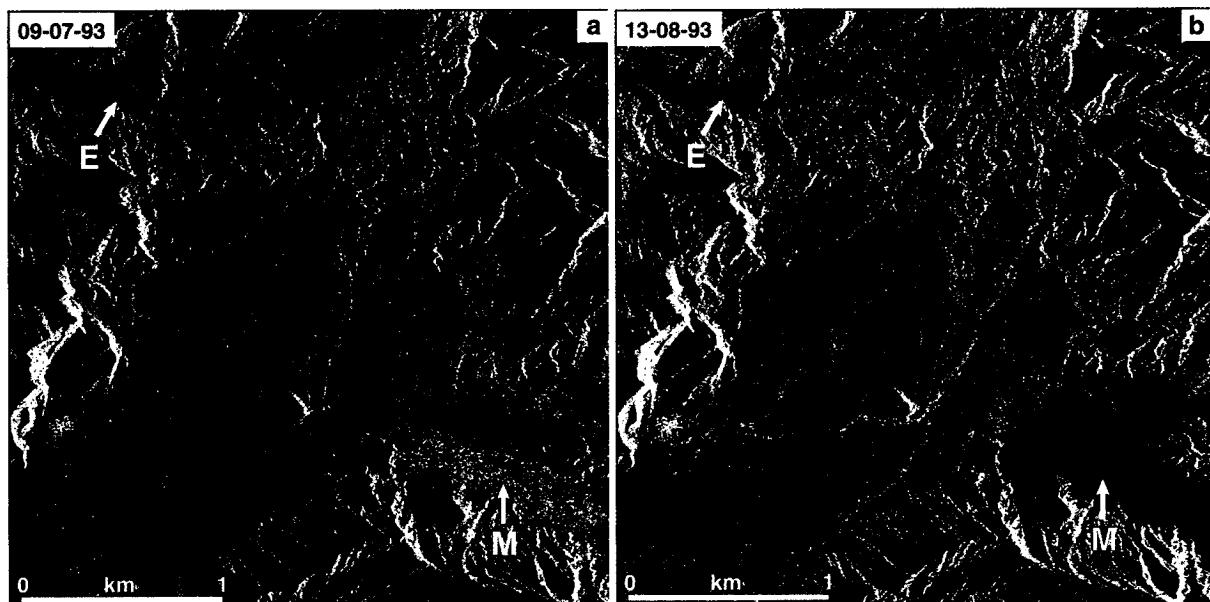


Figure 8-6: SAR ERS images of the Sto. Tomas-Marella river region

In the images (Figure 8-5b and Figure 8-6b), these active lahars are not really distinct from the other types of brilliant rough surfaces in the region. Active or just deposited lahars have relative high backscatter values for different reasons:

- 1) The surface of active running lahars may be wavy and tumultuous and consequently very rough
- 2) A just-deposited lahar is smooth in surface but very wet (although without free water at the surface), with a high dielectric constant value that yields significant backscattered energy

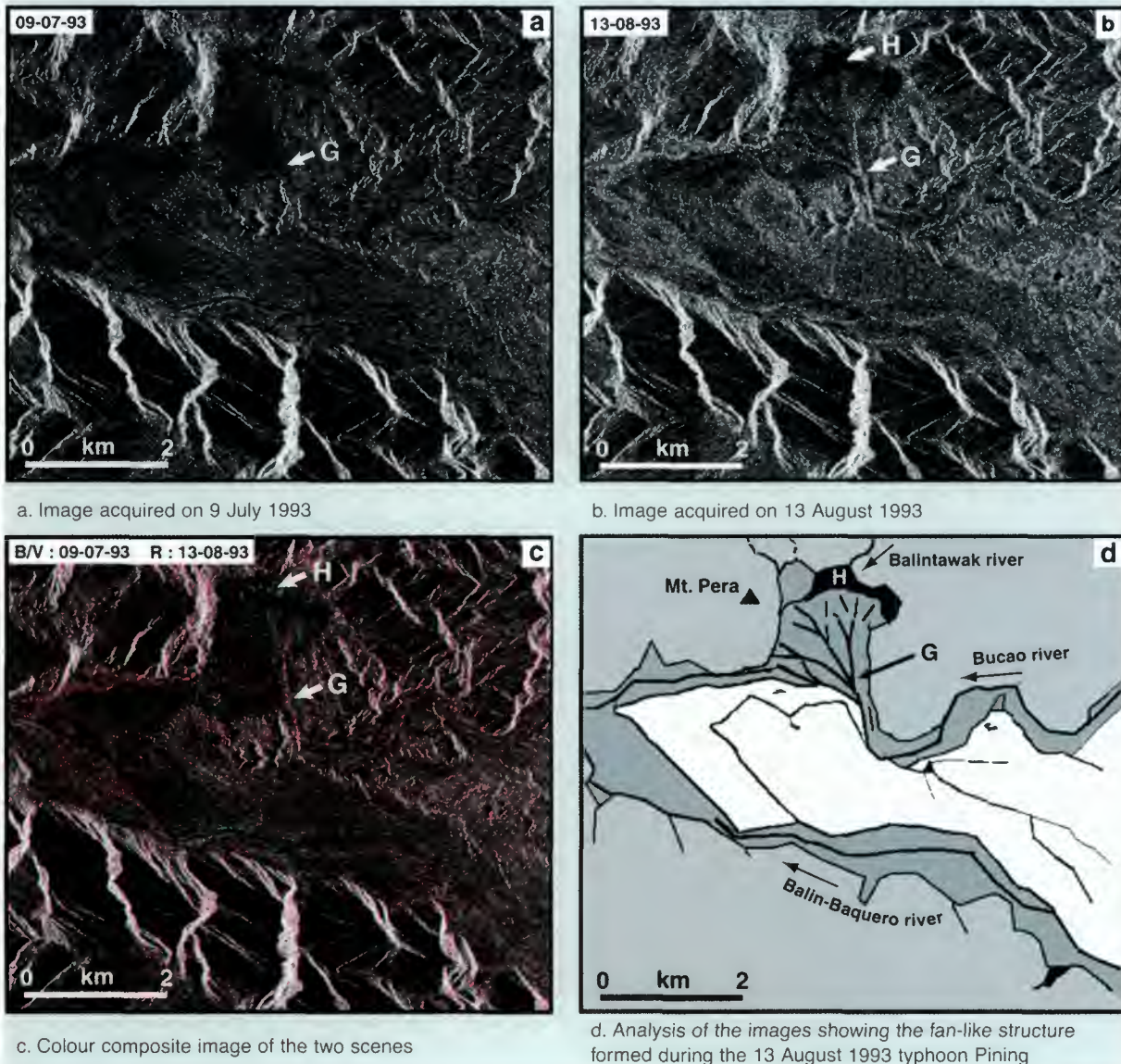
In the lower Bucao river, active rough lahars or wet, smooth, fresh lahars occurring on 13 August (**B** and **F**) were deposited over or beside flat, smooth-surfaced, dry lahar sediments or quiet shallow water shown on the 9 July image (**A** in Figure 8-5a).

In the flat lands, north of lower Bucao river, partial flooding due to typhoon Pining occurred, giving black surfaces corresponding to quiet standing water (**J** in Figure 8-5b) replacing rather light grey surfaces (**J** in Figure 8-5a). In the 13 August image, Digital Number (DN) values of the flooded areas are between 20 and 60 (mean 40). On the same image, DN values are between 30 and 80 (mean 60) for flat, smooth-surfaced, wet lahar deposits or gently running lahar streams located respectively at **E** and **F** in Figure 8-5b. It seems that flat, smooth-surfaced, wet lahar deposits or gently running lahars can be distinguished from flooded areas, which have significantly lower backscatter values. Some confusion may occur; however, flooded areas are often located in areas that are clearly not subjected to lahar deposits because these are situated apart from the main rivers.

Lake Mapanuepe (**M** in Figure 8-6) is light grey on 9 July 1993 and black on 13 August 1993, due to differences in local wind conditions. Windy weather on 9 July induced a light grey tone, and quiet air on 13 August induced the black tone of a smooth water surface. Apart from this, the wind effects in this data set are limited on the whole, because the wind blew only on 6 July when most surfaces were dry, running water being very limited in extension and depth. The lake occupies a larger area on 13 August 1993.

Textural characteristics are good indicators of the active lahars. In lower Bucao river (**B** and **F** in Figure 8-5b), anastomotic patterns of running lahars are clearly exposed. Morphological aspects have also to be considered. The tracks of some streams change between the two dates (see **B** in Figure 8-5a and b). A fan-like structure is evident in the 13 August 1993 image (**G** in Figure 8-5b and Figure 8-7b) but it is faint and with a significantly different shape from that of the 9 July image (**G** in Figure 8-5a and Figure 8-7a).

Changes in tones from grey to black (H) and from grey to white (G) (Figs. a and b) correspond to the development of active lahars along the Bucao river. These deposits have originated the closure and formation of a dam at the mouth of the Balintawak river. Changes in ground aspect between these two dates are represented on the colour composite image (Fig. c) by red and blue-green colours respectively, representing an accumulation area of pre-existing lahars that have developed along flooded plains (dark grey in Fig. d).



In this area, pyroclastic materials accumulated in the fan during the 13 August event, forming a dam that was responsible for the formation of a small lake immediately northward (H in Figure 8-5b and Figure 8-7b), corresponding to a black surface.

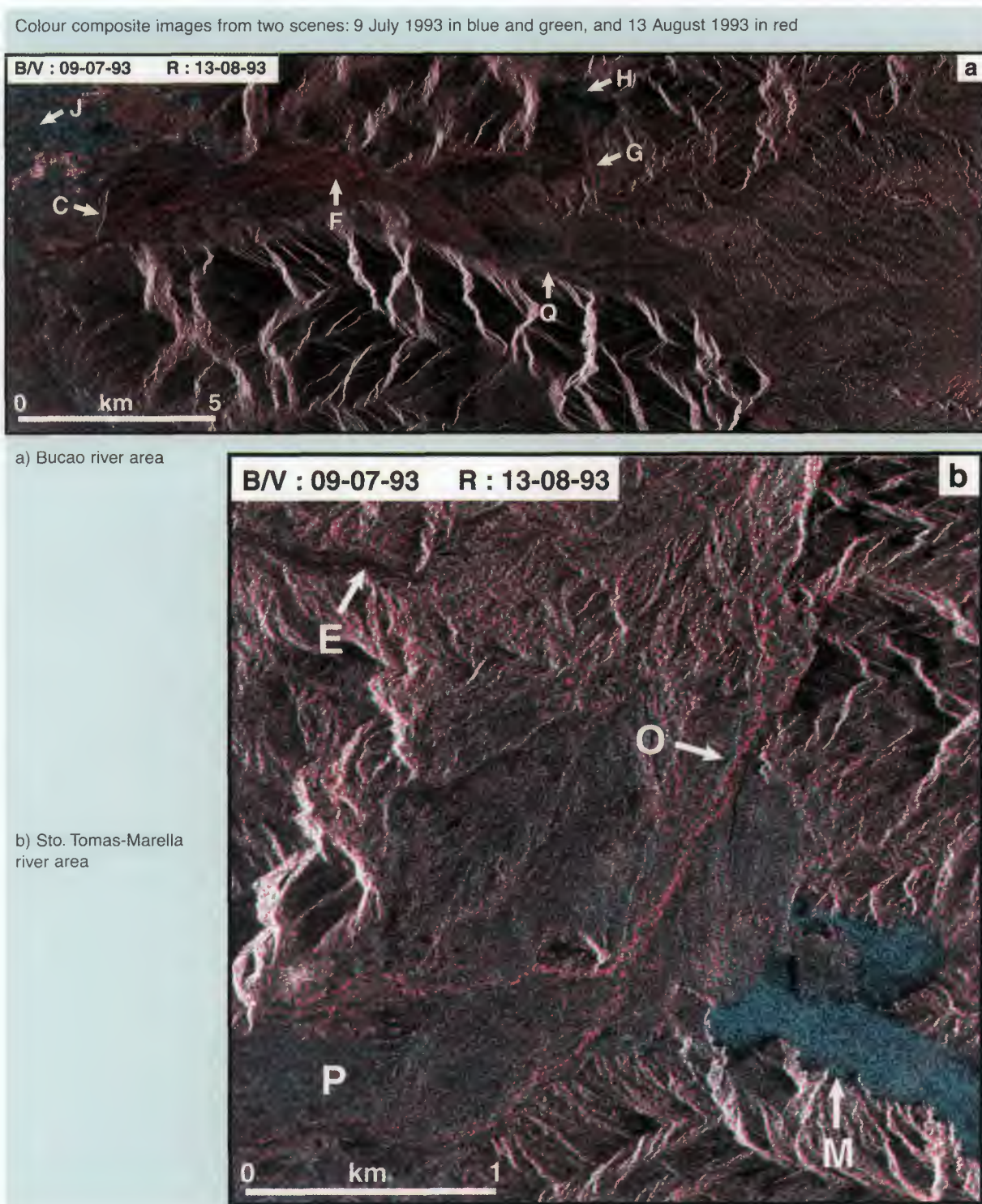
Figure 8-7: Fan-like structure formed during typhoon Pining

8.4 Colour composition

In order to obtain a view of the main changes between the two dates, one of the best and simplest methods is to generate a multi-date colour composite image. The two scenes, being acquired at a 35-day interval, perfectly match, and no geometric correction was applied. The two PRI scenes were also produced simultaneously by the concerned

Figure 8-8: Colour composite SAR ERS images for identification of lahars

Processing and Archiving Facilities (PAF), and uniform parameters were used. Instead of data calibration, the same parameters have been applied to both scenes during processing. The colour compositions of Figure 8-8 display the 9 July 1993 image in blue and green, and the 13 August 1993 image in red. The pertinent changes due to lahar events are located only in the valleys.



The distinct red colours in the lower Bucao valleys (**F**) indicate surfaces that have changed from dark tones (smooth-surfaced, flat, dry lahar deposits or quiet, shallow water) to bright tones (active, tumultuous running lahars, recently-deposited, flat wet lahars, or recently-deposited rough-surfaced lahars). Comparison of the areas covered by lake Mapanuepe (**M**) shows an increase in surface of the water. Red colours west of the lakeshore (Figure 8-8b) indicate that the increase in surface is due to active lahars adding to the surface.

Distinct red colours in the upper valleys correspond to fresh erosion or to active lahars, for which the roughness is higher than for ancient rough-surfaced lahar deposits; or possibly also to an increase in the surface roughness due to debris flow deposits. On the whole, all the red colours in the valleys seem to indicate effects of active and recent lahars.

Distinct blue-green colours are frequent in the coastal plains (**J**). In these areas, the blue-green colour is related to light grey tones in July and black tones in August. As black tones seem to be due to free water flooding the plains during a typhoon, blue-green has to be regarded as mainly related to flooding. The small lake that formed north of a lahar fan (**H**) is also coloured in blue-green because in July the corresponding surface is grey (rough surface) and in August quiet water appears in black. However, the blue-green colour also exists along the narrow upper Sto. Tomas-Marella riverbed (**O**). Corresponding black tones on the 13 August image indicate that flat surfaces are located over more ancient rougher surfaces. It seems that this pattern is due to the return of the upstream river segment to a quiet stream flow. Similar blue-green features can be observed in **P** and along some streams of the fan-like structure (**G**).

The radar characteristics of the main objects related to lahar events (running lahar flows, erosion, deposition of fans, formation of lakes, flooding) during typhoon can be recognised. However, different configurations may yield similar signals:

- 1) Active tumultuous rough-surfaced lahar (grey) flowing over ancient coarse-grained lahar deposits (grey)
- 2) Recent smooth wet lahars (grey) deposited over rough-surfaced lahar sediments (grey)
- 3) Faced running lahars (black) running in an area of smooth-surfaced dry lahars or quiet shallow water (black)

The successive lahar surfaces may then have the same backscatter values and consequently be displayed in white, grey or black. Active tumultuous lahars deposited over rough-surfaced lahars, giving a white colour, seem to be present at location **Q**. Active lahars are detected in August, up and downstream of this particular segment of the riverbed, coloured respectively in blue and red, and consequently they also had to run in-between at location **Q**, forming the white line. Field reports confirm mobilisation of lahars in this area.

8.5 References

- [1] Chorowicz J., Lopez E., Garcia F., Parrot J-F., Rudant J.-P., Vinluan R., 1997. Keys to analyse active lahars from Pinatubo on SAR ERS imagery. *Remote Sensing of Environment*, **62**: 20-29.

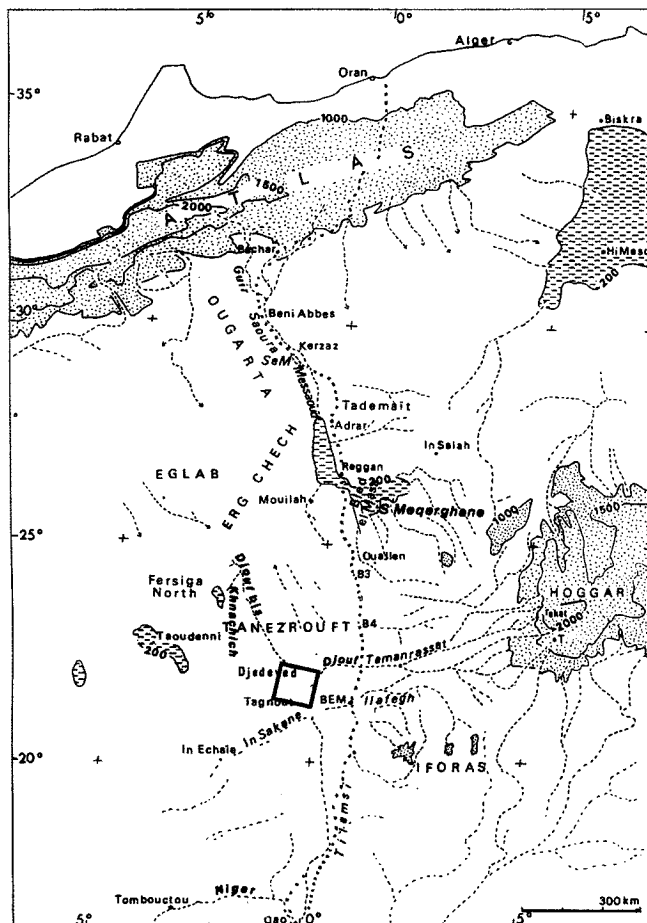
- [2] Punongbayan, R. S., Tungol, N. M., Arboleda, R. A., de los Reyes, P. J., Isada, M. L., Melosantos, M. L. P., Puertollano, J., Regalado, M. T. M., Solidum, R. U., Tubianosa, B. S., Umbal, J. V., Alfonso, R. A. and Remotique, C. T. (1994), Impacts of the 1993 Lahars and Long-term Lahar Hazards and Risks Around Pinatubo Volcano. *Philippine Institute of Volcanology and Seismology - UNESCO report*, 1-40.
- [3] Rodolfo, K. S., Umbal, J. V., Rosalito, A., Remotique, C. T., Paladio-Melosantos, M. L., Salvador, J. H. G., Evangelista, D. and Miller, Y. (1996), Two years of lahars on the western flank of Mount Pinatubo: Initiation, flow processes, deposits and attendant geomorphic and hydraulic changes.
In: Newhall, C. G. and Punongbayan, R. S. (eds), *Fire and mud-eruptions and lahars of Mount Pinatubo, Philippines*. Philippine Institute of Volcanology and Seismology, Quezon City and University of Washington Press, Seattle, 989-1013.

9. Drainage systems in desert areas covered by sand veil

Case study: Southern Tanezrouft system (Sahara)

The analysis of buried drainage networks in desert areas has principally resulted from analysis of images acquired by Synthetic Aperture Radars (SARs) aboard satellites (e.g. [3], [6]). Palaeo-channels show up as a result of microwave penetration into the ground for between a few centimetres and a metre ([5], [7]).

9.1 Overview of the studied area



Tanezrouft desert, showing main drainage networks and mountainous areas in West Africa.

High topography is shown by main elevation contour lines at 1,000m, 1,500m, and 2,000m.

Depressions are delineated by dotted lines within 200m elevation contour lines.

BeM: Borj el Mohtar

SeM: Sebket el Malah

The square is the location of images of Figure 9-2 and Figure 9-3.

Figure 9-1:
Location of the
Tanezrouft desert

Wadi Tamanrasset grades down from the Hoggar into the southern Tanezrouft region in Algeria, on the Algeria-Mali border. The precise pattern of its southern end across the Algeria-Mali border is questionable (Figure 9-1). It occurs in the complex area where Wadi Tamanrasset meets Wadi Djouf and Wadi Djouf bis.

The Tanezrouft desert is a 200,000 km² flat region located at around 350 to 300 m elevation in a hyper-arid zone of the Sahara (Figure 9-1). The hydrology is poorly known because Quaternary sand and gravel partly fill the wadis, plus the topographic surface is flat and channels are not shown by relief. The perennial vegetation of grass or bush has also vanished. Aerial photographs are useless for they each cover too small an area relative to the dimensions of geomorphic features, and dust clouds frequently obscure the region.

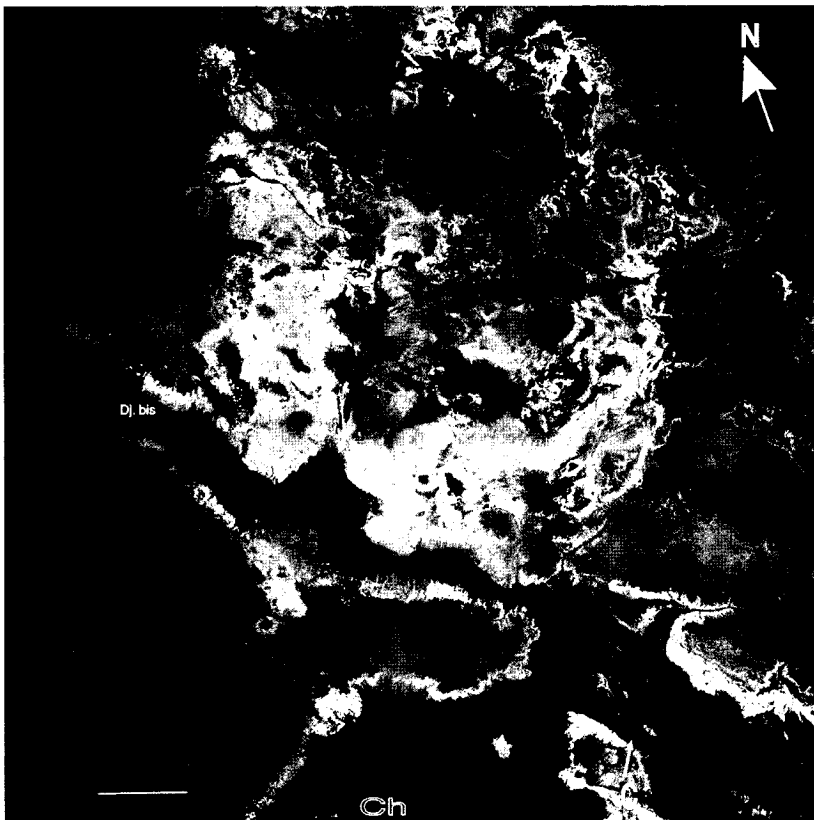
Rains that fall on the western slopes of the Hoggar massif do not stay on the Tanezrouft plateau, as attested by the lack of endoreic basins and evaporitic deposits in this region. Satellite images show that the Tanezrouft plateau is drained by four wadi systems of different sizes:

- The Ouallen wadi system, which collects water from the north-western Hoggar, runs to the north into the Sebkhia Meqerghane and Reggan depression.
- The central network covers 66,200 km², including the western slopes of the Hoggar massif. Palaeo-channels form a braided system inside the Tanezrouft.
- The Tamanrasset-El Djouf system drains a 54,000 km² area of the western slope of the Hoggar massif. Wadi Tamanrasset runs for 300 km from east to west, then entrenching into the piedmont area, diverging and vanishing between 3°E and 1°E, to reappear in the west beyond 1°E in Wadi El Djouf. The 1:1,000,000 IGN map features another wadi in western Tanezrouft, named 'El Djouf bis'. The idea generally admitted in the scientific community is that the south-eastern part of El Djouf bis is the continuation of the Tamanrasset-El Djouf system. This raises the question of how the Tamanrasset-El Djouf system connects with El Djouf bis near the Djedeyed wells.
- The Ilafegh wadi system in southern Tanezrouft runs westwards from the Hoggar massif and northern Iforas, then turns to the southwest and probably feeds the Holocene lakes of Erg In Sakane (Petit-Maire and Riser, 1983). As the wadi systems are sand covered, it is possible that the water from the wells of In Echaie feeds the Niger river near Tombouctou (Timbuktu), either directly or through underground nappes.

9.2 Analysis of southern Tamanrasset-El Djouf system

The data used are one ERS-1 SAR scene (Figure 9-2), and one SPOT Panchromatic (P) scene (Figure 9-3). The images were processed by simple linear contrast stretching.

The channel of El Djouf bis meanders uninterrupted over 270 km across the western Tanezrouft plateau and branches with the Tamanrasset-El Djouf channel.



SAR ERS-1 scene, orbit 9496, frame 3159, acquired on 21 December 1992.

Dj: wadi El Djouf-Tamanrasset

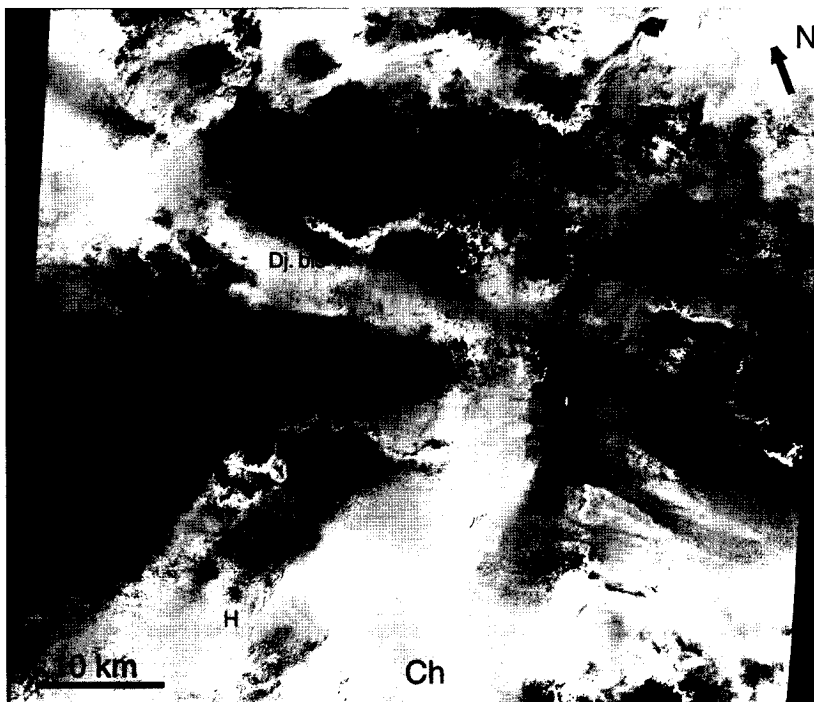
Dj: bis: wadi El Djouf bis

Ch: Charebba depression

C: connection of Wadi El Djouf with the Charebba depression

Figure 9-2: SAR ERS-1 image of southern Tamanrasset-El Djouf system

It is 1 to 2 km wide, without vegetation (no surface or ground water). Some loops are incised several metres into bedrock. El Djouf-Tamanrasset and El Djouf bis are both connected with the large Charebba depression near the Djedeyed wells. The SPOT image (Figure 9-3) shows, in the lowest areas, white irregular patches (H).



Scene SPOT 51/306

Dj: wadi El Djouf-Tamanrasset

Dj: bis: wadi El Djouf bis

Ch: Charebba depression

H: area with irregular patches

Figure 9-3: SPOT image of southern Tamanrasset-El Djouf system

These are lacustrine deposits, similar to others found in the region and belonging to the Holocene [1]. This suggests that the Charebba depression was recently formed, and that, formerly, water was flowing further northwest from Wadi Tamanrasset-El Djouf into Wadi El Djouf bis. On the SAR image, despite the sand cover expressed by the SPOT image, palaeo-channels strongly differ from nearby regs. This may be related to penetration of radar waves (C-band) into dry soil and changes in bedrock. Another, more probable reason is roughness variation. The pebble content of the sand may change, or the density of dead grass roots may vary. The physical properties of the soil in this area are still to be checked in the field, so the causes of different responses at optical and microwave frequencies remain speculative.

On the ERS-1 SAR image, an ancient continuity between El Djouf-Tamanrasset and El Djouf bis is visible. However, the present day pattern is that of El Djouf connecting in a southerly direction with the Charebba depression through a narrow channel (**Ch**) and not continuing into El Djouf bis. There is also a clear connection from El Djouf bis to the Charebba depression. If water usually flows from El Djouf-Tamanrasset and southern El Djouf bis into the Charebba depression, it must have evaporated in the lowest part of this depression, forming salt deposits. The lack of salt deposits implies that water coming from the wadis may form underground water percolating southward and possibly feeding the In Sakane lake, thus connecting with the Ilafegh wadi system (Figure 9-1) and finally through In Echaïe, reaching the river Niger.

This is the present-day pattern, which differs from a more ancient one when El Djouf bis was the exact continuation of the Tamanrasset-El Djouf system. The fact is that the catchment basin of El Djouf bis is surprisingly small compared with the size of the valley, which is similar in width and length to the Saoura valley in the Kerzaz region near Beni Abbes. From reports of recent (historic) flows, it is known that the Saoura valley is able to transfer water at a rate of 3,000 to 4,000 m³/s. The present tributaries of El Djouf bis could not bring such a flow.

9.3 Tectonic deformations

The western border of the Tanezrouft plateau has recently been uplifted. Uplift is also responsible for formation of the Taoudenni depression more to the west, which cuts Palaeogene lacustrine sediments west and north of Taoudenni. Uplift of the western Tanezrouft plateau consequently postdates the Palaeogene. Recent faults have been evidenced cutting El Djouf bis west of the study area, interrupting the regular slope of the valley bed [2].

Recent alluvial deposits filling the valley of El Djouf bis, abandoned by the last flood, are conspicuous on the SAR image, suggesting a recent (Holocene) age for the tectonic activity that affected El Djouf bis and interrupted flow running westward from Tamanrasset-El Djouf. This recent tectonic activity rejuvenated the Precambrian and Mesozoic fracture system [4]. Endoreic sedimentation settled in the Charebba depression, fed by Tamanrasset-El Djouf, and in the Fersiga depression, fed by north-western El Djouf bis.

It is likely that the unique Tamanrasset-El Djouf-El Djouf bis drainage system was previously connected to the south with wadi Ilafegh, and continued across In Echaïe (273 m) and from there towards the Niger near Tombouctou (260 m). Also, an older connection between wadis El Djouf bis and Mouilah may have collected the Guir Saoura waters from north, before subsidence of the Reggan-Meqerghane depression. The

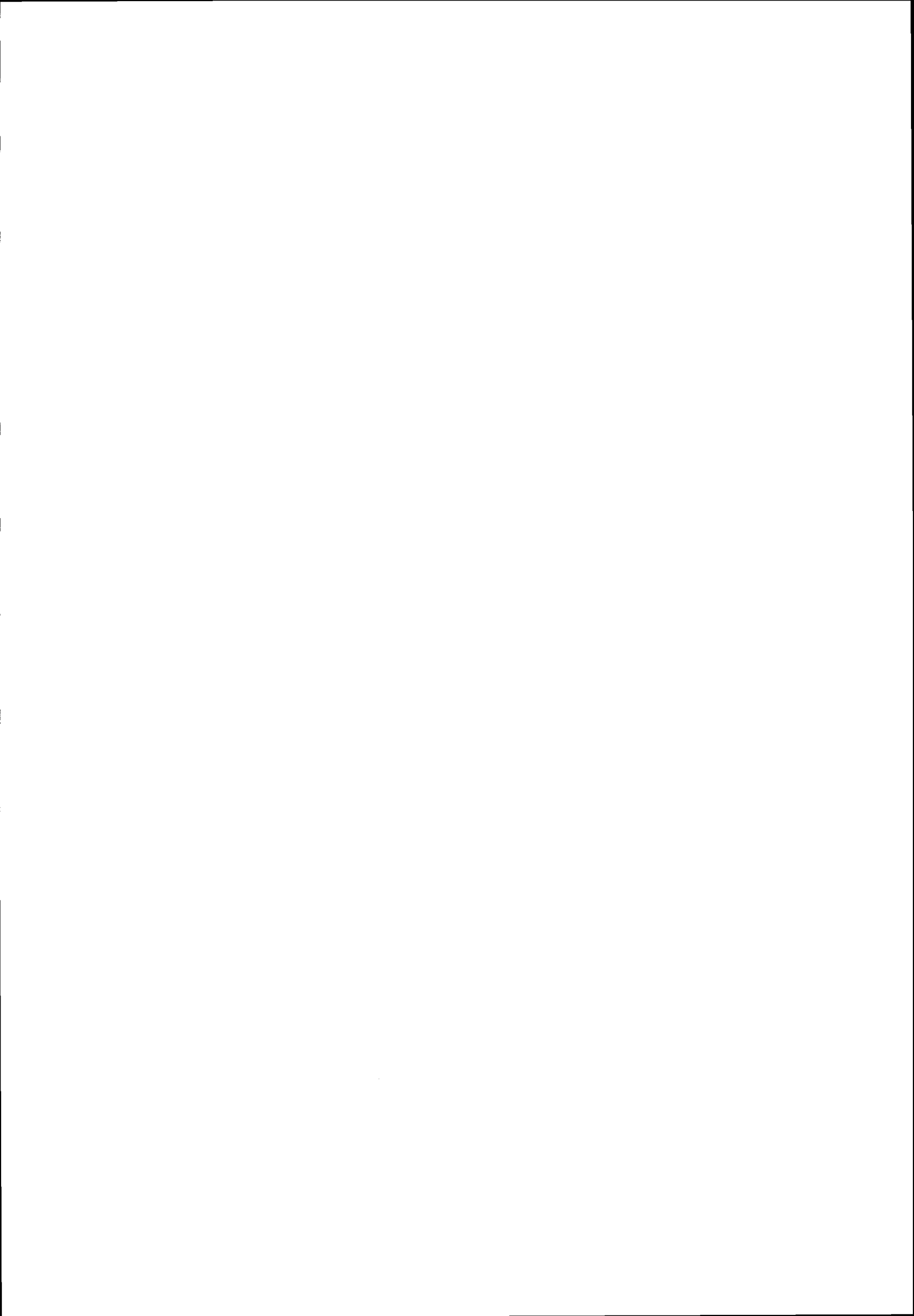
connection would have been interrupted by the capture of wadi El Djouf bis by the Fersiga depression, due to possible doming between Fersiga North and the upper part of wadi Mouilah.

9.4 Conclusions

Sand-buried palaeo-channels can be observed in the Sahara from SAR ERS-1 imagery. A continuous Tamanrasset–El Djouf–El Djouf bis system was flowing westward. Its present day separation into distinct wadi systems appears to result from recent tectonic activity, including fault-related uplift.

9.5 References

- [1] Bassot, J.P., Diallo, H.H. and Traoré, H., 1980. Carte géologique du Mali at 1:1.500.000, *B.R.G.M.*, Orléans.
- [2] Chorowicz J. and Fabre J., 1997. Organisation of drainage network from space imagery in the Tanezrouft Plateau (Western Sahara): implications for recent intracratonic deformations. *Geomorphology*, **21**, 139-151.
- [3] Elachi, C., Cimino, J. and Settle, M., 1986. Overview of the Shuttle Imaging Radar-B preliminary scientific results. *Science*, **232**, 1511-1515.
- [4] Fabre, J. and Kazi Tani, N., 1987. Part de l'héritage dans la déformation Phanérozoïque au Sahara central et occidental. *Current Research in African Earth Sciences*, in: Matheis G., Schandelmeir H. (eds), Balkema, Rotterdam, 241-244.
- [5] Farr, T.G., Elachi, C., Hartl, P. and Chowdhury, K., 1986. Micropenetration and attenuation in desert soil: a field experiment with the Shuttle Imaging Radar. *IEEE Transactions on Geosciences and Remote Sensing*, **GE-24**, 590-594.
- [6] McCauley, J.F., Breed, C.S., Schaber, G.G., McHugh, W.P., Issawi, B., Haynes, C.V., Grolier, M.J. and El Kilani A., 1986. Paleodrainages of the Eastern Sahara. The radar rivers revisited (SIR-A/B. Implications for a Mid-Tertiary Trans-African Drainage System). *IEEE Transactions on Geoscience and Remote Sensing*, **GE-24**, (4), 624-648.
- [7] Schaber, G.G., McCauley, J.F., Breed, C.S. and Olhoeft, G.R., 1986. Shuttle Imaging Radar: physical controls on signal penetration and subsurface scattering in the Eastern Sahara. *IEEE Transactions on Geoscience and Remote Sensing*, **GE-24**, (4), 603-623.



10. Rain and flood effects

Case study: Vaison-la-Romaine area (France)

On September 22, 1992, a heavy rainstorm occurred in a region of South-eastern France (Figure 10-1). This event was catastrophic, especially in the town of Vaison-la-Romaine, along river Ouvèze, but also in the Aigues valley, and it caused significant human and environmental casualties. During the 35-day cycle of ERS-1, one scene had been acquired 33 days before the event, and another acquired one day after, rendering possible the assessment of flooded areas.

10.1 Maps of the studied area

Figures 10-1 and 10-2 show the area where the flooding took place.

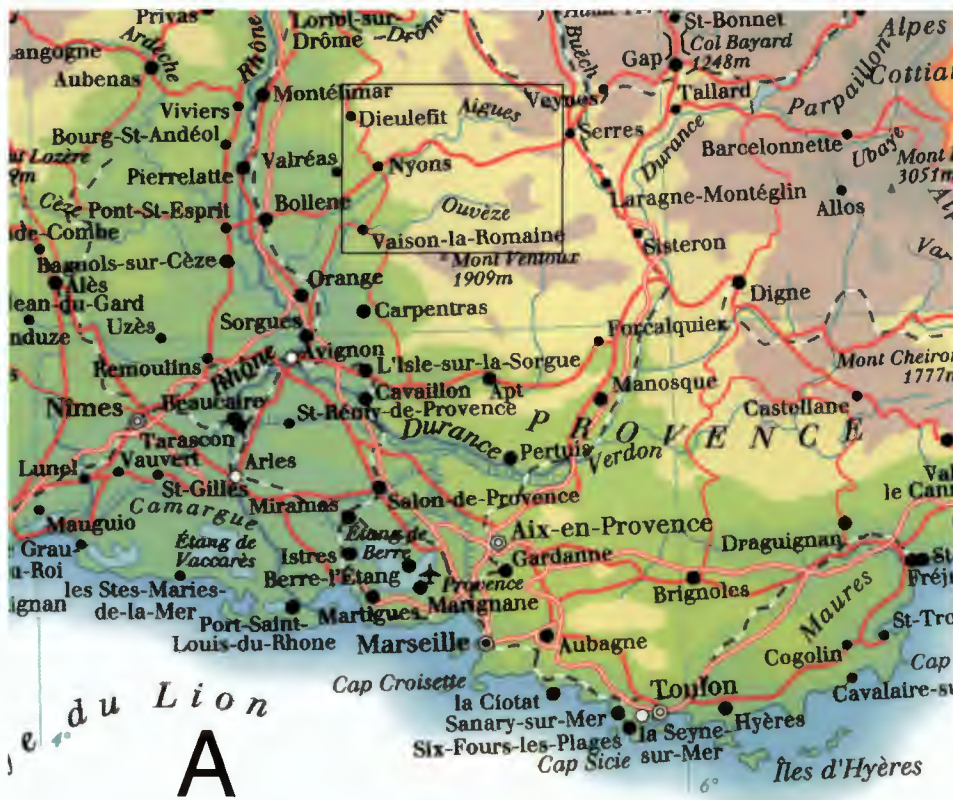


Figure 10-1:
Location in France

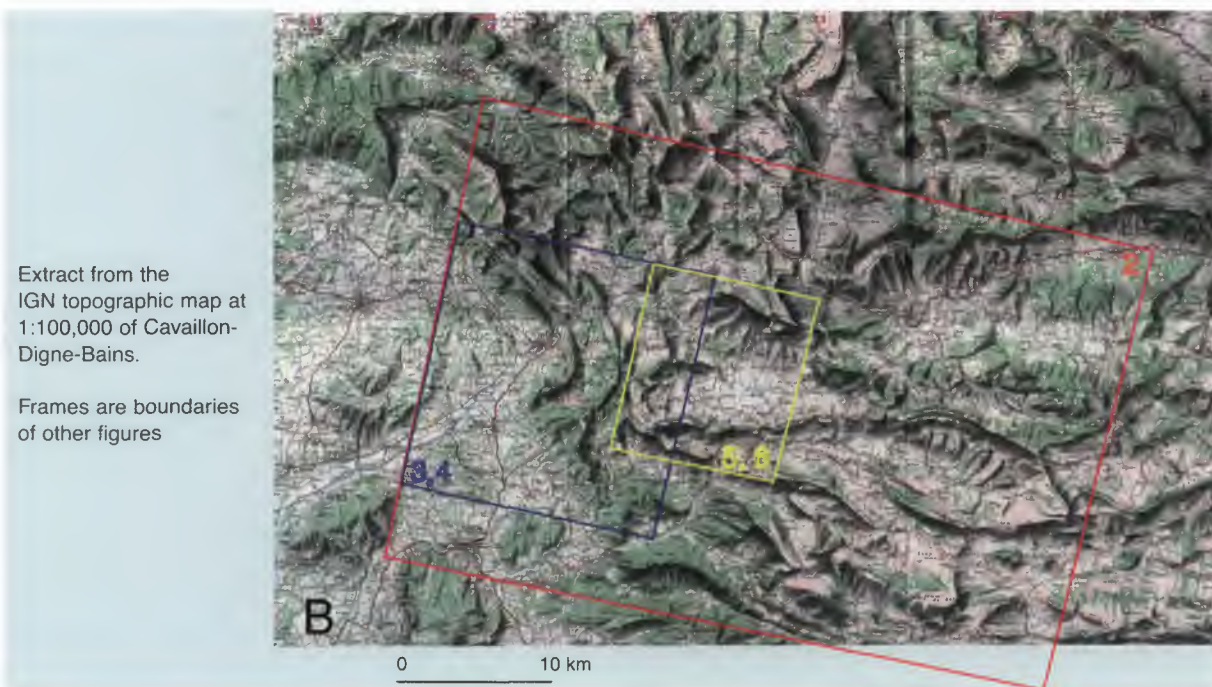
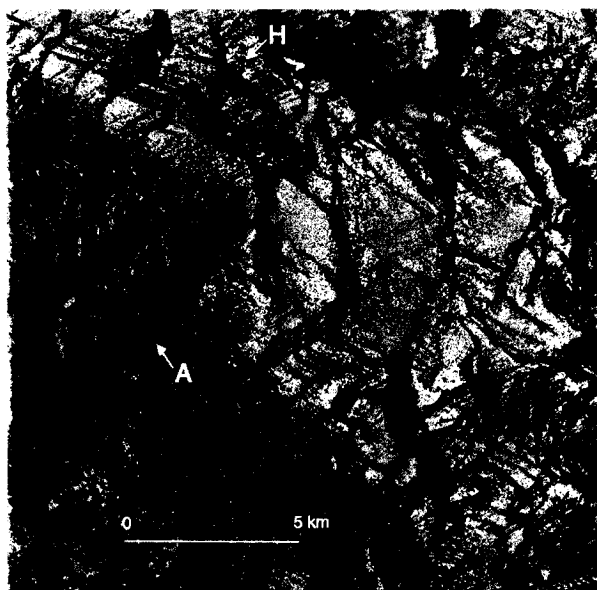


Figure 10-2:
Study area

10.2 Approach

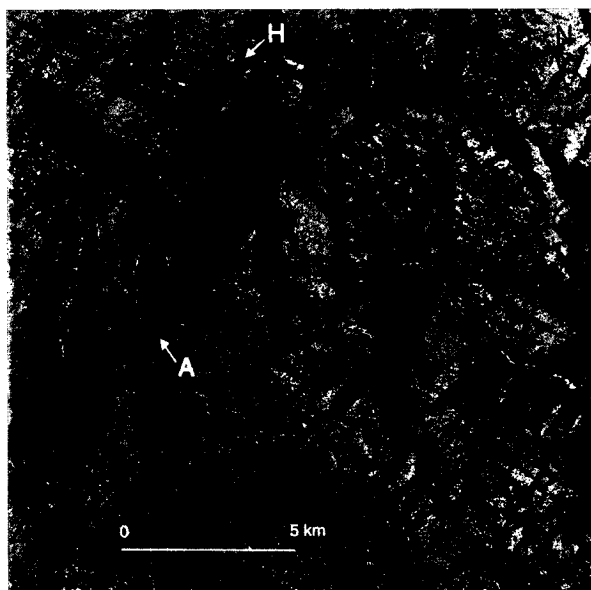
Two enlarged extracts of the images have been made, each before and after the flood (Figures 10-3 to 10-6). They are presented in negative black and white prints for a better comparison with the topographic map of Figure 10-2.



Negative print of extract from SAR ERS-1 scene acquired on 19 August 1992 (33 days before the event).

A: River Aigues is white (black in positive image), meaning a quiet surface.

H: Hill is with light grey tone (dark in positive image), meaning dry soil. Location in Figures 10-1 and 19-2.

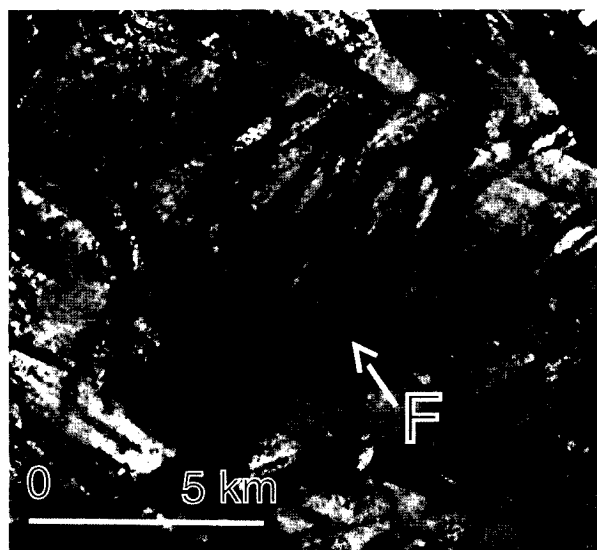


Negative print of extract from SAR ERS-1 scene acquired on 23 September 1992 (the day after the event).

A: The river is black (high values in the positive image) expressing rough water surface. The day after the rainstorm, the river is still in full spate.

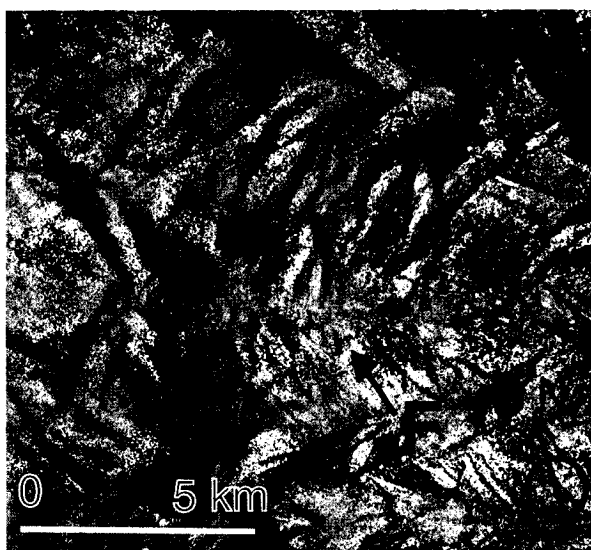
Figure 10-3: The river location before the flood

Figure 10-4: The river location after the flood



Negative print of extract from SAR ERS-1 scene acquired on 19 August 1992 (33 days before the event).

F: Forested surface with dark tone (light grey in positive image), meaning dry soil and forest



Negative print of extract from SAR ERS-1 scene acquired on 23 September 1992.

F: Forested surface with light grey tone (dark grey in positive image), meaning smooth free water in flooded forest.

Figure 10-5: The forested location before the flood

Figure 10-6: The forested location after the flood

10.3 Image analysis

In order to evidence the differences between the two scenes, the most classic method is to generate a colour composite image from the two scenes acquired at different dates (Figure 10-7). They were superimposed as positive prints without any geometric correction, because the ERS orbit is very precise and regular. The scenes are at a 35-day interval.

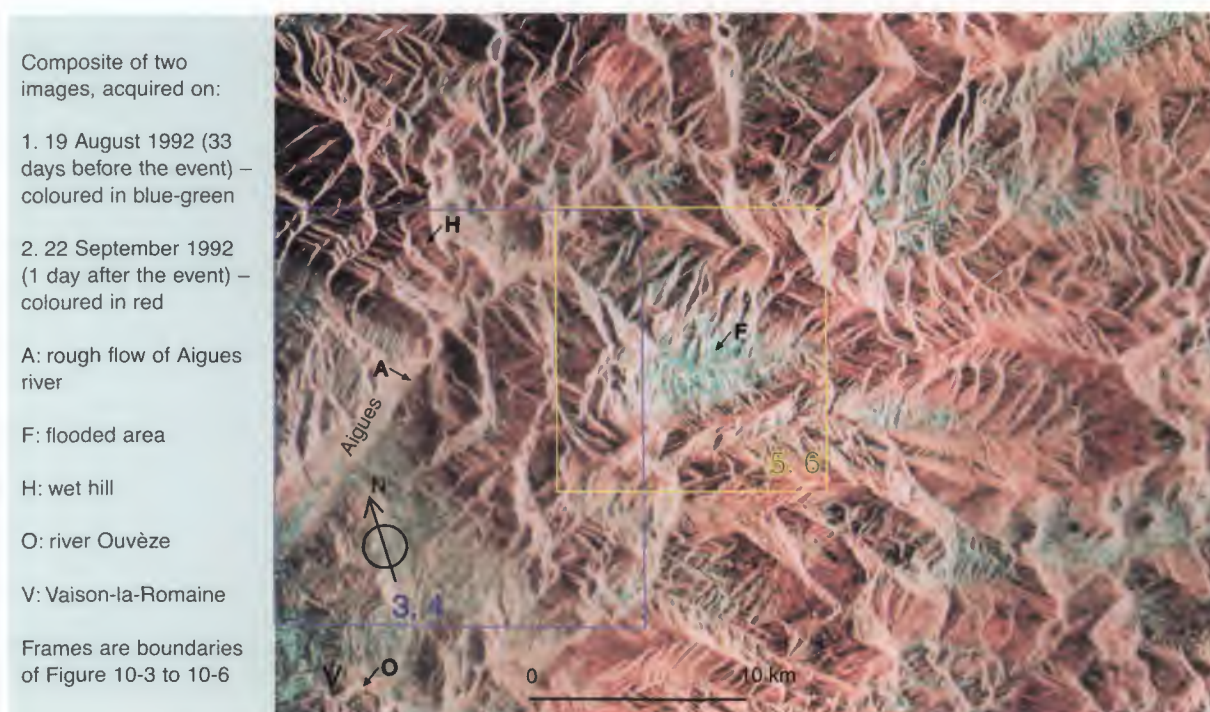


Figure 10-7: Colour composite image of positive SAR ERS-1

The 19 August positive image was coloured in blue and green and the 23 September positive image in red.

10.3.1 The rivers

In Figure 10-5, the river Aigues (A) shows up as a tiny red line, better than river Ouvèze (O).

In the 19 August negative image (Figure 10-3), river Aigues is white – meaning low values in the positive image. The water of the valley is quiet.

In the 23 September negative image (Figure 10-4), the river is black – high values in the positive image – expressing rough water surface. The day after the rainstorm, the river is still in full spate.

Low values of the river surface in the positive image on 19 August, coloured in blue-green, and high values in the positive image on 23 September, coloured in red, finally result in a pronounced red colour in the colour composite image.

10.3.2 Low topographic surfaces

In Figure 10-7, many low topographic surfaces are distinctly blue-green (e.g. **F**).

In the 19 August negative image (Figure 10-5), they have an overall dark grey tone – meaning the light grey of dry forest in a positive image – related to high roughness.

In the 23 September negative image (Figure 10-6), the tone is significantly light grey – meaning dark in a positive image, indicating smooth surfaces related to free water, i.e. a flooded area.

Putting blue-green colours over the grey tone and red over the dark tone of positive images results in a blue-green colour that shows the areas that are still flooded the day after the rainstorm.

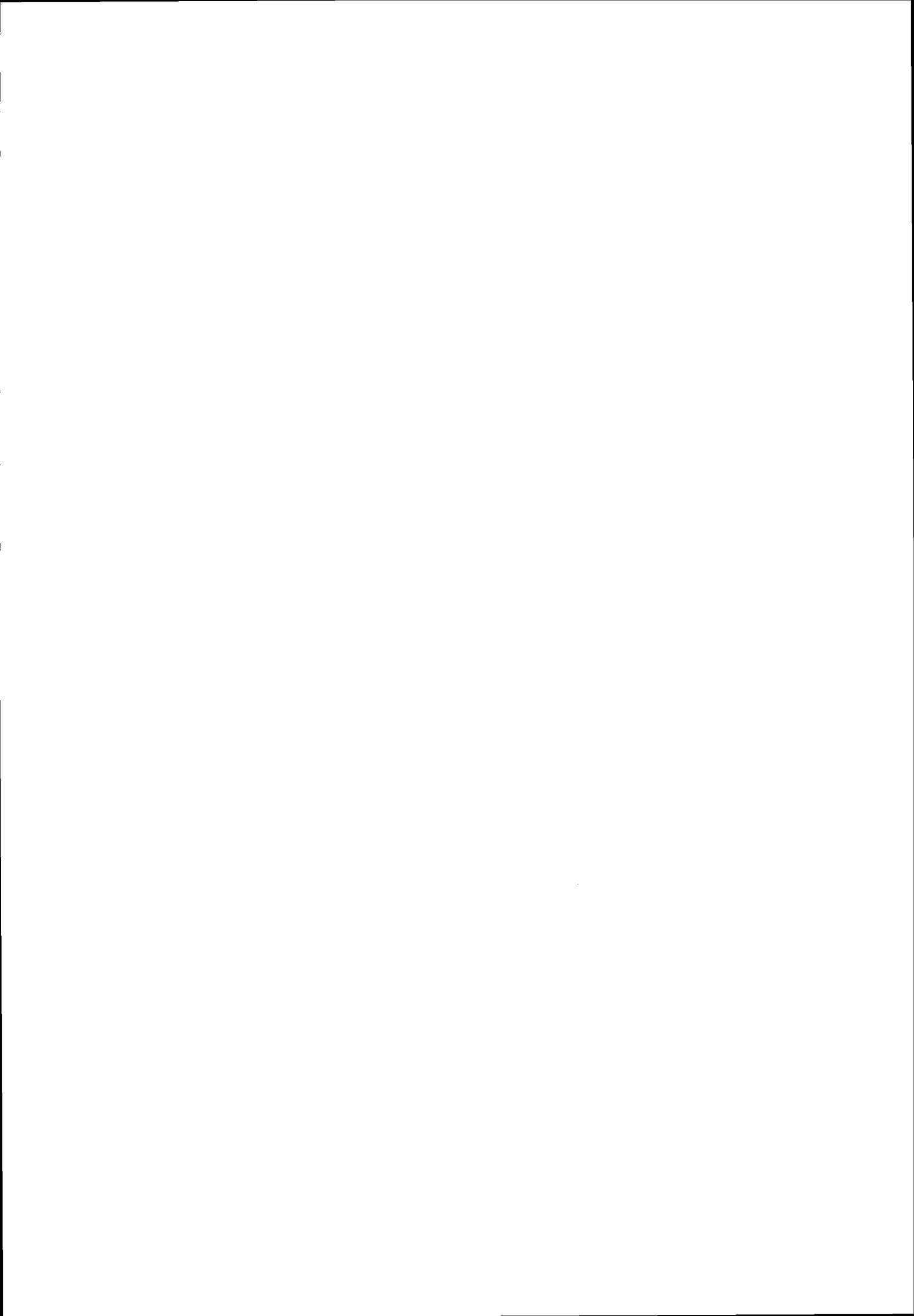
10.3.3 Hills

In Figure 10-7, all the hills have a pronounced pink colour, including hill **H**. This is due to an increase in backscattering with the increase of soil moisture the day after the rainstorm, as against 33 days before, whereas the roughness did not significantly change. The significant water content in the soil has induced a more significant backscattering, forming dark grey tones in this negative image of 23 September. On the other hand, in the negative image of 19 August, the grey tone is lighter, meaning less backscattering.

The colour composition being made from the positive images, the higher backscatter the day after the event results in a greater contribution of the red colour. The large distribution of pink colour over the whole area indicates that the soil is wet everywhere.

10.4 Conclusion

In conclusion, to assess the situation after a rainstorm event, careful examination of a colour-composite image of multi-date radar data is necessary, together with the black and white images taken independently.



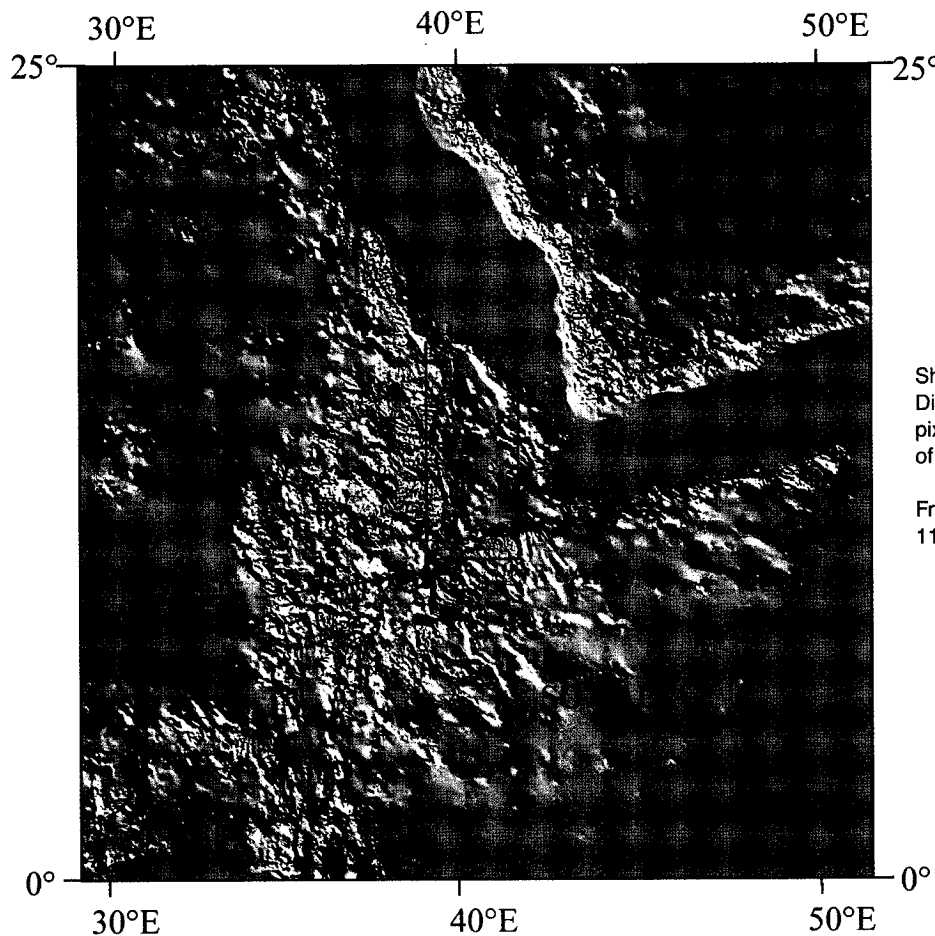
11. Morphology analysis and foreshortening effects

Case study: Rift tectonics in the West Afar Margin

11.1 Geologic framework

The Afar (Figure 11-1), which is considered to include a zone of oceanic accretion [3], is a tectonic depression with mean elevation at 300 m. It is bordered by the Red sea to the northeast, the Nubia plateau to the west and the Somalian plateau to the south. The Afar region has been subjected to subsidence and tectonic deformation of tilted blocks since 30 Ma.

Figure 11-1:
Location of the Afar
case study



Shaded images of the Digital Elevation Model at pixel size 500 m. The horn of Africa.

Frame: location of Figure 11-2.

The plateaus are mainly formed of early Cenozoic volcanic rocks (basalt and rhyolite), overlying Mesozoic sediments and a metamorphic basement made of late Precambrian (Neo-Proterozoic) units (Figure 11-2a). The anti-clockwise drift of the Danakil block (Figure 11-2b inset) has caused a rotation of 23°E since the Miocene (25 Ma), of which 11°E occurred since the Pliocene (6 Ma), and is responsible for the opening and subsidence of the Afar [2].

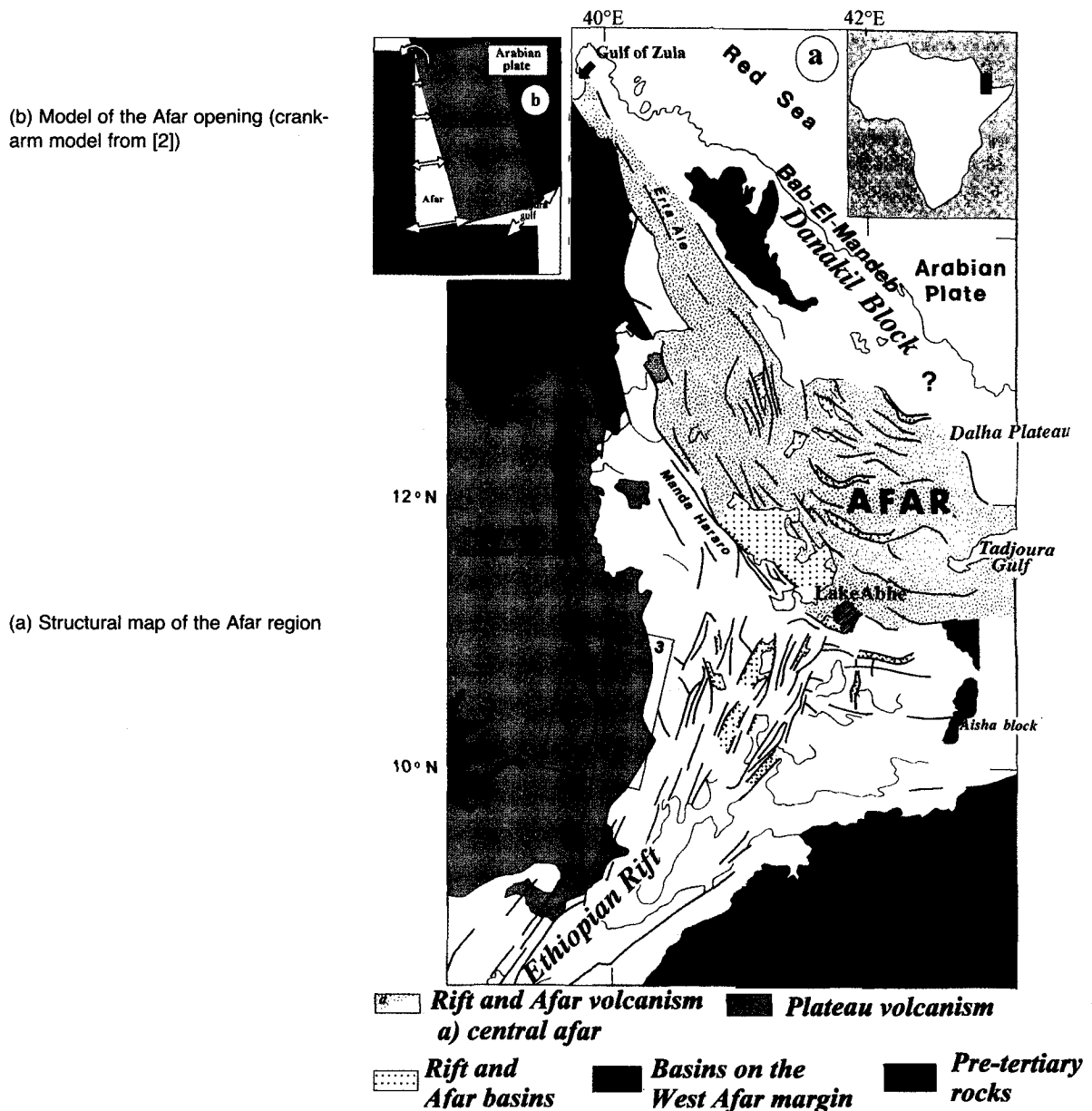


Figure 11-2:
Location of the Afar study area

The N-S trending western Afar margin, at the border of the Nubian part of the African plate, includes the Northwestern Ethiopian Plateau that is at a mean elevation of 3,400 m. The Pliocene-Quaternary (6 Ma to present) elongated basins (known as grabens) found in the western Afar margin are etched in the early Cenozoic volcanic rocks. They are separated from the Afar by a continuous line of large (~500 km long, ~60 km wide)

blocks. These basins, which stretch from the vicinity of the Ethiopian Rift in the south to the Gulf of Zula in the north, were not taken into consideration in the previous model of initial Afar opening by a simple motion of the Danakil block.

11.2 ERS SAR data analysis

Figure 11-3 shows a mosaic of two SAR ERS-1 scenes, acquired on 29 June 1993, covering the south-western margin of the Afar and the Borkena graben.

In order to emphasise the morphological features, the image is shown in 'negative' (histogram inversion). This means that the slopes facing SAR illumination appear dark, while those facing away appear grey. Figure 11-4 shows an annotated version of this image.

From west to east, the image features the edge of the North-Western Ethiopian Plateau, the escarpment zone (narrow in the south and wide in the north) and the Afar plain.

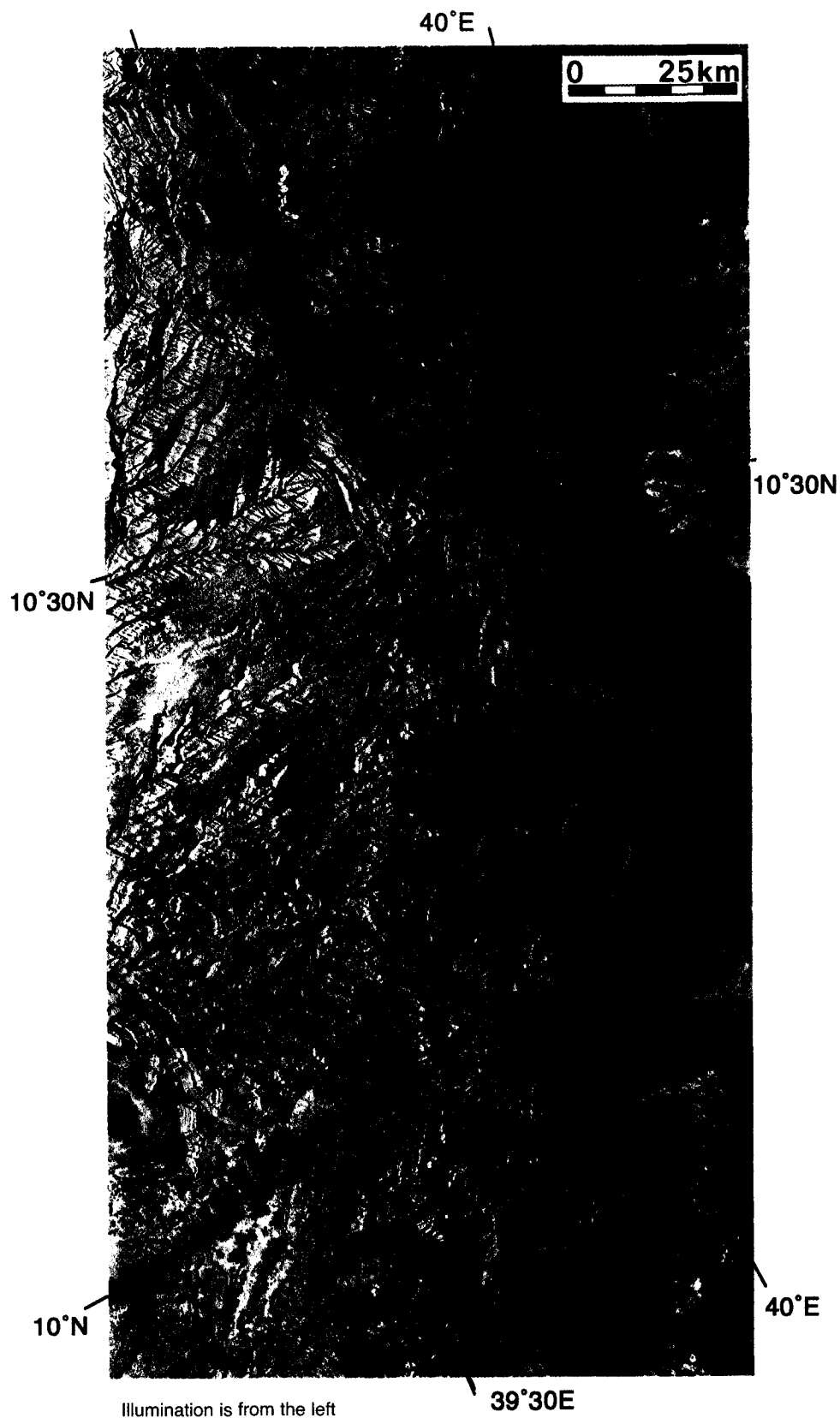


Figure 11-3: SAR mosaic of the Afar & Borkena graben

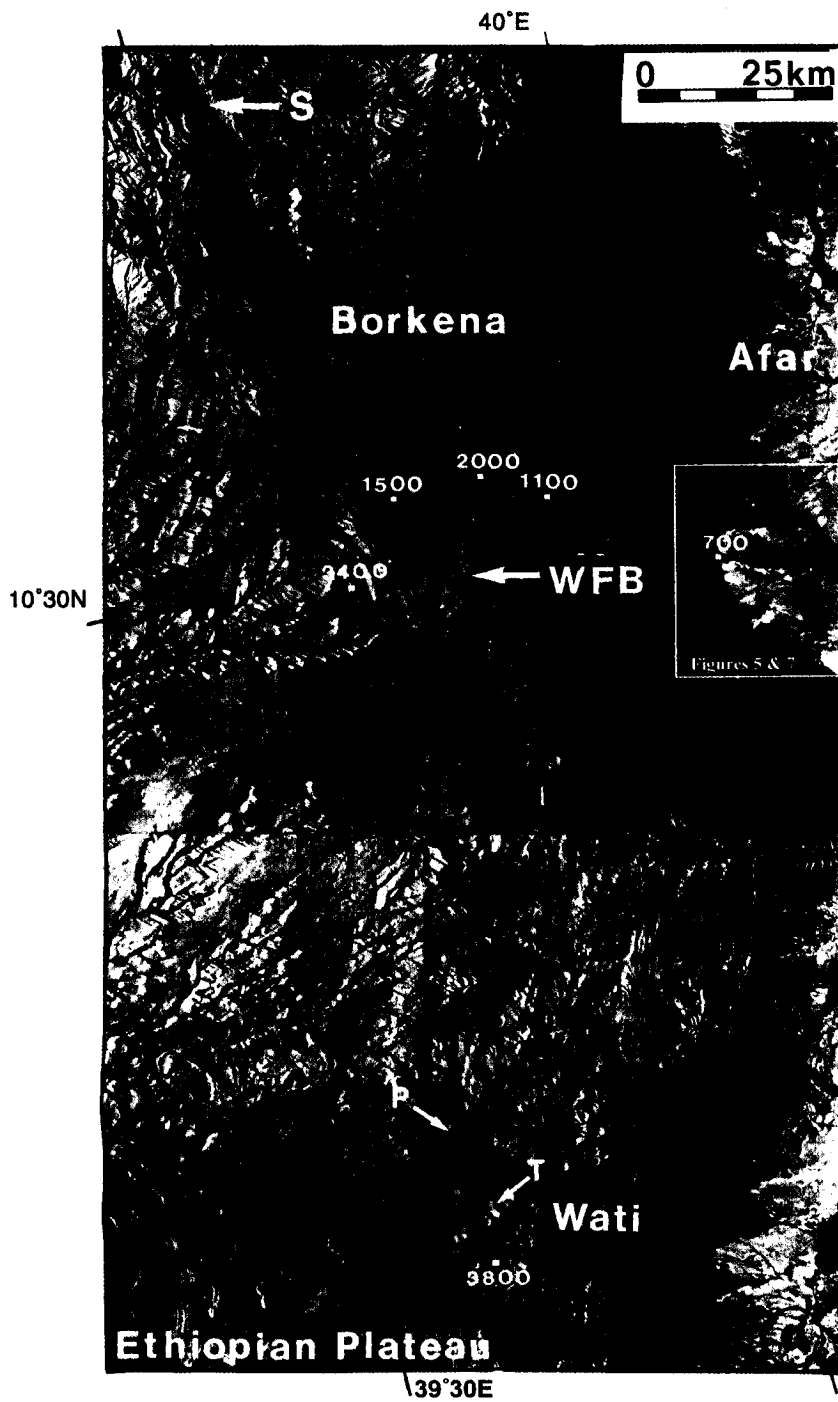


Figure 11-4: Key observations of Figure 11-3

The problem in this case is that radar illumination over mountainous areas causes a foreshortening/layover effect as described in chapter 1.4 (relief distortion), which can create a false interpretation of the morphology and geology.

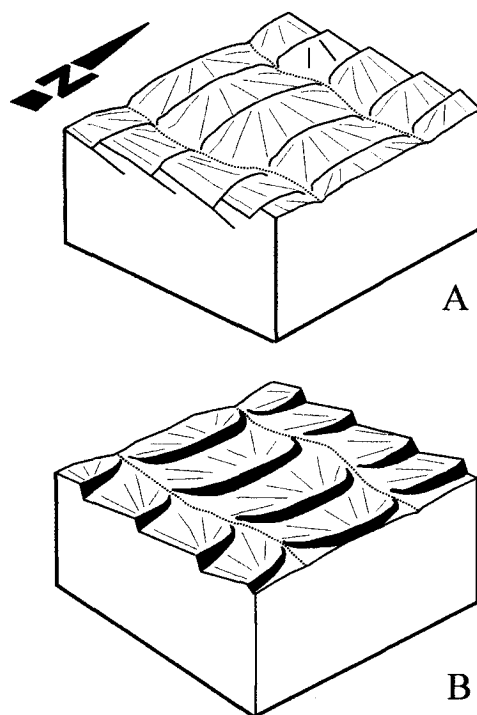
A series of thin upright curved lines that are the ground trace of banks can be seen in the transition area between the northern part of the Ethiopian Plateau and the Afar. In the

ERS SAR image, the banks seem to be west-dipping, as illustrated and explained in Figure 11-6.



Extracted window of the SAR ERS-1 scene covering the lower part of the West Afar margin, with layover effect giving false dips of layers (negative print)

Figure 11-5: Layover effect giving false dips



Relief distortion occurring in radar images.

- A) Actual dip of the banks, from Landsat image
- B) Incorrect interpretation of ERS SAR view

Figure 11-6: Explanation of relief distortion

In fact, field geologic cross-sections and Landsat imagery (Figure 11-7 and Figure 11-6A) show that these layers are dipping east (towards the Afar).

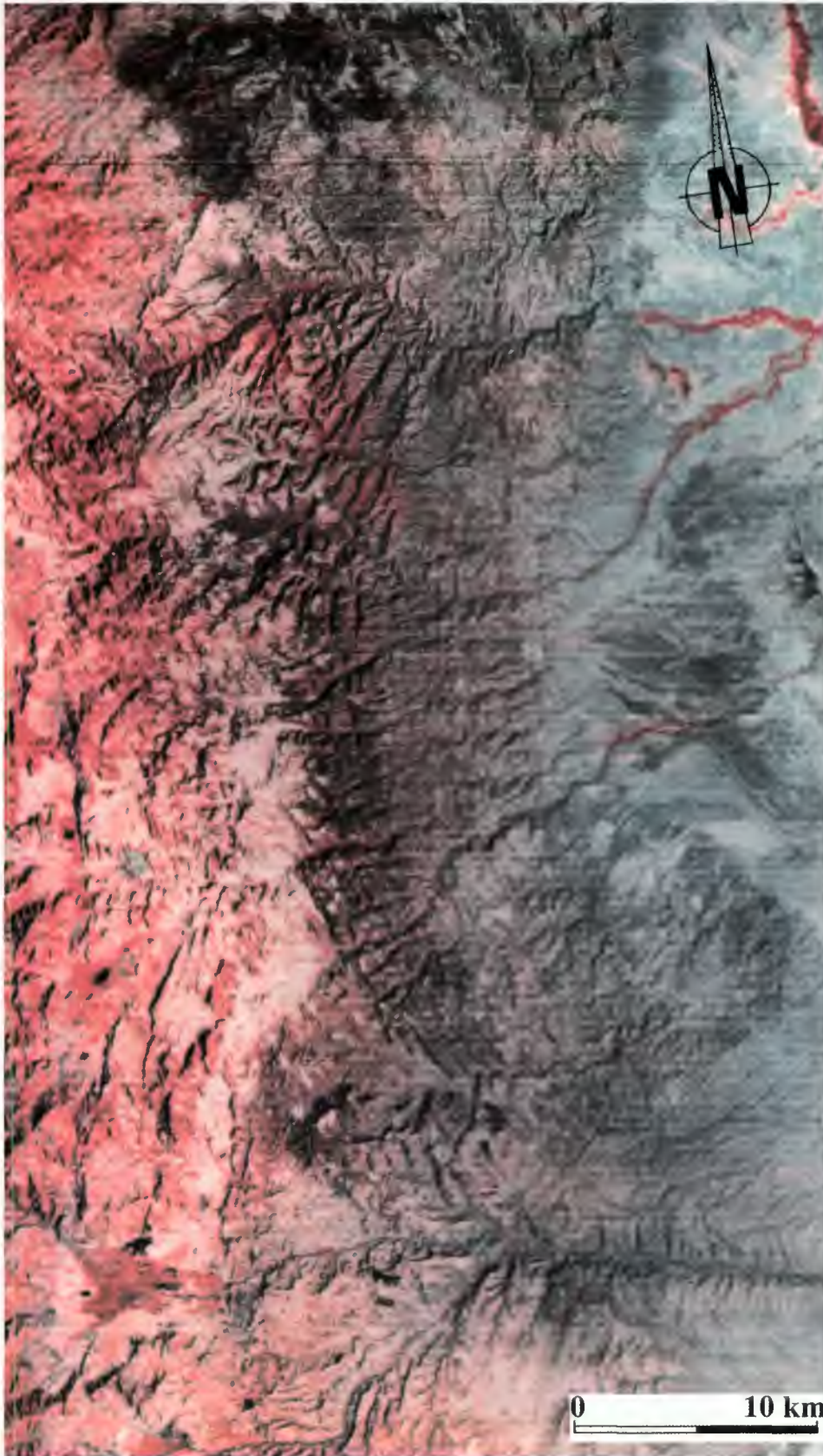


*Figure 11-7:
Landsat image of
the West Afar
margin shown in
Figure 11-5*

However, the image does permit observation of the faults and tectonic blocks. Analysis of the Borkena basin constrains the geometry of the deformation and mechanisms of opening of the Afar.

The N160°E-trending Borkena basin (Figure 11-8, located in the framed area of Figure 11-4) is part of the escarpment zone.

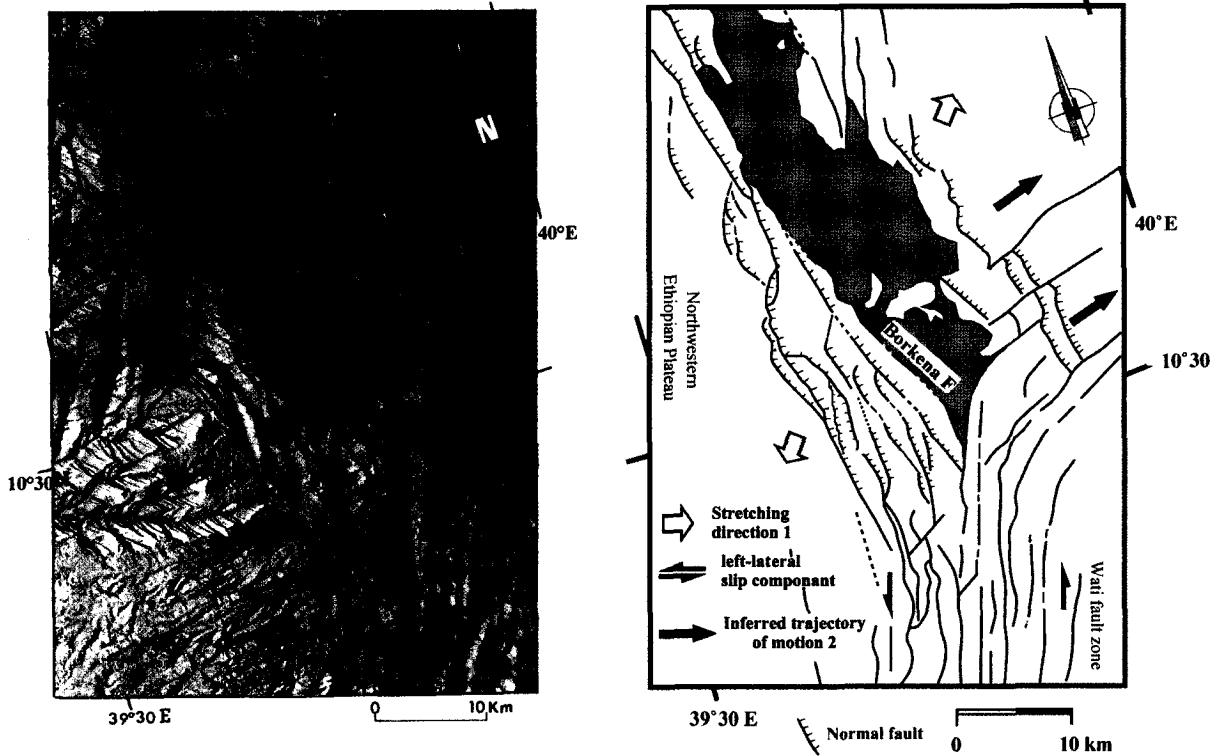


Figure 11-8: ERS-1 SAR image of the Borkena basin Figure 11-9: Structural interpretation of Figure 11-8

This graben is bordered along its western side by E-facing N160°E-striking fault scarps across which the elevation drops by about 2,000 m. These faults progressively connect southward with others, striking N20°E, forming the Wati fault zone (Figure 11-9).

Some faults of this system show a curved southward termination. The geometric pattern is that of successive spoon-shaped faults (P in Figure 11-4 and Figure 11-10b).

Similar second-order faults (T) end at the Wati volcano (Figure 11-4 and Figure 11-10c). T-faults terminate as open fissures from which lava was extruded. In this model the volcano is rooted at a fault end that opened in a tail-crack fashion (Figure 11-10c). The geometry of this tail-crack feature and of the spoon-shaped faults implies a left strike-slip component along the Wati fault zone.

The southern end of the Borkena basin is marked by the main scarp (WFB in Figure 11-4) of the Wati fault zone, progressively connecting northward with the N160°E-trending eastern border of the basin. Similarly, the northern end of the basin is formed by an alignment of fault scarps (S) oriented N20°E, the same orientation as the Wati fault zone. This means that the Borkena early basin was formed by the activity of the ~N20°E

trending fault system (Figure 11-10a). This interpretation is consistent with a sinistral slip component along the Wati fault zone.

Abbreviations: P = first-order fault; T = second-order fault

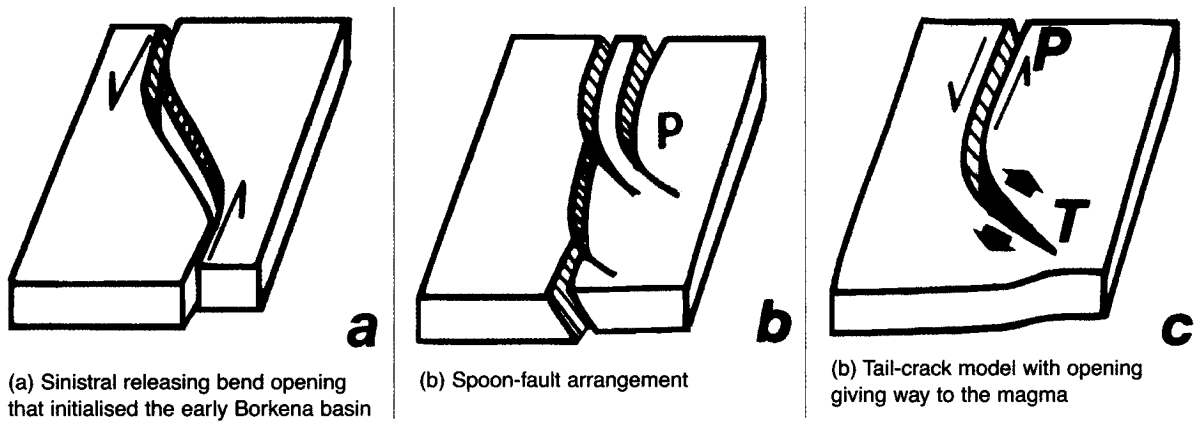
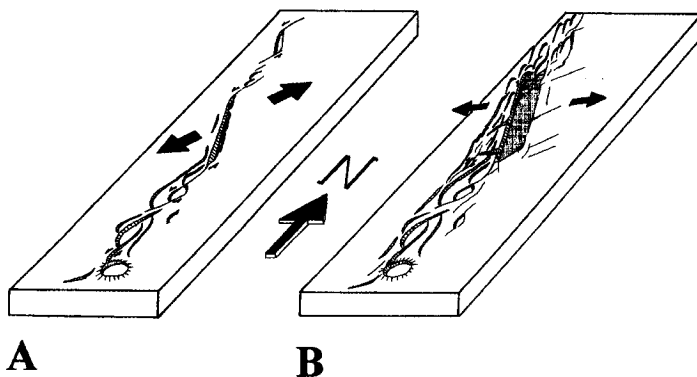


Figure 11-10:
Tectonic models

The Wati fault zone is the southern termination of the western Afar margin blocks (Figure 11-2). The western escarpment is strongly faulted, with N160°E major faults, including the Borkena fault (Figure 11-9). The faults face east, and bound west-dipping tilted blocks of the Northwestern Ethiopian Plateau. The Borkena fault turns and connects with the Wati fault zone, forming the south corner of the basin. The eastern border of the basin is a stratigraphic contact but, more to the east, it is bounded by small east-dipping normal faults, which define west-dipping tilted blocks. This geometry is that of an asymmetric basin, with the Borkena fault being the main detachment fault and the eastern basin being the shoulder of the corresponding rollover structure.

The faults in the northern part of the Wati fault zone turn eastward and cut the normal faults of the eastern border, forming a transfer fault system. This represents a key issue to date the last two tectonic stages that occurred in the area. Firstly, N20°E-directed motion of the margin block along the sinistral strike-slip Wati fault zone opened the Borkena early basin at a releasing bend (Figure 11-11).

Figure 11-11:
Model of the
Borkena graben
evolution in two
tectonic stages



A) Releasing bend structures are responsible for opening of the early Borkena basin, with NNE-trending extension paralleling the strike-slip motion.

B) Widening of the graben due to E-trending extension induced by gravity.

Secondly, an E-directed motion occurred along the transfer faults, inducing major extension inside the basin. Looking at Figure 11-3, the perception is of gravitational

collapse of the margin block into the Afar, the transfer fault zone forming the southern limit of the block.

11.3 References

- [1] Chorowicz J., Collet B., Bonavia F. and Korme T., 1999: Left-lateral strike-slip tectonics and gravity induced individualisation of wide continental blocks in the western Afar margin. *Eclogae geologicae Helvetiae*, **92**, 149-158.
- [2] Sichler, B. 1980: La biélette Danakil: Un modèle pour l'évolution géodynamique de l'Afar. *Bull. Soc. Géol. Fr.* **22**, 925-933.
- [3] Tazief, H. 1973: La signification tectonique de l'Afar. *Rev. Géogr. Physi. Géol. Dynam.* **2**, 15, 341-346.

12. Morphology and major faults

Case study: Large shear zones between the Dinarides-Albanides-Hellenides and the Balkans

12.1 Geological framework

The Albanian Sigmoid (Albanides) is the transition area from the Dinarides in the NW to the Hellenides in the SE (Figure 12-1).

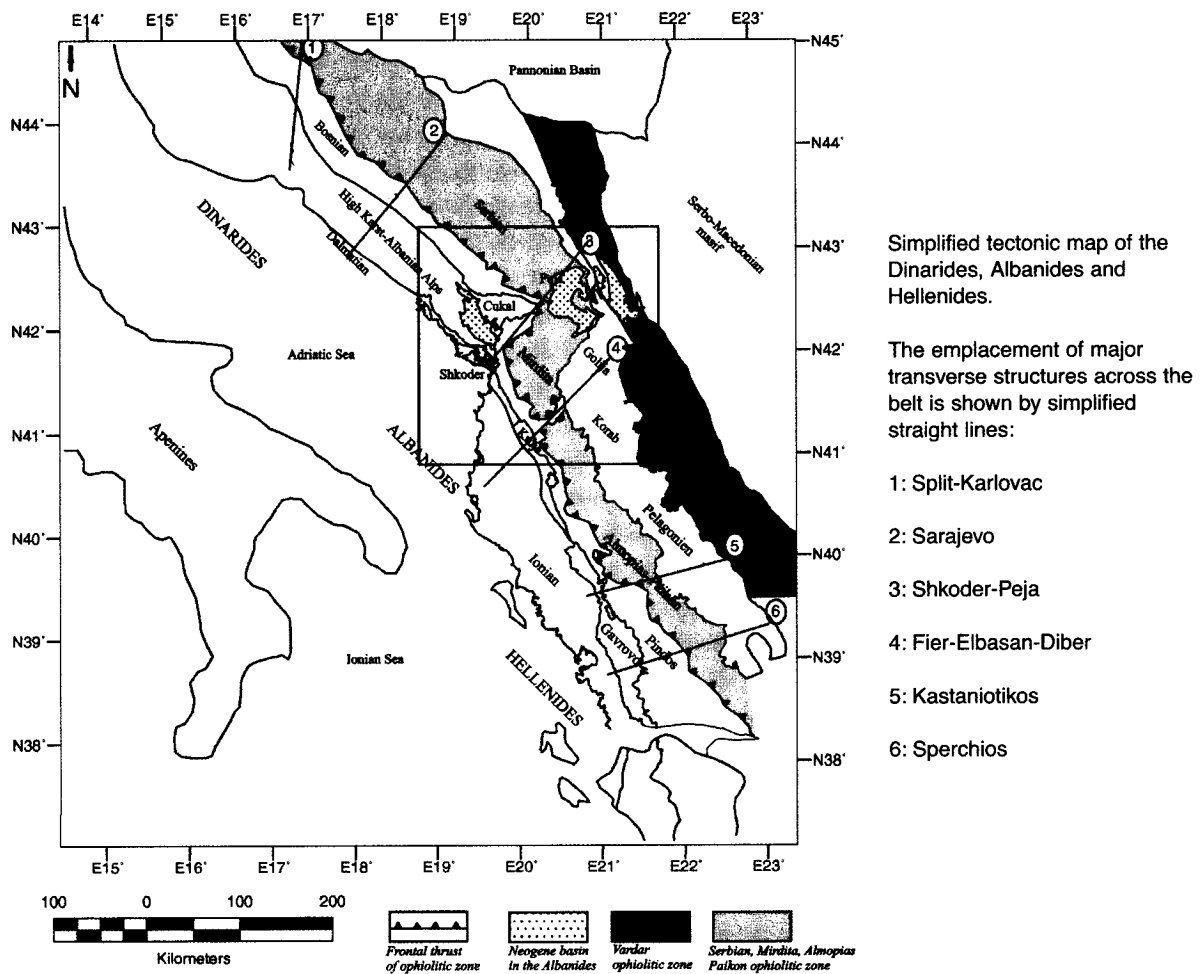


Figure 12-1: The studied area of the Balkans

The Dinarides-Albanides-Hellenides corresponded during the Mesozoic to the eastern margin of the Apulian continental block, a former promontory of the Palaeozoic African continent, belonging during the Mesozoic to the Adriatic plate. This belt comprises

important obducted ophiolitic sheets and has been progressively built up from the Inner (east) to the Outer (west) zones by collision of the Apulian continental block with the Eurasian continent.

This north-eastern margin of the Apulian continental block was formed during the opening of the Neotethyan Ocean. Rifting during the mid-late Triassic is responsible for individualisation of elongate pelagic basins, separated by shallow carbonate platforms. Spreading in the oceanic basin was achieved at the end of the middle Jurassic [1]. The westward obduction of the Mirdita ophiolites occurred during the late Jurassic. Late Cretaceous platform carbonates were disconformably deposited over the obducted ophiolites. During the early-mid Cenozoic, the Africa-Eurasia convergence resulted in collision with south-westward emplacement of large-scale allochthon units. During the Pliocene-Pleistocene, the outermost peri-Adriatic foreland basin was compressively deformed. Simultaneously, tensional Neogene basins lying over the Mirdita nappe were submitted to subsidence.

12.2 Data and image processing

Figure 12-2 shows a mosaic of three images from the Earth Remote Sensing satellite (ERS-1) Synthetic Aperture Radar (SAR). The images were enhanced using simple linear contrast stretching and afterwards combined into a single mosaic. A window showing the area of interest has been extracted from the mosaic (Figure 12-2A).

The two mosaics are made of three images from orbits and frames 9578-855, 9349-855 and 5112-837, acquired respectively on 05/15/1993, 04/29/1993 and 07/07/1992. The locations are shown in the frame of Figure 12-1

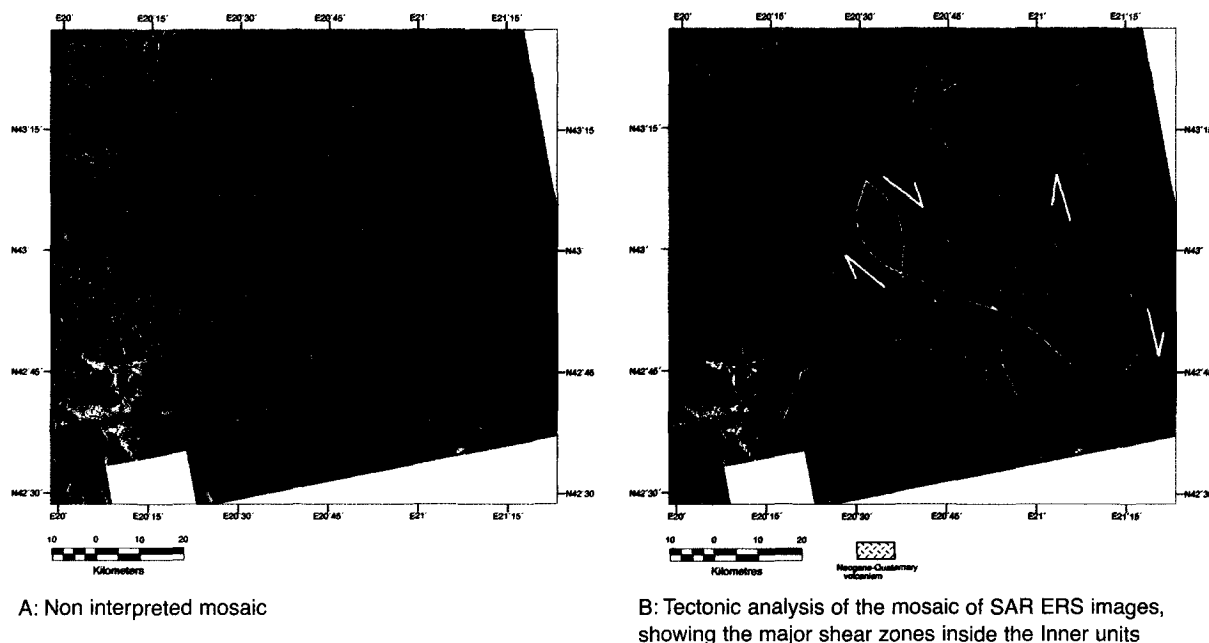


Figure 12-2:
Mosaic of three
SAR ERS images

Figure 12-3 shows a Landsat-TM scene, in which the data of the area of interest were extracted and processed into simple colour composite images. Three TM bands were used as inputs for displaying a RGB colour composite (Figure 12-3A). These bands are

individually informative in their specific spectral domain and also have minimal redundancy.

NE quarter image of Landsat-TM scene acquired on 18 August 1987, on path 186-row 31, shifted 60% southward, at 30m pixel size. The TM7, TM4, TM5 bands were used respectively for RGB colour composition

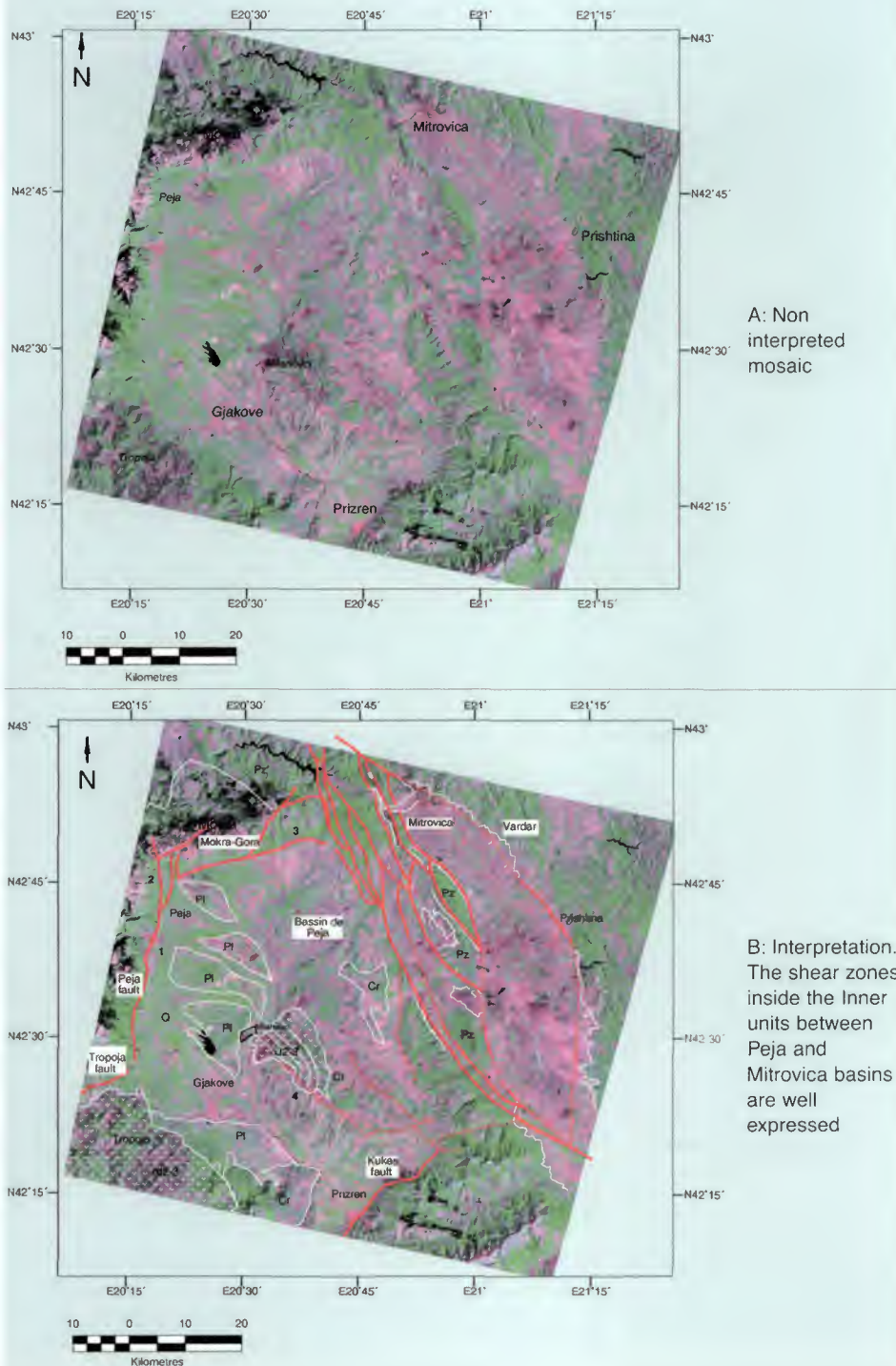
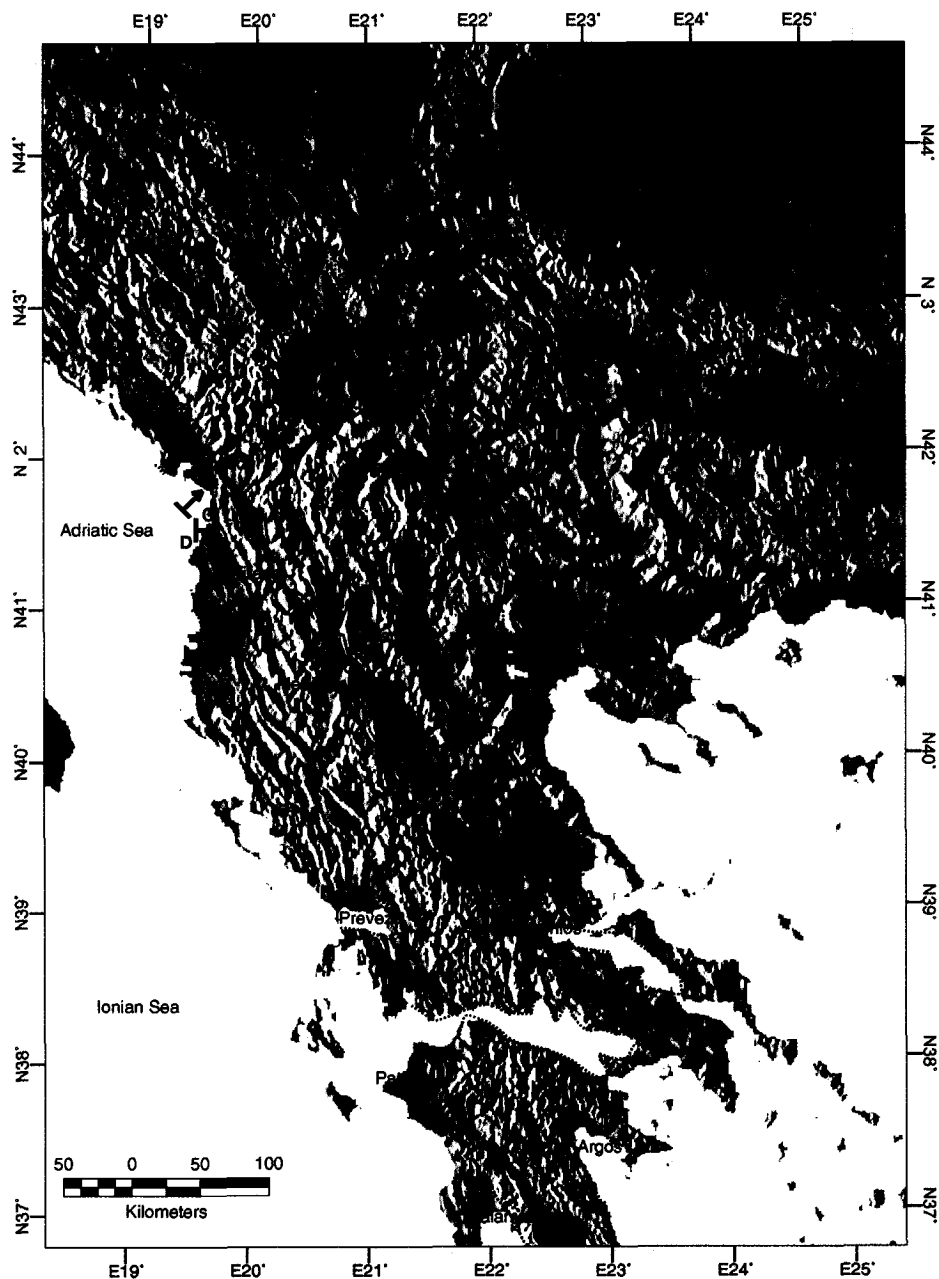


Figure 12-3: Landsat-TM scene as RGB colour composition

A Digital Elevation Model was extracted from the Global 30 arc second DEM database (GTOPO 30 from Eros Data Centre). The x-y co-ordinates of the grid nodes were converted from geographic co-ordinates to UTM-zone 34 co-ordinates. The data were re-sampled to have 1,000 m grid spacing (Figure 12-4A).

Shaded DEM from GTOPO_30, at 1 km pixel (illumination from SW)



Interpretation: The DEM shows the SE and NW prolongations of the shear zones (black lines) mapped in Figure 12-2B and Figure 12-3B. In the NW, the Tuzla and Pozega pull-apart basins testify to right-lateral motion. The low relief areas (bordered by dotted lines) are related to late Cenozoic extension.

Figure 12-4:
Digital elevation
model of the area

12.3 Analysis

The Landsat-TM image offers a synoptic but precise view of the Mitrovica area (Figure 12-3A). The NW-striking elongate Mitrovica basin is a large Z-shaped landform connecting at both extremities with N140°-striking fault scarps (Figure 12-3B). It can consequently be regarded as a subsiding area developed at the releasing bend of right lateral strike-slip faults. The last sequences of the Pliocene sediments (6 Ma) filling the basin seem to overlay major bounding faults in several places, especially along the north-eastern and eastern borders. In the SW part of the basin, fish-like hills, associated with narrow tectonic strips forming elongated depressions, can be interpreted as tectonic sigmoid slices belonging to a transcurrent shear zone, and their pattern is compatible with right-lateral movements. This complex NW-striking dextral shear zone lies inside the Inner Dinarides, forming the boundary between the Vardar unit on the north-eastern side and the Golija-Korab unit on the south-western side.

The north-western prolongation of the strike-slip shear zone can be analysed on ERS SAR images (Figure 12-2A). The main fault prolongating the NW end of the Mitrovica basin continues to the NW over a short distance and steps right, forming a dextral diffuse relay zone with extensional tectonics attested by the occurrence of Neogene-Quaternary volcanism (Figure 12-2B). The main fault then continues northwestward but there is also a south-eastern branch, which ends in a Neogene-Quaternary volcanic massif (Trepça massif) that can be regarded as another right-stepping tensional relay area of the shear zone.

East of the Trepça massif, there is a NNW-striking line corresponding to a fault, but its northern continuation is unclear. More to the east, the tips of the Podujevo pull-apart basin prolongate by faults, and the overall pattern suggests right-lateral motion along a fault zone progressively changing in strike from N150° to N170°.

The shear zones observed on the Landsat-TM and ERS SAR images also have a distinct expression on the DEM at 500 m pixel size presented as shadow image (Figure 12-4A). Northwest and north of Mitrovica, the two main branches, striking respectively NW and NNW, are well exposed (Figure 12-4B). They seem to continue further NW and join between the Pozega and Tuzla pull-apart basins. From the Mitrovica region, they can also be confidently prolonged SE-ward for some tens of kilometres at the front of the Vardar zone, cutting the NE-striking lines of the Golija units near Tetove at right angles.

The complementary Landsat-TM, SAR ERS and DEM images show the same faults from different sources and at various scales. These structures had been inferred by several geologists, but never observed in the field or on images. They are very important structures, forming the actual boundary between the Dinarides-Albanides-Hellenides and the Balkans. They are the expression of the NE border of the Apulian block indenting the Eurasian continent.

Collision in these belts began in the Palaeocene by thrusting of the Serbo-Macedonian massif over the Vardar zone. Convergent motion was partitioned into SE-ward relative motion of the innermost units along the Mitrovica fault zone, and SW-ward transmission of compression to the Inner margin continental blocks. South-westward progression of the collision with time was marked by a late Eocene event, which produced thrust sheets, together with transcurrent motion reactivating the NW-striking shear zones.

Continuing collision during the Oligocene produced thrusting of the High Karst and Pindos zones, together with their Inner units load, over the Dalmatian zone. Deformation

propagated SW-ward in the Ionic zone. New displacements along the shear lines in the Inner regions opened basins, which began to fill (e.g. the Mitrovica basin).

12.4 Reference

- [1] Aubouin, J., 1959. Place des Hellénides parmi les édifices structuraux de la Méditerranée orientale. *Annuaire géologique Pays hellénique*, X: 485-525.

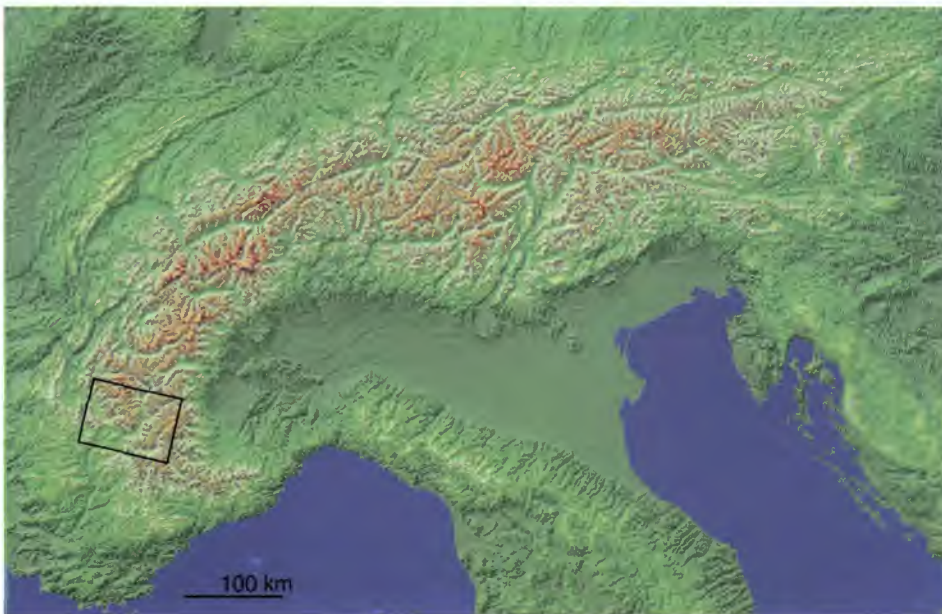
13. Evidence of mountain uplift from slope analysis using SAR ERS image

Case study: The Alps

Analysis of slopes is able to evidence recent deformations in mountainous areas. The Alps are a good example of ongoing uplift.

13.1 Geological context

The Alps form an arched belt, 1,000 km long and 150 to 200 km wide, the strike of which turns from NE-SW to N-S in its western part (Figure 13-1).

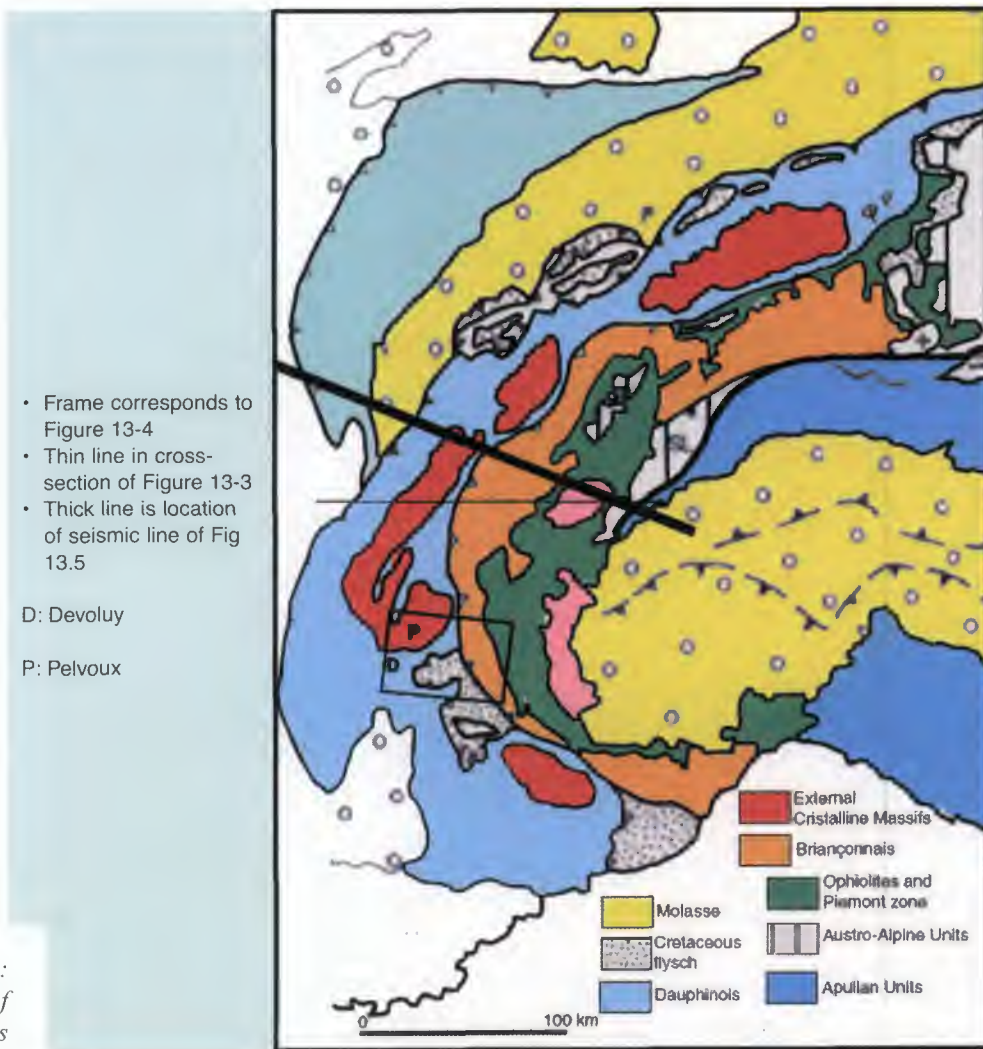


This image is derived from the GTOPO-30.

Frame is location of Figure 13-2.

Inside the External zones of the Western Alps, the Delphino-Helvetic (Dauphinois) zone includes uplifted basement units that outcrop along a strip forming the External Crystalline Massifs (Figure 13-2).

Figure 13-1: DEM showing a general view of the Alps



- Frame corresponds to Figure 13-4
- Thin line in cross-section of Figure 13-3
- Thick line is location of seismic line of Fig 13.5

D: Devoluy

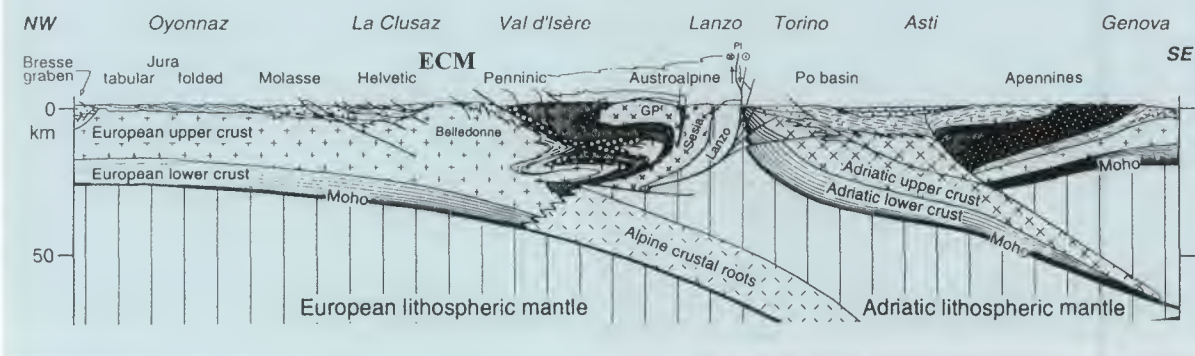
P: Pelvoux

Figure 13-2:
Structural scheme of the Western Alps

These massifs are slices of the para-autochthon crystalline basement, from which the sedimentary cover is detached and has moved westward due to gravity forces, forming the Sub-Alpine Belts of the Dauphinois zone (Figure 13-3).

Figure 13-3:
Geological cross-section of the Western Alps

Cross-section of the location indicated by the thin line in Figure 13-2

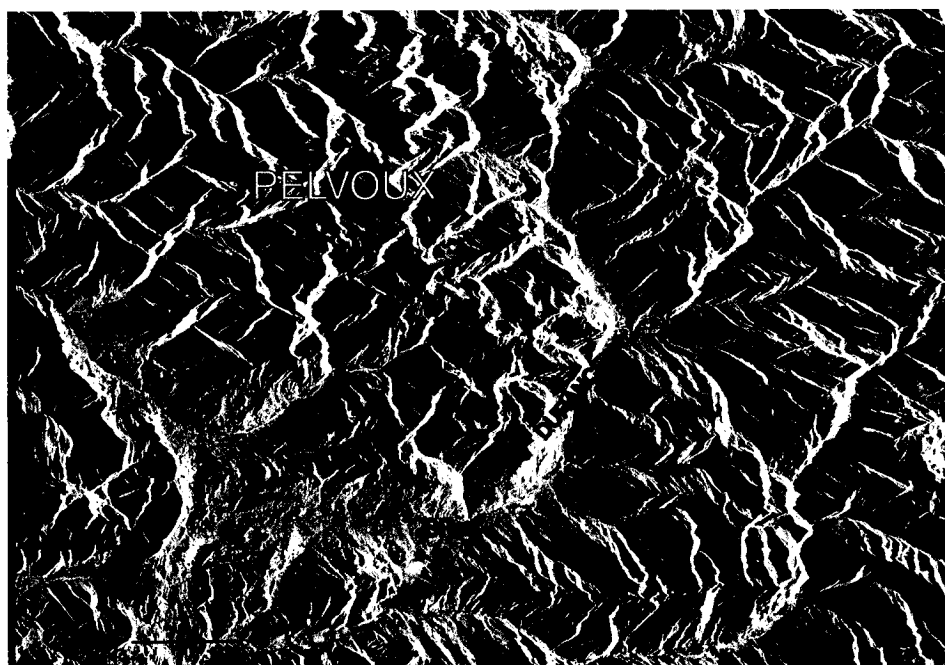


From a comparison of measurements of elevations at different dates ([1], [2]), it appears that the External Crystalline Massifs are presently uplifting at a higher rate in the Alps (1.5 mm/year) with reference to the Molassic Basin in the west, supposed fixed.

It is generally considered that uplifting areas have steep slopes due to the conjunction of higher reliefs and more intense erosion. The ERS SAR image is able to provide an approximate assessment of the steep slopes over a large area.

13.2 SAR ERS image

The SAR ERS image was acquired in descending node, illumination being from the east (Figure 13-4).



SP: Serre-Ponçon artificial lake

The slopes facing east are shortened and over-bright, providing no morphological information. In contrast, the slopes looking west, away from radar illumination, are elongated and display various grey tones essentially modulated by the slope variations.

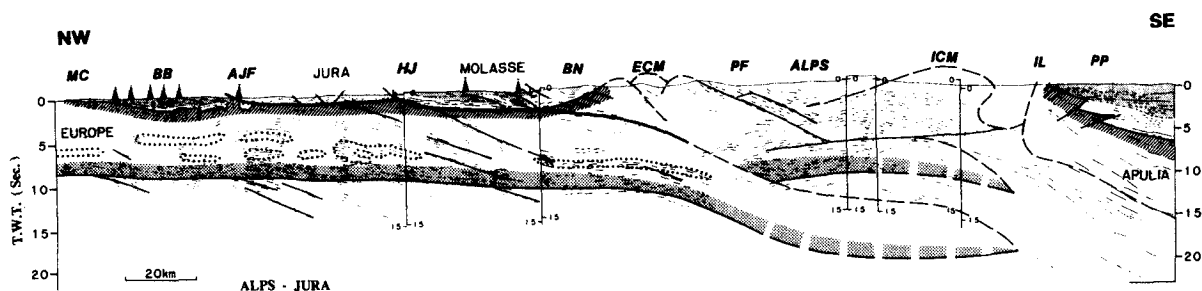
The main valley crossing the area is the river Durance, separating the Pelvoux (Ecrins) Massif, one of the External Crystalline Massifs, from the Briançonnais in the east or southeast, and from units belonging to the Sub-Alpine Belts in the south. The Sub-Alpine Belt developed here is the Devoluy Massif, in the southwest corner of the image. The river Durance includes the lake of Serres-Ponçon, related to a hydroelectric dam.

The striking fact shown by this image is that the tones of the western slopes in the Pelvoux (Ecrins) Massif are almost black, significantly darker than most of the slopes in the other regions. However, this area is characterised by high roughness. These large surfaces indicate that the slopes here are significantly steeper than in the other areas. Overall, this shows that the Pelvoux (Ecrins) Massif is submitted to active uplift and related erosion.

Figure 13-4: SAR ERS image of the studied area

13.3 Interpretation from ECORS-CROP profile

Deep seismic reflection profiling by ECORS-CROP has been made in the frame of a French-Italian cooperation. Several analyses have been proposed (e.g. [3]), which all interpret that there is a major thrust of internal crust over external crust (Figure 13-5).



This profile shows a major thrust of internal crust over external crust. The thrust surface comprises flat or ramp segments, upgrading north-westwards. The larger ramp has induced a crustal scale fold, which present-day uplift is responsible for steep slopes evidenced by the radar image in the ECM (External Crystalline Massifs)

Figure 13-5:
ECORS-CROP
profile
interpretation

The thrust occurs along flat surfaces, except under the External Crystalline Massifs where the motion occurs upon a pronounced ramp surface. This ramp has induced above a crustal scale fold with the External Crystalline Massifs (ECM) at its core. Uplift of the ECM shown by the ERS image indicates that the ramp and flat thrust system related to convergence is still active.

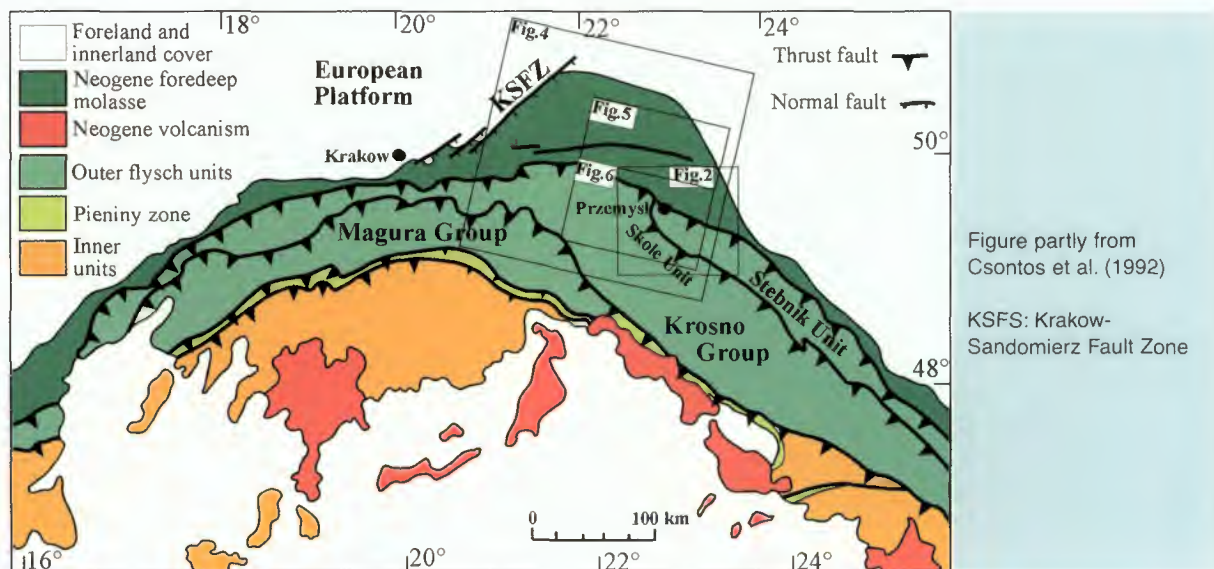
13.4 References

- [1] Darmendrail, X., 1994. Déformation récente et actuelle des Alpes Occidentales. *Mise en évidence, caractérisation et quantification par analyse géomorphologique et comparaison de nivellement*. Thesis, University of Savoie, Chambéry, 216p.
- [2] Jouanne, F., 1994. *Mesure de la déformation actuelle des Alpes Occidentales et du Jura par comparaison de données géodésiques historiques*. Thesis, University of Savoie, Chambéry, 254p.
- [3] Tardy M., Deville E., Fudral S., Guellec S., Menard G., Thouvenot F. et Vialon P., 1990. Interprétation structurale des données du profil de sismique réflexion profonde ECORS-CROP Alpes entre le Front Pennique et la ligne du Canavese (Alpes Occidentales), In *Deep Structure of the Alps, Mémoire Société géologique de France, Paris*, 156, 217-226.

14. Lithofacies change revealed by SAR ERS imagery

Case study: the sigmoid of Przemysl, Carpathians

The flysch rock units of the outer Carpathian Belt result from late Cenozoic tectonic inversion within the North-Neotethyan margin. The thrust faults within the flysch units generally parallel the main trend of the belt, except near Przemysl (Figure 14-1) the boundary area between the Eastern and Western Carpathians where a peculiar S-shaped pattern occurs, called the sigmoid of Przemysl. Key observations on lithofacies changes at regional scale allow a new interpretation of the sigmoid of Przemysl.



14.1 Regional geological framework

The Western and Central Carpathians include two major (inner and outer) structural units, separated by the Pieniny zone (Figure 14-1). The inner zone has been emplaced from the southeast as the result of lateral extrusion of crustal rocks due to the main middle Cretaceous collisional event in the Eastern Alps [2]. The Pieniny zone is a tectonic 'mélange' located at the front of the extruded inner zone. The outer units include several nappes made of Cretaceous-Palaeogene flysch rocks. Emplaced during the late Cenozoic, these flysch nappes thrust over a flexural molassic foredeep basin where late Cenozoic synorogenic detritic rocks cover the basement that belongs to the European platform.

Figure 14-1:
Structural
framework of the
Western and
Central
Carpathians

The flysch nappes of the outer zone are verging north to northeast in the studied area, and comprise the Magura group and the Krosno group, which includes the Skole, Boryslaw-Pokuty and Stebnik units (Figure 14-2). Southeast of Przemysl, the Skole nappe is built-up of Cretaceous flysch rocks. More to the north, the Stebnik unit, the lowest nappe of the outer Carpathians, is made of late Cenozoic rocks.

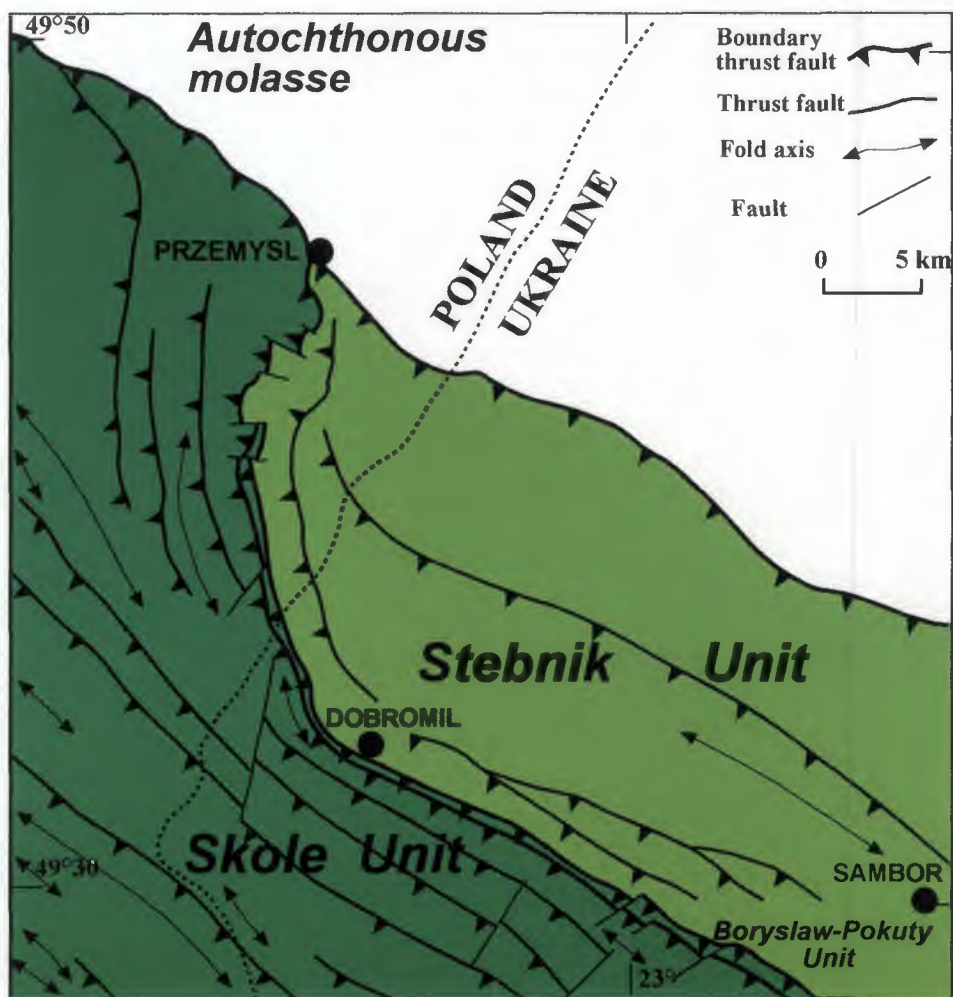


Figure 14-2:
Structural sketch-
map of the
Przemysl area
(location shown in
Figure 14-1)

14.2 The sigmoid of Przemysl

The sigmoid of Przemysl comprises a sharp S-shaped change in the strike (virgation) of the Skole unit thrust front, and the fold axes and reverse faults of the Skole and Stebnik units (it is the colour boundary in Figure 14-2).

The Carpathian thrust line – the boundary with the autochthonous molasses – shows no virgation, indicating that both nappes have simultaneously overthrust the autochthonous molasses.

Several models explaining the sigmoid of Przemysl have been proposed, including:

- 1) An uplift in the west and subsequent Burdigalian-Badenian (20 - 15 Ma) sedimentation of sandstone in the Stebnik basin in the east [3]

- 2) A NE-striking fault zone lying within the European platform at depth [4], dipping west, responsible for the uplift of the southeastern compartment during the late Cenozoic.

Authors have suggested that displacement of the Skole nappe over the Miocene rocks of the Stebnik unit – forming an obstacle – may have been partly hampered, inducing a virgation of the Skole unit. At the end of this tectonic activity, the upper part of the uplifted autochthonous rocks would have been finally detached and dragged out, forming the Stebnik nappe.

14.3 Analysis of the SAR ERS imagery

The SAR ERS-1 scene (Figure 14-3) was acquired in descending orbit, and illumination is from the E-SE.



Illumination is from the east-southeast; negative print

The negative image has been obtained by standard processing, and the slopes facing the radar seem like shadow whilst detailed information is well exposed by various gray tones in the slopes away from radar illumination. Polygonal surfaces characterised by higher backscatter values (dark in the negative print) correspond to forests, which can be distinguished from the light grey of meadows.

Figure 14-3: ERS-1 SAR image of Przemysl

Radar illumination being from E-SE, the main strike ridges trending NW are clearly expressed (Figure 14-4).

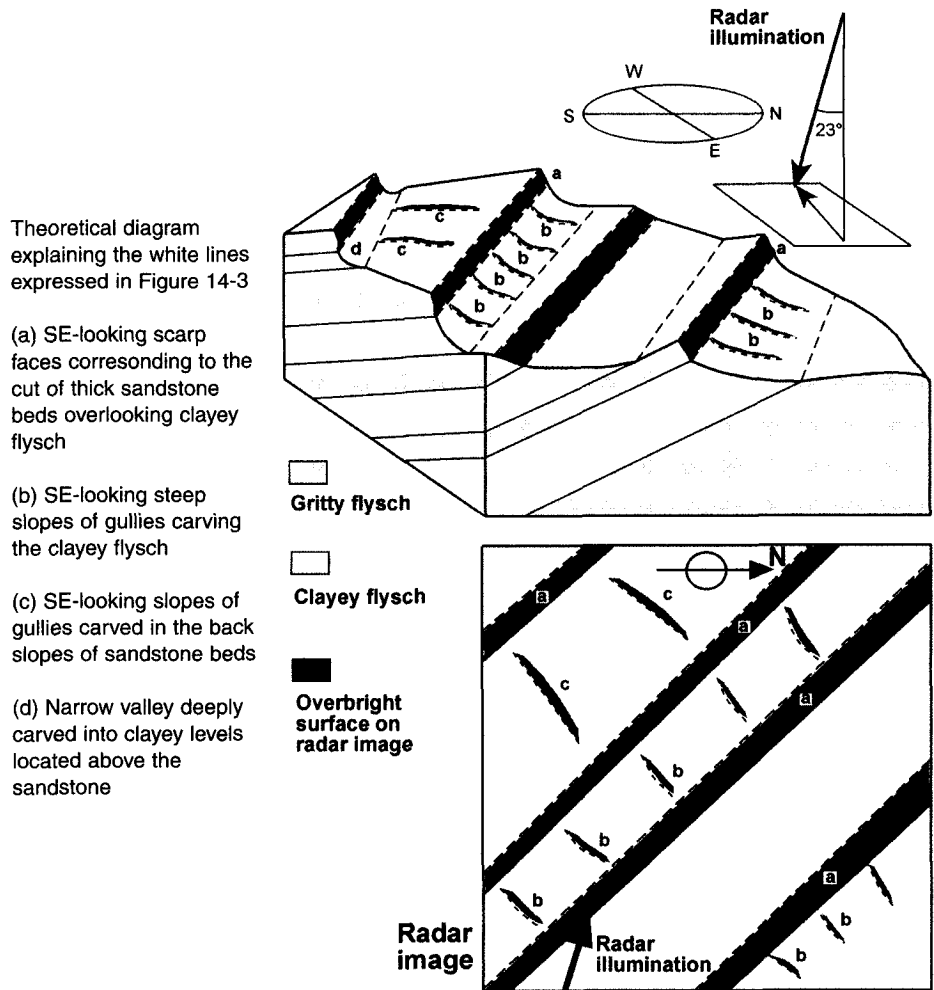


Figure 14-4:
Explanation of lines
in Figure 14-3

The steep slopes expressed by white pixels are of different categories, labelled a – d in Figure 14-4:

- a) The lines trending NW, formed in fact by a succession of short NE-trending lines, are scarp faces corresponding to the cut of thick sandstone beds overlooking clayey flysch
- b) Short, narrow and curved lines are the SE-looking slopes of gullies carving into the clayey flysch
- c) Short, narrow straight lines are the SE-looking slopes of gullies carved in the back slopes of sandstone beds
- d) The development of such gullies is related to a narrow valley deeply carved into clayey levels

In all cases, directly or indirectly, the white lines are related to the occurrence of clayey flysch.

This radar scene consequently shows that changes are related to variations in the topography and lithologic composition of the bed-rocks. In the southeast of the image in Figure 14-3, strike-ridges in the Skole unit, due to gritty flysch layers, are distinct and separated by elongated topographic depressions due to alternate clayey and gritty flysch beds. In the west of the image, the landscape of the Skole unit is more uniform. A detailed visual analysis of the image has permitted mapping of the progressive lateral end from southeast to northwest of the depressions due to clayey flysch rocks (Figure 14-5).

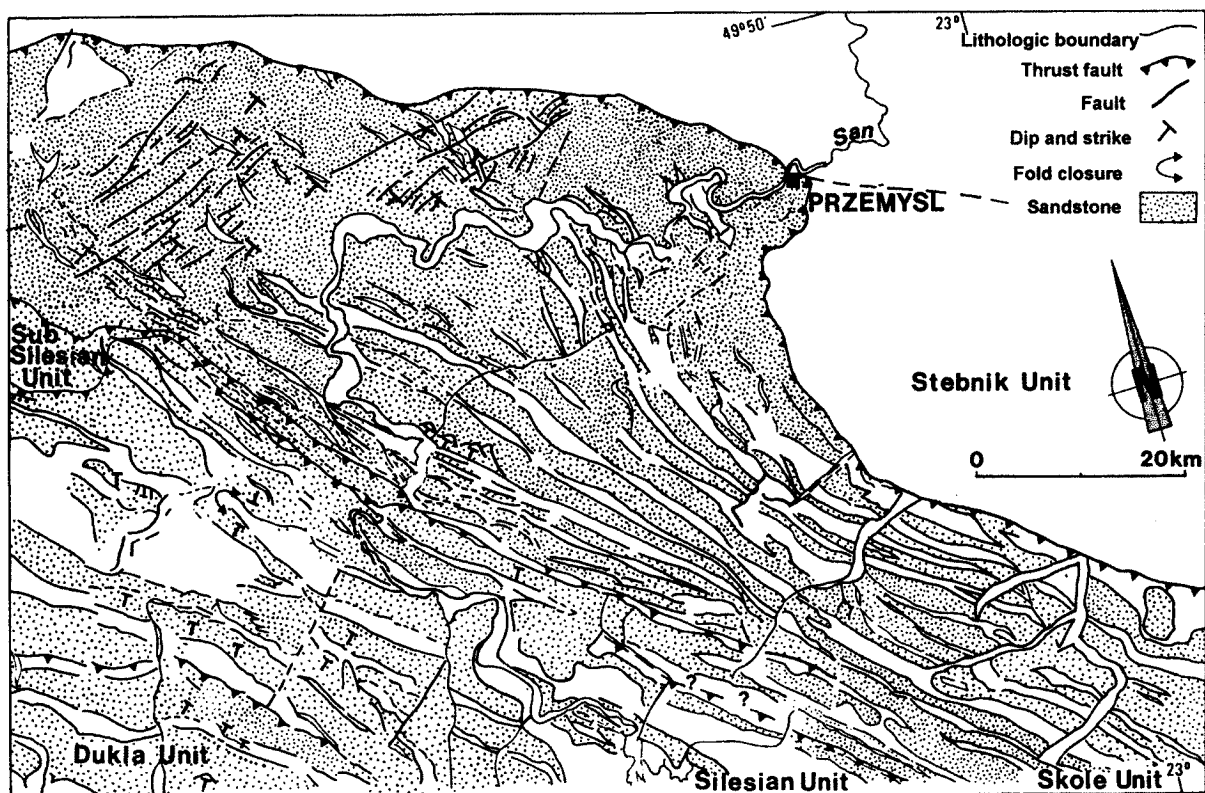


Figure 14-5 shows lateral lithofacies change in the Skole unit (location in Figure 14-1). Some of the faults which are indicated on the existing maps (Figure 14-2) have not been observed. This is probably because they are not clear enough in the morphology, whereas they were evidenced by field mapping of the lithostratigraphic units. Other faults which are not indicated in the existing maps have been drawn.

Figure 14-5:
Detailed analysis of
the SAR ERS image
of Figure 14-3
(southern part)

The image consequently shows, at regional scale, lateral lithofacies change from alternate clayey and gritty flysch levels in the southeast, to massive gritty flysch in the northwest. This lateral lithofacies change is principally located in the Skole unit. Dips are everywhere quite sharp and southwest directed, and consequently the interpretation of large western sandstone outcrops as being related to subhorizontal unconformable layers is excluded. It is also necessary to exclude interpretation in terms of tectonic repetition of the same gritty beds in the west, because the sandstone beds are not truncated by faults in the Skole unit.

14.4 Model of evolution

The line of lithofacies change within the Skole unit trends more or less northeast and can be linked to a paleofault (the Przemysl paleofault) situated within the Cretaceous Skole flysch basin, and forming part of a larger fault zone (Figure 14-6A). This Przemysl paleofault was the boundary between a northwestern marine platform characterized by gritty deposits, and a southeastern lower area with clayey sedimentation.

The model of structural evolution shown in Figure 14-6 takes into account lateral lithofacies change at regional scale in the Cretaceous layers of the Skole nappe, induced by the Przemysl syndepositional paleofault.

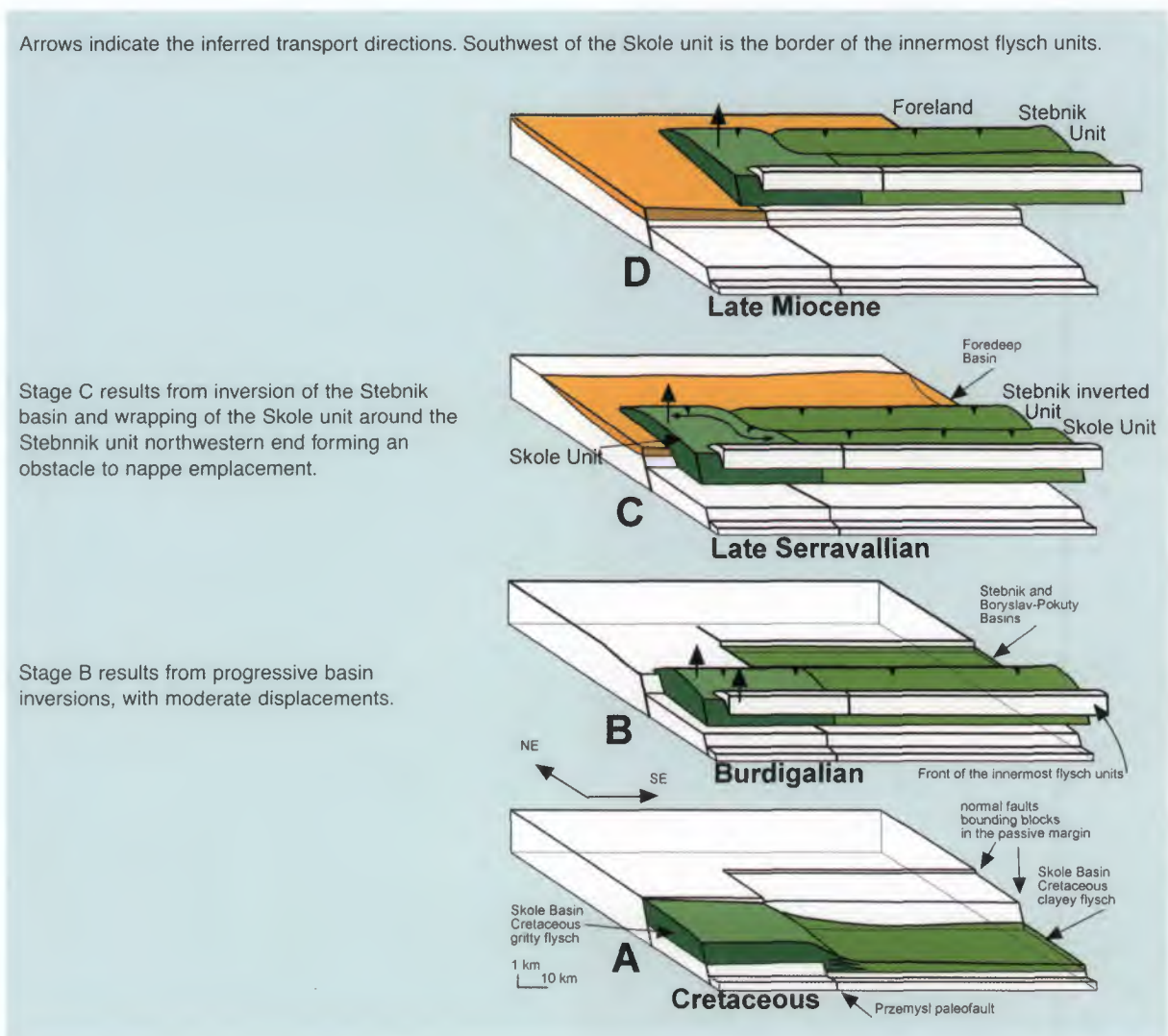


Figure 14-6: Model of structural evolution

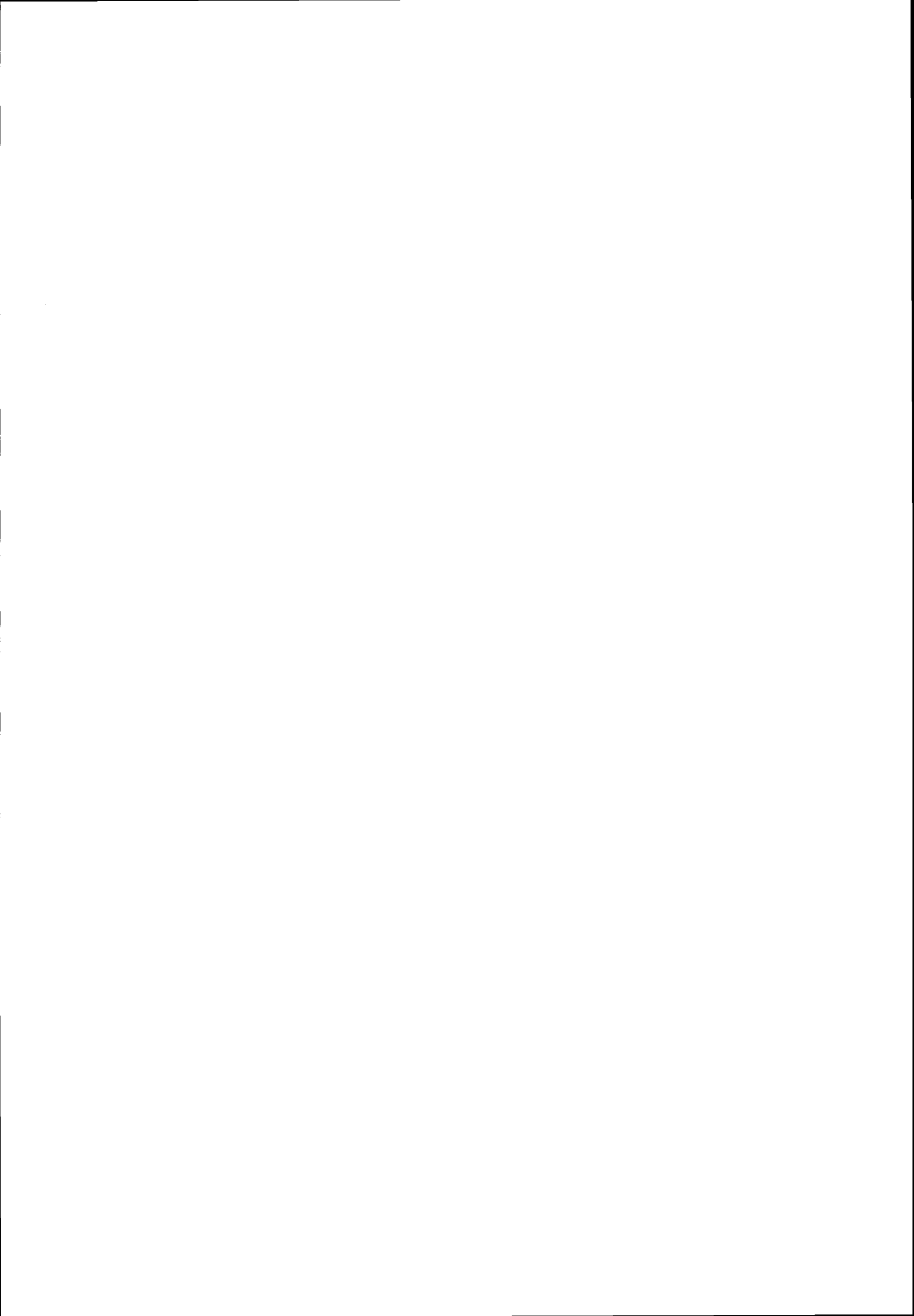
Tectonic inversion and NE-ward thrust of the Skole unit began during the Aquitanian, and was responsible for the successive formation of the Aquitanian-Burdigalian Boryslav-Pokuty basin and the Badenian (middle Oligocene) Stebnik foredeep basin (Figure 14-6B).

Later, during the Serravallian (Figure 14-6C) and late Miocene (Figure 14-6D), large horizontal nappe displacements occurred over the foredeep basin, with piggy-back transport of the previously inverted units. During these events, the Przemysl paleofault was transported far from its initial location. During the process of basin inversion affecting the Stebnik unit, the Skole unit could be prevented from moving further north by the uplift of the Stebnik unit occurring only east of Przemysl, whereas there was no bulge in the west (Figure 14-6C). The development of the sigmoid is the result of this difference in motion around the Stebnik unit, forming an obstacle to nappe progression.

This case study has shown that the ERS SAR image is particularly efficient at showing lateral lithofacies changes at regional scale, because it mainly expresses variations in morphology related to modifications in bed-rock composition.

14.5 References

- [1] Chorowicz J., Mering C., Raymond D., Szcuski R. and François R. 1999. Lithofacies change revealed by SAR ERS imagery in the Przemysl sigmoid, Carpathians: implication of a NE-striking paleofault on the North Tethyan passive margin. *Tectonophysics*, Vol. **304**, pp. 187-200.
- [2] Ratschbacher, L., Frisch, W., Linzer, H. G. and Merle, O., 1991. Lateral extrusion in the Eastern Alps, part 2: Structural analysis. *Tectonics*. **10(2)**: 257-271.
- [3] Wdowiarz, S., 1976. Ostosunku Karpat do zapadliska przedkarpackiego w Polsce. *Przegląd Geologiczny*, Warszawa, **24(6)**: 350-357.
- [4] Zytko, K., 1985. Some problems of a geodynamic model of the Northern Carpathians. *Kwartalnik Geologiczny*, Warszawa, **29(1)**: 85-108.
- [5] Csontos, L., Nagymarosy, A., Horvath, F. and Kovác, M., 1992. Tertiary evolution of the Intra-Carpathian area: a model. *Tectonophysics*, **208**, 221-241.



15. SAR ERS images used to relate tectonics to shape and distribution of volcanic vents

Case study: Iceland

15.1 Geodynamic setting

Iceland (Figure 15-1) is an emerged segment of the mid-Atlantic ridge, associated with plume activity.



Figure 15-1:
Location of the two SAR ERS scenes of Iceland

This case study is based on a paper from [1].

There is current tectonic activity in the central rift (Figure 15-2 inset), bounded by distinct scarps facing each other, and related to extension in the east-west direction [2].

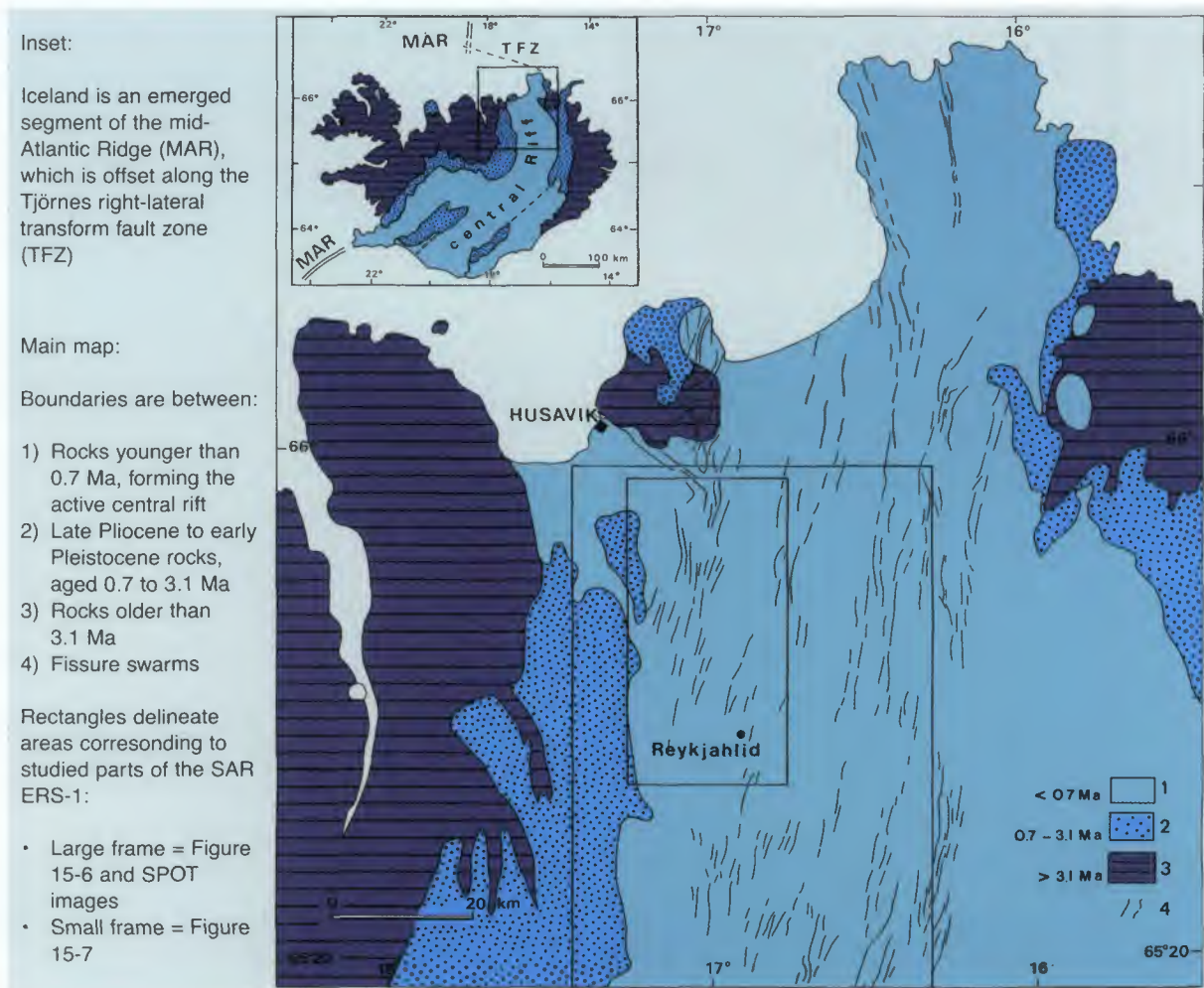


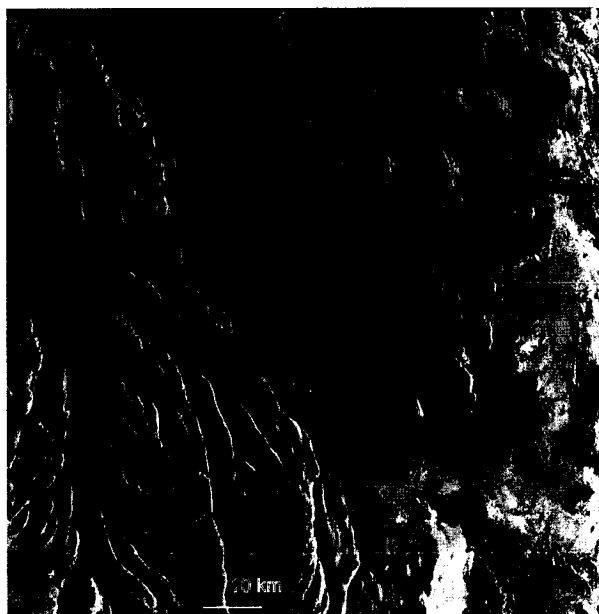
Figure 15-2: The studied area in Iceland

In the northern part of the central rift, there are parallel active fault swarms and associated volcanoes of Holocene age, forming elongated bands (volcanic systems) 50 to 100 km long and several kilometres wide [4]. Vents are often related to fissures, and even when no fissure is visible the common alignment of several vents suggests that their location is controlled by fissures or faults. Faults and volcanoes in the study area are coeval because lava flows bury faults and are also cut by more recently reactivated sections of the same fractures. This region is a reference for the understanding of tectonic emplacement of volcanic vents.

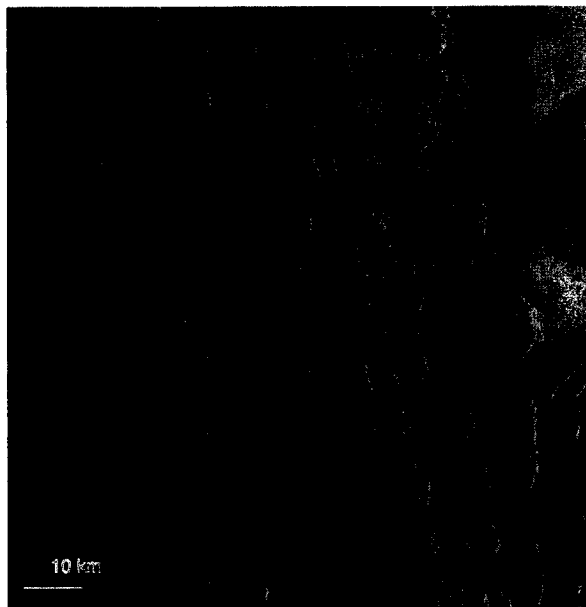
15.2 Satellite imagery analysis

15.2.1 Data

Two SAR ERS-1 scenes are used to map the tectonic and volcanic features of the Krafla fissure swarm (Figure 15-3 and Figure 15-4).



Orbit 5894, frame 2277, positive print



Orbit 5436, frame 2277, positive print

Figure 15-3: SAR ERS-1 scene of 31 August 1992

Figure 15-4: SAR ERS-1 scene of 30 July 1992

They were acquired in descending orbits. The straight white lines are artefacts due to a gap in the scene file. These two scenes partly overlap, giving the possibility to analyse key regions in stereoscopy (Figure 15-5 and Figure 15-6).

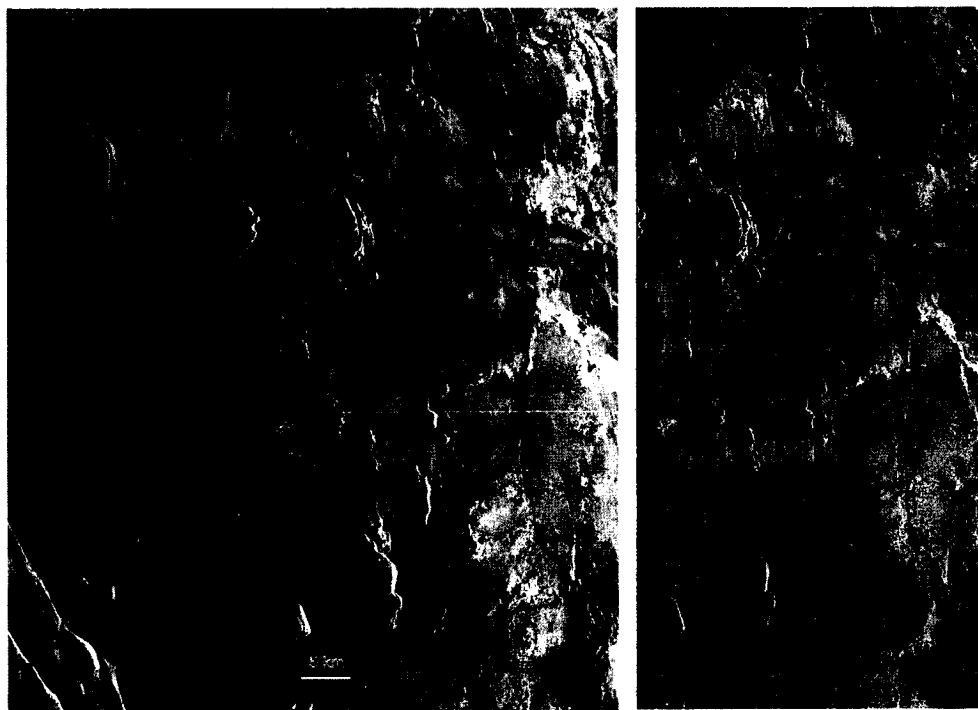


Figure 15-5:
Stereo set of SAR
ERS images

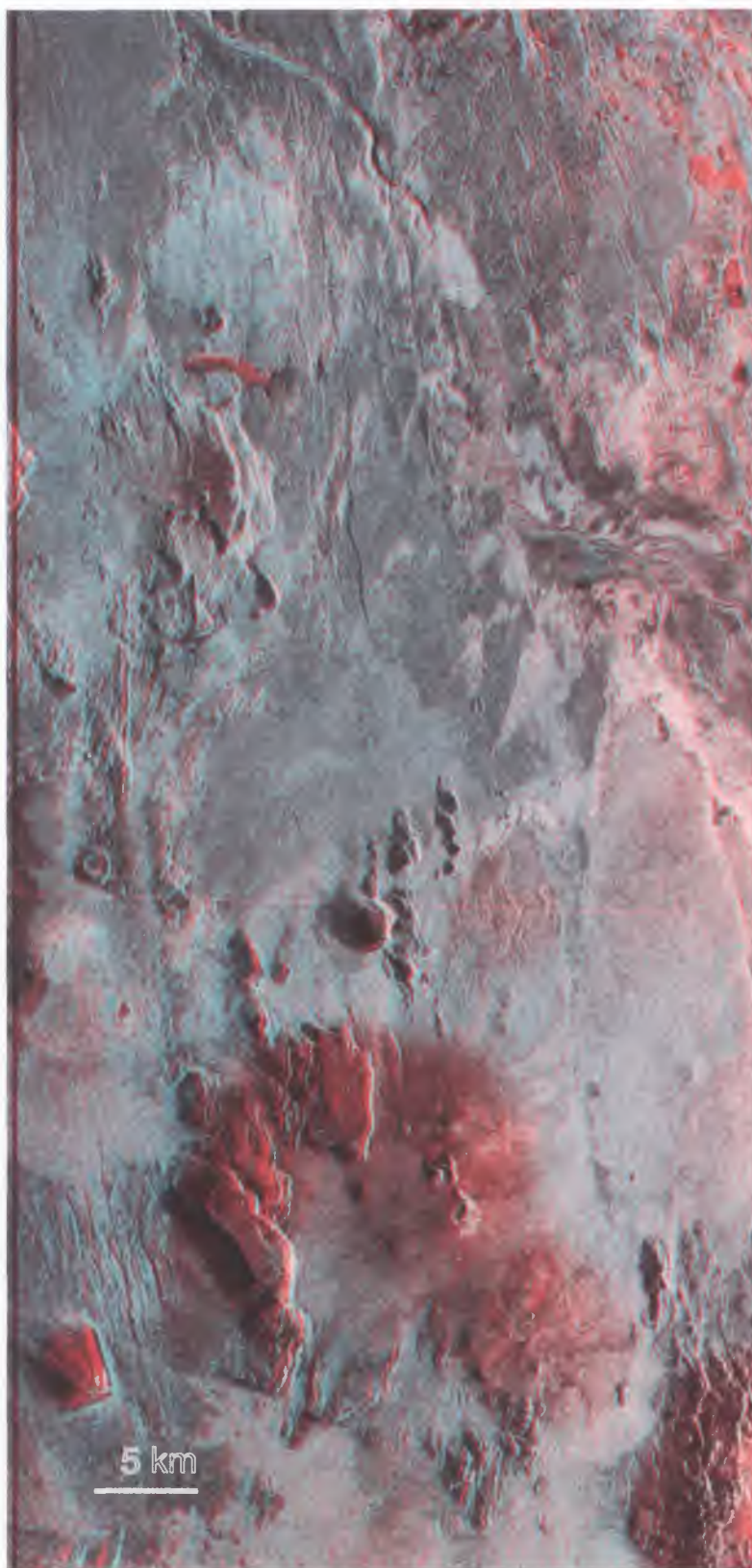


Figure 15-6:
Anaglyph image of
the stereo set of
Figure 15-5 (3-D
glasses required)

In addition, a SPOT Panchromatic scene yielding 10 m ground resolution was used. A test zone centred on the Krafla fissure swarm was extracted (Figure 15-7).



Window extracted from SPOT panchromatic scene (KJ 717-214) over the test area in Iceland (see location in Figure 15-2)



1: fracture; 2: extension fracture; 3: normal fault; 4: volcano; 5: fissure eruption

15.2.2 Distortion effects

To characterise the shape of volcanoes, the outlines of the lowermost floors of volcanic edifices (which are generally horizontal) have to be considered. To estimate the elongation of a volcano, the ratio of the largest to the smallest diameter (L/l) has to be determined. The direction of elongation of a volcano is that of the largest diameter. Fissures and faults are narrow elongated objects, for which the direction is easy to measure on a satellite image.

However, the radar acquisition system is responsible for distortion effects. Before measuring the fissure and fault direction and the elongation of volcanoes, it is necessary to assess the distortion effects for different geometric configurations. For instance, an apparent fault direction may be different from the real one, or a circular crater may be registered as an ellipse if the rim is not horizontal.

Figure 15-7:
Window from SPOT
over Iceland, and
its interpretation

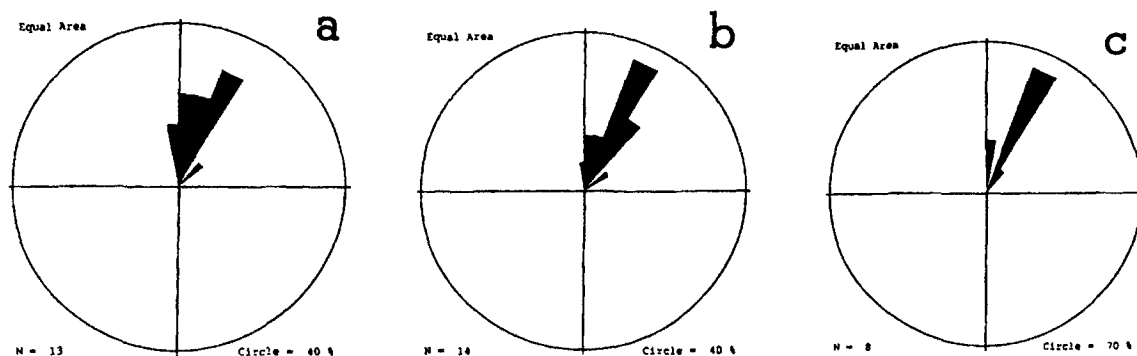
The best way to check the distortion effects in measuring directions of radar images is to study a test area where both SAR ERS-1 data (oblique view – Figure 15-3) and SPOT data (vertical view – Figure 15-7, with interpretation) are available.

Volcanoes can be more thoroughly mapped on a SPOT image, in non-cloudy areas, whereas faults are more easily sensed on the SAR ERS-1 images. 16 elongated volcanoes (ratio ≥ 1.3) are common to the two types of images.

For the SPOT panchromatic image, the point of view is near vertical and the deformation small. The directions of elongation range from N350°E to N30°E, with maximum between N20°E and N30°E (Figure 15-8a). On the SAR ERS-1 images (descending node), they range from N350°E to N40°E, with a maximum between N20 and N30°E (Figure 15-8b).

These differences between the two sets are not significantly distinct from the uncertainty of the diagrams (10°). The uncertainty in directions of elongation given for Iceland in the following section is consequently of the order of 10°.

Rose diagrams show percentages of cumulative lengths at 10° azimuth intervals relative to the total of the lengths in all directions. Each segment corresponds to a direction (or strike), and shows the percentage of the total length that is in that direction, i.e. a longer line indicates a greater percentage. For each diagram, the percentage value represented by the circle is given, and N is the number of samples.

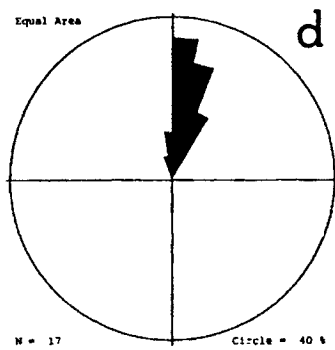


a. Directions of largest diameter for elongated volcanoes ($L/l \geq 1.3$) on SPOT Panchromatic imagery, in the common area with SAR ERS-1 imagery (descending node).

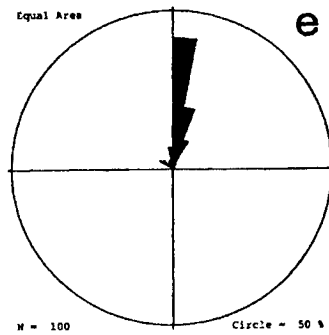
b. Apparent directions of elongation for elongated volcanoes ($L/l \geq 1.3$) on SAR ERS-1 imagery (descending node), in the common area with SPOT Panchromatic imagery.

c. Apparent strike measured on radar images of narrow grabens closing progressively at both ends and considered as extension fractures.

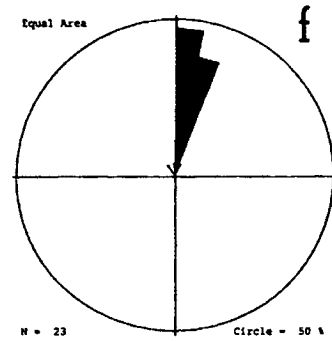
*Figure 15-8:
Statistics
concerning
structural and
volcanic features in
Iceland*



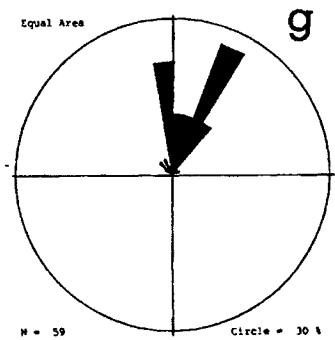
d. Apparent strike measured on radar images of narrow grabens closing abruptly at both ends.



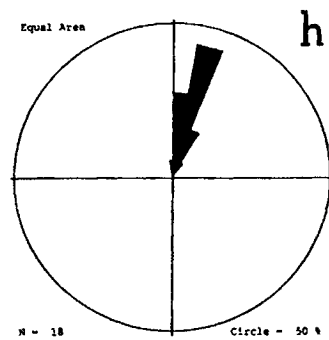
e. Apparent strike of normal faults, measured on radar images.



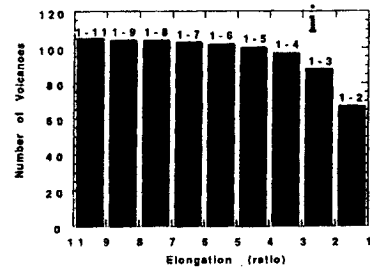
f. Trend of linear clusters, made of aligned volcanoes close to each other, measured on radar images.



g. Trend of largest diameters of elongated volcanoes (ratio between 1.3 and 3), measured on radar images.



h. Trend of fissure eruptions (ratio ≥ 3), measured on radar images.



i. Cumulative histogram of the elongation (ratio of smallest against largest diameters) of the outlines of lowermost floors of volcanic edifices.

Figure 15-8
(continued)

15.3 Tectonics

In the Holocene Krafla fissure swarm, straight scarps are related to recent faults that are very clear in the SAR ERS-1 images (Figure 15-5), and drawn in the interpretation map (Figure 15-9).

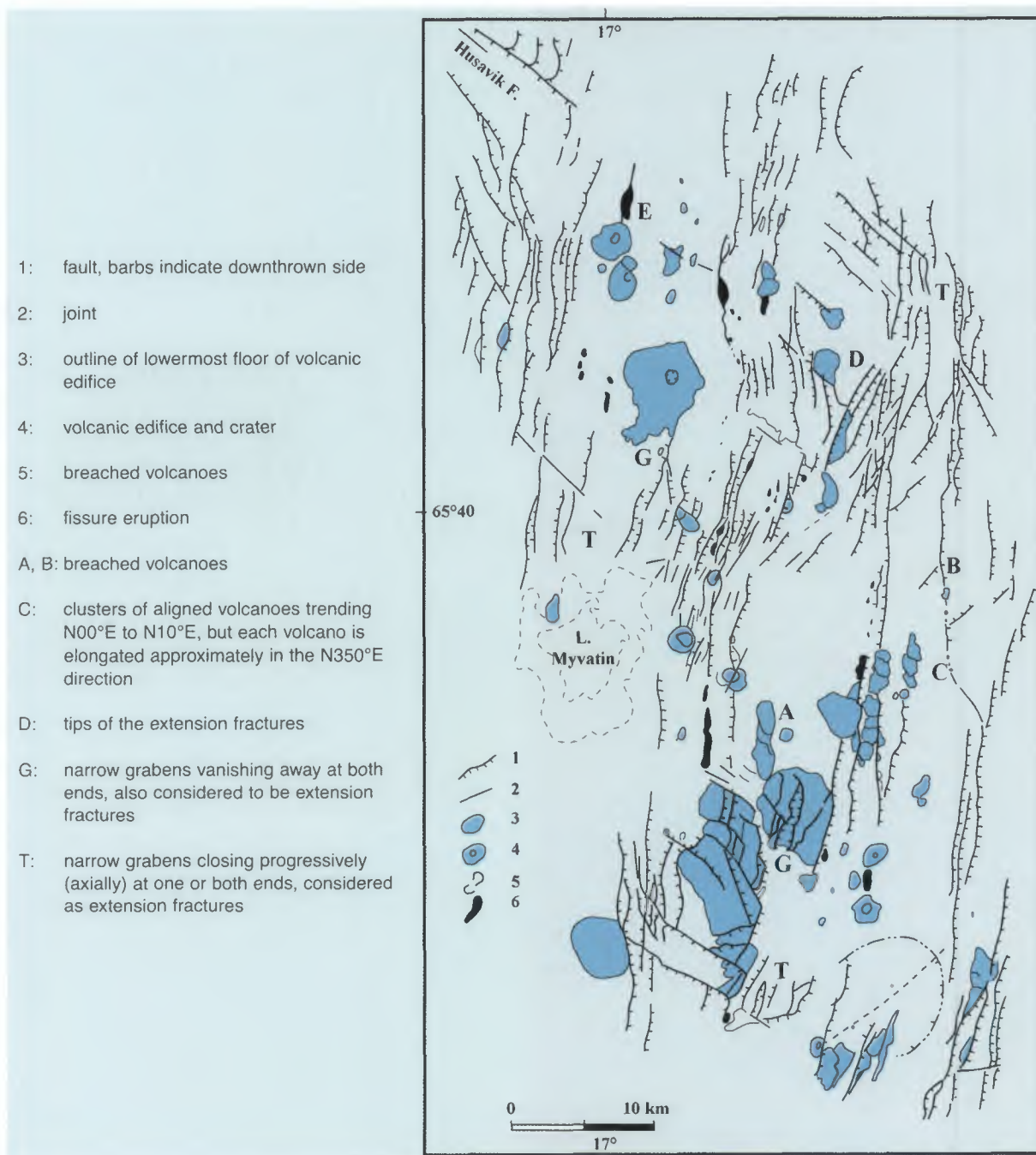


Figure 15-9:
 Interpretation of the
 right-hand image of
 Figure 15-5

Several faults face each other at a distance of 200 to 800 m, delineating narrow grabens (e.g. T in Figure 15-9) which progressively close at one or both ends and can be interpreted as extension fractures.

These extension fractures strike N00-40°E, with a maximum between N20°E and N30°E (Figure 15-8c). There are also narrow elongate grabens of similar dimensions, which end abruptly (e.g. G in Figure 15-9) and can also be regarded as formed by extension. The rose diagram of graben directions (Figure 15-8d) has the same shape as in Figure 15-8c. The rose diagram of fault directions (Figure 15-8e) is very similar to the previous ones (Figure 15-8c, d): faults have a preferred strike between N350°E and N30°E, with a maximum between N00°E and N10°E, except for faults striking about N125°E, parallel to the west-north-west striking Husavik fault (Figure 15-9), considered to belong to the Tjörnes transform fault [3]. Normal faults connected with the Husavik faults in the northeast (Figure 15-9) form drag folds, testifying to a dextral strike-slip movement component. SAR imagery also shows faults and joints striking parallel to the Husavik fault.

15.4 Volcanic vents

SAR imagery shows the spatial relationships between tectonic features and the location and shape of volcanic vents. In some places, volcanic material fills open fissures that gradually thin out along the strike and have the shape of extension fractures. The main trends of these fissure eruptions range from N350°E to N40°E, with the maximum from N10°E to N20°E (Figure 15-8h). Some variations in trend of the fissure eruptions may be locally associated with the occurrence of calderas.

Nearly all the volcanoes are located on faults or in the prolongation of faults. An important fact is that some volcanic edifices are aligned and close to each other, forming linear clusters composed of several volcanoes. This category of linear clusters includes groups of two volcanoes, which are almost adjacent to each other. Directions of linear clusters range from N350°E to N30°E with a maximum from N00°E to N20°E (Figure 15-8f).

Because volcanic edifices are commonly elongate, a cumulative histogram represents the ratio of largest to smallest diameters (Figure 15-8i). It ranges from 1 to 11, but most values are between 1 and 2. Elongation can be considered to be significant for a ratio ≥ 1.3 . In case of a ratio ≥ 3 , the edifice may be regarded as a fissure eruption. The larger diameters of elongate volcanoes trend from N350°E to N40°E, with maximum at N350-360°E and N20-30°E (Figure 15-8g).

In location **B** in Figure 15-9, three small, elongate breached volcanoes occur, located along the same fault and close to each other. Their elongation is parallel to the fault. The medial traces of the breaches are superimposed on the fault. In addition, regarding the largest volcano, at the two loci of the crater rim where the fault intersects the long axis of the crater, a breach occurs. It seems that the faults are (at least partly) responsible for the location of breaches.

15.5 Geometric relationships between tectonic features and vents

Figure 15-8 shows that fissure eruptions, clusters of aligned adjacent volcanoes and elongate volcanoes trend parallel to the narrow grabens that are considered to be extension fractures. Therefore, these volcanoes are located on extension fractures. The major axes of these vents coincide with the main extension fractures.

Analysis at a local scale provides more details on these relationships. For instance, in locations **A** and **C** in Figure 15-9, clusters of aligned volcanoes trend parallel to normal faults, i.e. N00°E to N10°E, but each volcano is elongated approximately in the N350°E direction. The linear cluster in this particular case is not an isolated extension fracture but a N00°E to N10°E-striking fault consisting of a set of en-echelon extension fractures forming elongated volcanoes. However, the tips of the extension fractures, where they are well expressed (as is the case in locations **A**, **C**, **D** and **E** in Figure 15-9) consistently trend N10°E. This is also the trend of the fissure eruptions.

In conclusion, the regional tension direction trends N100°E, at right angles to the trend of the tips of extension fractures. This result agrees with determination of extension trends from fault slip data analysis [2].

In summary, this study in Iceland, with the use of SAR ERS-1 imagery, shows that

- 1) Volcanic vents are located on extension fractures
- 2) The direction of elongation of volcanoes coincides with the strike of extension fractures
- 3) A cluster of aligned volcanoes commonly represents an extension fracture or several extension fractures aligned on a fault
- 4) The trend of extension fracture tips indicates the perpendicular local tension direction

15.6 References

- [1] J. Chorowicz, J.M. Bardintzeff, G. Rasamimanana, P. Chotin, C. Thouin and J. P. Rudant, 1997. *Tectonophysics*, **271**, 263-283.
- [2] Bergerat, F., Angelier, J. and Villemin, T., 1990. Fault systems and stress patterns on emerged oceanic ridges: a case study in Iceland. *Tectonophysics*, **179**, 183-197.
- [3] Gudmundsson, A., Brynjolfsson, S. and Jonsson, M. T., 1993. Structural analysis of a transform fault-rift zone junction in North Iceland. *Tectonophysics*, **220**, 205-221.
- [4] Saemundsson, K., 1974. Evolution of the axial rift zone in Northern Iceland and the Tjörnes fracture zone. *Geol. Soc. Am. Bull.*, **85**: 495-504.

16. Expression of morpho-structures on SAR ERS imagery – escape tectonics at a front belt

Case study: SW Irian Jaya (West Papua)

16.1 Geologic framework

The island of New Guinea is built up on a salient of the Australian continental lithosphere, forming the foreland basin (Figure 16-1).

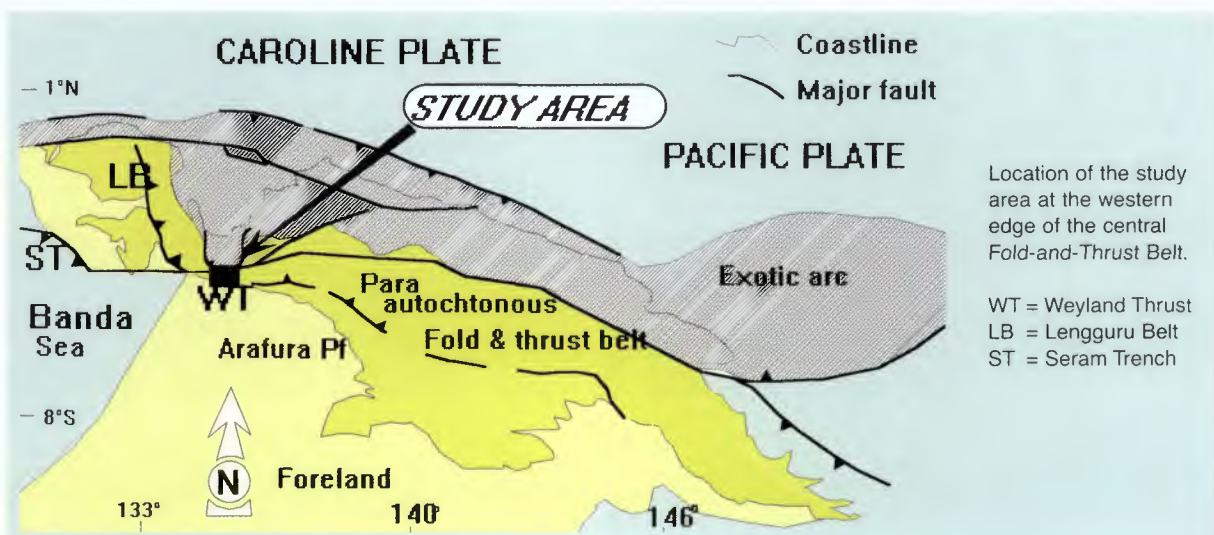


Figure 16-1: Simplified geodynamic setting of New Guinea

Two mountain ranges lie parallel to the Caroline-Pacific/Australian plate boundary. The northern one is a discontinuous alignment of exotic arc terranes belonging to the Melanesian arc. The southern one, forming the para-autochthonous fold-and-thrust belt, has been subjected to arc-continent collision since the Pliocene (6 Ma).

The front of the belt exhibits 'transported fault-anticlines' prograding south-westward in Irian Jaya, in addition to the wrench faulting.

16.2 Morphotectonics and satellite imagery analysis

The study area is practically inaccessible for field observation, being one of the last unexplored regions of the earth. The thick vegetation blankets details of the topography. The morphology is well expressed using a SAR ERS-1 image, from which an area was extracted (Figure 16-2 and Figure 16-3).

The southern flank of the westernmost Fold-and-Thrust belt of Irian Jaya.

Positive view, ascending orbit

Illumination is from the west-southwest

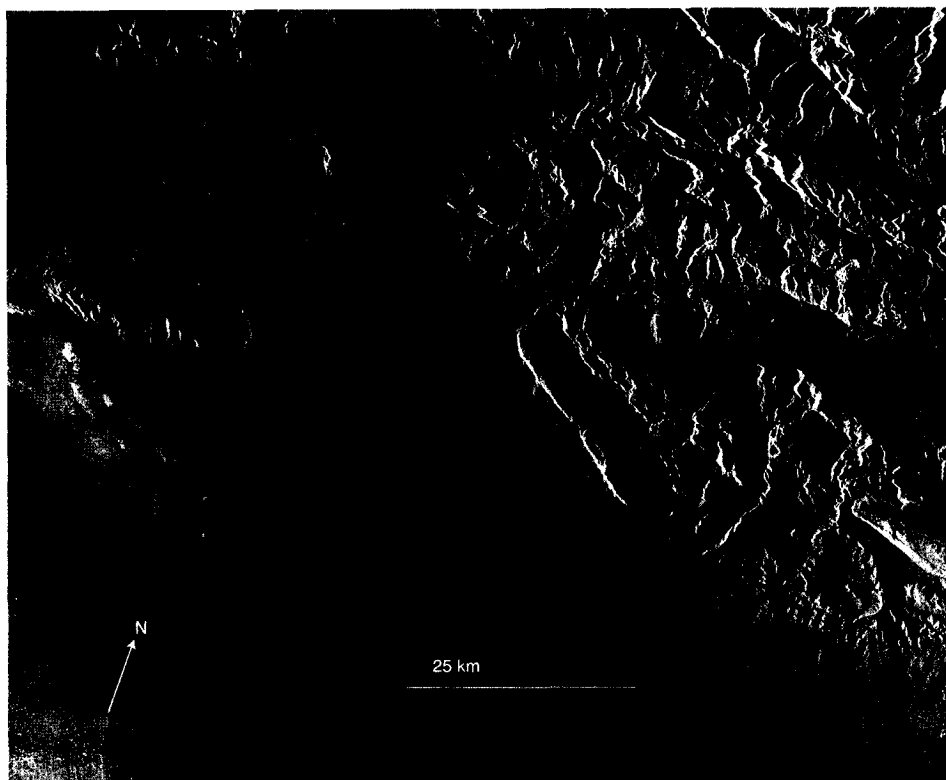
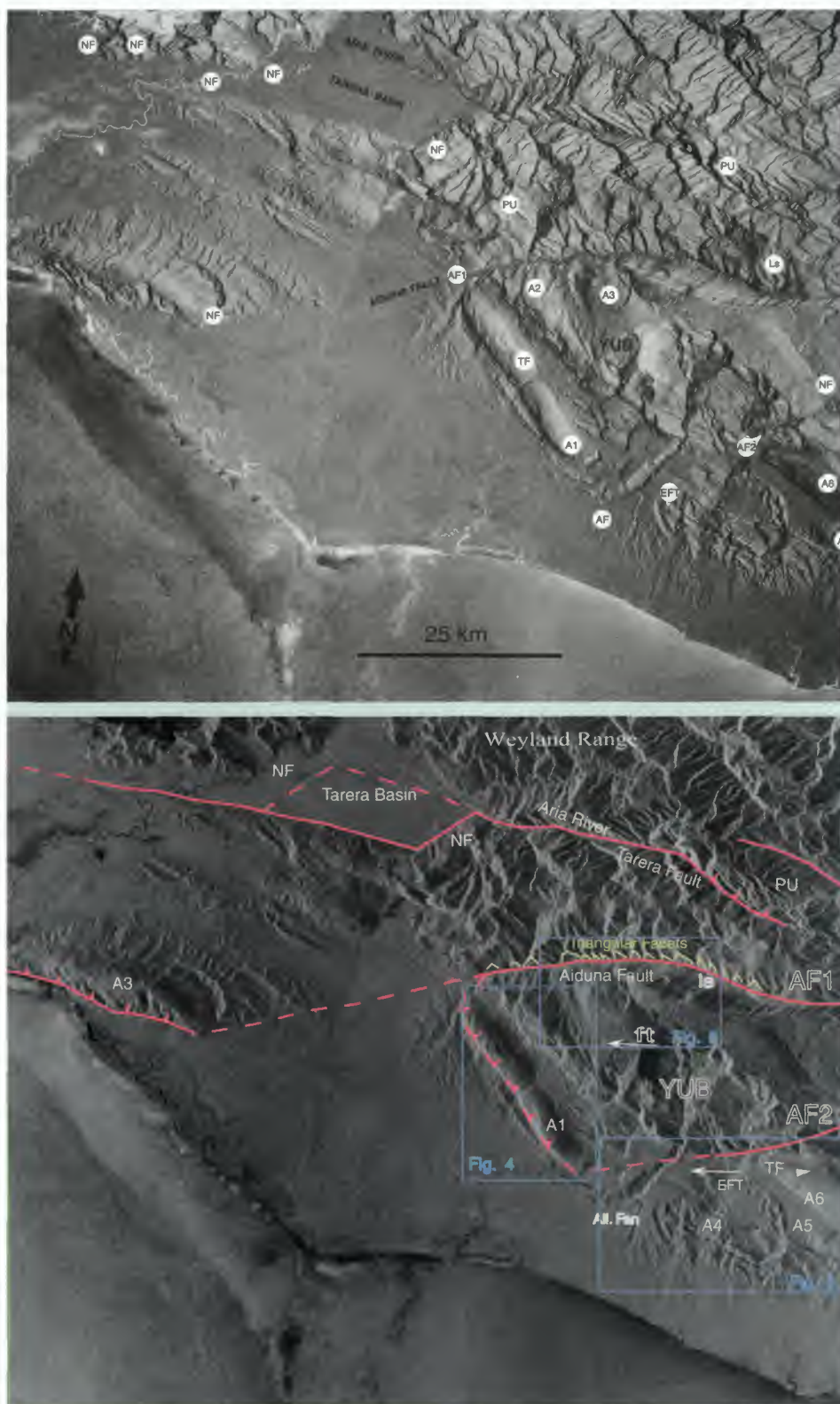


Figure 16-2: SAR ERS-1 image of Irian Jaya



a. SAR ERS-1 image
(negative view)

A1to A6 = anticlines

AF1 = aiduna Fault

AF2 = East Yera Umar
Fault

EFT = en echelon tear
faults

NF = normal fault (or
flexure east of the
image)

Ls = river

PU = push-up structure

YUB = Yera Umar Block

b. Interpretation of the
SAR ERS-1 image;
(positive view)

All. Fan = alluvial fan

Tf, ft = Tension fractures

Frames are location of
Figures 16-4 – 16-6.

Figure 16-3: Interpretation of the SAR ERS-1 image of Figure 16-2

Figure 16-3:
Interpretation of the
SAR ERS-1 image
of Figure 16-2

black in the negative image of Figure 16-3a, giving a sensation of shadowed image, illuminated from ENE.

The aim of this work is to identify and observe the structures on the radar image, and to compare their geometry with optical Landsat TM imagery. In the optical images (parts 'a' of Figure 16-4 and Figure 16-5), the same features as on the ERS-1 images could generally be observed because the sun elevation is low during acquisition. However, in the optical images the geomorphology is less distinct than in the radar imagery.

The study focuses on the major features, which brought a new interpretation of the neotectonics.

16.3 Early compression

Compression, which began around 7 Ma ago, is the dominant regime in the northern part of the area (Weyland Range, Figure 16-3b) as well as in the south in the Yera Umar block (YUB). This is the prominent geomorphic feature of the scene, exposing a smooth radar texture, which reflects the weathering-resistant Eocene to Miocene limestone.

Compression is responsible for recumbent folds and thrusting affecting N090°E-striking bedding. AF1 and AF2 acted as lateral ramps, bounding the YUB. AF1 is described as the Aiduna fault on the 1/250,000 map of Panggabean and Pigram [5]. Bedding tends to jam into the ramp wedges producing micro folds with N100°E axes, consistent with the N030°E tensional fractures (TF in Figure 16-3) observed on the ERS-1 image on top of the A6 anticline. Other tension fractures appear on the SAR ERS-1 in an eroded sector of the YUB core (ft in Figure 16-3b). There, fan-shaped extrados fractures are exposed in cross section on the cliff (eastern YUB, Figure 16-3a). N020°E and N050°E faults also occur at various places in the area. Some have been observed in the field, along the Aiduna River. Bedding disruptions, on which striations remain parallel to the bedding, correspond with pre-folding faults. This fracture pattern is commonly thought to reflect the early stage of the compression that later resulted in proper folding. Out of the two conjugate faults underlining the deformation, the radar image shows only the one that is perpendicular to the beam incidence.

The south-western flank of the YUB is an anticline (A1) that looks very steep (if not recumbent) to the south, but because of scarce dip measurements (up to 80° from [5]), a layover effect of the radar on dip estimate cannot be precluded. In other words, the incidence of the SAR toward the radar beam being 23° from the vertical, any resistant strata protruding from the surface with an actual dip over 67° may result in apparent dips away from the source. Hence, the flat irons of the Neogene rocks in the southernmost part of the image (lowlands) appear very steep or overturned to the northeast (Figure 16-4).

The images of Figure 16-4 are centred on the ramp anticline propagating toward the SW above the frontal decollement. The SAR ERS-1 image expresses well the morphology of flat lands and fine structural features such as the conjugate faults whose direction (N-S) is perpendicular to the radar beam. Extrados fractures appear along the conformal anticline axis on both images, although they are best exposed on the SAR image at various locations. Bedding traces inside the flexural basin situated northeast of the fold are evidenced on the Landsat image, whereas the thrust underlying A2 is better displayed on the SAR.

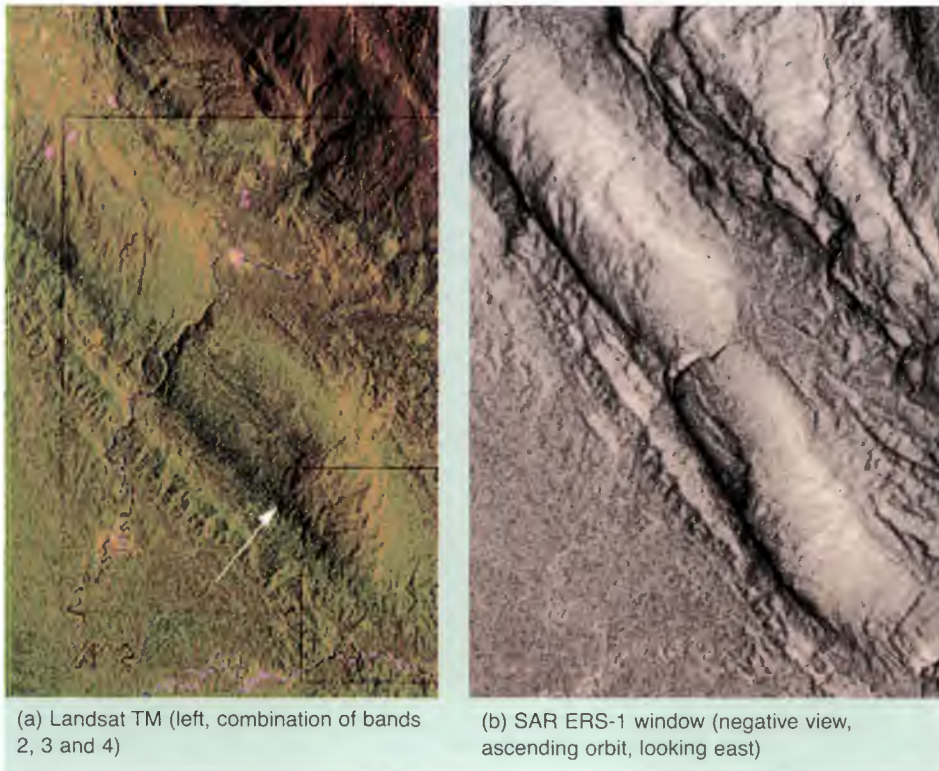


Figure 16-4:
Landsat and ERS-1
views of the SW
Yera Umar Block

The river was captured during the basin development and forced to flow through the fold, making use of a large tension gash (see also Figure 16-3b). The river is antecedent to the fold formation, thus indicating an in-sequence stacking of units. Note the differences in the apparent dips on each image along the SW fold limb (dipping SW on Landsat TM, NE on SAR-ERS).

Some of the Neogene stratas of the southern foothills are intersected and overlaid by a secondary thrust carrying the hard core of the anticline A1 (see white arrow on Figure 16-4 left). The Landsat image confirms the high angle dips, but indicates that only normal polarity is present.

The ERS SAR image shows the termination of the folds as they approach the Aiduna Fault (AF1, Figure 16-3b). Similarly, the eastern opposite pericline of the fold and the fault branches on AF2 (Figure 16-3 and Figure 16-4) further support the interpretation that AF1 and AF2 are two lateral ramps. Southeast of AF2, three other anticlines (A4, A5, A6) repeat this configuration. Field observations within the fusulins-bearing limestone and quartzite reveal pure strike-slip motion along the Aiduna fault (AF1). These are either left-lateral or right-lateral, most likely reflecting the differential displacements between the northern and the southern blocks. It was not possible to establish the relative chronology of the different horizontal striations, because they are parallel. This suggests that the faults and the anticlines are cogenetic, and represent the early motion along AF1 and AF2 acting as lateral ramps.

The SAR ERS image shows a rhomb-shaped basin filled with Quaternary sediments (Tarera Basin). This basin is limited to the south by discrete linear fault scarps. The westward extension of the fault notably guides the drainage and vanishes into the Quaternary sediments. It is also known from offshore seismic data [4]. The northern fault parallels the Aria River (Figure 16-3) to the east, but is offset by bayoneted left-stepping

N030°E fault scarps that affect the Quaternary sediments (NF on Figure 16-3b). The overall geometry indicates that this basin is in a pull-apart position along the left-lateral Tarera Fault. To the east, the linear Tarera fault extends into the mountainous area. In the eastern part of the image, it bends southward and forms a relaying fault system bounding a ridge, which is interpreted as a push-up structure (PU). The southern fault is a thrust, because it is curved and intersects the bedding traces. This structure was controlled in the field: the area exhibits vertical schistosity whose strike varies from N090°E to N115°E and is micro-folded along N110°E axes. The southern flank of the Weyland Range (Figure 16-3) shows a well preserved planar schistosity associated with overturned kink microfolds whose axial planes strike between N050°E and N070°E, intersected by E-W vertical strike-slip left-lateral shear zones.

16.4 Aiduna fault zone: wrenching followed by normal faulting

The left-lateral Aiduna Fault (AF1) has been reactivated as a normal fault as evidenced along the northern flank of the Yera-Umar block [2]. This fault zone coincides with a sharp valley (Ls in Figure 16-3; Figure 16-5).

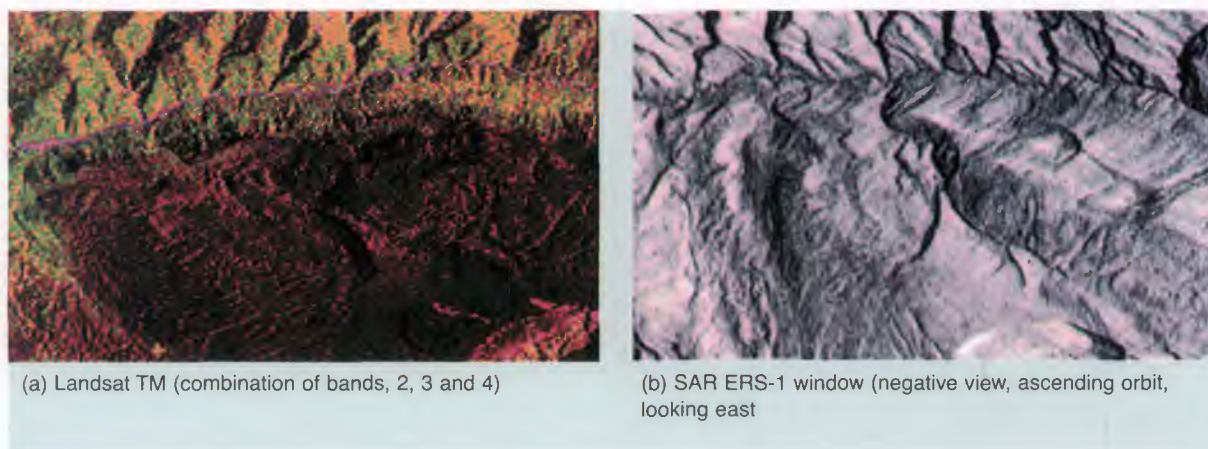


Figure 16-5:
Landsat and ERS-1
views of the Aiduna
River

The river underlines a major fault, which separates different textural domains. Fault facets on the northern flank of the N080°E valley are visible in both images, but the N110°E bedding appears only on SAR ERS-1, because it represents less prominent features (e.g. steps on the slopes) that are highlighted by the low incidence angle. N-S and NE-SW conjugate faults consistent with the compression (e.g. orthogonal to the fold axis) appear on the Landsat image, but only one direction (N-S, perpendicular to the beam) is enhanced by the SAR.

The valley is roughly parallel to the incidence of the radar beam, but tributaries emphasise south-dipping triangular facets restricted to the northern flank. Facets are generally regarded as the fault plane, not yet eroded, indicating recent activity of the fault. They are large and jointed. To the east, the Aiduna Fault is almost parallel to the bedding traces, and triangular facets cannot be distinguished from flat irons. However, field observations have shown that the N100°E to N110°E trend underlines the short limb of a south-dipping anticline, whose bedding planes are occasionally reactivated as a normal fault, post-dating the other tectonic features. In the western part, the facets

underline the fault plane dipping south. Normal faulting is underlined by the difference in erosion between the northern (eroded) and the southern (less eroded) compartments.

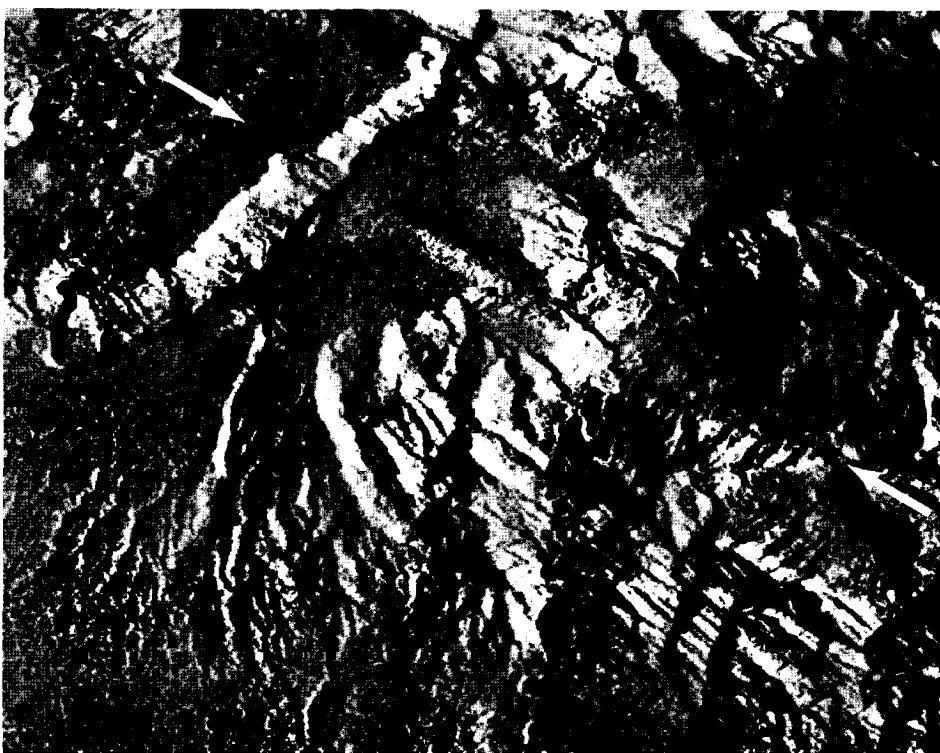
In the western coastal area, west of the image, bedding traces define an anticline (A3 in Figure 16.3) whose SE closure is truncated and thrown downward. It is likely that the vertical offset is the result of both strike-slip and normal motions along AF1, which juxtapose two different advancing segments of the flexural basins at different stages of subsidence. The fault scarp is covered by sediments, but due to low erosive potential, and the high rainfall, conclusions on its present activity are still questionable. This fault is assumed to correlate with the Aiduna fault.

16.5 Late escape tectonics

The Aiduna Fault, being a lateral ramp, principally underwent a strike-slip motion. But the ERS image has shown that the last motion occurring on this fault was normal, on the basis of the triangular facets and the Yera Umar tilt. In the Yera Umar Block (YUB), a large alluvial fan (**All. Fan** in Figure 16-3b), seals the frontal fold end and the fault AF2. The alluvial apron is divided by a series of 'en echelon' tensional faults (EFT in Figure 16-3b; Figure 16-5) compatible with left-lateral reactivation of AF2.

The alluvial apron is also flexured, with the axis being parallel to that of the early folds. This late moderate folding is probably associated with the uplift and erosion of both extremities of the frontal anticline A1. While the receding (northern) end of the YUB is undergoing extension along the Aiduna Fault, the southern edge is the locus of compression. This extensional area is also affected by a linear flexure parallel to the folds. This kind of mild topographic variation is underlined by a diffuse linear shade on the Landsat TM image.

*Figure 16-6:
Extract of a SAR-
ERS-1 image of the
fossilised, uplifted
and eroded alluvial
fan*



SAR ERS-1 window of the fossilised uplifted and eroded alluvial fan. Negative print, ascending orbit, looking east.

The two white arrows trending WNW-ESE mark an anticline back-stepping flexure (location in Figure 16-3b).

The depositional area covered by the alluvial fan underwent several stages of activity. A large thick alluvial fan (upper terrace) was uplifted and deformed (flexure) due to the formation of the frontal ramp anticline, and later eroded in its external southern part. As a result the central river appears to be antecedent and deeply encarved into the alluvial apron.

This overall pattern testifies to present day SW-verging gravitational tectonics. Early Pliocene compression is responsible for regional folds and thrusts trending N110°E (N100°E-120°E, north of Tarera fault). These folds and thrusts were controlled laterally by N070°E ramps where strike-slip motion prevailed (AF1 and AF2). Thickening and uplift was associated with the thrusting. The second event (Quaternary) is a response to the thickening and perturbation induced by the Tarera fault. The late deformation affecting the southern unit (YUB) is the result of large gravitational collapse, simultaneously producing normal faulting in the north and folding in the south. The Aiduna (AF1) fault may consequently be considered as a wrench fault evolving as a detachment fault. This uplifting belt therefore shows incipient and active denudation by gravitational collapse.

The Tarera fault is the active northern boundary of the Australian Plate [1], which represents incipient wrenching within the Fold-and-Thrust belt (Figure 16-7).

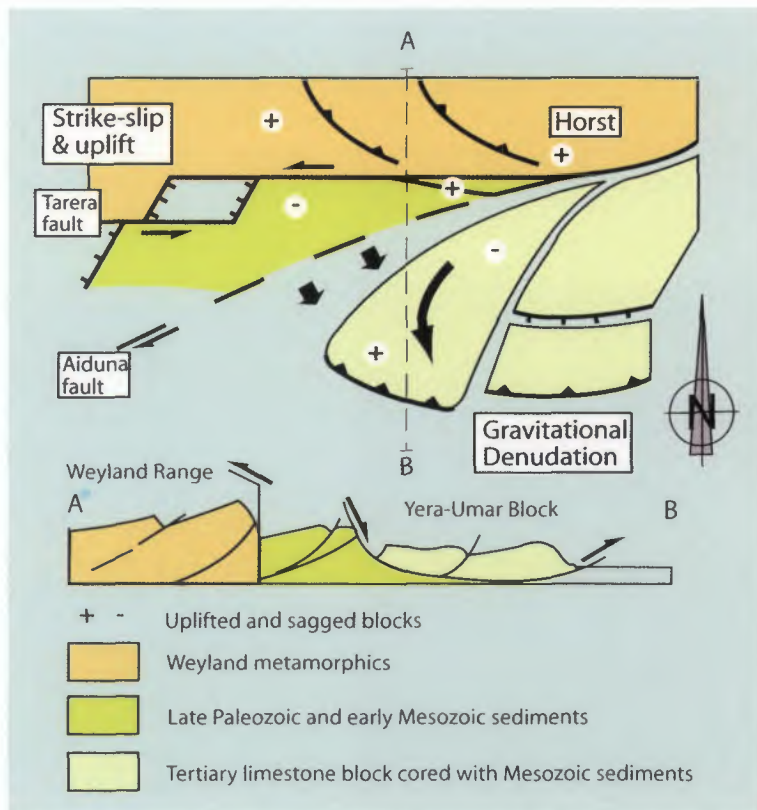


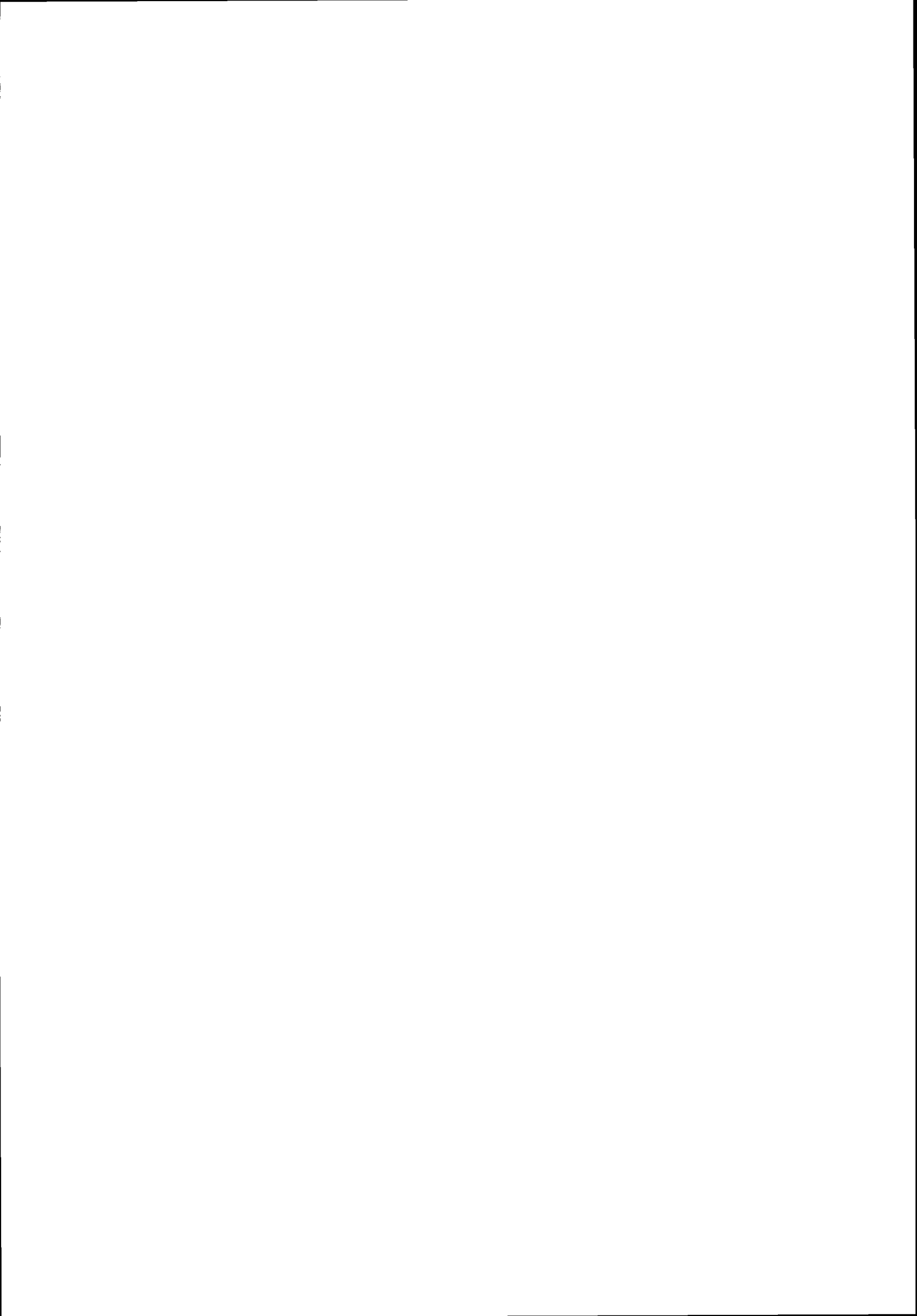
Figure 16-7: Map sketch and cross section of the post-collisional setting

North of the Tarera Fault, compression has been observed as large south-verging thrusts cutting through the Miocene Utawa diorite (the Weyland Thrust; [3]). South of the Tarera-Fault, gravitational denudation is currently beginning as a result of the mountain uplift. The regime on the northern boundary of the YUB (Aiduna Fault) is extensional whereas the front is undergoing compression and uplift, as shown by the uprising alluvial

fan carved by the river (**All. Fan** in Figure 16-3). In addition, the block protrudes from the adjacent part of the front of the range. Thus, the newly-born Tarera fault may represent a major strain boundary, north of which the compression is still acting. Advancing flat-and-ramp tectonics of the early stage may be responsible for this geometry. However, the sagging of the northern part, combined with compression in the south at the leading edge of the block, rather suggests a denudation of the block by collapse and tilting within an extensive regime. Gravity alone is sufficient to explain the normal faulting at the receding side of the YUB, as part of late orogenic radial thrusting over the edge of a collapsing basin.

16.6 References

- [1] Pubellier M., Deffontaines B., Chorowicz J., Rudant J.P. and Permana H. 1999. Active denudation morphostructures from SAR ERS-1 images (SW Irian Jaya) *Int. J. Remote Sensing*, 1999, **20**, n°4, pp.789-800
- [2] Abers G. and MacCaffrey R. 1988, Active deformation in the New Guinea Fold and Thrust Belt, seismological evidence for strike-slip faulting and basement involved thrusting. *Journal of Geophysical Research* v. **93**, B11, p. 13,332-13,354.
- [3] Chorowicz, J., Deffontaines, B., Huaman, D., Pubellier, M., Rudant, J.P., 1994, Geomorphic objects detected by ERS-1 images in different geodynamic contexts. *Proc. second ERS-1 symposium - Space at Service of our Environment*, p. 923-929, Bonn
- [4] Dow D.B., Robinson G.P., Hartono U. and Ratman N., 1988. *Geology of Irian Jaya, GRDC & BMR Cooperation, Preliminary Geological Report*, 373 p. (unpublished)
- [5] Jongsma D., Huson W., Woodside J.M., Suparka S., Sumantri T., & Barber A.J., 1989, Bathymetry and Geophysics of the Snellius II triple junction and tentative seismic stratigraphy and neotectonics of the Northern Aru Trough. 1989., *Netherlands Journal of Sea Research* v. **24** (2/3), p. 231-250.
- [6] Panggabean, H, and Pigram C.J., 1989. Geologic map of the Waghete, scale 1:250,000, *GRDC Systematic Geological Map Indonesia*. Bandung



17. Texture analysis for geological mapping in tropical Africa

Case study: Côte d'Ivoire

Geological mapping in tropical areas, particularly in Africa, is still incomplete and imprecise, in spite of the existence of reconnaissance geological maps at 1/150,000. This is due to the scarcity of outcrops and thick lateritic soil that render the traditional fieldwork difficult.

Côte d'Ivoire is a typical tropical country with important mineral resources, needing extensive geological mapping. Satellite images, generally Landsat and SPOT, have already been used in this area (e.g. [2]).

17.1 Regional geological context

The Côte d'Ivoire area (Figure 17-1) is part of the 'Dorsale of Man', which comprises two main units separated by the Sassandra fault zone. The square shows the test zone.

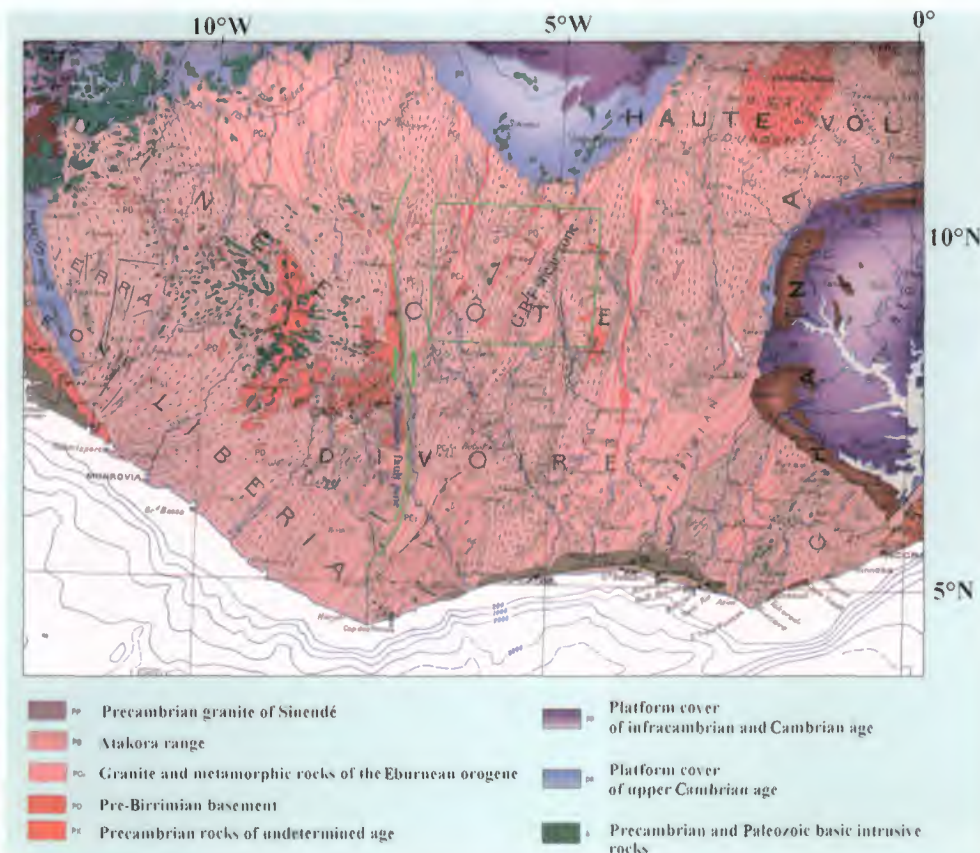


Figure 17-1:
Geological framework of Côte d'Ivoire study

To the west, the Kenema-Man unit belongs to the Catarchean (older than 2,900 Ma), ending at the Leonian orogenesis, and to the Archaean (2,900-2,400 Ma) ending at the Liberian orogenesis. It is primarily made up of gneiss, tonalite, charnockite, amphibolopyroxenite, migmatitic gneiss and quartzite.

To the east, the Baoule-Mossi unit, affected by low-grade metamorphism, is of Palaeoproterozoic age (2,400-1,600 Ma), ending at the Eburnean orogenesis. It comprises:

- (1) Birimian sedimentary and volcanic rocks
- (2) Tarkwaian fluvio-deltaic rocks
- (3) granitic rocks [4]

17.2 Local geomorphological context

The test-zone of Ferkessedougou (Figure 17-1 and Figure 17-2) is located in the north of Côte d'Ivoire and belongs to the Baoule-Mossi unit.

The tropical climate of wet Sudan type, with two contrasted seasons, has favoured savannah-forest and gallery-forest vegetation. This environment has developed on the Precambrian basement, a peneplain (elevation 300 to 400 m) with hills due to differential erosion. Rocks such as granite form inselbergs, whereas layered rocks are generally found in plains. The basement is almost entirely covered by more than 10 m of hardened, ferralitic lateritic soil, with high clay content.

The Palaeoproterozoic lithologic succession is given in the legend of Figure 17-1 (from reconnaissance geological mapping of [1], Couture (1968) and [6]). The major structural features are N025°E-striking strike-slip faults.

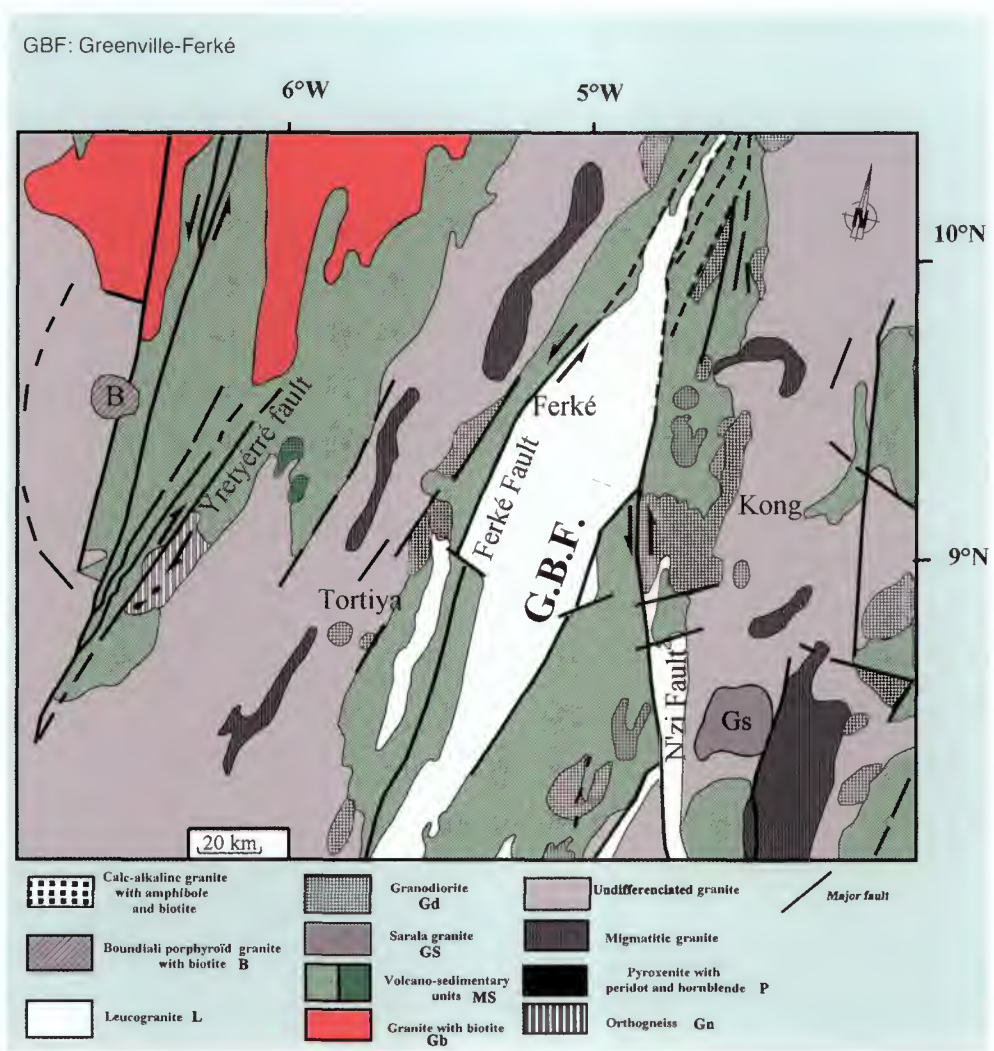


Figure 17-2:
Synthetic geological map of the Côte d'Ivoire region studied

17.3 Method of analysis

Two SAR ERS scenes were used, acquired in ascending nodes, looking ENE (Fig. 17-3).

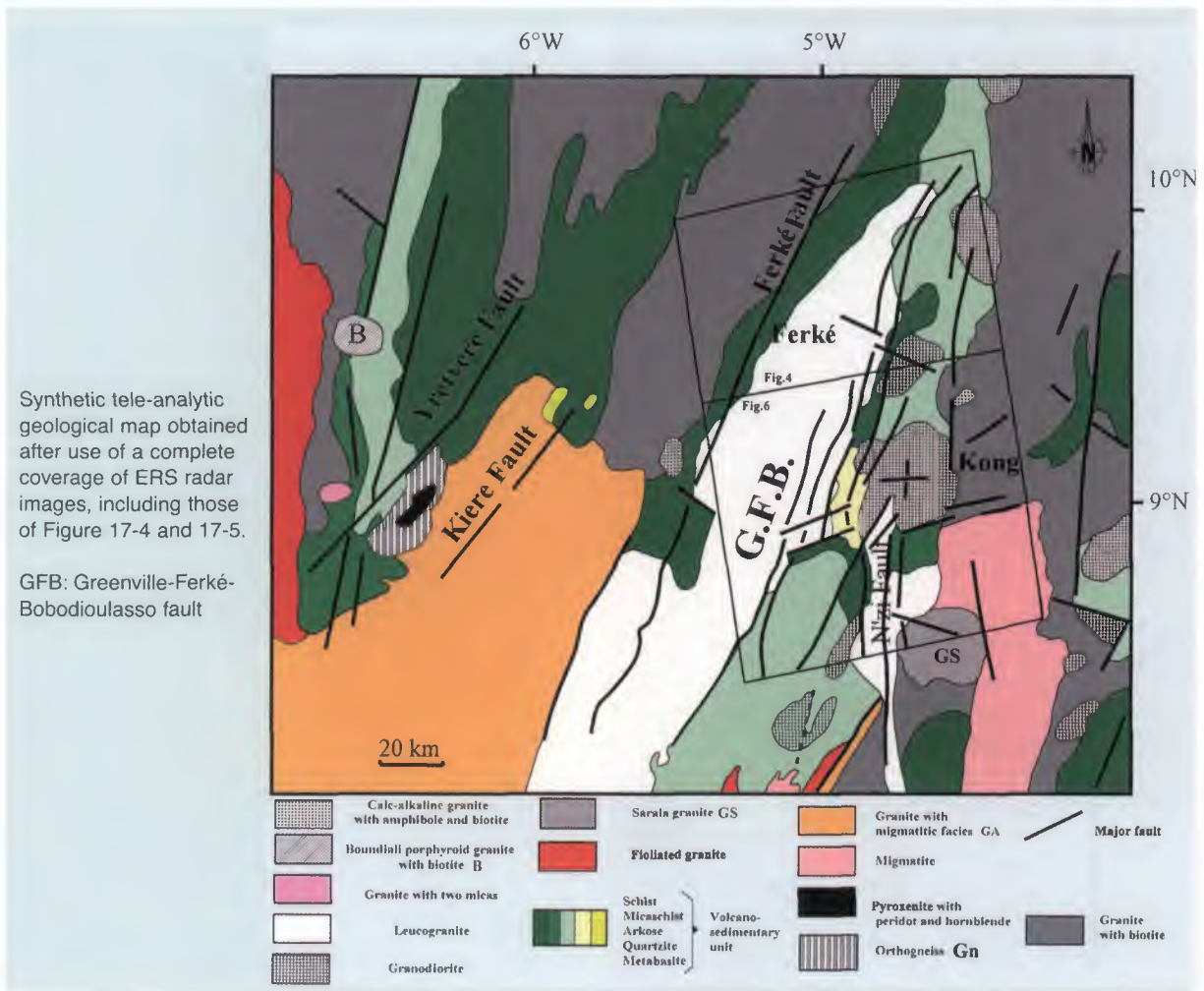


Figure 17-3: Synthetic tele-analytic geological map

The radar images were produced as negative prints by simple inversion of the values, followed by stretching. Negative images provide a more natural vision of the landscape, with a view similar to that of shadowed surfaces. The forest galleries, of strong roughness and thus bright, appear in black. Rivers and lakes (smooth surfaces) are light grey.

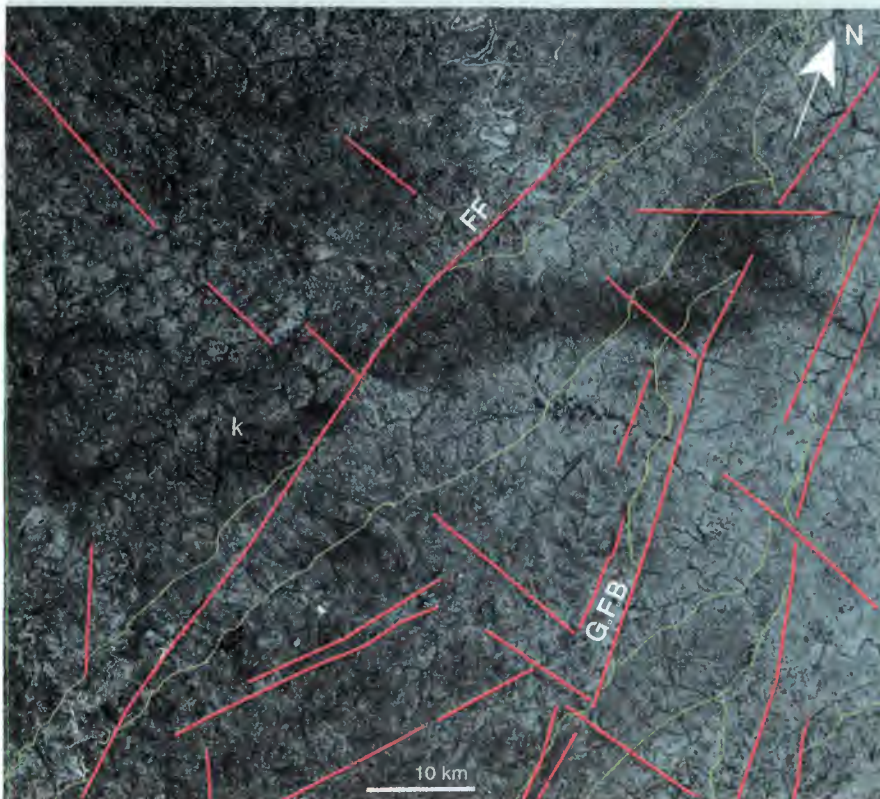
In images of tropical areas, identification of the geological objects takes into account features that result from actions of climate, erosion and vegetation on the geological basement. Information is thus given by the analysis of grey levels, textures, shapes and context. In peneplains covered with lateritic soil, the geological objects are better expressed on the radar images by the macro-texture that is mainly correlated with the drainage network.

In Côte d'Ivoire, grey level variations in the radar images may correspond to particular vegetation, which is related to the lithology, but also to climatic conditions or human activity. For example, Figure 17-4 shows, in the centre of the radar image, an E-W-trending elongate dark surface almost 12 km in width. In this negative image, dark means high backscatter.



a. Negative image window extract (Northern Côte d'Ivoire, see location in Figure 17-3).

Ascending node, orbit 12342, frame 189, date 24/11/93.



b. Image with key information

FF: Ferkessedougou fault

GFB: Greenville-Ferké-Bobodioulasso fault

k: ancient fault

Figure 17-4: SAR ERS scene of Ferkessedougou-Ouangolodougou region

This area includes several types of macro-textures. According to the existing geological maps ([1], [6]), there is no particular lithological unit at this place. Strong backscatter corresponds to the classified forest of Silue.

The method of analysis is simple visual interpretation. A first study was done initially at small scale in order to observe the objects of regional dimensions (e.g. large faults). Construction of mosaics allowed a synoptic vision that facilitates analysis at very small scale. Enlargements were then made in order to observe the details. The objects that are mapped comprise:

- Lithologic traces
- Boundaries of image-facies principally based on the macro-texture
- Discontinuities due to faults

Table 17-1:
Characteristics of
major image-facies
in the
Ferkessedougou
area

The maps obtained are systematically compared with the existing cartographic data. They are afterwards completed with field observations, especially in order to know the geological nature of the objects.

Image facies	Characteristics		
	Grey levels (negative prints)	Texture	Lithology
Gb	Generally grey to light grey with stripes and dark spots	Thin dark lines forming circular structures of approximately 2.5 km radius, and dark spots. Dendritic drainage network comprising narrower talwegs spaced 2.5 km (granite of Ouangolodougou, Figures 17-3 and 17-5). Thick and dark lines, underlined by a dendritic to rectangular drainage network, comprising broad (eroded) segments spaced approximately 2.5 km; these features are influenced by the fracturing. The lines form parallelepipeds delimiting light homogeneous surfaces, with locally some fuzzy spots (Figures 17-6 and 17-7).	Granite with biotite, locally with migmatitic facies
MS	Variable, generally dark in the schist and micaschist and light grey in arkoses, or dark with light spots; light colour in the metabasites	Sub-parallel rather thin dark lines delimiting areas of diameter approximately 2.5 km. The drainage network is sub-parallel trending NNE, with SSW trending segments spaced approximately 1.5 km in schist and micaschist. Rectangular in arkoses. The metabasite is characterised by a generally elongate shape, and forms inselbergs (Figures 17-5 and 17-7).	Volcano-sedimentary unit
Gd	Generally clear to light grey	Thin lines delimiting round surfaces approximately 2 km in diameter. Dendritic drainage network spaced approximately 2 km (Figures 17-3 and 17-5, 17-6 and 17-7).	Granodiorite
GS	Dark with clearer stripes	Rather clear broad lines, sometimes curved, bounding dark elongate or round areas. Dendritic drainage network with tight talwegs spaced less than one km (Figures 17-6 and 17-7).	Granite of Sarala
L	Light grey with dark bands	Dark thin lines forming circular structures. Dendritic drainage network with talwegs, less eroded and spaced approximately 2 km (Figure 17-6 and Figure 17-7)	Leucogranite with two micas

17.4 Lithologic mapping

The satellite image appearances corresponding to the different lithological units of Figure 17-2 are described in Table 17-1 on the previous page. They can be seen in Figures 17-4 and 17-5, or Figures 17-6 and 17-7, as appropriate.

17.5 New mapping of the granites

Radar imagery enables new distinctions in the granitic areas. The granites of Ouangolo (Figure 17-5) and Kong (Figure 17-7) present different image-facies, characterised for instance by the grey levels, the size and density of the drain channels and circular lines. These image-facies correspond in fact to slightly different granites.

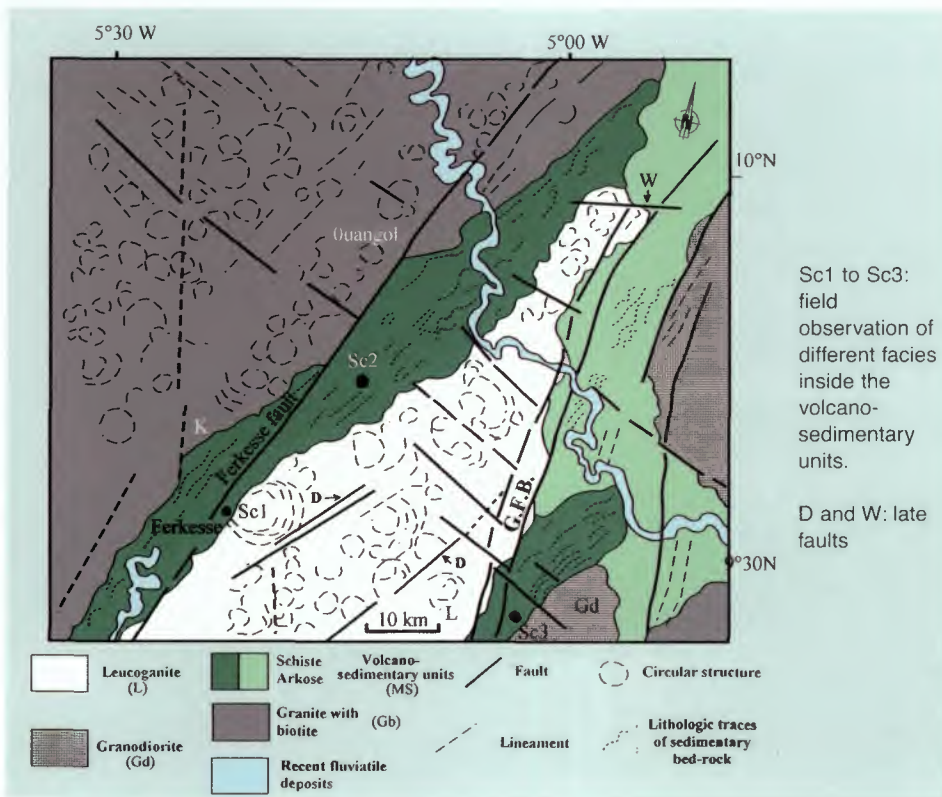


Figure 17-5: Tele-analytic geological map from SAR ERS image of Figure 17-4

Granodiorite intrusions are generally already known, but their contours on the radar images are different as compared with the geological maps of reference. For example, it is possible to considerably reinterpret the contours of the granodiorite in the centre of the image of Figure 17-6. A dark and continuous curved band marking its boundary, 2.5 km in width, can be interpreted as a metamorphic aureole.

A: Negative image window extracted from SAR ERS scene of Tafiré region

Northern Côte-d'Ivoire, see location in Figure 17-1 and 17-3.

Ascending node, orbit 12342, frame: 171, date: 24/11/93



B: A with interpretation.

N.F.: N'Zi fault

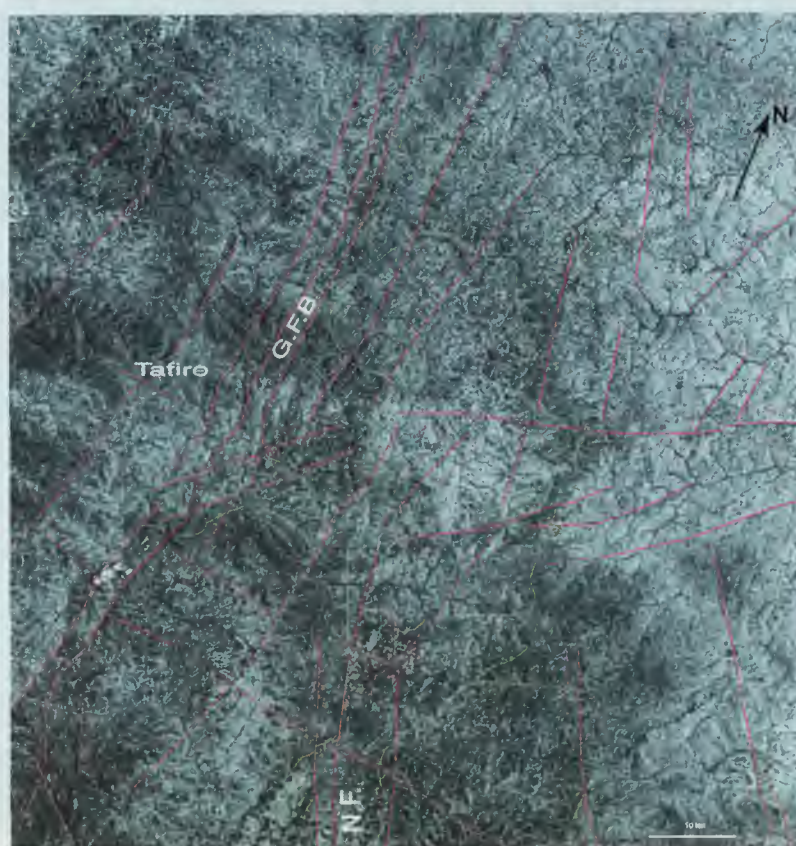


Figure 17-6:
SAR ERS scene
of Tafiré region

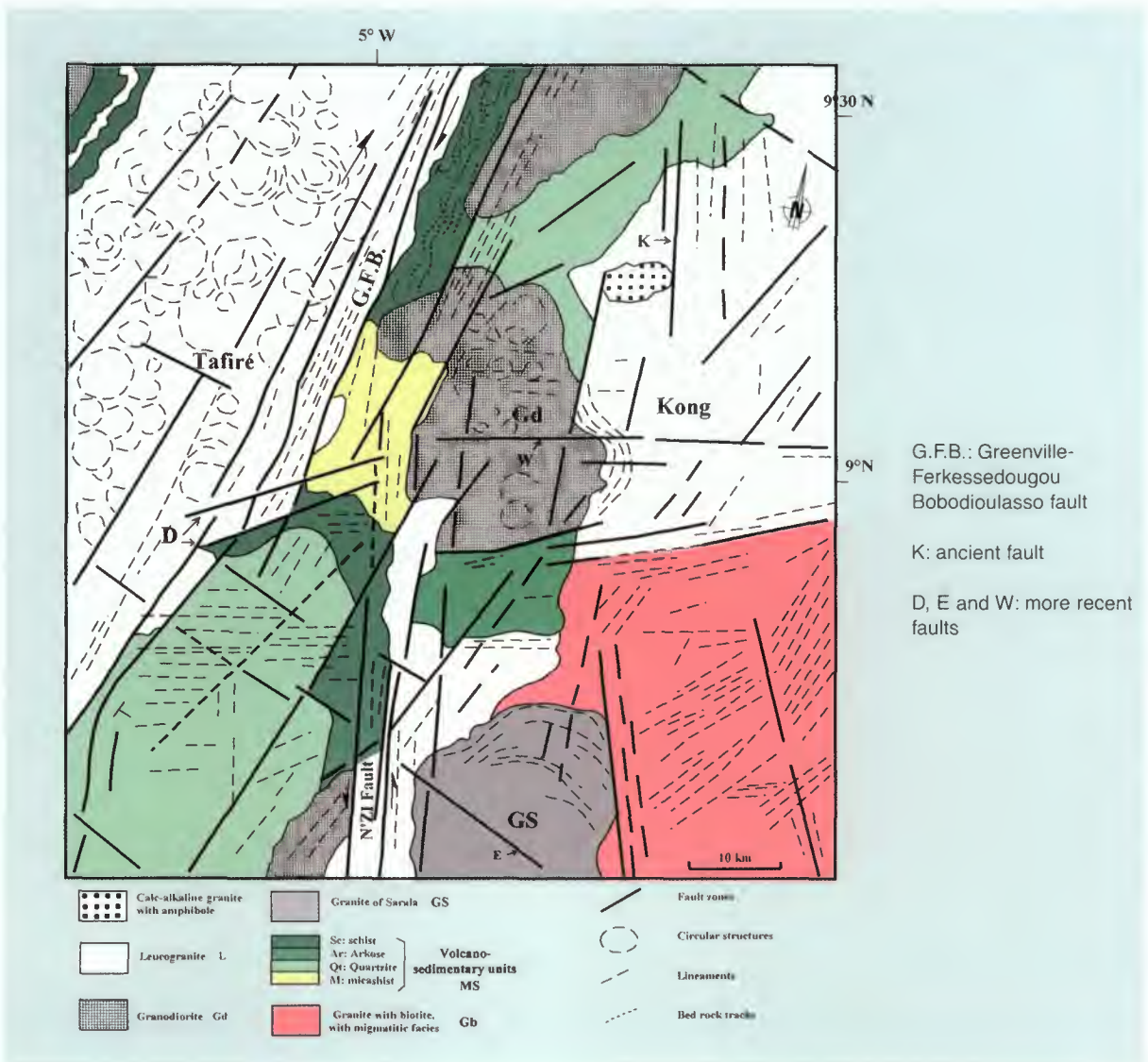


Figure 17-7: Tele-analytic geological map obtained from SAR ERS image of Figure 17-6

17.5.1 Circular structures inside the leucogranite

The aluminous-potassic leucogranite batholite (L), elongated NNE, lies along the ductile Greenville-Ferkessedougou-Bobodioulasso (G.F.B.) shear zone (Figure 17-3). It was emplaced at 2,096 Ga [3]. Two principal models were proposed to explain the intrusion of this batholite:

- 1) Post-orogenic intrusion in collisional context [7]
- 2) Intrusion favoured by tectonic friction, causing heating, due to motion along lithospheric scale faults [3]

A better mapping of the massif, using radar and field data, has allowed examination of its internal structure and analysis of relationships with the ductile fault zones. It is confirmed that the massif is made of many circular structures, either concentric or in half-circles, generally more than 3 km in diameter. These structures are interpreted as being overlapping successive intrusions of granitic magma. Heterogeneity of the

leucogranite in the field supports this interpretation. Depending on outcrops, the granite presents a pegmatitic facies or is fine grained.

17.6 Distinction within the volcano-sedimentary series

The volcano-sedimentary series were already mapped (Figure 17-2) ([1], [5]) but without distinction of different lithological facies. The imagery makes it possible to define four image-facies corresponding to different lithological units (Figure 17-5 and Figure 17-7). These image-facies have morphological and textural aspects that indicate schist, micaschist, arkose and quartzite. This has been confirmed in the field, for example in sites Sc1, Sc2 and Sc3 (Figure 17-5).

17.7 Mapping of known ductile faults

ERS imagery allows the observation and more precise mapping of the already known ductile fault zones such as N'zi, Greenville-Ferkessedougou-Bobodoulasso (G.F.B), Ferké and Yretyéré (Figure 17-2 and Figure 17-3). They are underlined by discontinuous en echelon parallel lines and by dark tones (negative views), or by the alignment of rivers.

The NS-striking N'zi fault zone (NF) is well exposed on the radar image of Figure 17-6. It is sinistral [5]. It cuts the western edge of the Sarala granite and, in the north, it is cut by the NNE-striking G.F.B. fault zone.

The NNE-striking G.F.B. fault swarm was characterised as being a sinistral transcurrent fault [5]. This fault zone is clearly visible in the studied area (Figure 17-4 and Figure 17-6). In the area of Tafiré (Figure 17-7), it comprises a right-stepping en echelon fault system, characterising sinistral slip motion.

The NNE-striking Ferkessedougou fault (FF) was considered to form the western boundary of the leucogranite massif (Figure 17-2). Using the synoptic view offered by the radar images, it is possible to propose a modification of its mapping (Figure 17-5). It is well exposed on the radar images, and parallels the G.F.B. fault. As is the case for the G.F.B. fault, it cuts the leucogranitic massif as well as the volcano-sedimentary formations and granites. It seems to left-laterally shift the volcano-sedimentary series, and thus does not mark the western boundary of the leucogranite (Figure 17-5). This indicates that the G.F.B. shear zone was active after intrusion of the leucogranite. Faults due to lithospheric tension may have controlled the genesis of the leucogranite during formation of a basin. The Ferkesse Fault (FF) may have subsequently cut it and the G.F.B. faults as well, during closure of the basin, in a transpressive context.

17.8 New mapping of faults

Faults that were charted for the first time (families D, E, K and W, in Figure 17-5 and Figure 17-7) are underlined on the radar image by thin, discontinuous, broken lines. The D, E and W sets, respectively striking NE, NW and E, are the latest fractures affecting the area, for they cut all the other faults previously described. The K set, striking north, seems more ancient.

17.9 Conclusions

The previously existing geological maps have been improved. This has been achieved by using the radar images, because priority has been given to analysis of the macro-texture, which is mainly related to the different organisations of the drainage network.

17.10 References

- [1] Arnould, M., 1963. Carte géologique de reconnaissance à 1/500.000. Feuille Katiola. *Dir. Mines Géol.* Côte-d'Ivoire, Abidjan.
- [2] Deroin, J. P., Delor, Cl., Siméon, Y. et Yao, B., 1995. Contribution of remote sensing and other techniques to the geodynamic setting of the Palaeoproterozoic in Ivory Coast (West Africa): comparison to field data. *Géodynamique du Paléoprotérozoïque*, Orléans, 17 novembre 1995, séance spécialisée de la société géologique de France.
- [3] Doumbia, S., Pouclet, A., Kouamélan, A.N., Peucat, J., Vidal, M. and Delor, C., 1998. Petrogenesis of juvenile-type Birimian granitoids of Central Côte-d'Ivoire (West Africa): geochemistry and geochronology. *Precambrian Research*, **87**, 33-63.
- [4] Feybesse, J. L. and Milési, J. P., 1994. The Archaean/Proterozoic contact zone in West Africa: a mountain belt of decollement, thrusting and folding on a continental margin related to 2.1 Ga. convergence of Archaean cratons. *Precambrian Research*, **69**, 199-227.
- [5] Lemoine, S., 1990. Le faisceau d'accidents Greenville-Ferkessedougou-Bobodioulasso (Libéria, Côte-d'Ivoire, Burkina-Faso) témoin d'une collision oblique éburnéenne *15ème Colloq. Géol. Afr.*, 10/13 septembre 1990. Publication occasionnelle CIFEG, 20, 29.
- [6] Milési, J. P., Ledru, P., Feybesse, J. L., Dommange, A., Ouedraogo, M. F., Marcoux, E., Prost, A. E., Vinchon, C., Sylvain, J. P., Johan, V., Tegye, M., Calvez, J. Y. et Lagny, Ph., 1989. Les minéralisations aurifères de l'Afrique de l'Ouest. Leurs relations avec l'évolution lithostructurale au Protérozoïque inférieur. *Chron. Rech. Min.*, **497**, 3-98.
- [7] Yobou, R., 1993. Pétrographie des granitoïdes du Protérozoïque inférieur du Centre-Nord de la Côte-d'Ivoire (Ferkessedougou-Marabadiassa). *Evolution magmatique et contexte géodynamique*. Thèse de doctorat, Université de Paris-sud, centre d'Orsay, 294p.

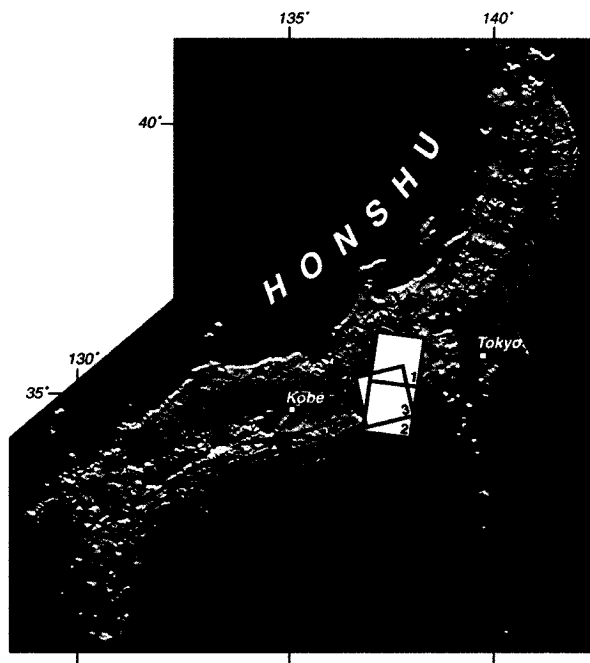


18. Detection of active compressional structures on SAR ERS imagery

Case study: the Central Japan seismic area

18.1 Structural framework

The Hyogo-Ken Nanbu earthquake on 17 January 1995 and the Great Kanto earthquake on 1 September 1923, both in Japan, attracted attention because of the serious damage that occurred in the Kobe and Tokyo urban areas respectively ([1], [2], Figure 18-1).



The frames are boundaries of the SAR ERS-1 scenes, Figures 18-3, 18-4 and 18-5.

Scenes 1, 2 and 3 have respectively the orbit-frames 3955-2899, 3955-2907, 7913-693.

Figure 18-1: DEM of Japan and location of the studied area

Seismic activity in Japan results from the convergence of the Pacific, Philippine and Eurasian plates, intersecting along three zones of subduction (Figure 18-2). The overall geometry induces both compression and strike-slip tectonics due to shear partitioning.

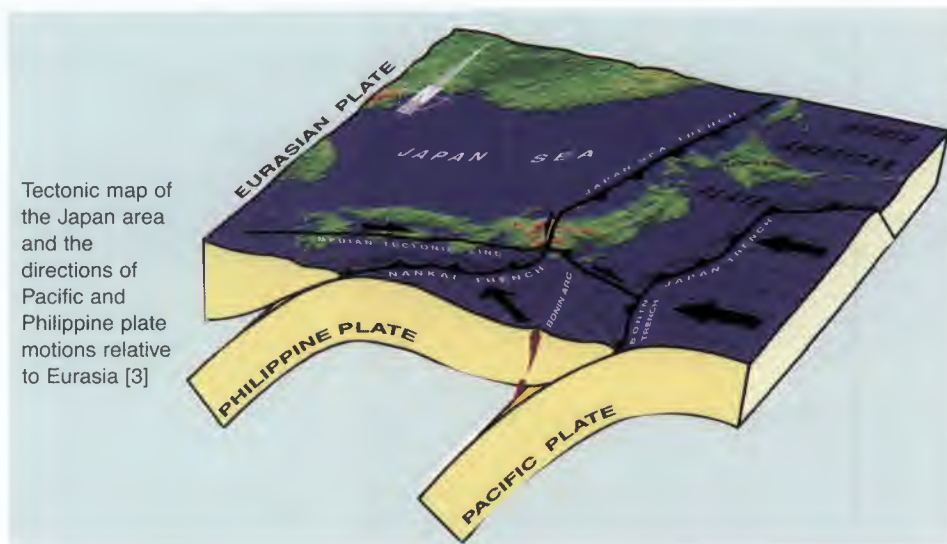
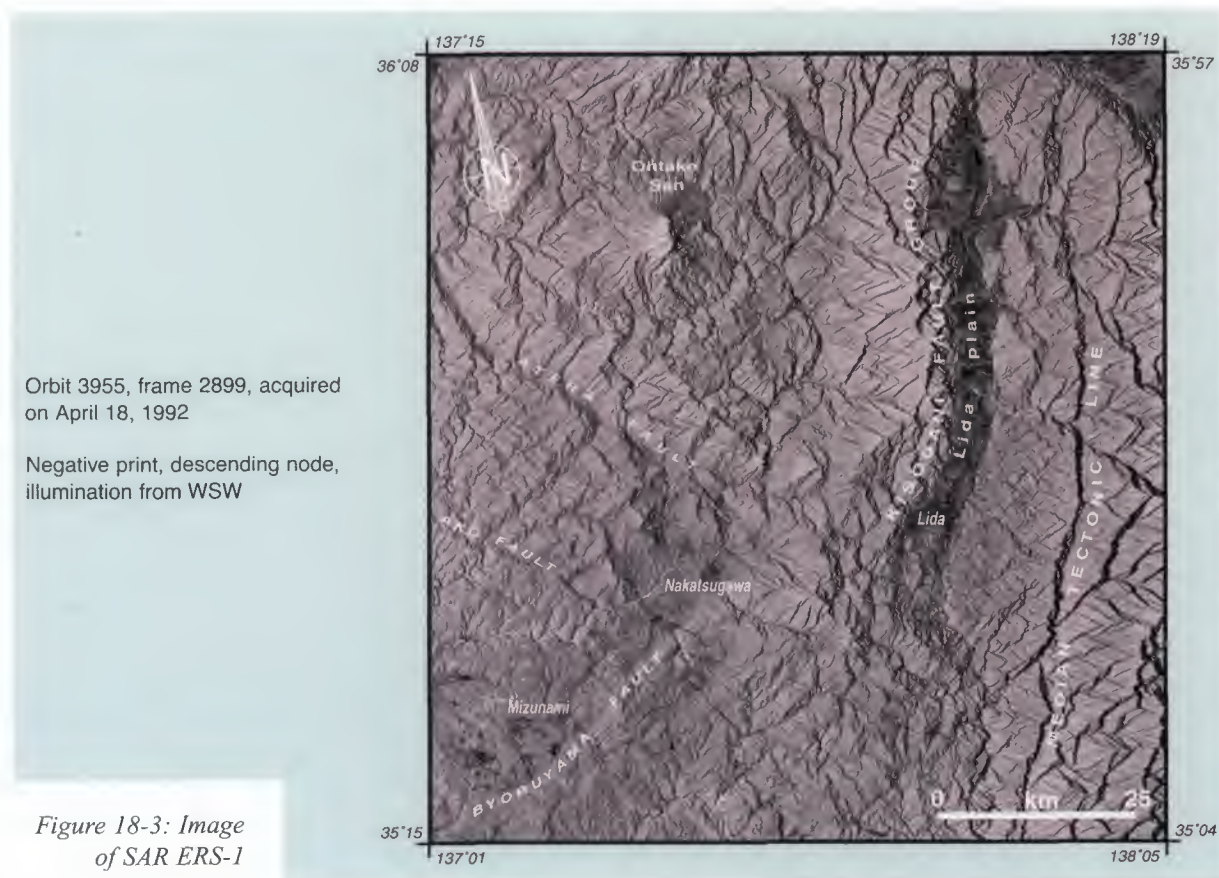
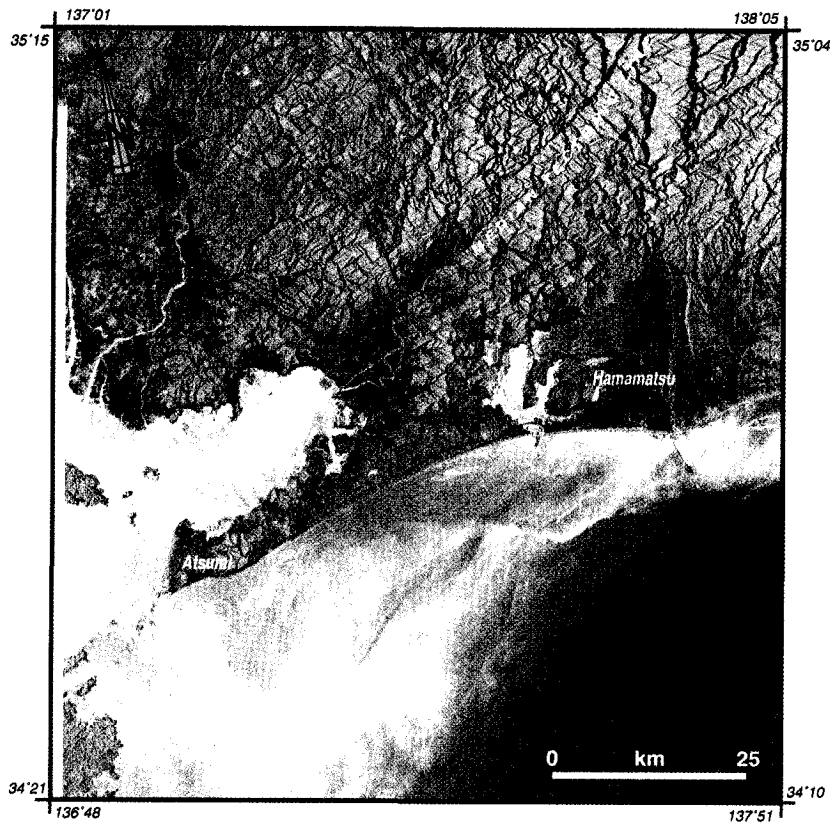


Figure 18-2: Plate diagram of the Japan area

18.2 SAR ERS imagery

Three ERS-1 SAR scenes have been used in the median region between Kobe and Tokyo (shown in Figure 18-1). Two scenes (Figure 18-3 and Figure 18-4) were acquired along the same descending orbit, whilst another (Figure 18-5) was acquired in ascending orbit, the illumination being from ESE and WSW respectively.

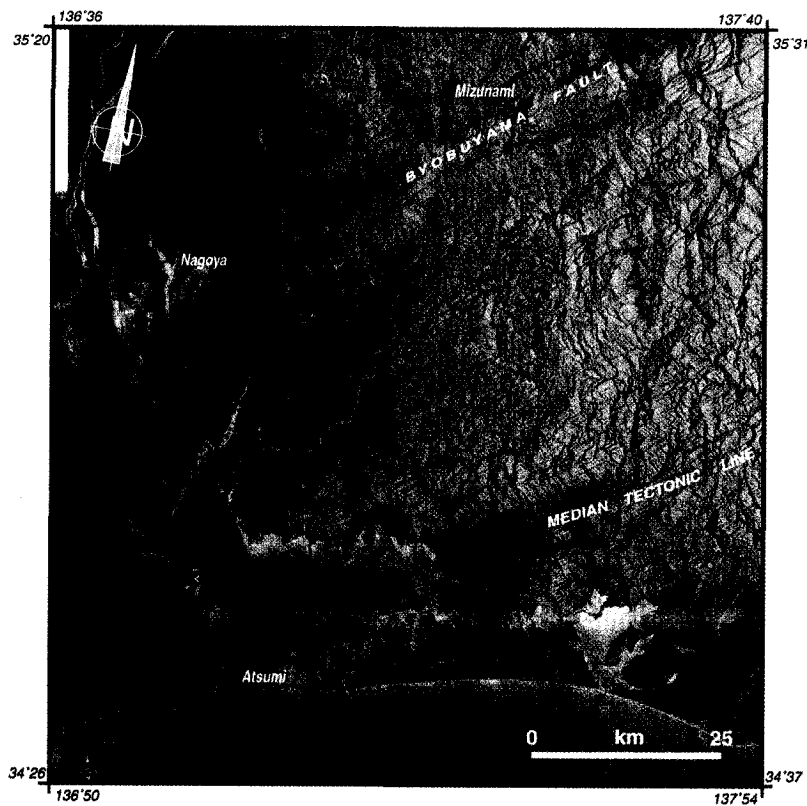




Orbit 3955, frame 2907, acquired on April 18, 1992

Negative print, descending node, illumination from WSW

Figure 18-4: Image of SAR ERS-1 scene 2



Orbit 7913, frame 693, acquired on January 19, 1993

Negative print, ascending node, illumination from ESE

Figure 18-5: Image of SAR ERS-1 scene 3

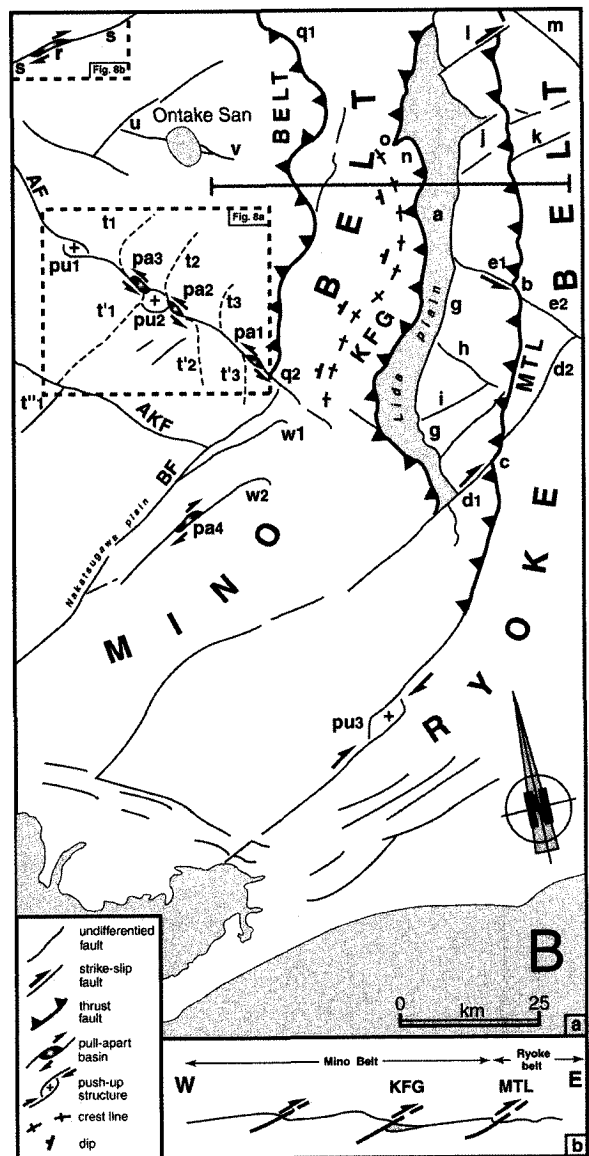
Figure 18-6:
Synthetic map of
tectonic and
volcanic features
from SAR ERS
images

Observations from the SAR ERS images have been used to map the recent faults (Figure 18-6A). These features have been consolidated into a complete map (Figure 18-6B). Recent faults, interpreted as active or inactive, are determined from their distinct or poorly eroded scarps, or because they affect Quaternary rocks. The images have been systematically compared with geological maps in order to carefully separate the scarps formed by fault planes (active) from those resulting from differential erosion of contrasted lithologies (ancient).

AF: Atera fault, AkF: Ako fault, BF: Byobuyama fault, KFG: Kisodani Fault Group, MTL: Main tectonic Line
Further explanation is in 18.3 below



A. Structural map superimposed on the radar images from ERS SAR



Ba. Structural analysis of the radar image

Bb. Topographic cross-section along the grey line of Ba, showing active W-dipping reverse faults and dragging fold associated with thrust motion

18.3 Observations and interpretations

18.3.1 The Median Tectonic Line

The key structure in the area is a NNE-trending distinct scarp of the Median Tectonic Line (**MTL**), located along the eastern side of Figure 18-3. It has a continuous trace over 100 km, with changes in height. For these reasons, it has to be interpreted as a fault scarp and not as a simple strike ridge due to contrasted lithologies (Figure 18-6A). The fault scarp is recent because it is poorly eroded and never crossed by valleys, except in locations (**b**) and (**c**). In these places, the fault line has a V shape across the valleys, indicating that it dips westward. The higher relief being located on the western side, the MTL is a reverse fault thrusting ESE-ward.

At point (**c**), the valley crossing MTL is composed of two rectilinear segments (**d1** and **d2**). Segment (**d1**) is a right-lateral strike-slip fault because it dextrally offsets the MTL, as well as another N-trending structural feature (**g**). The rectilinear segment (**d2**), although striking as (**d1**), does not constitute its eastern prolongation. Similarly, the valley (**e1**) is a structural line, which slightly left-laterally displaces the MTL at point (**b**) and then continues following (**e2**) but not along the same line. Other rectilinear features, interpreted as fault lines, are parallel either to (**e**), as is the case for (**h**) and (**m**), or to (**d**) like (**i**), (**j**), (**k**) and (**l**). Fault (**l**) also slightly right-laterally displaces the MTL. The pattern is that of conjugate faults striking N60°E to N75°E (right-lateral) and N130°E to N140°E (left-lateral). All these faults are poorly eroded and have to be regarded as active. This feature is particularly evident considering the high fault scarp (**m**) in the NE corner of Figure 18-6.

To explain why the (**d1-d2**) and (**e1-e2**) pairs do not each form a continuous line across the MTL, it is necessary to consider that the faults (**d**) and (**e**) are early conjugate strike-slip faults that formed before initiation of the MTL. They have subsequently been cut and displaced due to eastward thrusting of the MTL. Assuming that the motion along this main active fault is N90°E, i.e. parallel to the bisector of the (**d**) and (**e**) lines (Figure 18-7), the offsets of the (**d1-d2**) and (**e1-e2**) faults correspond to a compressive displacement of 2.3 km.

The MTL continues southward (Figure 18-4 and Figure 18-5) and progressively turns SW to strike parallel to (**d**). At point (**pu3**), a left stepping 'dog leg' structure, accompanied by a push-up hill, testifies to right-lateral slip component.

Motion along the MTL is assumed to be parallel to the bisector (grey arrow) of the (d1-d2) and (e1-e2) pairs

The conjugate ancient strike-slip faults are cut by thrusting during compressive motion

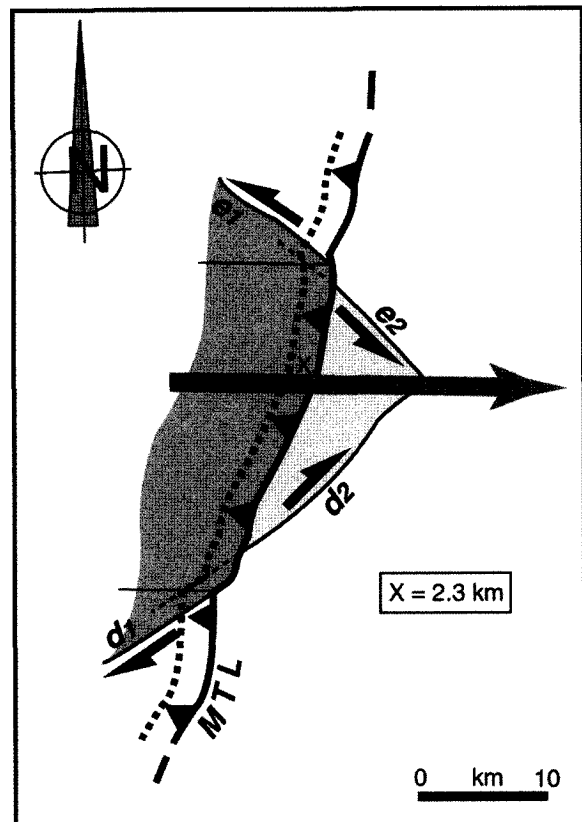


Figure 18-7:
Estimate of the
displacement X of
the Main Tectonic
Line

18.3.2 The Kisodani Fault Group

The image of Figure 18-3 shows a dark stripe (**a**) running parallel to the MTL at some distance in the west. The texture is rough (dark in the negative print) and can be interpreted as a planar ground surface covered with rice fields. It corresponds to the Plio-Quaternary deposits of the Lida alluvial plain, which has not yet been structured by a drainage network. The surface is overlooked in the west by a bold and complex scarp zone referred to as the Kisodani Fault Group (**KFG**) (1/200,000 Geological Map of Japan, Lida sheet, 1990). The scarp has a quite similar length to the **MTL**, is poorly eroded, and is not cut by valleys, testifying that the KFG is an active fault zone. The KFG is interpreted as a reverse fault because the western side overlooks and is older than (**a**), and is affected by a dense drainage network. It is a main fault zone along which the Mino Belt, principally made of Jurassic sediments and Cretaceous volcanic rocks, thrusts over the Ryoke belt, made of early Cretaceous metamorphic rocks and late Cretaceous intrusive rocks.

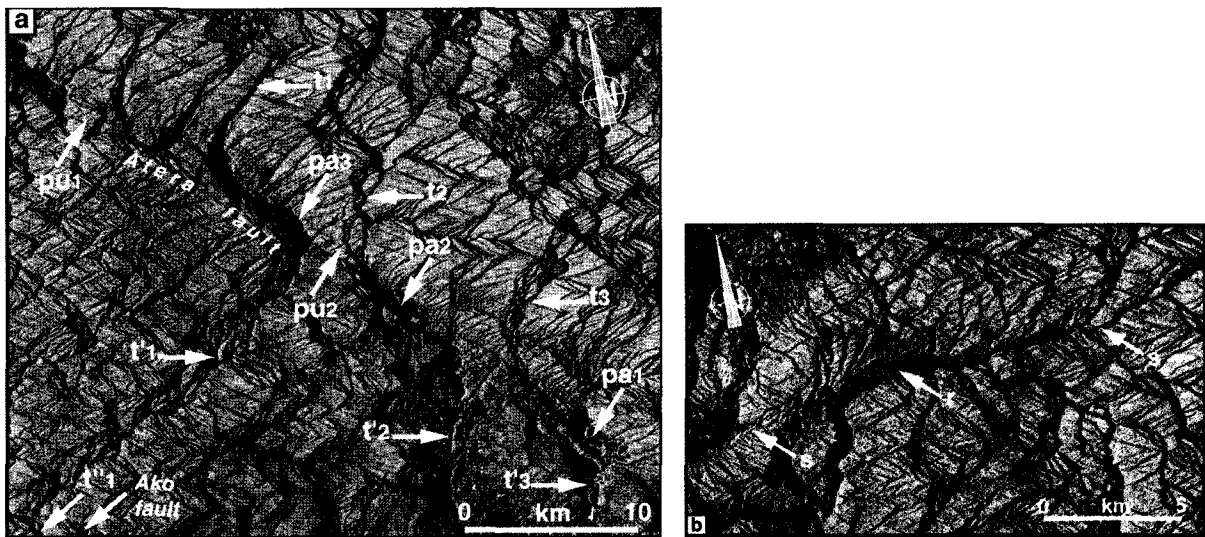
The crest line in the uplifted compartment, represented by crosses in Figure 18-6, runs parallel to the fault scarp. This crest line is interpreted as corresponding with the hinge of an N20°E-trending anticline that can be regarded as the dragging fold associated with thrust motion along the KFG. In this context, the Lida alluvial plain (**a**) is the syncline drag fold formed in the footwall side. The southern end of the KFG ends against fault (**d1**), which south-western prolongation can be seen in Figure 18-4 and Figure 18-5.

18.3.3 The Mino Belt

The Mino Belt is located west of the Kisodani Fault Group (Figure 18-6). A scarp (**q1-q2**) parallel to the KFG can be interpreted as a reverse fault because its trace is continuous and sinuous. Its south-western prolongation corresponds with the Byobuyama fault (**BF**, beyond **q2**), which is not well evidenced on the radar images, acquired in descending node (Figure 18-3 and Figure 18-4) but is rather well exposed when the radar illumination is from WSW (Figure 18-5, ascending node). It turns towards the N65°E direction in the south and the SE facing scarp can be followed by an alignment of drainage anomalies. The Byobuyama fault continues across the Plio-Quaternary alluvial deposits of the Nakatsugawa plain, attesting it is active. A horsetail structure formed by appended faults (**w1** and **w2**) and a rhomb-shaped pattern (**pa4**) show right-lateral strike-slip movement along the Byobuyama fault (Figure 18-6).

One of the well-expressed structural lines in the belt is a N145°E-trending straight valley corresponding to the Atera Fault (Figure 18-8a). Tributaries of the valleys (**t1-t'1**, **t2-t'2** and **t3-t'3**) are left-laterally displaced with the same interval, yielding ~7.5 km of sinistral motion. Left-lateral displacement is confirmed by the occurrence of pull-apart basins (**pa1** to **pa3**) and push-up hills (**pu1** and **pu2**). South of the Atera fault lies the Ako fault (**AKF** in Figure 18-6), which is less marked. Left-lateral motion along the fault is evidenced by ~2.5 km sinistral displacement of **t''1** relative to **t'1**.

Numerous NE-trending lines are observed and supposed to be fault zones. One of them (**s**) can be determined as an active right-lateral strike-slip fault, because a small releasing bend (**r**) filled with Quaternary deposits has formed (Figure 18-8b).



a. The Atera fault zone (AF in Figure 18-6) is laid out with pull-apart basins (pa) filled with recent alluvial deposits and push-up hills (pu). Tributaries t, t' and t'' are left-laterally displaced yielding ~7.5 km sinistral motion along the Atera fault and ~2.5 km sinistral motion along the Ako fault (AKF)

b. Releasing bend structure (r) filled with recent alluvial deposits, initiated from left-lateral motion along fault strands (s)

The only volcano in the area is the Plio-Quaternary (mainly Pleistocene) Ontake San (Figure 18-6). The summit of the crater is aligned both with an N110°E-trending deep valley in the west (**v**) and another valley in the east (**u**) striking in the same direction. These valleys do not correspond with a fault line, which would continue far from the

Figure 18-8:
Windows extracted
from the SAR
images (location in
Figure 18-6)

volcano. The strike of the (u) and (v) valleys is approximately the same as the bisector of the ~N65°E-trending Ako and ~N145°E-trending Atera faults. These faults can be interpreted as conjugate faults initiated in a strike-slip regime of deformation where the maximum and minimum stress components (σ_1 and σ_3 respectively) are both horizontal. The Ontake San volcano is interpreted as being rooted upon an open vertical tension fracture allowing the magma to reach the surface. Formation of the open vertical tension fracture can be accounted for by the same strike-slip tectonic regime. The strike of the (u-v) fracture indicates N20°E extension and N110°E compression. The orientation of the compression agrees with the geometry of the compressive structures of the area. σ_1 is perpendicular to the axis of the anticline associated to the KFG, as well as the mean strike of the Byobuyama fault, the KFG and the MTL.

18.4 Conclusions

Structural analysis of the radar images finds a coherent pattern of active structures resulting from N110°E-trending compression (Figure 18-6b). Reverse faulting is accompanied by drag folds, with horizontal axes trending N20°E. This compression is also associated with a strike-slip regime of deformation characterised by a system of conjugate strike-slip faults. Right-lateral and left-lateral strike-slip faults trend respectively ~N65°E and ~N145°E, and this is consistent with a ~N110°E σ_1 as the bisector. Strike-slip faults are associated with pull-apart, releasing bend and push-up features. The reverse faults act like frontal ramps that laterally end in strike-slip lateral ramps. The Plio-Quaternary Ontake San volcano being clearly associated with the ongoing deformation, the active tectonics began in the Pliocene. This age is consistent with that of the sediments filling the pull-apart basins along strike-slip faults and the alluvial plains, regarded as syncline drag folds associated with reverse faulting.

18.5 References

- [1] Dhont, D., Chorowicz, J., Cadet J.P. (2003). Detection of compression structures from SAR ERS imagery: example of the central Japan seismic area. *Int. J. Remote Sensing*, **24**: 559-571
- [2] Bouchon, M., Sekiguchi, H., Irikuna, K., Iwata, T. (1998), Some characteristics of the stress field of the 1995 Hyoko-ken Nanbu (Kobe) earthquake. *J. Geophys. Res.* **103**: 24271-24282.
- [3] Sato, T., Graves, R. W., Somerville, P. G., and Kataoka, S. (1998), Estimates of regional and local strong motions during the Great 1923 Kanto, Japan, Earthquake (Ms 8.2). Part 1: source estimation of a calibration event and modeling of wave propagation paths. *Bull. Seism. Soc. Am.* **88**: 183-205.
- [4] Jolivet, L., Faccenna, C., d'Agostino, N., Fournier, M., and Worrall, D. (1999). The Kinematics of Marginal Basins, examples from the Tyrrhenian, Aegean and Japan Seas. *Continental Tectonics*, edited by C. Mac Niocaill & P. D. Ryan, Special Publication, **164**, 21-53, Geological Society, London.

19. Radar imagery observation

Case study: the Levant transform structure in Lebanon

19.1 Geologic framework

The Levant Fault Zone (LFZ) is a plate boundary between Arabia to the east and Africa to the west (Figure 19-1).

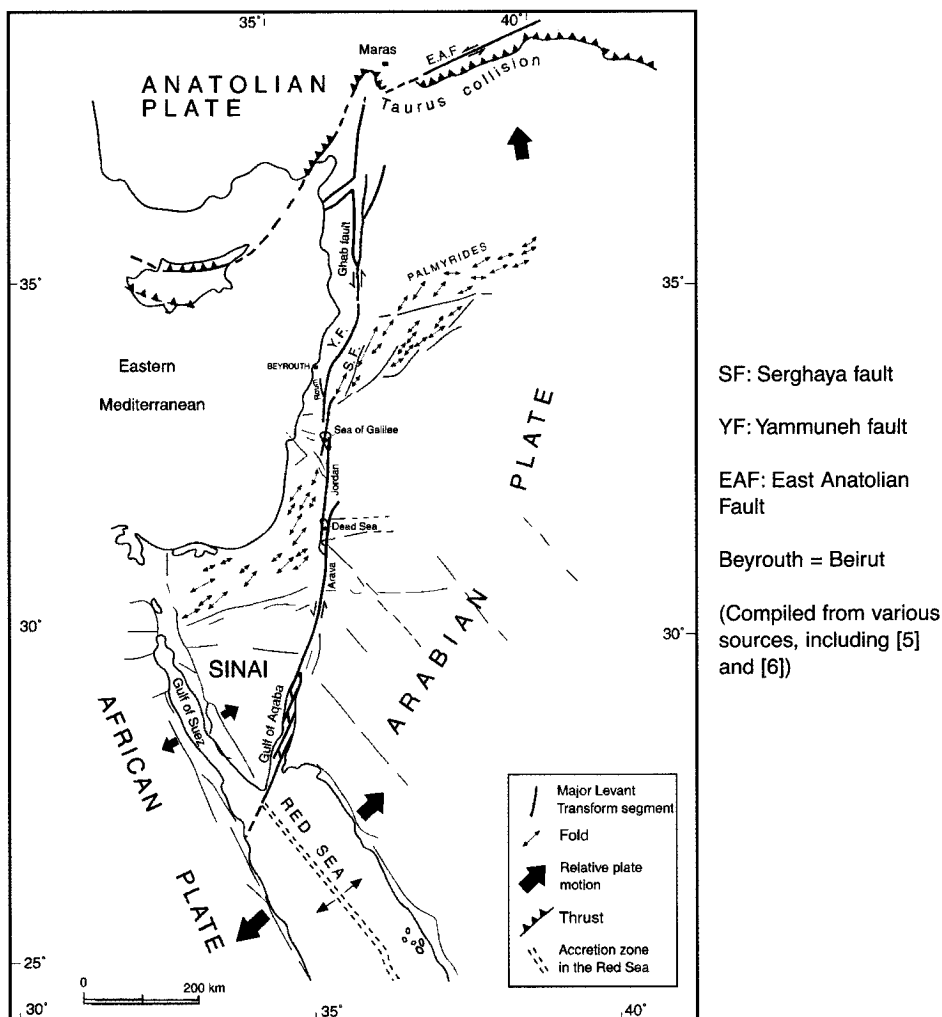


Figure 19-1:
Tectonic setting of
the Levant
Transform Zone

The fault zone runs for more than 1000 km from the Red Sea to the Taurus Range in Turkey. The LFZ is not a single transform but rather a succession of fault zones that have different orientations and structures, i.e. (from south to north) the Aqaba, Arava, Dead Sea, Jordan, Yammuneh and Ghab fault zones. In areas where the fault zones are oblique to the relative plate motion, transtension or transpression occurs, creating respectively

This case study is based on [1].

pull-apart extensional basins (e.g. Aqaba and the Dead Sea) or push-up compressional ranges (e.g. Yammuneh). From the Gulf of Aqaba to the Jordan fault, the finite left-lateral displacement has been estimated to be 105 km. Near Beirut, the major Roum, Yammuneh and Serghaya faults divide Lebanon into several blocks.

19.2 Satellite imagery analysis

19.2.1 Northern region

On the Landsat-TM image, the Yammuneh fault is expressed as a NNE-trending straight line (Figure 19-2).

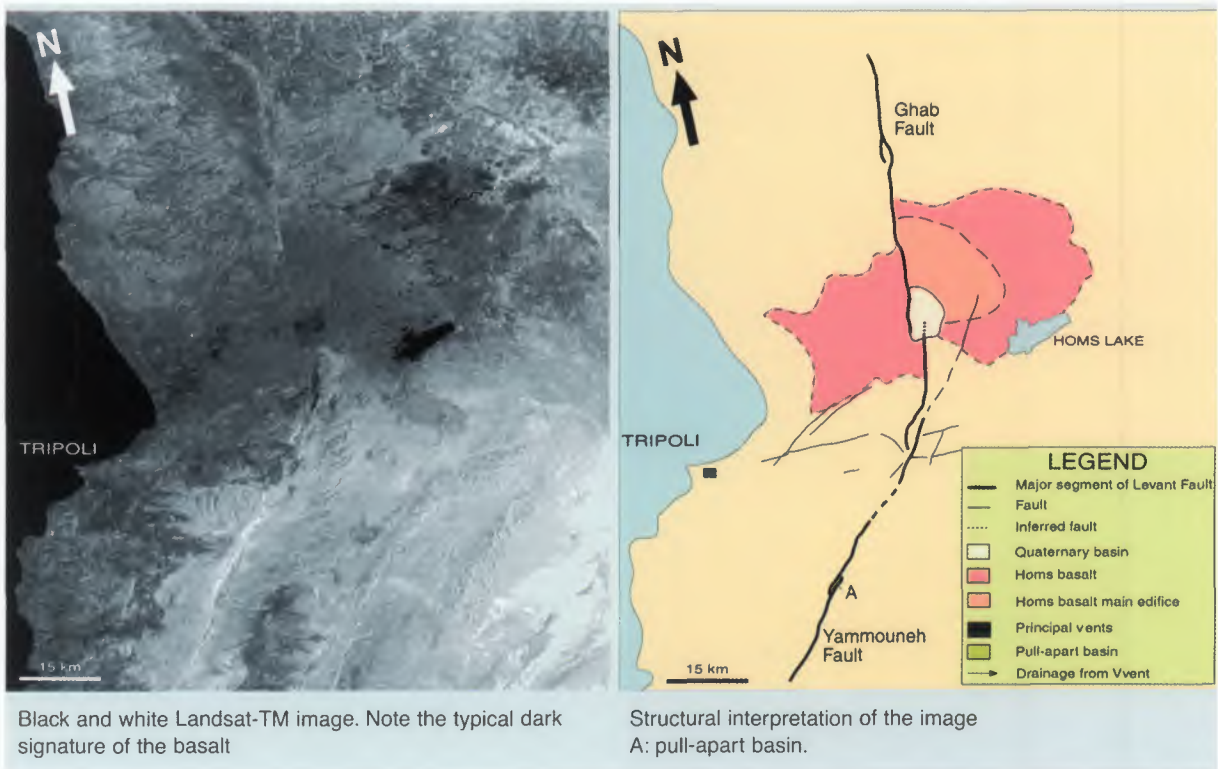


Figure 19-2:
Northern Lebanon
and Western Syria

It mainly affects Mesozoic-Paleogene limestone and Mio-Pliocene continental sediments. Southeast of Tripoli along the fault, at A in Figure 19-2, is a small basin (4.5 km long, 1 km wide). It is filled with Quaternary sediments, and has the rhombohedral shape of a pull-apart structure (Figure 19-3).

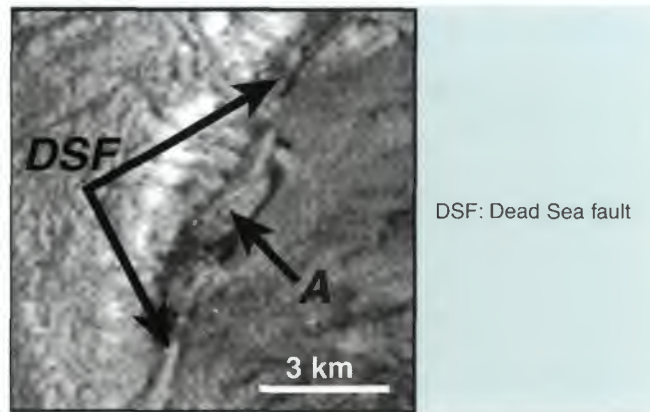


Figure 19-3: Detail of the pull-apart structure A from Figure 19-2

On the radar image, two poorly eroded push-up patterns (A and B in Figure 19-4) indicate local transpression along the Yammuneh fault.

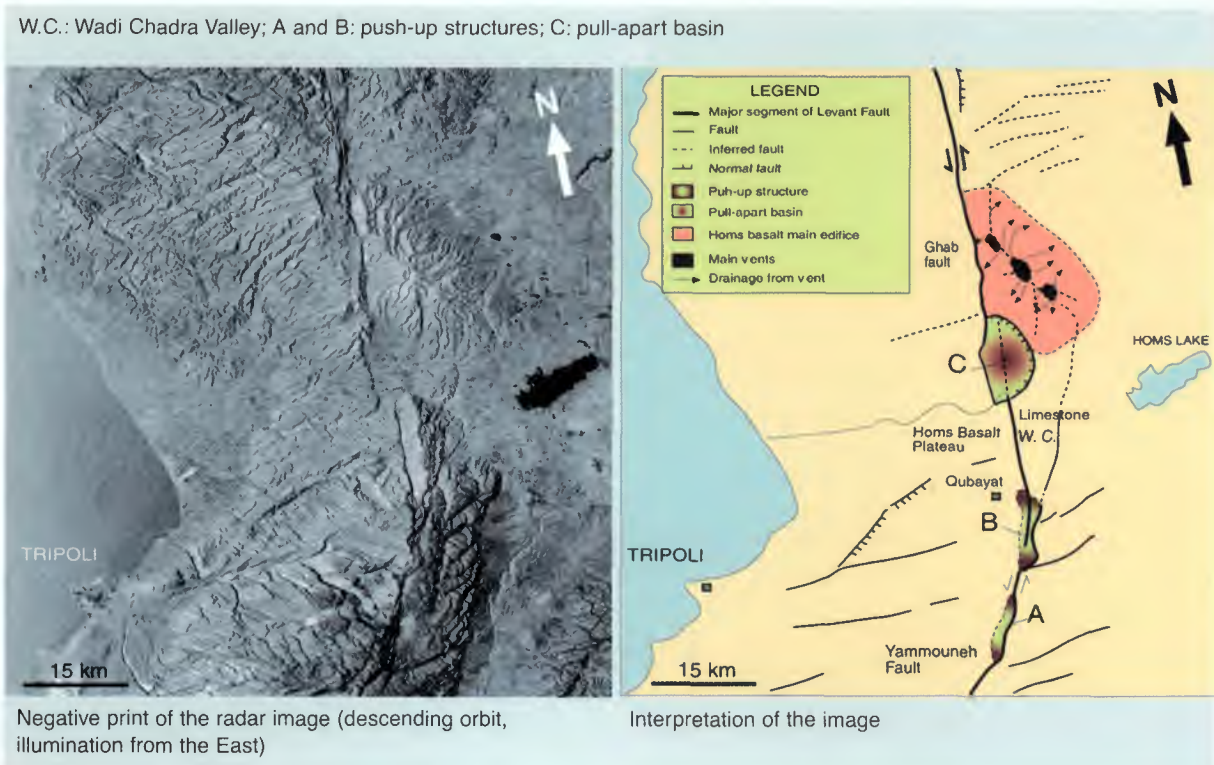


Figure 19-4: SAR ERS image covering Northern Lebanon and Western Syria

To the north, the fault turns N-S and is superimposed by the Wadi Chadra valley. It is clear on the radar image that this valley is the boundary between the Homs Basalt plateau to the west and the Cenomanian limestone to the east. Northward, the Yammuneh fault enters into a Quaternary basin. Here its trace becomes well visible on the Landsat image. North of the Quaternary basin, the Yammuneh fault is relayed by the Ghab fault.

Comparison of ERS and Landsat images shows that both the fault traces and the morphology of pull-apart and push-up structures are much more evident on the ERS SAR image (C in Figure 19-4, with detailed view in Figure 19-5).

The pull-out structure C (Figure 19-4) is best evidenced on the radar image (b) rather than the Landsat one (a)

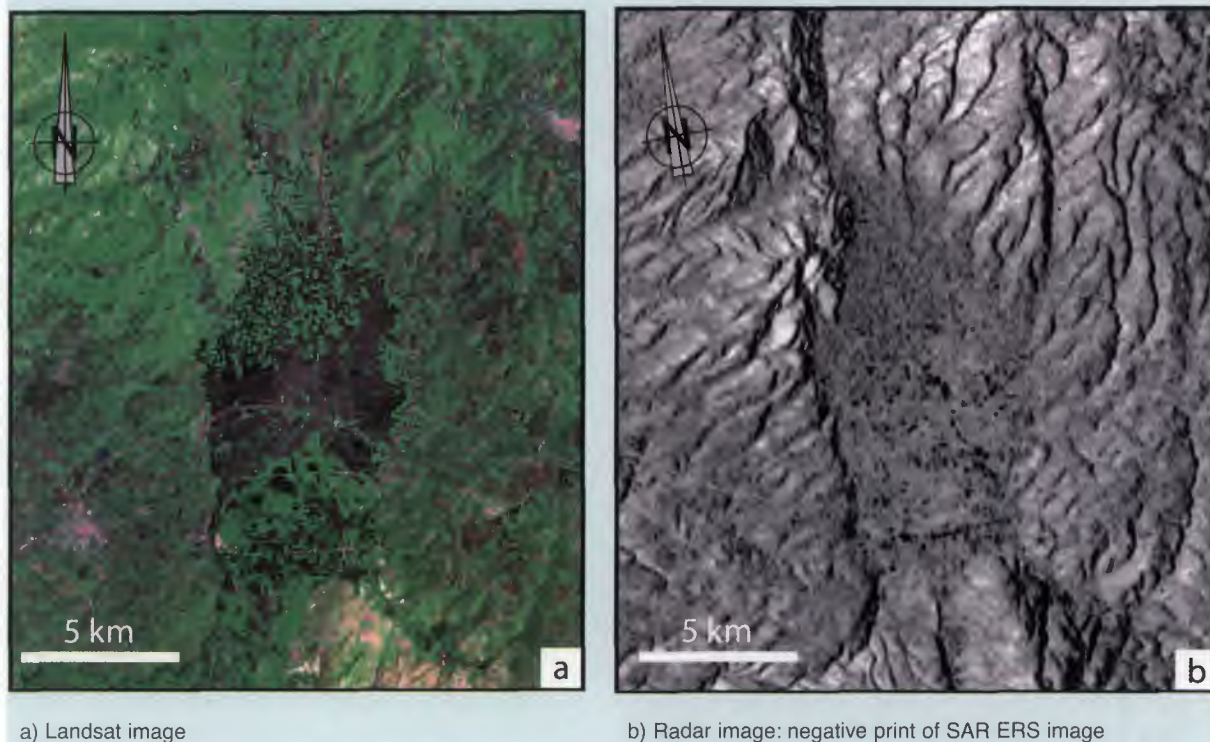


Figure 19-5: Detail of the pull-apart basin, C

From the pattern of its southern, western and northern straight borders, at right angles to each other, the Quaternary basin where the Yammuneh fault ends up can be interpreted as a pull-apart structure created in a transtensive left-stepped relay zone. The round shape of the eastern border suggests gravity collapse and eastward increase of the area of sedimentation.

The boundaries of the basalt can be approximately traced on the Landsat image (Figure 19-2) from its dark spectral signature. The basalt boundaries have the same offset in the south and north, implying that the Homs basalt plateau has been displaced by the fault for approximately 8 km since 5.2 Ma (age of the basalt estimated by [2] using radiometric methods).

In the upper centre of the ERS image (Figure 19-4), it is possible to identify an elongate volcanic edifice crossed by a NW trending fissure line showing also the volcanic vents.

This fissure line and related vents can be considered as the principal open fracture [3] that permitted emission of the basalt on the eastern side of the Ghab fault. Since this line is linked southward with a fault striking NNE which is the straight prolongation of the Yammuneh fault, this structure can finally be interpreted as a tail-crack termination. Thus, the basalt is a direct consequence of the activity of the Yammuneh fault. The elongate volcanic edifice is well characterised and delineated by its texture and radial morphology. It is clear that its centre, corresponding with the line of vents, is mainly located on the eastern side of the fault. Thus, the Yammuneh-Ghab line across the basalt cannot be the effect of a paleorelief, which would imply two sources of basalt. In this hypothesis the Pliocene basalt (Homs plateau and the basalt on the eastern side of the

Ghab fault) represents a unique volcanic edifice, which is cut by the Yammuneh and Ghab faults.

Field studies southwest of Qubayat [1] have evidenced several vertical tectonic slices (1 m thick, 5 m long) of limestone inside the basalt, at a distance of 3 km from the Yammuneh fault. Even if this is not directly on the Yammuneh fault, it means that this fault system was active even after basalt emplacement.

Several ENE-trending lines [8] are well exposed on the Landsat and radar images, but do not show up in the basalt. In the field, some of these lines (Figure 19-6) are normal faults affecting late Jurassic limestone and early Cretaceous deposits.

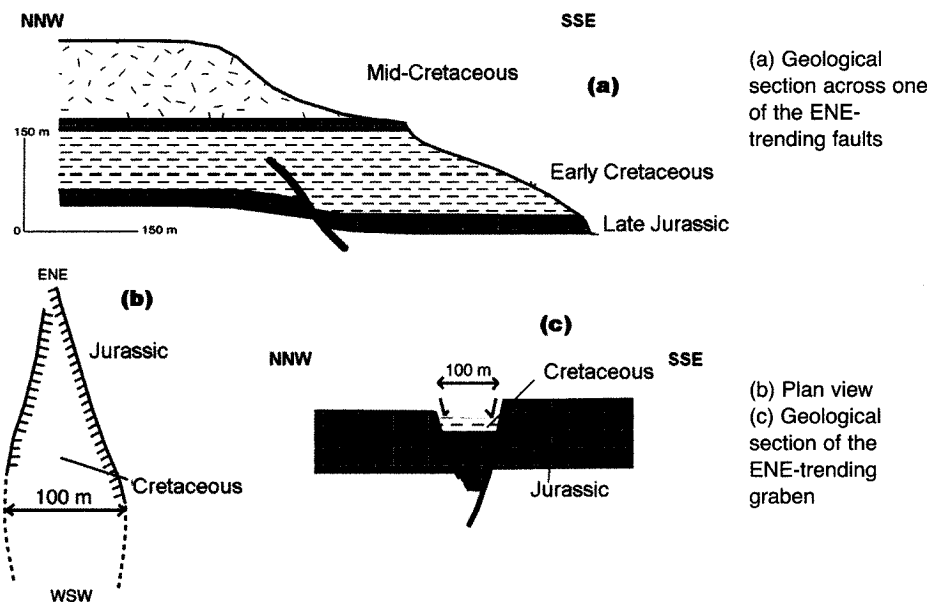


Figure 19-6:
Structural
observations in the
Faraya Valley, east
of Beirut City

Some fault surfaces contain vertical striations and delineate small (150 m wide, 500 m long) ENE-striking grabens with downthrown Cretaceous layers bounded by Jurassic limestone through tectonic contacts (Figure 19-6 and C in Figure 19-7).

This is a pattern of rifting that occurred during the Mesozoic, testifying to a NNW-extension episode.

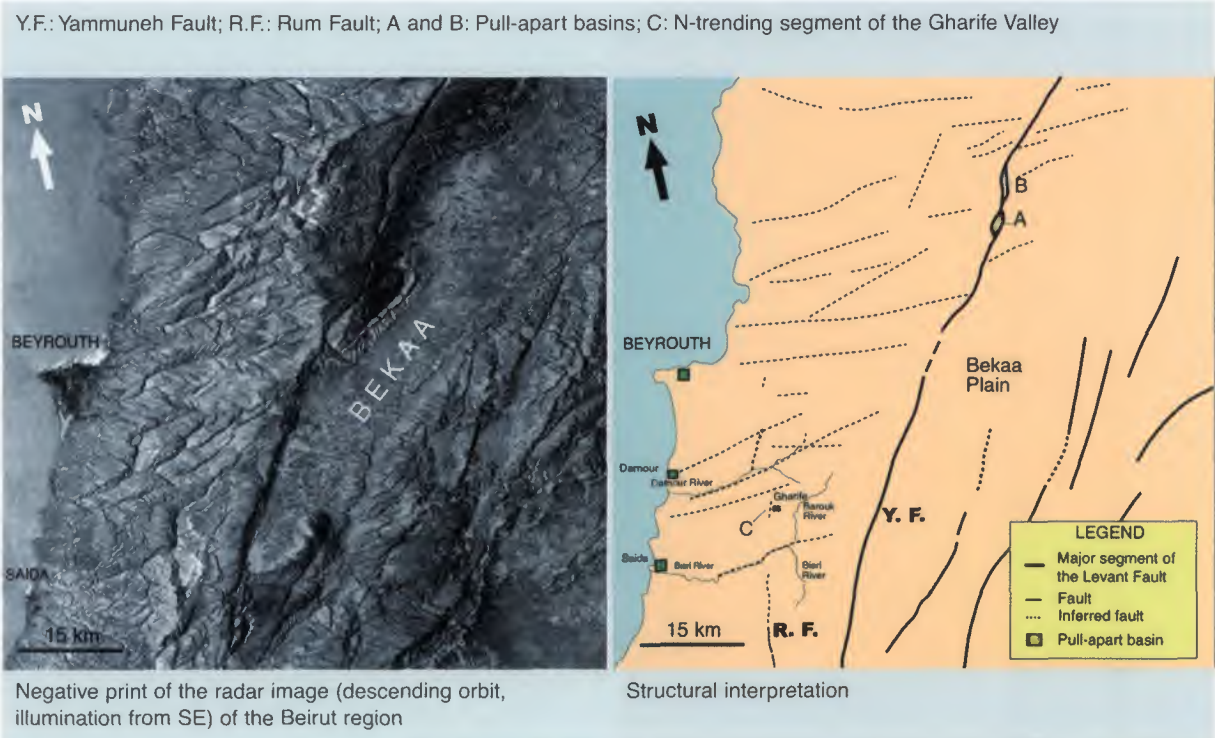


Figure 19-7: SAR image of the Beirut region

19.2.2 Southern region

In the southern part of the Yammuneh structure (Figure 19-7), the fault line is even more visible than it was in the northern part. This is also due to the look direction of the SAR sensor (SE-NW), which is almost perpendicular to the fault direction.

On the contrary, the N-striking Rum fault is marked only by an alignment of rivers, which runs from the south northward up to the Bisri river. From the Bisri river northward, the fault line disappears in the image and also in the field. These observations confirm the mapping of Dubertret [4] which does not continue the Rum fault northward. This is also consistent with the lack of seismic activity north of the Rum fault [7].

There are other valleys in the prolongation of the Rum fault more to the north, but they form only short discontinuous lines and do not show changes in height. These lines can be interpreted as being inactive faults that have guided hydrologic drainage.

In the ENE-looking image (Figure 19-8), the Yammuneh Fault is less evident, but the scarps are well expressed.

The size and continuity of the main scarp reveal an important and recent activity. The image is centred more to the north and does not cover the Rum fault mapped by [4], but if the fault continued northward it would have been distinguishable because the SAR illumination (ERS ascending orbit) is almost perpendicular to the tectonic lineament.

The active Levant Fault Zone in Lebanon has been controversially discussed in terms of activity of its fault strands. For example, some authors have suggested that the active strand may be the Rum and not the Yammuneh fault. On the other hand, analysis of satellite images, mainly based on ERS SAR data, shows that the Rum Fault is not the active segment and that the Yammuneh Fault is a more active Quaternary structure. There

are no large faults that could fit with a major lithospheric boundary along the Rum strand. This fault may be a Mesozoic structure that was partly re-activated, but the evidence is that there is no active transcurrent segment north of the Bisri river.

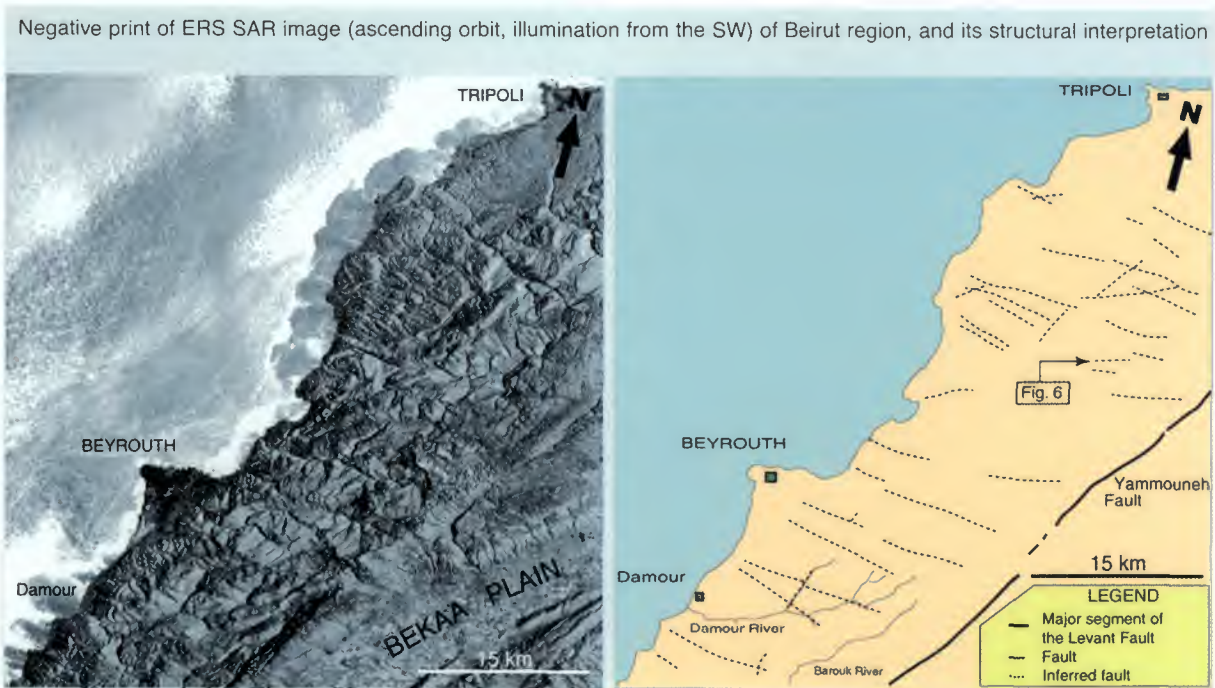


Figure 19-8: ERS SAR image of Beirut region, ascending orbit

The Yammouneh fault corresponds to push-up structures and steep, poorly eroded scarps, associated with pull-apart basins filled with Quaternary sediments. This fault cuts and left-laterally displaces the Homs basalt volcanic vents (Pliocene). It corresponds with an active plate boundary. Its transpressive/transpressive movements are consistent with a plate motion (SSW-NNE) oblique to the fault strike (N-S).

A precise location of the plate boundary is important for the zonation of seismic hazards. Radar images provide synoptic but detailed views of the morphology. Thus ERS SAR data can be fruitfully used, together with field data, for studying the relationship between tectonic activity and morphology.

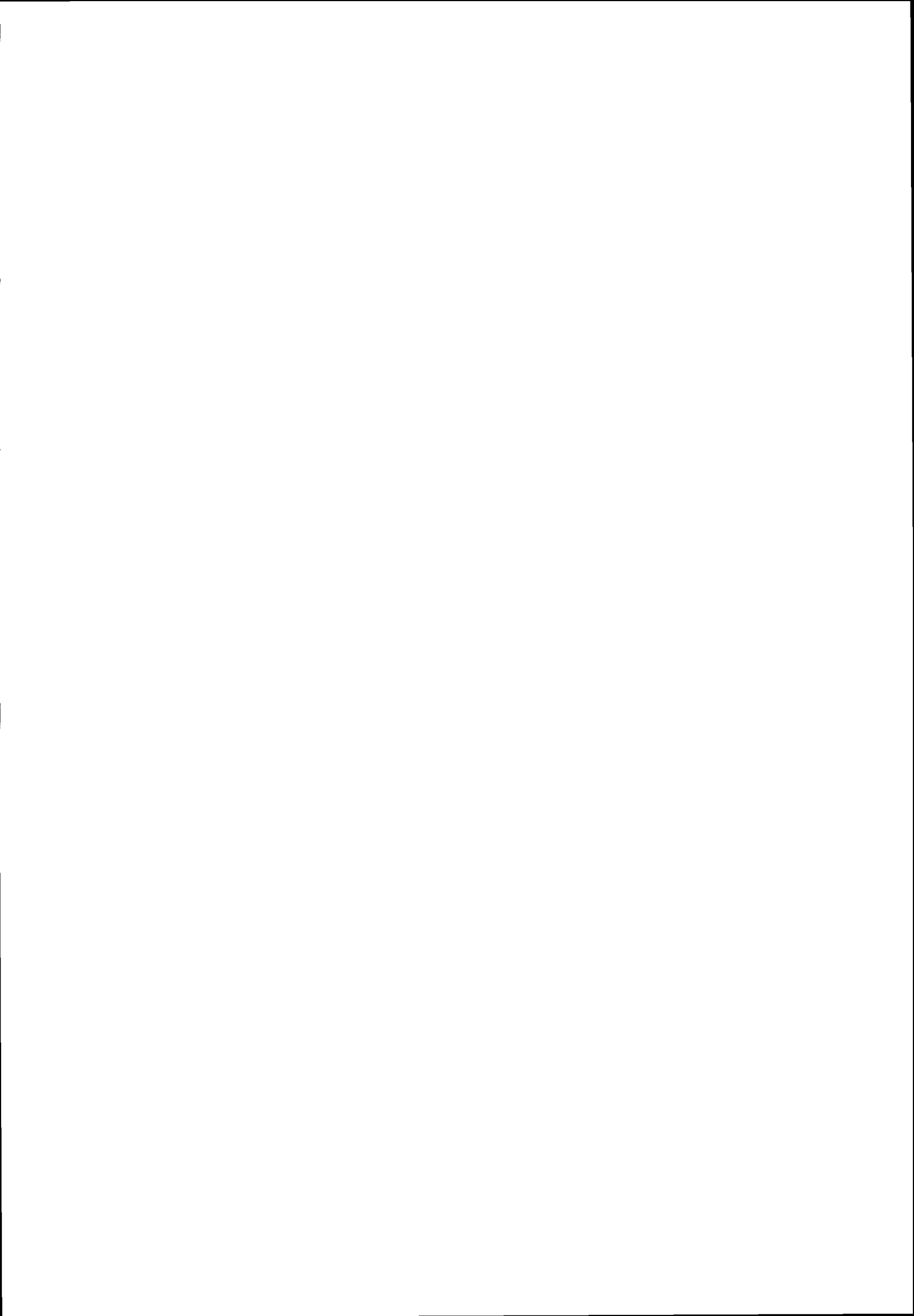
19.3 References

- [1] Fleury J., Chorowicz J. and Somma J., 1999. Discussion on transcurrent fault activity on the Dead Sea Transform in Lebanon and its implications for plate tectonics and seismic hazards. *Journal of the Geological Society*, London, **154**, 757-760.
- [2] Butler, R., Spencer S. & Griffiths H. M. 1997. Transcurrent fault activity on the Dead Sea Transform in Lebanon and its implications for plate tectonics and seismic hazard. *Journal of the Geological Society* London, vol. **154**, 757-760.
- [3] Chorowicz, J., Bardintzeff, J.M., Rasamimanana, G., Chotin, P., Thouin, C. & Rudant, J.P. 1997. An approach using SAR ERS images to relate extension fractures to volcanic vents: examples from Iceland and Madagascar. *Tectonophysics*, **271**, 263-283.

- [4] Dubertret, L. 1955. *Carte Géologique du Liban*, Ministère des Travaux Publics, Beyrouth (1/ 200 000, 1/ 50 000).
- [5] Garfunkel, Z., Zak, I. & Freund, R. 1981. Active faulting along the Dead Sea Rift. *Tectonophysics*, **80**, 1-26.
- [6] Girdler, R.-W. 1990. The Dead Sea Transform fault system. *Tectonophysics*, **180(1)**, 1-13.
- [7] Plassard, J. & Kogol, B. 1981. *Seismicité du Liban*, Conseil National de la Recherche Scientifique, Beyrouth.
- [8] Walley, C.-D. 1998. Some outstanding issues in the geology of Lebanon and their importance in the tectonic evolution of the Levantine region. *Tectonophysics*, **298**, 37-62.

Part III

Potential applications of ERS SAR data



20. Monitoring sea ice

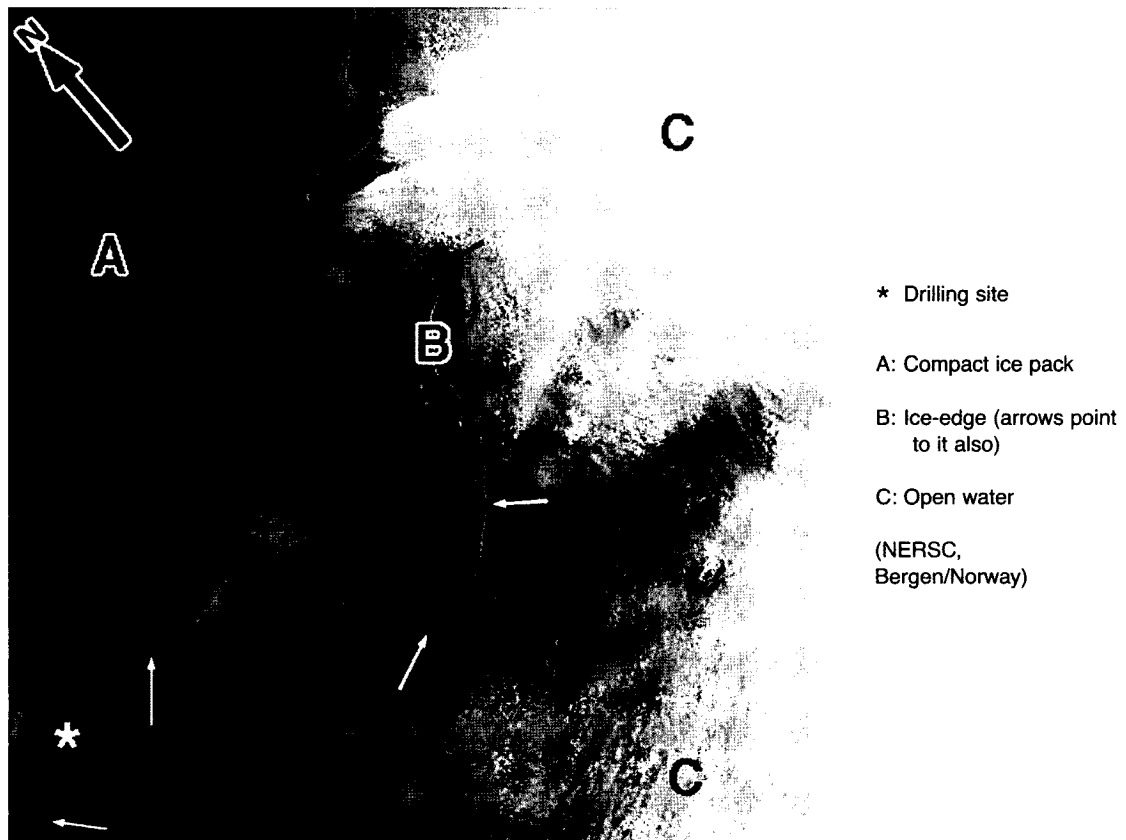
20.1 Drilling activities in polar regions

The interest of the scientific community in sea ice monitoring and mapping is due partly to its relevance to global climate variations, but also to the need to assure access to sites in very high latitudes for expeditions or operational work (e.g. offshore oil drilling). Continuous and accurate observation of sea ice has only been possible since the launch of ERS-1.

Drilling sites situated in polar regions of the Earth must be monitored by means of accurate ice maps before starting field operations. ERS SAR images are mainly used for detecting the ice edge and ice sheet movements. In order to operate in its vicinity, the extent and variation of ice must be available on a daily basis.

Figure 20-1 shows an ERS SAR image acquired on 22 August 1993 in the Fram Strait ($81^{\circ} 05' N$, $7^{\circ} E$), close to a drilling site (marked by an asterisk). The image evidences the compact ice pack (A), and arrows point to the ice edge (B). C indicates open water.

Figure 20-1: ERS SAR image of the Fram Strait (between Greenland and Norway)



Drilling operations might need to be stopped due to the presence of ice. The use of ERS images in these cases is very helpful for planning and managing the operations.

20.2 Offshore operations

The precise knowledge of the ice coverage extent is not only relevant for drilling activities, but also for other engineering works carried out at high latitudes. An example is pipeline deployment operations in the southern Kara Sea (northern Russia), for connecting the gas pipeline on the Yamal peninsula with the main pipelines of western and central Russia.

In this case the most important contribution provided by ERS SAR imagery for ice monitoring is towards understanding the ice behaviour during the freezing phase in early winter, in order to predict the time when operations have to stop and the approximate duration of the hold. Figure 20-2 shows a comparison between two ERS SAR images acquired on 1 November 1993 (left) and 17 November 1993 (right) over the operation site.

(NERSC, Bergen/Norway) Image is 100 x 100 km



Image acquired on 1 November 1993

Most of the bay is covered by ice stripes oriented in the same direction as the wind field



Image acquired on 17 November 1993

Two weeks later, new ice is growing along the eastern coast

Figure 20-2: ERS SAR images of the pipeline project site

Most of the bay, in the left image, is covered by ice stripes oriented in the same direction as the wind field (SW-NE). The white bank on the eastern coast represents ice coverage of about 50 km across, which was accumulated in 1-2 weeks of freezing conditions. The image to the right shows the situation two weeks later: winds are always blowing from the SW and new ice is growing along the eastern coast. It is important to know about such aggravating conditions in order to plan working operations effectively, e.g. to push the workload as far as possible into late autumn.

21. Coastal zones

21.1 Ocean floor and coastal zone surveys

Although microwaves cannot penetrate water, they can be used to observe its surface behaviour in great detail and with high accuracy. Sea surface roughness is constantly altered by wind and current and also by surface-smoothing agents such as mineral oil, or by the impact of heavy rain roughening the sea surface. Some of these phenomena are the subject of operational use of space-borne SAR data, mainly for coastal zone topography mapping or for oil spill monitoring.

Under favourable meteorological and hydrodynamic conditions (moderate winds of 3 to 10 m/s and significant tidal currents of about 0.5 m/s), air- or space-borne Synthetic Aperture Radar (SAR) imagery shows features of the bottom topography of shallow seas, (Figure 21-1 and Figure 21-2, [1], [16]).

Figure 21-1: Geo-referenced ERS SAR image along the Belgian coast

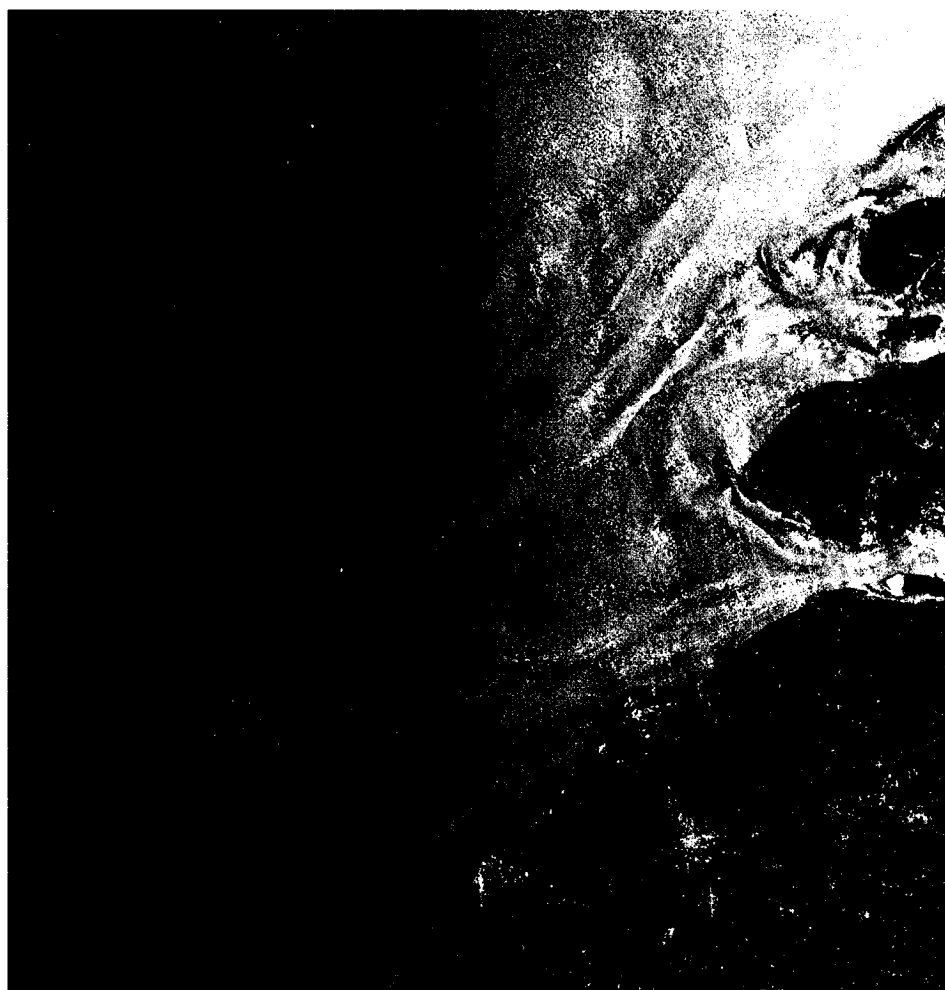


Image recorded 12 April 1997. Bottom topography features are well visible, indicated by surface roughness changes. 100 x 100 km. North is approximately up.

The blue box indicates the location of Figure 21-2.

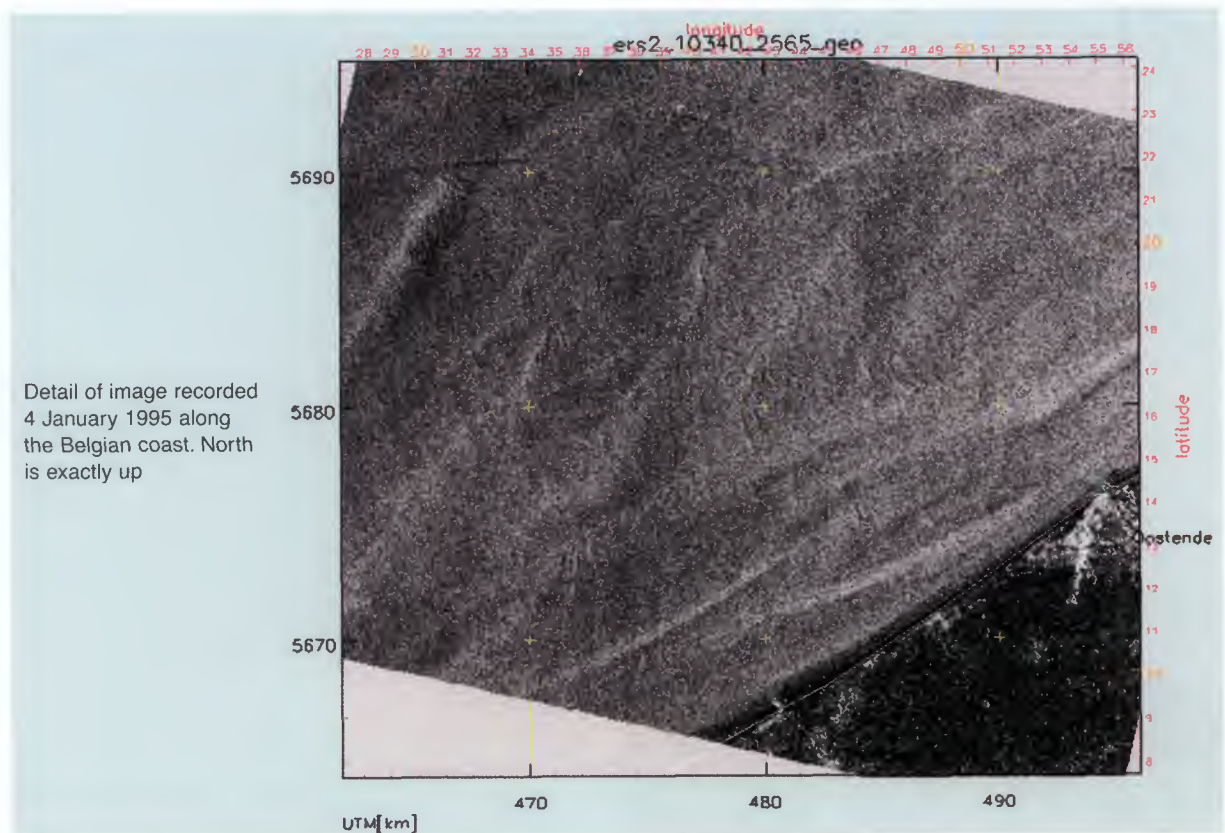


Figure 21-2: Detail of the geo-referenced ERS SAR image

Figure 21-3 shows the SAR mechanism for imaging the sea bottom in shallow water.

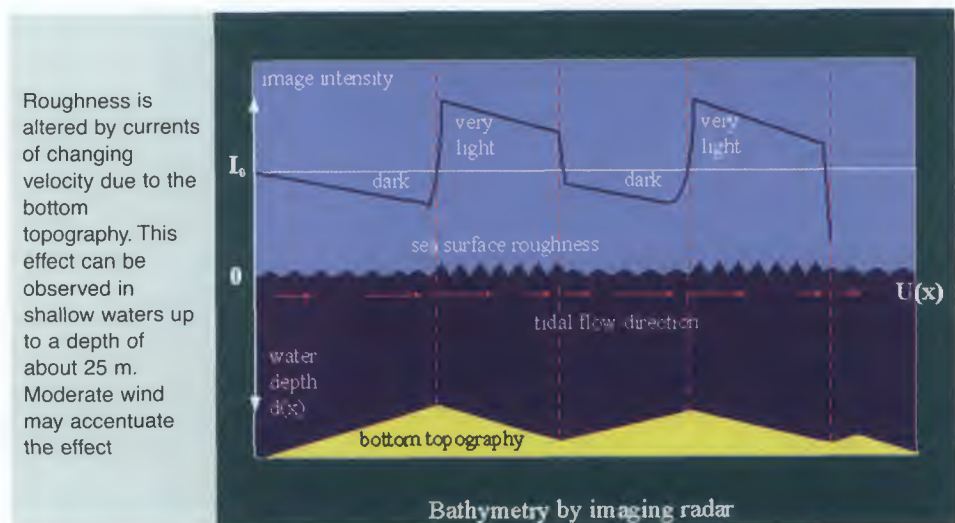


Figure 21-3: Imaging mechanism of SAR of a sea surface

Roughness is altered by currents of changing velocity due to the bottom topography. This effect can be observed in shallow waters up to a depth of about 25 m. Moderate wind may accentuate the effect

The imaging mechanism (Figure 21-3) of mapping sea bottom topography by imaging radar consists of three stages (a more detailed mathematical formulation is given in [3]):

- 1) The interaction between (tidal) flow and bottom topography results in modulations in the (surface) flow velocity. This relation can be described by several models with an

increasing level of complexity: the continuity equation, shallow water equations, and/or the Navier Stokes equations.

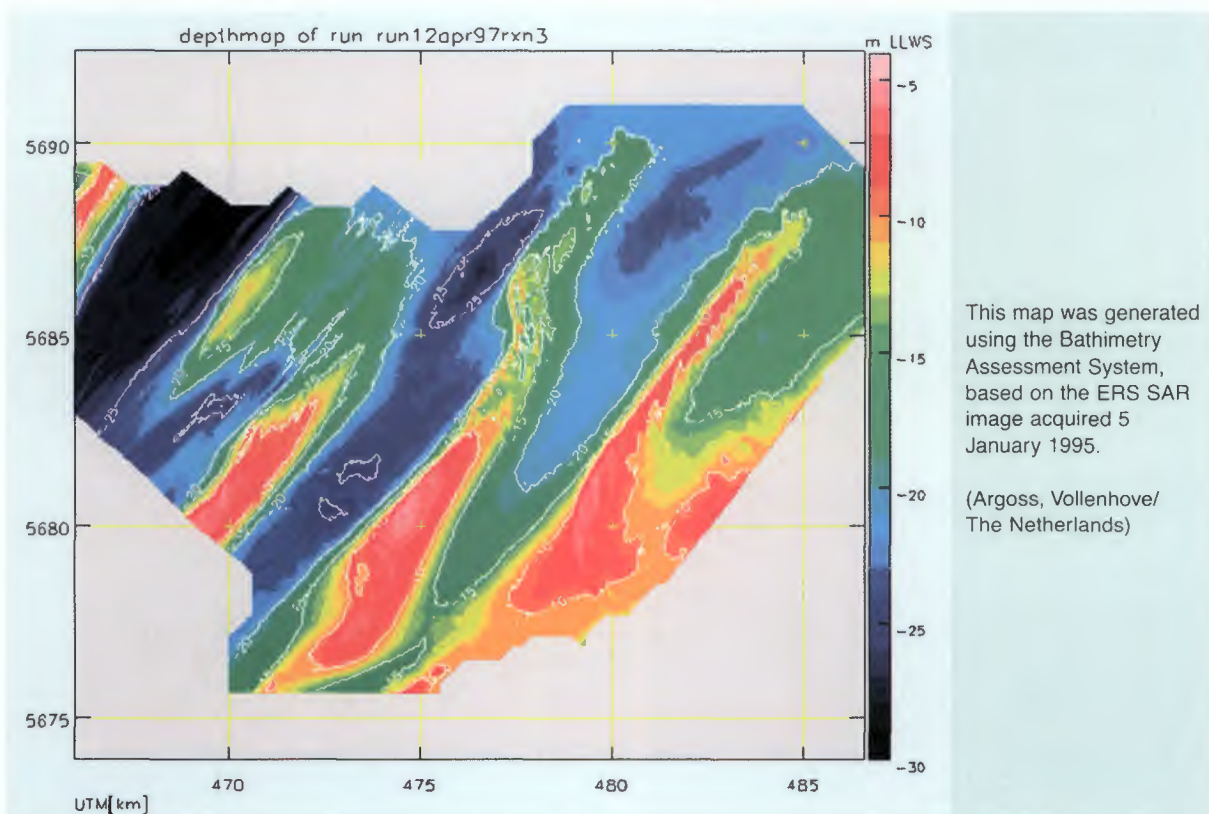
- 2) Modulations in surface flow velocity cause variations in the surface wave spectrum. This is modelled with the help of the action balance equation, using a relaxation source term to simulate the restoring forces of wind input and wave breaking.
- 3) Variations in the surface wave spectrum cause modulations in the level of radar backscatter. To compute the backscatter variations a simple Bragg model can be used, but also available are two-scale [8] and first iteration Kirchoff (Holliday) models.

Based on the above three-stage mechanism, the Bathymetry Assessment System (BAS), a suite of computer models, has been developed at ARGOSS (<http://www.argoss.nl>). Models with different levels of complexity and physical detail are available for each step. These models describe the flows, waves, and electromagnetic scatter, and can be used for a quantitative analysis of radar imagery.

This suite of computer models generates the radar backscatter given the (initial) bathymetry and the wind. In order to invert this depth-radar backscatter relation, a data assimilation scheme has been developed, minimising the difference between the calculated and the measured radar backscatter by adjusting the bottom topography. At present, a data assimilation scheme using one-dimensional models is implemented.

Using BAS these images were combined with ship's soundings along tracks that are 1 km apart, to create a digital depth map on a 25 m grid. Although the interval between the tracks is relatively large compared to the final map resolution and the scale of the seabed features, an evaluation showed that the produced map provides realistic quantitative

Figure 21-4:
Bottom topography
map



depth results (Figure 21-4). SAR imagery can be used to eliminate part of the traditional sounding effort and thereby reduce the costs of map production.

21.2 References

- [1] Alpers, W., and Hennings, I., A Theory of the Imaging of Underwater Bottom Topography by Real and Synthetic Aperture Radar. *Journal of Geophysical Research*, Vol. **89C**, pp 10,529-10,546, 1984.
- [2] Calkoen, C.J., van Halsema, d., Jähne, B., Janssen, J.A.M., Oost, W.A., Snoeij, P., and Vogelzang, J., 1990. VIERS-1 progress report, *BCRS-report*, bcrs **90-27**.
- [3] Calkoen, C.J., Wensink, G.J. and Hesselmanns, G.H.F.M., 1993. ERS-1 SAR imagery to optimise the NOURTEC ship-based bathymetric survey: feasibility study. *DELFT HYDRAULICS* report **H1875**.
- [4] Calkoen, C.J., Wensink, G.J., Vogelzang, J. and Heinen, P.F., 1995. EIBERS, Efficiency Improvement of Bathymetric surveys with ERS-1, *BCRS report* **95-01**.
- [5] Van Cauwenberghe, C.. 1996. Multibeam echosounder technology: a time series analysis of sandbank movement. *The Hydrographic Journal* No. **81**.
- [6] Van Cauwenberghe C. 1997. A practical evaluation of the multi-beam surveys on board the Belgian hydrographic vessel 'Ter Streep': Trials with motion sensors Datawell Hippy 120, Datawell Mose 40 en Seatex MRU-5. *Report no.43 of the Hydrographic Service*.
- [7] Davies, A.M., 1988. On formulating two-dimensional vertically integrated hydrodynamic numerical models with an enhanced representation of bed stress. *Journal of Geophysical Research*, **C93**, 1241-1263.
- [8] Donelan, M.A., and Pierson, W.J., 1987. Radar scattering and equilibrium ranges in wind generated waves with application to scatterometry. *Journal of Geophysical Research*, **92C**, 4971-5029.
- [9] Hasselmann, K., 1960. Grundgleichungen der Seegangsvorhersage, *Schiffstechnik*, **7**, 191-195.
- [10] Hesselmanns, G.H.F.M., 1996. *Validatie ERS-1 Loswal Noord*; ARGOSS.
- [11] Hesselmanns, G.H.F.M., 1996. *SAR survey Zeegat van Ameland*, ARGOSS.
- [12] Leendertse, J.J., 1967. Aspects of a computational model for long-period water wave propagation, The Rand Corporation, memorandum RM-5294-PR, Santa Monica.
- [13] *Monthly Bulletin North Sea*, 1996. KNMI, de Bilt.
- [14] Valenzuela, G.R., 1978. Theories for the interaction of electromagnetic and oceanic waves - A review, *Boundary Layer Meteorology*, **13**, 61-85.
- [15] Shuchman, R.A., Lyzenga, D.R., and Meadows, G.A., 1985. Synthetic aperture radar imaging of ocean-bottom topography via tidal-current interactions: theory and observations. *International Journal of Remote Sensing*, **6**, 1179-1200.
- [16] Vogelzang, J., Wensink, G.J., de Loo, G.P., Peters, H.C. Pouwels, H., and van Gein, W.A., 1989. Sea bottom topography with X-band SLAR, *BCRS report*, BCRS-**89-25**.
- [17] Willebrand, J., Energy transport in a nonlinear and inhomogeneous random gravity wave field. *Journal of Fluid Mechanics*, **70**, 113-126.
- [18] Zitman, T.J., 1992. Quasi 3-dimensional current modelling based on a modified version of Davies' shape function approach. *Continental Shelf Research*, **12**, 143-158.

22. Open ocean

22.1 Sea surface height

The surface of the ocean bulges outward and inward, mimicking the topography of the ocean floor. These bulges, too small to be seen, can be measured by a radar altimeter aboard a satellite. Over the past year, data collected by the altimeters on the European Space Agency's series of ERS satellites, along with recently declassified data from the US Navy Geosat altimeter, have provided detailed measurements of sea surface height over the oceans.

These data provide the first view of the ocean floor structures in many remote areas of the Earth. For scientific applications, the Geosat and ERS-1 [2] altimeter data are comparable in value to the radar altimeter data recently collected by the Magellan spacecraft during its systematic mapping of Venus.

22.2 Seafloor mapping

The geologic and topographic structures of the ocean floor primarily reflect plate tectonic activity that has occurred over the past 150 million years of the 4.5 billion year age of the Earth. Seafloor geology is far simpler than the geology of the continents because erosion rates are lower, and also because the continents have suffered multiple collisions associated with the opening and closing of ocean basins (the Wilson Cycle). Despite their youth and geological simplicity, most of this deep seafloor has remained poorly understood because it is masked by 3-5 km of seawater. For example, the Pacific-Antarctic rise, which has an area about equal to South America, is a broad rise of the ocean floor caused by sea floor spreading between two major tectonic plates (see Figure 22-2, southeast of New Zealand).

To the west of the ridge lies the Louisville seamount chain which is a chain of large undersea volcanoes having a length equal to the distance between New York and Los Angeles. These features are unfamiliar because they were discovered less than 20 years ago. The Louisville seamount chain was first detected in 1972 using depth soundings collected along random ship crossings of the South Pacific. Six years later the full extent of this chain was revealed by a radar altimeter aboard the Seasat (NASA) spacecraft. Recently, high-density data collected by the Geosat (US Navy) and ERS-1 (European Space Agency) spacecraft show the Pacific-Antarctic Rise and the Louisville Ridge in unprecedented detail. To date, only a small fraction of the sea floor has been charted by ships.

22.3 Marine gravity anomaly measurements

Theoretically, the surface of the ocean is at the same level everywhere on Earth, and Earth's 'sea level' can be roughly represented by a perfect ellipsoid. While this ellipsoidal shape fits the Earth remarkably well, the actual ocean surface deviates by up to 100 metres from the ideal. These bumps and lows in the ocean surface are caused by minute variations in the Earth's gravitational field, and they are represented by another

theoretical surface, the 'geoid', which is a surface at mean sea level that has equal gravitational potential everywhere.

For example, a typical undersea volcano is 2000 m tall and has a radius of about 20 km. The extra gravitational attraction due to such a massive mountain on the ocean floor attracts and accumulates water towards it, causing a local bump in the ocean surface of the order of centi- or decimetres. This bump cannot be seen with the naked eye, because the slope of the ocean surface is very low.

The tiny bumps and lows in the geoid height can be measured using a very accurate radar altimeter mounted on a satellite (Figure 22-1).

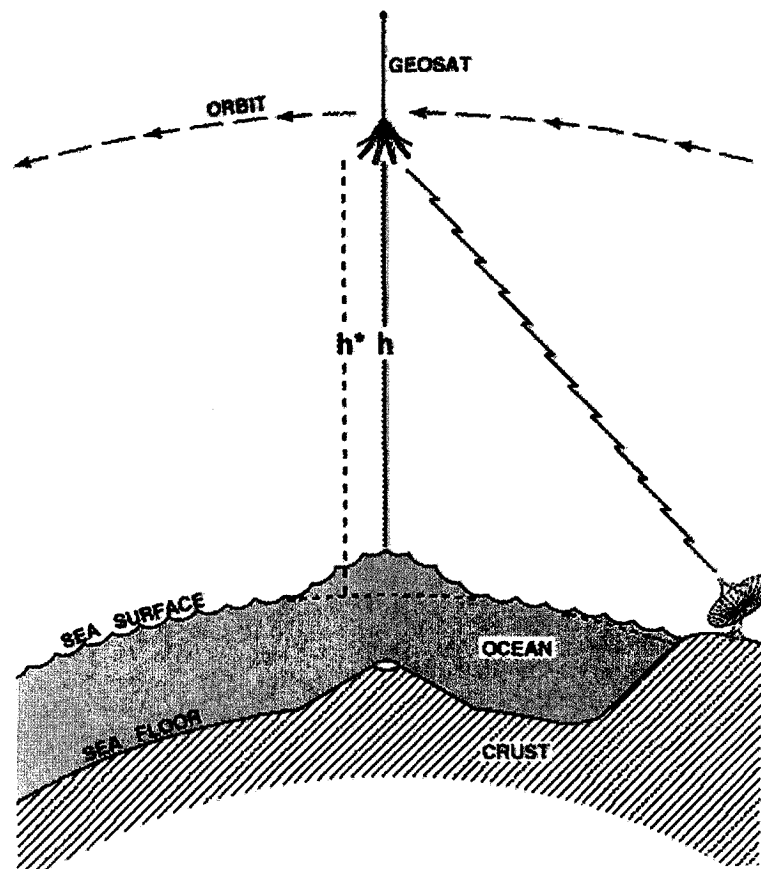
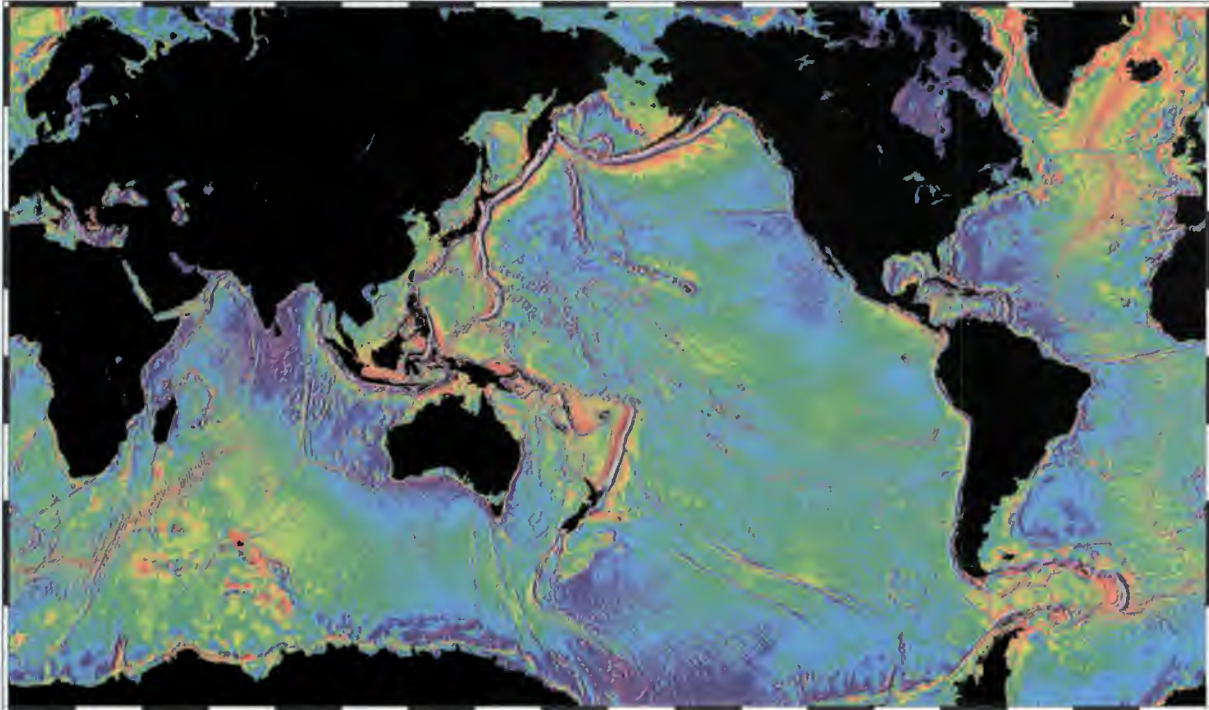


Figure 22-1:
Measuring the effect
of a seamount on
water surface

For example, the Geosat satellite was launched by the US Navy in 1985 to map the geoid height at a horizontal resolution of 10-15 km (6 - 10 mi) and a vertical resolution of 0.03 m. Geosat was placed in a nearly polar orbit to obtain high latitude coverage ($\sim 72^\circ$ latitude). The satellite orbits the Earth 14.3 times per day, resulting in an ocean track speed of about 7 km per second. The Earth rotates beneath the fixed plane of the satellite orbit, so over a period of 1.5 years the satellite maps the topography of the surface of the Earth with a ground track spacing of about 6 km [3].

As the spacecraft orbits the Earth, it collects a continuous profile of the geoid height across an ocean basin. Profiles from many satellites, collected over many years, are combined to make high-resolution images. Figure 22-2 shows gravity anomaly derived

from geoid height measurements over 4.5 years of Geosat measurements and 2 years of ERS-1 measurements.



A new method was used to convert these raw geoid height measurements, which have a variety of accuracies, track spacings and data densities, into images (or grids) of gravity anomaly. Moreover, after the conversion, the satellite-derived gravity measurements can be compared and combined with gravity anomaly measurements made by ships.

*Figure 22-2:
Gravity anomaly
map derived from
satellite geoid
height
measurements [1]*

22.3.1 Plate tectonics

These satellite altimeter data provide an important and definitive confirmation of the theory of plate tectonics. Indeed, almost everything apparent in the marine gravity field was created by the formation and motion of the plates. The Indian Ocean Triple Junction (27 deg S latitude, 70 deg E longitude) is a textbook example of seafloor spreading (Figure 22-3).

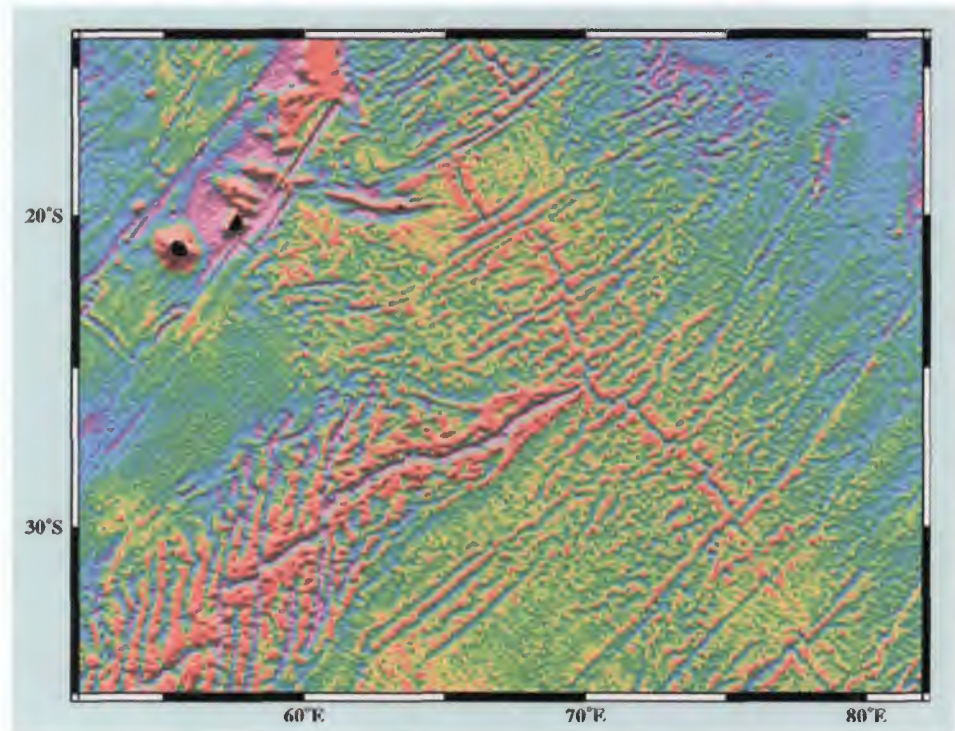


Figure 22-3: The Indian Ocean Triple Junction [1]

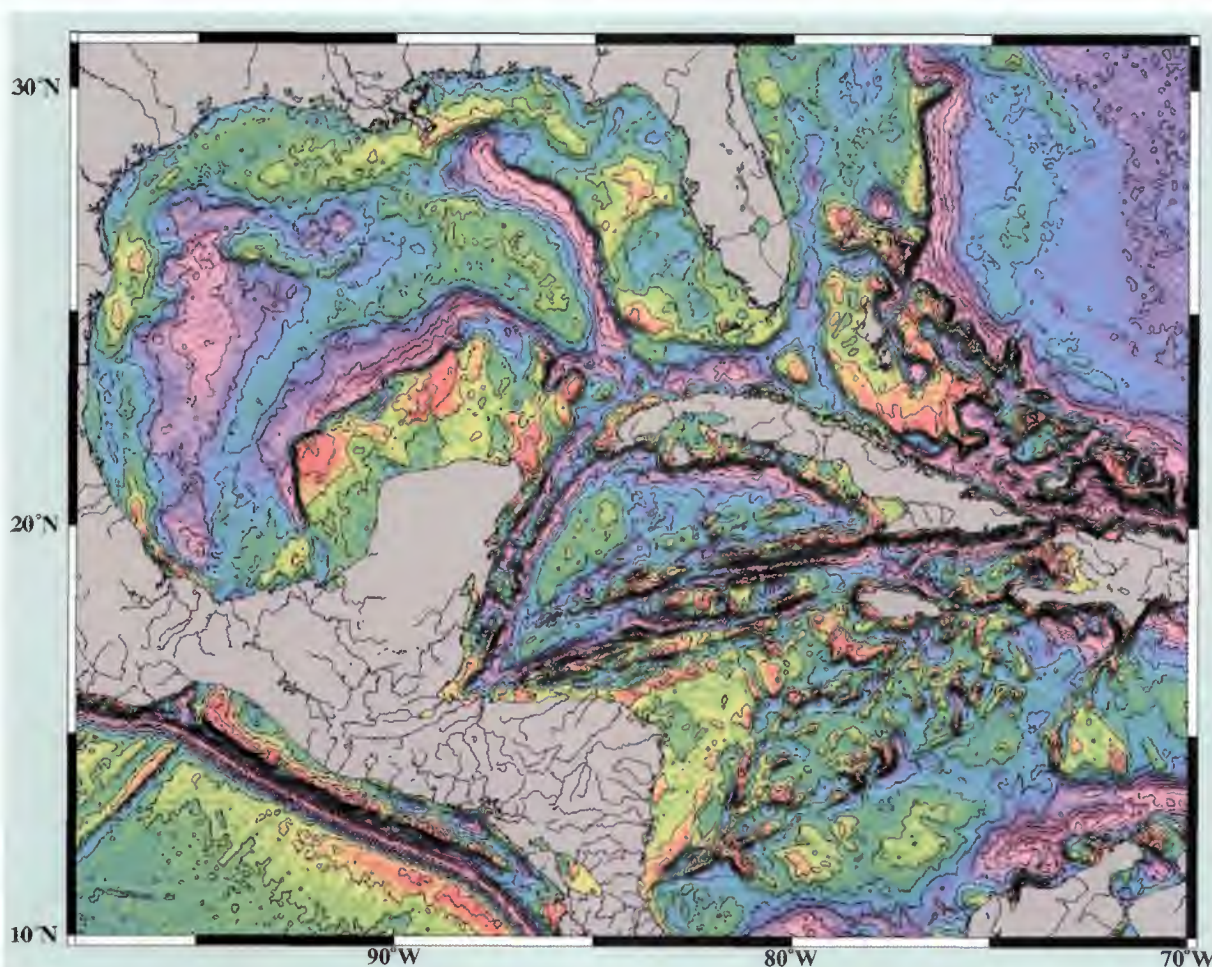
Spreading ridges are characterised by an orthogonal pattern of ridges and transform faults. The scar produced in the active transform valley is carried by seafloor spreading out onto older seafloor leaving evidence of the past plate motions. At this Indian Ocean site, three spreading ridges intersect, forming a triple junction as described by plate tectonic theory. The theory predicts that the ridges would intersect at 120° angles if the three ridges were spreading at exactly the same rate. In this case, one can measure the intersection angles and infer the relative spreading rates of each ridge.

Plates are created at spreading ridges, and subducted (destroyed) at the deep ocean trenches. All of the major ocean trenches are evident in the gravity map as linear troughs. The deep ocean basins away from the trenches are characterised by fracture zone gravity signatures inherited at the spreading ridge axis. This pattern is sometimes overprinted by linear volcanic chains that are believed to be formed as the plate moves over a stationary mantle plume. The hot plume head melts the mantle rocks, which erupt on the surface as a hot spot. Because all of these major features are evident in the gravity maps, the geologic history of the ocean basins can now be established in great detail.

22.3.2 Petroleum exploration

All of the major petroleum exploration companies use satellite altimeter gravity data from Geosat and ERS-1 to locate offshore sedimentary basins in remote areas. This

information is combined with other reconnaissance survey information to determine where to collect or purchase multi-channel seismic survey data. Currently, the regions of most intense exploration interest are the continental shelves of Australia and the former Soviet Union. Recently certain companies have expressed interest in the Caspian Sea. Developments in offshore drilling technology now make it economical to recover oil from continental slope areas in water once thought prohibitively deep. Figure 22-4 shows a relatively detailed gravity map of the Gulf of Mexico of the type routinely used in any type of exploration effort. It was derived from space-borne altimeter data.



22.3.3 Lithospheric structure

There are numerous other scientific applications that cannot be described in a short report. One of the traditional uses of marine gravity measurements is to estimate the thickness of the elastic portion of the tectonic plates. When a volcano forms on the ocean floor it provides a large downward load on the plate causing it to deform. This deformation appears in the gravity field as a donut-shaped gravity low surrounding the gravity high associated with the volcano itself. By measuring the amplitude and width of the gravity low and relating this to the size of the volcano as measured by a ship with an echo sounder, one can establish the thickness and strength of the elastic plate. The new satellite-derived gravity data enable researchers to perform this type of analysis

Figure 22-4:
Gravity map of the
Gulf of Mexico

everywhere in the oceans. Thus scientists can now probe the outermost part of the Earth using these and other methods [4].

22.4 References

- [1] <http://www.ngdc.noaa.gov/mgg/bathymetry/predicted/explore.HTML>
[NB case sensitive!]
- [2] *ERS User Handbook*, 1993. ESA SP-1148 Revision 1.
- [3] *McGraw-Hill Yearbook of Science and Technology*, p. 178-180, 1995.
- [4] Sandwell, D. T., 1990. Geophysical Applications of Satellite Altimetry, *Reviews of Geophysics Supplement*, p. 132-137.

Annexes



Annex A: Key points of ESA SAR missions and data application

Observations of the Earth using SAR instruments on board ERS and Envisat have a wide range of practical applications, including those listed below.

On the oceans

- Most man-made illegal or accidental oil spills are clearly visible on radar images.
- Both natural and man-made seepage from oil deposits can be observed.
- Ships can be detected, tracked from their wakes, and often their speeds assessed.
- Scientists can study the radar backscatter from the ocean surface related to winds and currents, fronts, eddies and internal waves.
- In shallow waters, SAR imagery allows inference of the bottom topography.
- The ocean waves and their direction of displacement can be derived from data provided by ERS SAR sensors operating in 'Wave Mode'. This provides inputs for forecasting sea conditions and for marine environmental studies.
- At high latitudes, SAR data is very useful for local and regional ice monitoring. Information such as ice type and ice concentration can be derived, and open leads detected. This is essential for navigation and operation in ice-infested waters.

On land

- The ability of SAR to penetrate cloud coverage makes it particularly valuable in frequently cloudy areas such as the tropics. Image data serves both for land mapping and monitoring and for forestry and agriculture studies.
- Geological and geomorphological features are enhanced in radar images thanks to the oblique viewing of the sensor and to its ability to penetrate – to a certain extent – vegetation coverage, and dry and unconsolidated sediments.
- Due to the precisely-known orbit of ERS, SAR data can be used for geocoding other satellite images and also to update thematic maps frequently and cost-effectively, due to its availability regardless of weather conditions.
- In the aftermath of a flood, the ability of SAR to penetrate clouds is extremely useful. Here SAR data can help to optimise rescue operations and to assess damage.

- The emergent technique of SAR interferometry (InSAR) can be used, under suitable conditions, to derive digital elevation models (DEM), or to detect small surface movements (of the order of few centimetres) caused by earthquakes, landslides or glacier movement. This is called differential interferometry. During the so-called ERS-1/ERS-2 tandem phase, which lasted for about nine months until May 1996, and occasional subsequent acquisitions in this configuration up to March 2000, data could be collected worldwide with two data acquisitions of precisely the same area within 24 hours.

Envisat

Envisat was launched on 1 March 2002. Like ERS, it is a polar-orbiting Earth observation platform, which provides data about the atmosphere, oceans, land, and ice, over at least a five-year period. Regarding the sensors and instruments on board, there are several new products with respect to the ERS payload. Nevertheless, Envisat will ensure the continuation of measurements and images provided by ERS-1/2. Envisat data follows the ERS endeavour in supporting Earth science research, and continues monitoring environmental and climatic changes.

With respect to SAR data applications, the Advanced Synthetic Aperture Radar (ASAR) on board Envisat, operating at C-band, ensures continuity of SAR image and wave mode data provision. The ASAR has a greater coverage, range of incidence angles, and polarisation, and more modes of operation. This enhanced capability is provided by significant differences in instrument design:

- Full active array antenna equipped with distributed transmit/receive modules which provide distinct transmit and receive beams
- Digital waveform creation for pulse (chirp) generation
- Block adaptive quantisation scheme, and a ScanSAR mode of operation by beam scanning in elevation

Compared with ERS-AMI, the ASAR is a significantly advanced instrument employing a number of new technological developments that allow extended performance. The most important change consists of the replacement of AMI's centralised system (a high-power amplifier with a passive waveguide slot array antenna) by an active phased-array antenna system based on the use of distributed elements. This new development will allow the selection of different swaths with maximum swath coverage of more than 400 km by using ScanSAR techniques. The possibility of changing transmission and reception polarisation modes will allow multi-polarisation analysis of the same image.

The ERS high-resolution products PRI, SLC, GEC and GTC remain unchanged for ASAR image mode, and, on user request, they will be generated also for alternating polarisation mode.

Annex B: Finding out more

This annex provides information about the different ways of accessing information and data from ESA and from its Earth observation satellites ERS and Envisat.

General information about ESA and its programmes may be found on the internet at:

www.esa.int

Specific information on Earth observation, the services provided and the description of the different missions and their products are located at:

<http://earth.esa.int>

This address also gives access to free software for reading and processing ERS and Envisat data, to data examples and applications, and to the on-line and off-line catalogues such as the EOLI Multimission on-line catalogue:

<http://odisseo.esrin.esa.it/eoli/eoli.html>

and the EOLI Envisat on-line catalogue:

<http://muis-env.esrin.esa.it/servlets/template/welcome/entryPage2.vm>

For the scientific use of ESA Earth observation data, an on-going 'Announcement of Opportunity' has been established. Access to the relevant information is through:

<http://eopi.esa.int/esa/esa>

An educational website has also been created for secondary schools and lower university level. Please connect to:

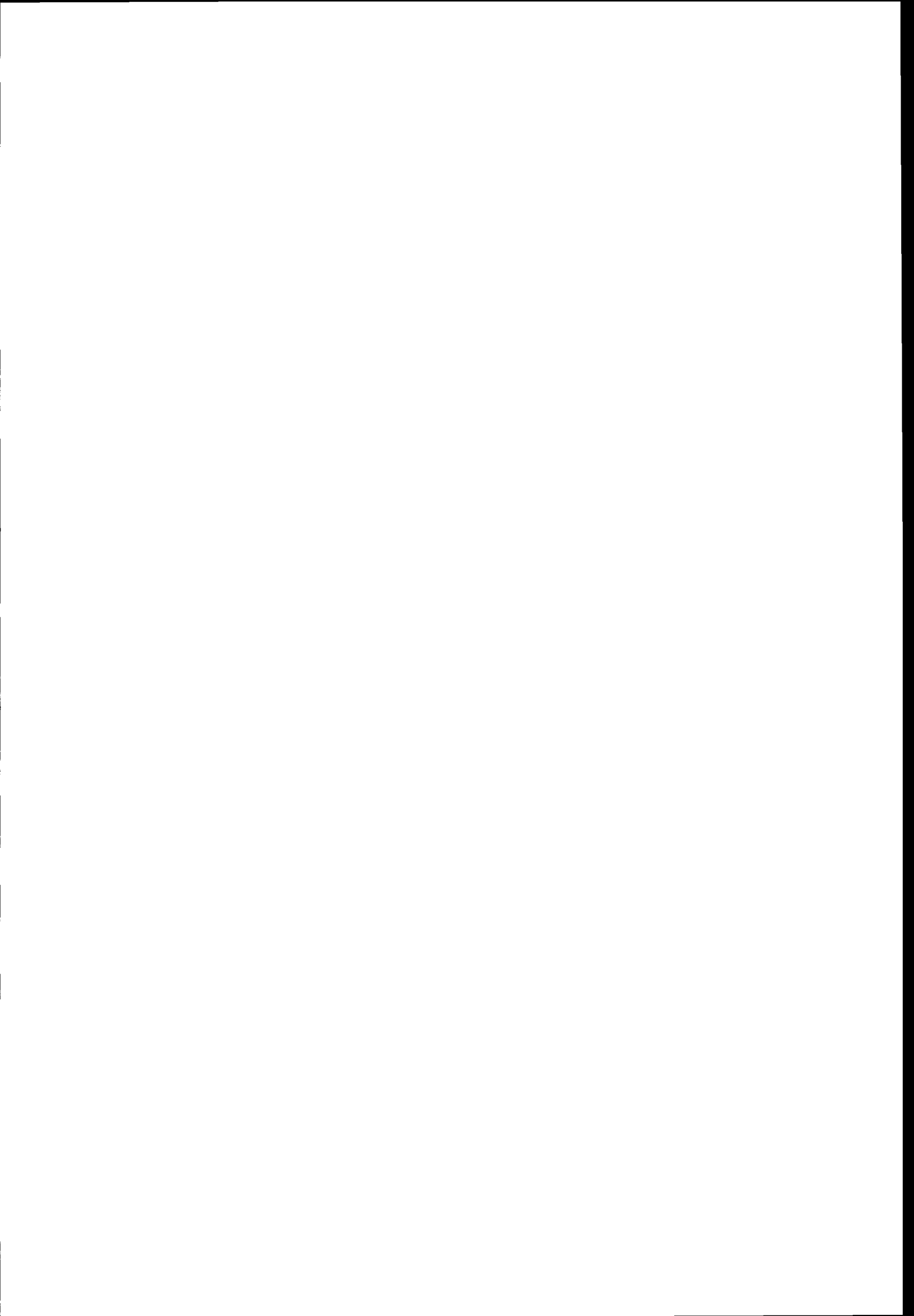
www.eduspace.esa.int/

Any further information, especially regarding data access and products, as well as paper copies and CDs of relevant ESA publications, can be obtained through the EO Helpdesk:

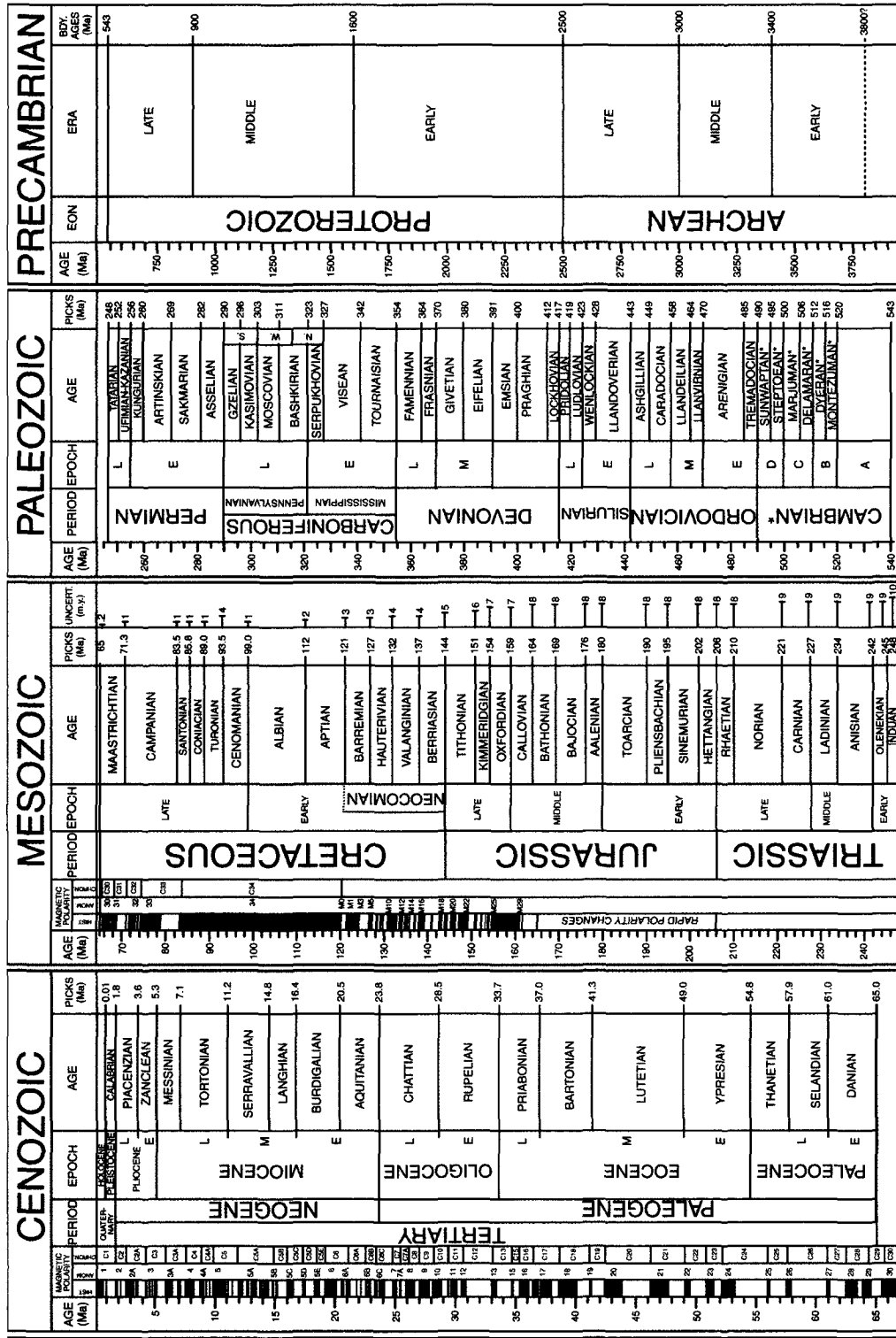
EOHELP

ESA ESRIN
Via Galileo Galilei
CP64
00044 Frascati, Italy

Tel. 39 06 941 80 666
Tel. 39 06 941 80 777
Fax. 39 06 941 80 272



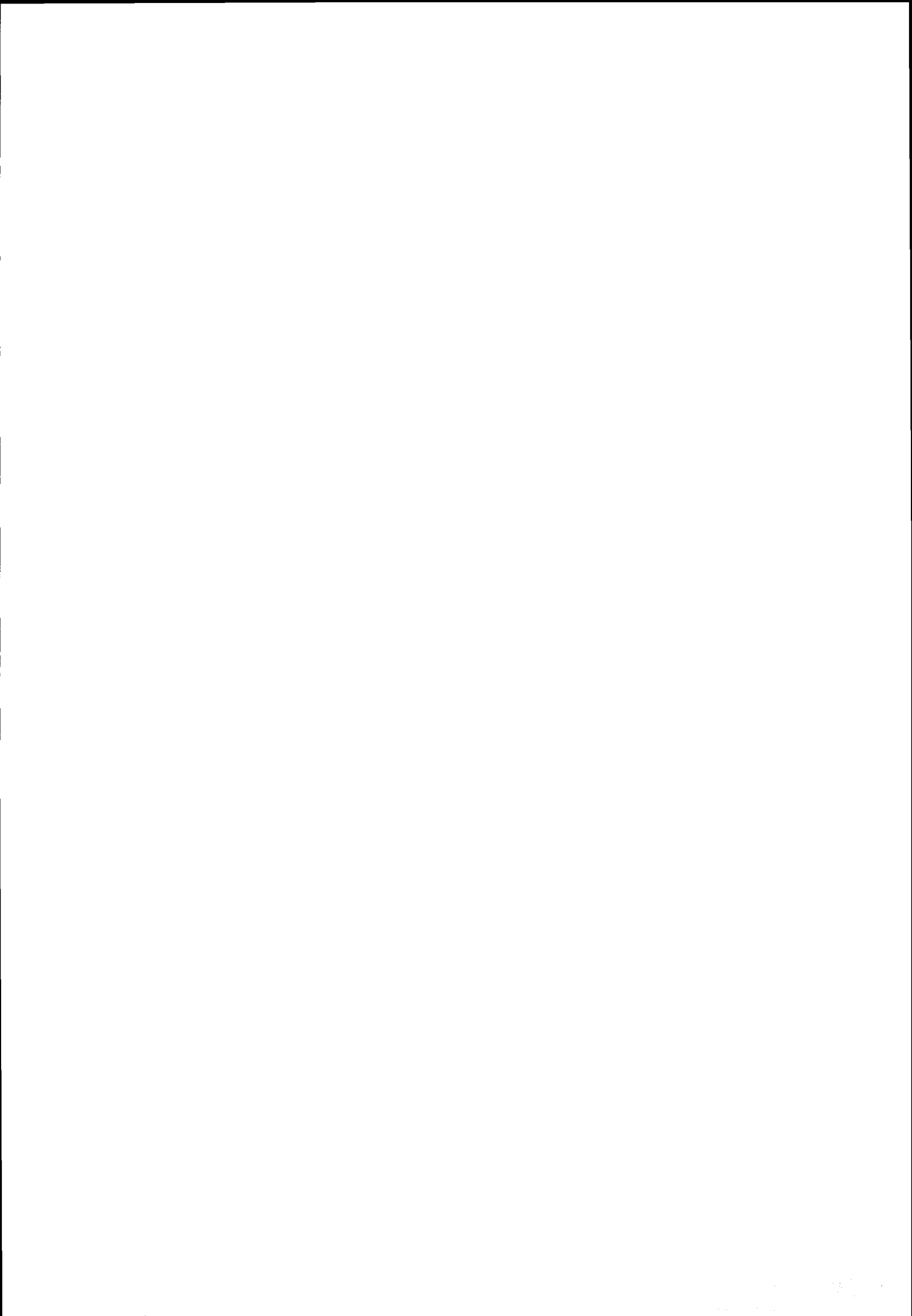
Annex C: Geological timescale



© 1999, The Geological Society of America. Product code CTS004. Compilers: A. R. Palmer, John Geissman
 *International ages have not been established. These are regional (Laurentian) only. Boundary pickets were based on dating techniques and fossil records as of 1999. Paleomagnetic attributions have errors. Please ignore the paleomagnetic scale.

Sources for nomenclature and ages: Primarily from Gradstein, F., and Ogg, J., 1996, *Episodes*, v. 19, nos. 1 & 2; Gradstein, F., et al., 1995, *SEPM Special Pub. 54*, p. 95-128; Berggren, W. A., et al., 1995, *SEPM Special Pub. 54*, p. 129-212; Cambrian and basal Ordovician ages adapted from Landing, E., 1998, *Canadian Journal of Earth Sciences*, v. 35, p. 329-338; and Davidek, K., et al., 1998, *Geological Magazine*, v. 135, p. 305-309. Cambrian age names from Palmer, A. R., 1998, *Canadian Journal of Earth Sciences*, v. 35, p. 323-328.

GEOLOGICAL SOCIETY OF AMERICA



wrench fault

A type of strike-slip fault in which the fault surface is vertical, and the fault blocks move sideways past each other. Given the geological complexity of some deformed rocks, including rocks that have experienced more than one episode of deformation, it can be difficult to distinguish a wrench fault from a strike-slip fault. In addition, areas can be deformed more than once or experience ongoing structuring such that fault surfaces can be rotated from their original orientations.

terrane	Any rock formation or series of formations or the area in which a particular formation or group of rocks is predominant
Tethys	The Tethys sea was a shallow sea that existed during the early Mesozoic Era. It was the body of water that separated the landmass of Laurasia in the north from Gondwanaland in the south. It covered what is now southern Europe. (Laurasia was the northern supercontinent, and included what are now North America, Europe, Asia, Greenland, and Iceland; Gondwanaland, also known as Gondwana, was the southern supercontinent and included what are now South America, Africa, India, Australia, and Antarctica.)
topography	Configuration of a surface including its relief and the position of its natural and man-made features
transcurrent	Two compartments separated by a large fault that have moved horizontally in opposite directions, parallel to the fault line.
transform	Transform plate boundaries that are characterized by transcurrent movements
transpression	The simultaneous occurrence of strike-slip faulting and compression, or convergence, in the Earth's crust. In areas of transpression, rocks can be faulted upward to form a positive flower structure.
transtension	The simultaneous occurrence of strike-slip faulting and extension, rifting, or divergence in the Earth's crust. In areas of transtension, rocks can be faulted downward to form a negative flower structure.
UPS	Universal Polar Stereographic [coordinate system]
UTM	Universal Transverse Mercator [coordinate system]
VH	Vertical polarisation for Tx, horizontal for Rx
virgation	A change in strike of fault lines
VV	Vertical polarisation for Tx and Rx
WGS 84	World Geodetic System 1984: an Earth-fixed Cartesian coordinate system based on an ellipsoid, used as the reference for GPS
Wilson Cycle	In plate tectonic theory, Earth history, at its simplest, is one of plates rifting into pieces diverging apart and new ocean basins being born, followed by motion reversal, convergence back together, plate collision, and mountain building. This cycle of opening and closing ocean basins is the Wilson Cycle.

speckle	A variation caused by coherent radiation. It is explained by the presence of the scattering from many different objects within each resolution cell interfering positively or negatively with each others. The resulting brightness is random, but it is grouped around a typical mean value for a homogeneous object observed. Visually it creates a 'salt and pepper' effect.
strike	The horizontal direction component of a planar geological feature. The strike is always at a right angle to the dip of the plane.
strike slip	A fault in which two sections of rock have moved horizontally in opposite directions, parallel to the line of the fracture that divided them. Strike-slip faults are caused by shearing stress.
structural contour maps	Representations of subsurface stratigraphic and tectonic contacts between geologic units
structural sections	Observed or inferred distribution of rock deformations on a vertical plane
subduction	A plate tectonic process in which one lithospheric plate descends beneath another into the asthenosphere at a convergent plate margin
suture zone	The area where two continental plates have joined together through continental collision. Suture zones are found in mountain ranges, such as the Himalayas and the Alps.
syncline	A folded rock unit in which the beds dip towards each other from either side
syndepositional	Sedimentation (deposition) was occurring at the same time as faulting
synorogenic	Formed or occurring during an orogenic movement
synthetic aperture	The distance travelled by the radar while the object was in view
talweg	The line of lowest points along a valley floor, normally the stream channel
tectonic escape	Lateral motion of tectonic wedges driven by forces applied to their boundaries; material being squeezed out by tectonic plates colliding
tectonics	Deformation of the Earth's lithosphere or the forces involved in or producing such deformations, and the resulting rock structures and external forms The unifying geologic theory developed to explain observations that interactions of the brittle plates of the lithosphere with each other and with the softer underlying asthenosphere result in large-scale changes in the Earth.

Schmidt projection	The equal area projection, also known as the Lambert projection, is generated by the following method: a point A on the surface of the sphere is projected to point B by swinging it in an arc centred at the point of contact of the sphere and a horizontal surface upon which it stands. If this process is repeated for a number of points, defined by the intersection of equally spaced longitude and latitude circles on the surface of the sphere, an equal area net will be generated. This net has a larger diameter than the sphere.
seamount	Isolated or comparatively isolated submarine mountain rising above the deep-sea floor, commonly between 1,000 and 3,000 metres, and having the summit 300 to 2000 metres below sea level
sigma nought, sigma zero (σ^0)	Radar backscattering coefficient: average reflectivity per unit area of the scene Sigma nought (decibel) = 10 log (digital value + calibration constant)
sigmoid	Curved in two directions like the letters S or Z
sill	Sills are magmatic intrusions along open fractures
sinistral	Pertaining to a strike-slip or left-lateral fault in which the block observed across the fault moves to the left of the observer; also called a sinistral strike-slip fault. If it moves to the right, the relative motion is described as dextral.
slant range	The distance from the radar to each feature in the scene. This can be converted by analysis into ground range
SLAR	Side-Looking Airborne Radar
SLCI	Single-Look Complex Image
slickensides	The smooth, striated, or partially polished surfaces of a fault, supposed to have been produced by the sliding of one surface rock on another
spatial resolution cell	The detail discernible in an image is dependent on the spatial resolution of the sensor, which refers to the size of the smallest possible feature that can be detected. The area on the Earth's surface that is 'seen' at one particular moment in time is called the resolution cell and determines a sensor's maximum spatial resolution.

pyroclastic	A pyroclastic flow is a ground-hugging avalanche of hot ash, pumice, rock fragments and volcanic gas that rushes down the side of a volcano as fast as 100 km/hour or more. The temperature within a pyroclastic flow may be greater than 500° C, sufficient to burn and carbonise wood. Once deposited, the ash, pumice, and rock fragments may deform (flatten) and weld together because of the intense heat and the weight of the overlying material.
RADAR	RAdio Detection And Ranging
radar backscattering coefficient	Average reflectivity per unit area of the scene (σ°)
range	Sideways direction (relative to satellite travel)
RAR	Real Aperture Radar
reg	A vast stony plain in a desert
relay zone	The deformed zone between two overlapping faults striking in the same direction
rollover structure	A monoclinial half anticline structure affecting layers in a graben, bounded on the one side by a large (large throw) listric (concave in vertical section) normal fault, and progressively connecting with sub-horizontal layers on the other side. Numerous small (small throw) normal faults affect the rollover structure. This is the result of extension in the crust along a normal fault.
rose diagrams	Rose diagrams explain the frequency of fractures in a given orientation
SAR	Synthetic Aperture Radar
satellite path length	Distance between the object and the sensor
scarp	A line of cliffs produced by faulting or erosion
schistosity	Schistosity develops when mica, chlorite, and talc form larger, visible crystals and, as a result, the rock develops a planar orientation with crystals large enough to see
Schmidt nets	Symbolic plots representing structural objects (planes, poles of planes, lines on nets, also known as stereographic or equal-area plots of poles).

NDVI	Normalized Digital Vegetation Index, computed: $\text{NDVI} = (\text{NIR} - \text{VIS}) / (\text{NIR} + \text{VIS}),$ where NIR is Near InfraRed wavelength, VIS is a Visible wavelength
obducted	During convergence between two plates, the oceanic crust of one plate may laterally be pushed over the continental crust of another one
ophiolitic	Ophiolitic rocks were formed by magmatic effusions in the sea, especially at accretion ridges or in backarc volcanic regions. The weathering in contact with seawater is responsible for a greenish aspect of snake-like skin.
orogeny	The process of mountain-making, especially by uplift of the Earth's crust
PAF	Processing & Archiving Facilities
palaeo channels	Ancient drainage channels
Palaeotethys	An ancient ocean of Palaeozoic age
PC	Principal Component
PCA	Principal Component Analysis
pegmatite (pegmatitic)	A natural igneous rock formation consisting of a variety of granite that is usually characterised by extremely coarse texture due to the occurrence of crystals of large dimension
pelagic	Of, relating to, or constituting a biogeographic realm consisting of the open sea and especially those portions beyond the outer border of the littoral zone which are above the abyssal zone and to which light penetrates
penepplain	A land surface reduced by erosion to the general condition of a plain, but not wholly devoid of hills; a base-level plain
pericline	The round shape of layers at one end of a fold
piedmont	Any area forming the foot of a mountain
polje	An extensive depression having a flat floor and steep walls but no outflowing surface stream and found in a region having karst topography (as in parts of Yugoslavia)
PRI	PRrecision Image [SAR product]
prograde	To build outward toward the sea by deposition of sediment

lineament	A topographic feature, especially one that is rectilinear or gently curved, of great length, and generally considered to reflect deep structures in the crust
lithofacies	A facies characterised by a particular lithologic aspect
lithology	The character of a rock formation expressed in terms of its structure, mineral composition, colour & texture
lithosphere	1. The solid portion of the Earth (distinguished from atmosphere, hydrosphere). 2. The crust and upper mantle of the Earth
littoral	Coastal zone, tidal zone
littoral zone	The shore zone between high and low water marks
look direction	The angle between geographic North and the direction in which the radar beam is pointing, i.e. perpendicular to the flight direction.
Ma	Unit: million years
marl	A loose or crumbling earthy deposit that contains chiefly calcium carbonate or dolomite mixed with clay
massif	A block of the Earth's crust bounded by faults or flexures and displaced as a unit without internal change
metabasites	Metamorphosed magmatic rocks characterised by low content in quartz, issued from the mantle
molasses	Rock units composed of alternating beds of coarse-grained or conglomeratic material and of thin-grained or clayey material, that were deposited in a continental environment, mainly from erosion of uplifting mountains
morphology	The external structure of the Earth in relation to the development of erosional forms or topographic features due to geodynamics
MSS	Multi-Spectral Scanner (Landsat product). A Landsat MSS image of a scene consists of four separate digital images taken in different spectral bands.
NAF	North Anatolian Fault
nappe	A large landmass thrust over other rocks by thrust faulting

ground truth	Measurements taken for calibration of satellite measurements. A person on the ground (or in an aeroplane) makes a measurement of the same thing the satellite is trying to measure, at the same time the satellite is measuring it. The two answers are then compared to help evaluate how well the satellite instrument is performing.
GTC	Geocoded & Terrain Corrected (ERS product)
HH	Horizontal polarisation for Tx and Rx
HV	Horizontal polarisation for Tx, vertical for Rx
IHS	Intensity, Hue, Saturation
InSAR	Interferometric SAR
inselberg	An isolated mountain, partly buried by the debris derived from and overlapping its slopes
karst	A limestone region marked by sinks, abrupt ledges, irregular protuberant rocks, caverns, and underground streams
kernel	A type of filtering
lacustrine	Of, relating to, or formed in lakes
lahar	A rapidly flowing mixture of rock debris and water that originates on the slopes of a volcano. Also referred to as volcanic mudflows or debris flows. They form in a variety of ways, chiefly by the rapid melting of snow and ice by pyroclastic flows, intense rainfall on loose volcanic rock deposits, breakout of a lake dammed by volcanic deposits, and as a consequence of debris avalanches.
laterite (lateritic)	Soil rich in hydroxides of aluminium and iron, and formed under conditions of humid tropical or sub-tropical climate, over rocks that are originally poor in silicium
layover	An extreme form of relief displacement (foreshortening) that occurs in hilly and mountainous regions, where the tops of mountains appear closer to the radar than the bottoms. In layover, the slope angle is steeper than the wave front
lead	A channel of water through a field or floe of ice
leucogranite	White granite, poor in ferro-magnesian minerals
levee	The very low ridge sometimes built up by streams on their floodplains on either side of their channels

foreshortening	Relief displacement; compression of the range dimension of an elevated object towards the direction from which the radar is looking. [see also: layover] In foreshortening, the radar wave front is steeper than the slope angles
fusulins	A type of microfossils that are characteristic of the late Palaeozoic, associated with a shallow marine environment
GEC	GEOCoded image (ERS product)
geodesy	A branch of applied mathematics that determines by observation and measurement the exact positions of points and the figures and areas of large portions of the Earth's surface, the shape and size of the Earth, and the variations of terrestrial gravity and magnetism
geodetic	Pertaining to geodesy
geoid	The imaginary surface within or around the Earth that coincides with mean sea level in the oceans, and approximates to the shape of an ellipsoid of revolution An imaginary surface employed by geodesists, which has the property that every element of it is perpendicular to the plumb line where that line cuts it (it is everywhere normal to the direction of gravity). Predicted height of surface due to gravity alone. Compared with the 'spheroid of reference', the surface of the geoid is in general depressed over the oceans and raised over the great landmasses.
geomorphic	Relating to the form of the Earth or its surface features
GIS	Geographic Information System
graben	A depressed segment of the Earth's crust, bounded by faults, and generally of considerable length as compared with its width
granodiorite	Granodiorite is an intermediate-coloured, medium- to coarse-grained igneous rock derived from magma that has cooled and solidified deep in the crust of the Earth. It falls between granite and quartz diorite, containing more dark minerals than granite but less than quartz diorite.
gravity waves	A wave propagated in the surface layers of water or other liquid because of the tendency of gravity to maintain a uniform level.
ground range	The distance along the ground in the direction between the spacecraft and the imaged object. This is generated by analysis from the slant range.

EOLI	Earthnet On Line Interactive [ESA remote-sensing catalogue]
ERS	Earth Remote Sensing
exotic arc terranes	Arc terranes that come from another region
extension fracture	Fracture in which the sides did not slip against each other but moved apart, forming an open gap
extrados	The exterior curve of a fold
facies	The appearance and characteristics of a rock, esp. as they reflect the conditions and environment of its formation and evolution.
fault	A fracture in the Earth's crust accompanied by a displacement of one side of the fracture with respect to the other and in a direction parallel to the fracture
ferralitic	Red soil forming in humid tropical climate, poor in Si and rich in hydroxides of aluminium and iron
firn	Granular, partially consolidated snow on high glaciers that has passed through one summer melt season but is not yet glacial ice. Also called old snow.
flatirons	(In the Western U.S.) a triangular hogback that resembles a flatiron resting on its base. Main steps in creating the Flatirons: deposition of relatively flat layers of sediment which were covered with younger layers and transformed to rock followed by later uplift, folding and erosion.
flexure	Half a fold between layers that have the same dip and strike
flysch	A thick and extensive deposit, largely of sandstone alternating with clay, that was formed underwater in a basin adjacent to a rising mountain belt and is especially common in the Alpine region of Europe
fold	A bend into an arch or trough produced in rock by forces operative after the deposition or consolidation of the rock
foredeep	A sedimentary basin fronting a mountainous land area
foreland	The loading of a thrust belt produces an asymmetric depression, conventionally regarded as a fixed foreland, with its deepest point next to the belt. In many fold-thrust belts, the foreland continued to subside even after folding and thrusting began. Material eroded from the uplifted thrust belt is deposited in the depression, forming a type of sedimentary basin known as a foreland basin.

decollement	<p>A detachment fault; a fault where crustal deformation causes separation along a boundary of rock types, typically between so-called crystalline 'basement' rock and overlying sedimentary rocks.</p> <p>A fault surface parallel to a mechanically weak horizon or layer, or parallel to bedding, that detaches or separates deformed rocks above from undeformed or differently deformed rocks below. Decollements, or decollement surfaces, are typical of regions of thrust faulting such as the Alps.</p>
DEM	Digital Elevation Model
dendritic (pattern)	An arrangement of stream courses that, on a map or viewed from the air, resemble branching habit of certain trees, such as oaks or maples
DESCW	Database available at ESA
detachment fault	A nearly horizontal extensional fault at the base of a fault system.
dextral	Pertaining to a strike-slip fault or right-lateral fault in which the block across the fault moves to the right. If it moves left, the relative motion is described as sinistral.
diorite	A granular crystalline igneous rock that is poor in quartz
disconformity	A break in a sequence of sedimentary rocks, with differences in dip and strike between the ancient and more recent units; there is also often an interruption of sedimentation generally by an interval of erosion
DN	Digital Number
drag fold	A minor geological fold produced along a fault or in soft or thinly laminated beds lying between harder or more massive beds in the limbs of a major fold
ductile	Type of rock deformation that is characterised by the re-arrangement of elements (minerals or groups of minerals) without fracturing
EAF	East Anatolian Fault
endoreic	Referring to a region of interior drainage; a region whose water drains to interior lakes and is lost only by evaporation, but otherwise never returns to the oceans
en echelon	An arrangement of geologic features (as mountains, folds, fractures) in a pattern resembling that of a military echelon [in a series of steps, each behind and to the side of the previous one]

bedding plane	Surface separating layers of sedimentary rocks. Each bedding plane marks termination of one deposit. Rock tends to separate, or break, readily along bedding planes.
breccia	A rock consisting of sharp stone fragments embedded in a fine-grain matrix (as sand or clay)
caldera	A crater whose diameter is many times that of the volcanic vent because of the collapse or subsidence of the central part of a volcano or because of explosions of extraordinary violence
chirp technique	Variation of frequency within a pulse
CIR	Colour infrared film
clastation	Physical disintegration and chemical decomposition of earthy and rocky materials on exposure to atmospheric agents, producing an in-place mantle of waste
clastic	Being or pertaining to a sedimentary rock composed primarily from fragments of pre-existing rocks or fossils
clinometry	Measurement of angles of slope, elevation or inclination
coeval	Originating in the same era or epoch
competent (adj.)	Describes relatively brittle, solid strata that deform by faulting, fracturing or folding, rather than flowing under stress. Incompetent beds are more ductile and tend to flow under stress, so their bed thickness changes more readily during deformation.
conjugate faults	Describes a pair of intersecting (or nearly intersecting) faults of the same age, the slip motions of which are opposite (e.g. right-lateral and left-lateral), so as to accommodate the rotation of the block they bound.
continental shelf	Low lying area of the continental crust that is covered by shallow seawater at the border of an ocean.
craton	Relatively non-deformable part of the Earth, generally large central portion of a continent. Cratons were formed during the Archean time
DDS	Direct Decorrelation Stretch

apron	An extensive usually unconsolidated alluvial, glaciofluvial, eolian or marine deposit spread outward from an identifiable source
arc terrane	Series of rock units that were formed by activity of back-arc volcanism and subsequently displaced under the effects of plate movements to finally be added to another continental crust
arkose	A sandstone derived from the rapid disintegration of granite or gneiss, and characterised by feldspar fragments associated with quartz grains
ASAR	Advanced SAR
atmospheric artefacts	Erroneous phase changes in InSAR images caused by variable atmospheric conditions
aureole	An aureole zone is where rocks show the effect of intruding hot igneous rock, also called contact metamorphism.
autochthon	Rock essentially in its place of origin
azimuth	The direction of travel of the satellite
back-arc volcanism	Clusters of cinder cones and shields in extensional settings, composed of magmas with low to negligible slab signatures and rare olivine phenocrysts. Formed by decompression melting. Moderate Holocene activity
backscatter	<p>The scattering of radiation in a direction approximately opposite to that of the incident radiation and due to reflection from particles of the medium traversed</p> <p>The (microwave) signal reflected by elements of an illuminated scene back towards the radar. It is named to make clear the difference between energy scattered in arbitrary directions, and that which returns to the radar and therefore may be received and recorded by the sensor.</p>
BAS	Bathymetry Assessment System [a suite of computer models]
basalt	The commonest type of solidified lava issued from the mantle
batholite	A great mass of intruded igneous rock that for the most part stopped in its rise a considerable distance below the surface, before erosion, and that extends downward to unknown depth
bathymetry	The measurement of depths of water in oceans, seas and lakes
bayoneted	The shape of linear features that are like the zigzag pattern of a bayonet

Annex D: Glossary

accretion	The increase or extension of the boundaries of plates by the gradual or imperceptible action of natural forces, mainly in oceanic ridges
active tectonics	On-going deformation of the Earth crust
asthenosphere	The relatively plastic layer of the upper mantle of the Earth on which the tectonic plates of the lithosphere move. The asthenosphere is approximately 200 km thick and, owing to its depth below the Earth's surface, warm (~1400°C) but not molten. Here the mantle deforms by plastic flow, in response to high applied pressures.
allochthon	An overthrust block of rocks that have been sub-horizontally moved along a gently dipping fault for a great distance from their place of origin
altitude of ambiguity	<p>The fringe rate due to topography can be reformulated to provide the error in the elevation model that will produce one fringe (2π) error in the interferogram</p> <p>The perpendicular baseline (B_{perp}, or across-track separation between the two satellite positions) means a difference in path to the same point on the ground as previously described. Each complete 360-degree fringe cycle represents a specific elevation interval for all fringes across the interferogram. This interval is known as the altitude of ambiguity, Δz, and is a function of radar wavelength, satellite altitude, incidence angle and B_{perp}</p>
alluvium (pl. alluvia)	Clay, silt, sand, gravel or similar detrital material deposited by running water during recent geologic time, the deposits ordinarily occurring on the floodplains of streams or as alluvial fans or cones at places where streams issuing from mountains lose their velocity and deposit their contained sediment on a valley floor
anastomotic	The connection of separate parts of a branching system to form a network, as of leaf veins, blood vessels, or a river and its branches
antecedent	Established before the deformation of a surface and persisting after the deformation has taken place and in spite of it – used of drainage, a stream or a valley
anticline	An upfold or arch of stratified rock in which the beds or layers dip downwards in opposite directions from the crest or axis of the fold



